A physical model for the variability properties of X-ray binaries

ADAM RUSSELL INGRAM

A physical model for the variability properties of X-ray binaries

by Adam R. Ingram

A thesis submitted to the University of Durham
in accordance with the regulations for
admittance to the Degree of Doctor of Philosophy.

Department of Physics
University of Durham
July 2012

A physical model for the variability properties of X-ray binaries

Adam R. Ingram

Submitted for the degree of Doctor of Philosophy

July 2012

Abstract

Emission from X-ray binaries is variable on a wide range of timescales. On long timescales, changes in mass accretion rate drive changes in spectral state. There is also rapid variability, the power spectrum of which consists of a low frequency quasi-periodic oscillation (QPO) superimposed on a broad band noise continuum. Here I investigate a model intended to quantitatively explain the observed spectral and variability properties. I consider a truncated disc geometry whereby the inner regions of an optically thick, geometrically thin accretion disc evaporate to form an optically thin, large scale height accretion flow. The QPO is driven by Lense-Thirring precession of the entire hot flow and the broad band noise is due to fluctuations in mass accretion rate which propagate towards the central object. Mass conservation ties these two processes together, enabling me to define a model for the QPO *and* broad band noise which uses only one set of parameters. I am thus able fit the model to data. The accretion rate fluctuations drive fluctuations in the precession frequency, giving rise to a quasi-periodic oscillation rather than a pure periodicity. The model thus predicts recent observations which show the QPO frequency to correlate with flux on short timescales. I then investigate a more unique model prediction. As the flow precesses, the patch of the disc preferentially illuminated by the flow rotates such that a non face on observer sees a quasi-periodic shift between blue and red shift in the iron K_α line. An observation of such an effect would constitute excellent evidence for the model.

Contents

List of Figures

Declaration

Declaration

Portions of this work have appeared in the following papers:

- Ingram A., Done C., Fragile P. C., 2009, MNRAS, 397, L101
- Ingram A., Done C., 2010, MNRAS, 405, 2447
- Ingram A., Done C., 2011, MNRAS, 415, 2323
- Ingram A., Done C., 2012a, MNRAS, 419, 2369
- Ingram A., Done C., 2012b, submitted to MNRAS

Acknowledgements

First of all, a huge thank you to my supervisor, Professor Chris Done, who has been an indispensable source of knowledge, ideas and (extreme) enthusiasm. Working with Chris involves a lot of white boards and many friendly arguments of which the winner is ultimately science. I also want to thank the rest of the X-ray group and the astronomy department as a whole, not just for useful discussions about science, but also for making this a great place to live and work. In particular, I'd like to thank Mari Kolehmainen and, the gravitational powerhouse, Matt Middleton.

Fundamentally intertwined in the pages of this thesis are my experiences over a wonderful 4 years in which I met my gorgeous girlfriend Natalie, who I would like to thank for her love, support and general good influence on me! This has only been the first chapter of our life together and I can't wait for the rest. I also simply have to mention the 32 Highgate days with Rog Johnson and Chris Egan, who's enthusiasm for their PhDs was one of the main factors which drove me to apply in the first place. Also, any summary of my PhD wouldn't be complete without a mention of Prodding Juliet. From the first few weeks of my PhD when I was writing the songs and talking 'big picture' with Rog, to the last few weeks when me and Tom Mitchell have been finishing off the recordings, PJ has never been far from my heart over the last 4 years. Thanks guys, I'll never forget what a great band we were!

I'd also like to thank my A-level Physics teacher, Mr McHarry, who really sparked my enthusiasm for the subject in the first place. Without his witty outbursts, who knows what I'd be doing! Last but by no means least, a big thank you to my family and, in particular, my Mam and Dad for always supporting me in everything I've done.

Chapter 1 | *Introduction*

1.1 X-ray binaries

In this thesis, I develop a physical model designed to self-consistently explain the spectral and timing properties of the X-ray emission driven by mass accretion onto a black hole or neutron star. Since black holes are the simpler of the two classes of object, they are the focus of most of my efforts. However, I also make attempts to use the same model in order to explain the common observational properties of the two object classes. In this section, I introduce these objects and the systems in which they reside.

1.1.1 Compact objects

When a star runs out of fuel to power fusion reactions, its ultimate fate is determined by its mass. For the most massive stars, a supernova explosion leaves behind the remains of its core in the form of a compact object. If degenerate neutron pressure can arrest the collapse of the core, a neutron star is formed. If the progenitor was sufficiently massive for gravitational collapse to overcome even this force, the core collapses into a singularity and a black hole is formed. A black hole has only two properties: mass and spin (in theory, a black hole could also have a charge but this is unlikely for an astrophysical black hole). The black hole horizon is defined as the point where the escape velocity is the speed of light. For a Schwarzschild black hole (non spinning), this is given by $R_S = 2GM/c^2 = 2R_g$. Here, R_g is a gravitational radius. Because this is a characteristic size scale, it is often convenient to write distances in units of

R_g. Thus, hereafter I will use the convention $R = rR_g$. Generally, the black hole is spinning and its angular momentum J_{BH} can be expressed with the dimensionless spin parameter $a_* = J_{BH}/(McR_g)$. In this case, space-time is well described by the Kerr metric and it can be shown (e.g. Kato, Fukue & Mineshige 1998) that the horizon generalises to $r_H = 1 + \sqrt{1 - a_*^2}$, which reduces to $r_H = 2$ in the Schwarzschild limit. It is also clear from this expression that $a_*^2 \leq 1$.

A key prediction of general relativity is that, in a strong gravitational field, there is a region in which there are no stable orbits. Again using the Kerr metric, it can be shown that a test mass orbiting interior to the radius of the last stable orbit, r_{lso}, will be sure to eventually fall beyond the horizon if gravity is the only force present (see e.g. Kato, Fukue & Mineshige 1998). Figure 1.1 shows the dependence of the last stable orbit on spin. Positive values of a_* are for prograde motion and negative values are for retrograde.

The fundamental difference between black holes and neutron stars is that a neutron star has a solid surface and black holes do not. However, the gravitational field experienced by the accretion flow is similar for both objects because a neutron star outer radius coincides approximately with its own last stable orbit. The exact value of neutron star mass and outer radius depends on its equation of state and is still an active area of research but for canonical assumptions, they are thought to be $M \approx 1.4 M_\odot$ and $R \approx 10$ km (see e.g. Haensel et al 2007).

1.1.2 Mass transfer in X-ray binaries

A binary system consists of two stars orbiting around a common centre of mass. In an X-ray binary (XRB), one of the stars is a compact object and mass is transferred from the companion star. The gravitational energy lost by this accreting gas can be converted very efficiently into emission which peaks in the X-rays, giving rise to the term X-ray binaries. In a high-mass X-ray binary (HMXRB), the companion star has

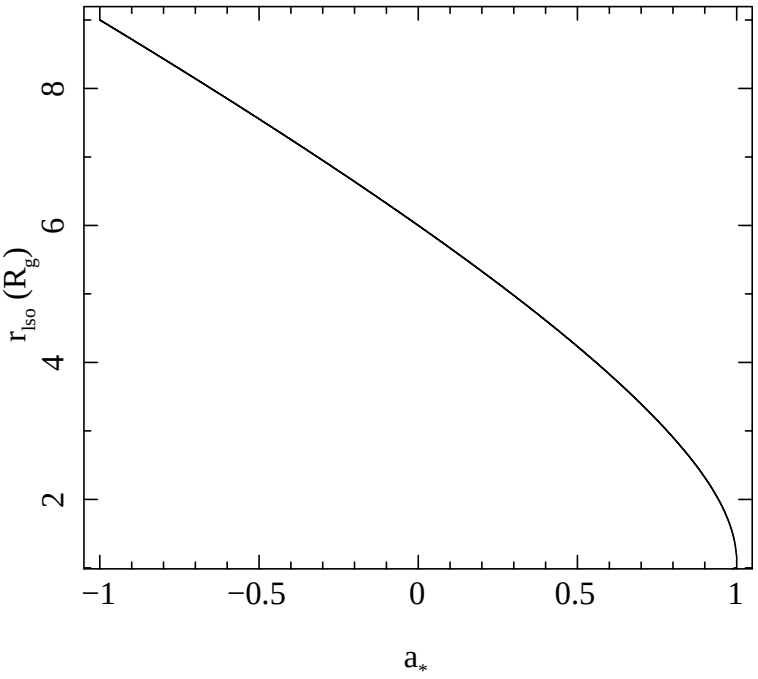

Figure 1.1: Last stable orbit as a function of the dimensionless spin parameter, a_*.

a mass typically larger than 10 $M_\odot$ meaning that it is very luminous, of spectral type O or B and is younger than $\sim 10^7$ years. In a low-mass X-ray binary (LMXRB), the companion star is typically smaller than ~ 1 $M_\odot$ and so is generally older. Figure 1.2 illustrates the Roche potential created by the gravitational pull of the two stars. If the companion star fills its Roche-Lobe, either by expansion through stellar evolution or by contraction of the binary orbit, mass can pass through the L_1 point and fall onto the compact object (see e.g. Frank, King & Raine 1992). In this thesis, I concentrate on systems in which accretion is dominated by this process of Roche-Lobe overflow (in general, accretion can also be powered by a large scale wind). This encapsulates all LMXRBs and some HMXRBs.

Gas which passes through L_1 cannot fall straight onto the compact object because it has angular momentum. Instead, particles orbit the compact object to form an accretion disc. Viscosity erodes the angular momentum of these orbits, meaning that

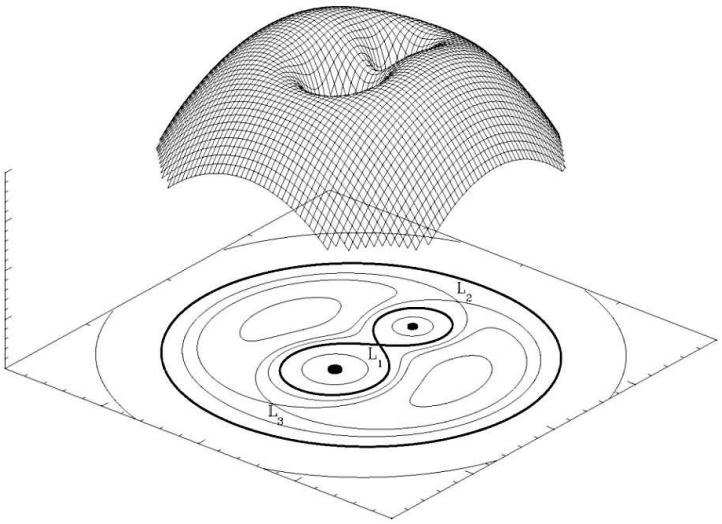

Figure 1.2: The Roche potential in a binary system. Here, the more massive of the two stars is in the foreground.

material spirals slowly inward. In a simple system, the disc will be truncated by gravity at the last stable orbit where material, rather than spiralling slowly inward, enters free fall.

The rate of gravitational energy loss in an accretion disc is proportional to the mass accretion rate, $\dot{M}$. If the disc is in thermal equilibrium, the temperature at any point of the disc is related to the luminosity as $L \propto T^4$ and therefore $T^4 \propto \dot{M}$. The mass accretion rate is not constant over long timescales if the disc is subject to the hydrogen ionisation instability. For low mass accretion rates, the disc is cool so the material is mostly neutral. Because neutral material has a much lower opacity than free electrons (e.g. Cannizzo & Reiff 1992), radiation can escape and cool the disc. However, a small increase in temperature may lead to photons in the high energy Wien tail of the thermal distribution becoming energetic enough to ionise hydrogen in some region of the disc. The resulting photo-ionised absorption edge drives a sharp rise in opacity. This heats the disc, meaning more photons can ionise hydrogen and further increase the opacity.

This runaway heating increases the local mass accretion rate, making it higher than the input mass accretion rate (coming through L_1). This reduces the density in the region thus reducing the pressure. The region cools and hydrogen recombines leading to runaway cooling (Frank, King & Raine 1992; Kato, Fukue & Mineshige 1998; Cannizzo 1993). This is a local instability but an increase in mass accretion rate will flow through to the next disc annulus, heating that region and sparking off runaway heating there. Heating and cooling waves can therefore run through the entire disc leading to a global instability. Cooling is, however, slowed because the luminous inner disc irradiates the outer disc, keeping hydrogen from recombining even at large radii (van Paradijs & McClintock 1994; van Paradijs 1996). Eventually, since the mass accretion rate is higher than that provided by the companion, the inner regions become starved of material which reduces the luminosity enough to allow hydrogen to recombine in the outer regions (King & Ritter 1998; Lasota 2001).

Although all XRBs show long time scale (i.e. days, weeks, years) variability, not all are subject to the hydrogen ionisation instability. Thus sources can be placed in one of two categories: persistent and transient. Persistent sources have been 'on' since the birth of X-ray astronomy whereas transient sources are usually 'off' but occasionally rise to outburst. Figures 1.3, 1.4 and 1.5 (reproduced from Done, Gierliński & Kubota 2007) show 1.5-12 keV light curves as seen by the all sky monitor (ASM) on board the Rossi X-ray timing explorer (*RXTE*). The luminosity is expressed as a fraction of the Eddington luminosity which is the limit whereby outward radiation pressure balances inward gravitational force giving

$$L_{Edd} = \frac{4\pi G M m_p c}{\sigma_T}, \tag{1.1}$$

where m_p is a proton mass and σ_T is the Thompson cross-section. All the sources in Figure 1.3 are black hole (BH) HMXRBs with mass transfer dominated by Roche-Lobe overflow, Figure 1.4 is for BH LMXRBs and Figure 1.5 is for neutron star (NS) LMXRBs. We see that all of the BH HMXRBs are persistent sources and all of the

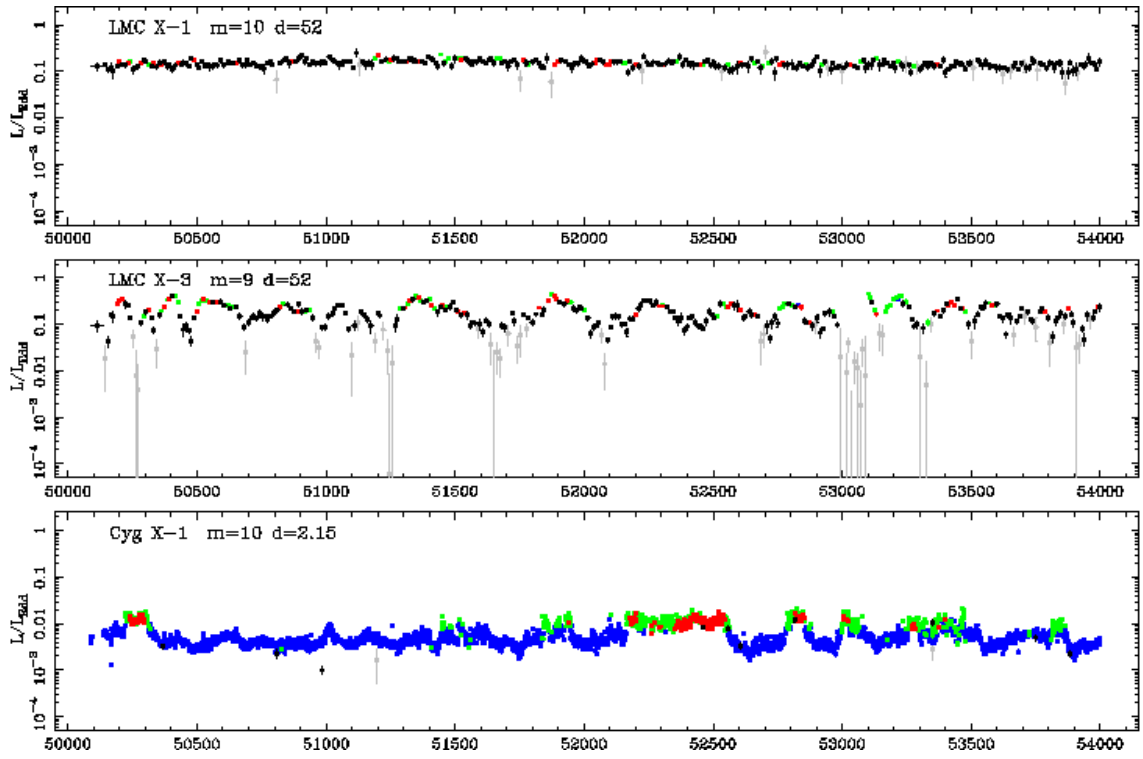

Figure 1.3: Long term light curves for a selection of BH HMXRBs as seen by the *RXTE* ASM (with mission days on the x-axis).

BH LMXRBs are transient sources. Thus the outer disc in BH HMXRBs is always hot enough for hydrogen to be ionised. This is partly because of a high input mass accretion rate and also due to irradiation from the companion star (van Paradijs 1996; Menou, Narayan & Lasota 1999). The outer disc for BH LMXRBs, in contrast, is cooler thus the hydrogen ionisation instability causes transient behaviour. Figure 1.5 shows that many (in fact most) NS LMXRBs are persistent and some are transient. This is because neutron stars are less massive than black holes meaning that the binary separation is less so the outer edge of the disc has a higher temperature (King, Kolb & Burderi 1996; King et al 1997; Dubus et al 1999; Chakrabarty & Morgan 1998; Ergma & Antipova 1999; Gladstone, Done & Gierliński 2007; Done, Gierliński & Kubota 2007).

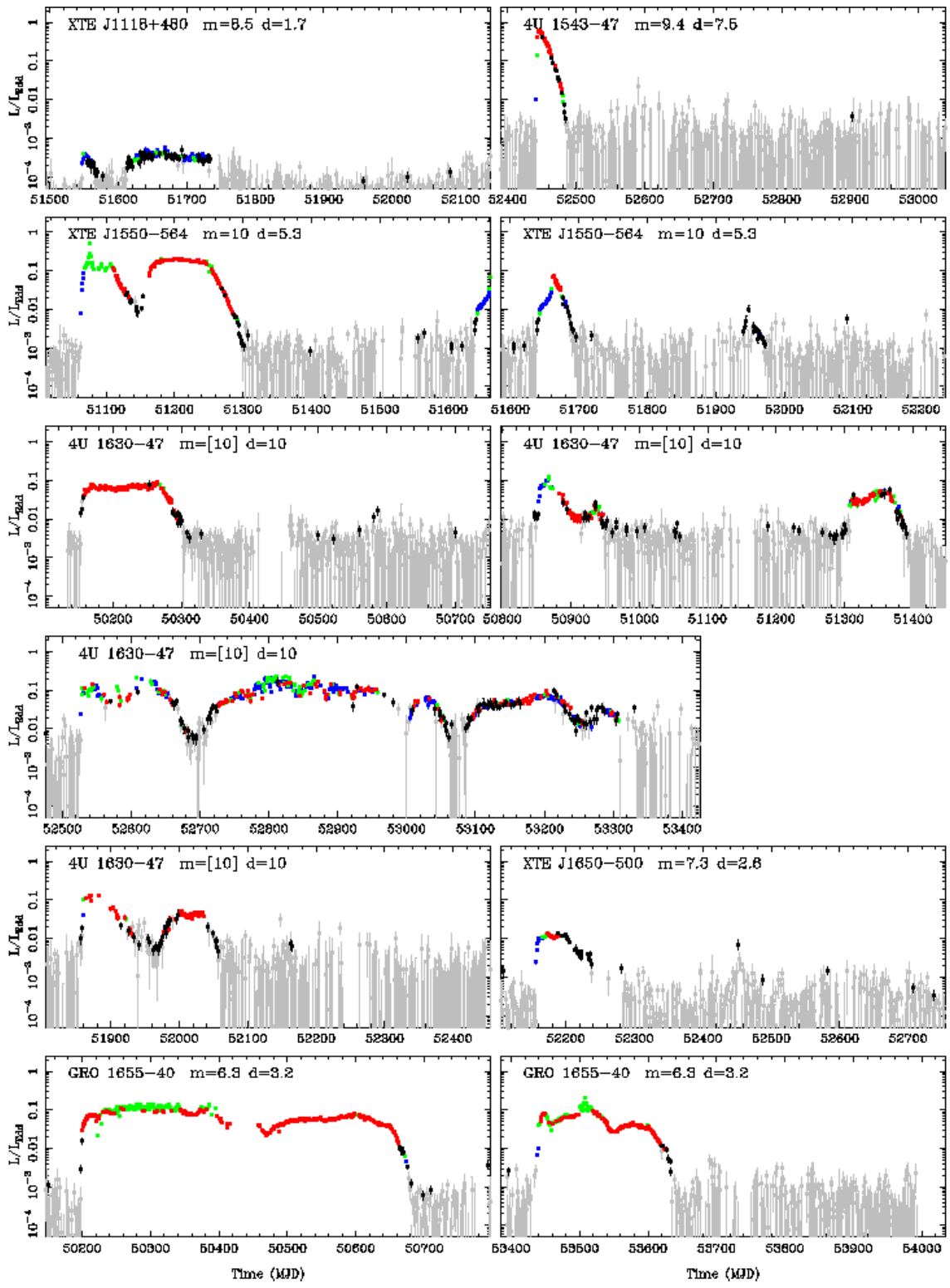

Figure 1.4: Long term light curves for a selection of BH LMXRBs as seen by the *RXTE* ASM (with mission days on the x-axis).

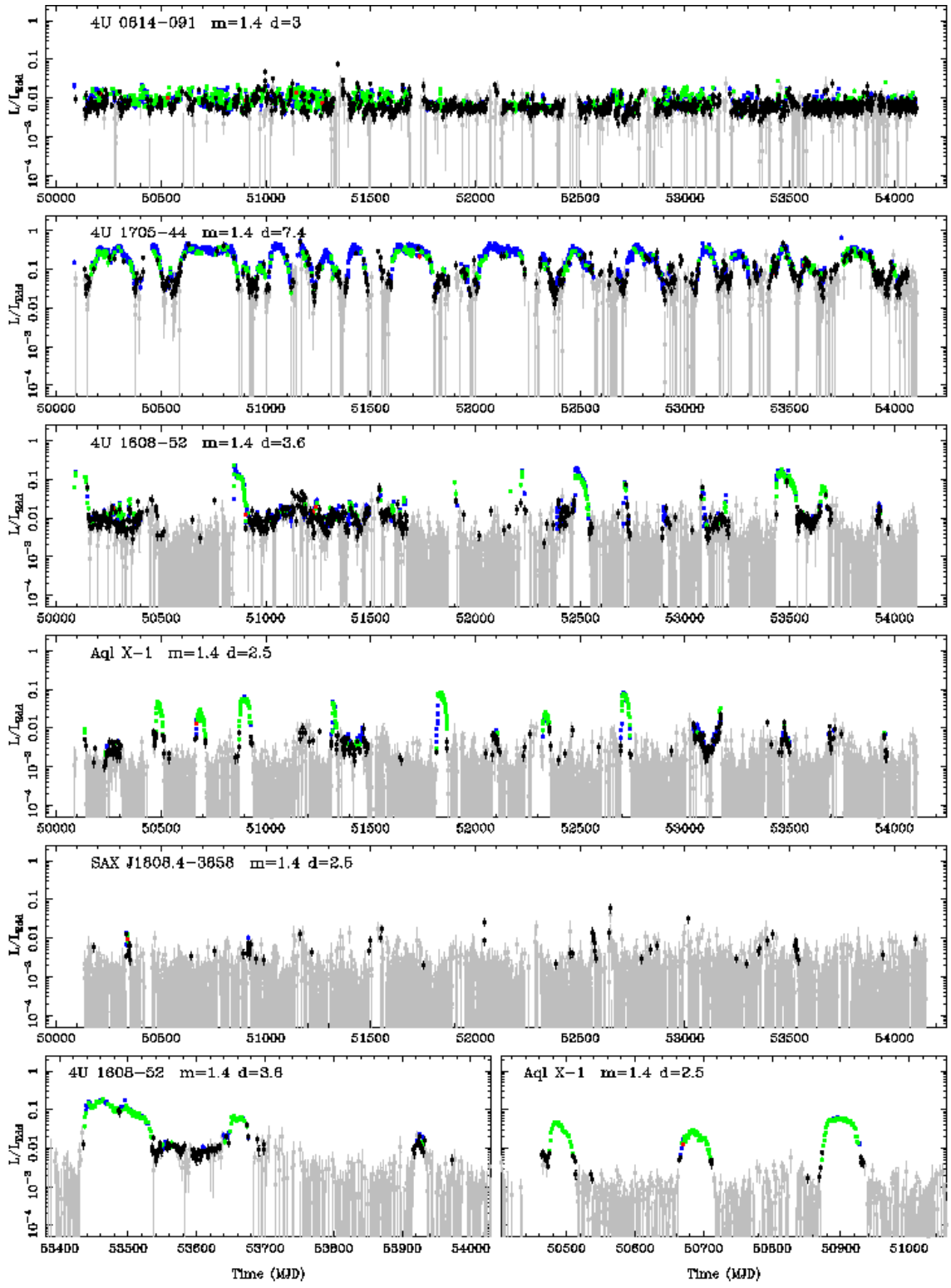

Figure 1.5: Long term light curves for a selection of NS LMXRBs as seen by the *RXTE* ASM (with mission days on the x-axis).

1.2 Radiative processes in X-ray binaries

Wheather transient or persistent, the observed spectrum of an XRB is dramatically different for different X-ray luminosities (and therefore mass accretion rate). Figure 1.6 shows the spectrum of the BH LMXRB GRO J1655-40 for 4 different mass accretion rates during its 2005 outburst (plotted in units of energy × flux in order to show where the flux peaks on a logarithmic scale [1]). The most striking difference is between the red line and the blue line. The red line is dominated by a thermal component whereas the blue line is dominated between ∼3-100 keV by a power law. Because of their comparative luminosities and the band pass in which they peak, these two spectral 'states' are referred to as the high/soft state (red line) and the low/hard state (blue line).

We can identify the high/soft state (HSS) spectrum with the sort of thermalised accretion disc discussed in the previous section. An accretion disc also seems to be present at low energies in the low/hard state (LHS) but clearly a few more physical processes are at work. If some corona containing energetic electrons is present near the disc, photons from the disc will be Compton up-scattered resulting in a power law spectrum. Some fraction of photons emitted from the corona will then reflect off the disc to give a reflection spectrum with the most prominent feature being the iron K_α line visible at ∼6.4 keV. In the transition from LHS to HSS, the source passes through intermediate states depicted by the green and black lines. These intermediate states clearly contain the same spectral components as the HSS and LHS. During the transition from LHS to HSS, the power law becomes softer as the disc component becomes stronger. The observed spectra also display absorption features resulting from interaction between the intrinsic photons and the extrinsic interstellar medium. The spectral states of black hole binaries (BHBs) can therefore generally be explained with four radiative processes: quasi-thermal emission, Comptonisation, absorption and

[1] On a logarithmic scale, $dlogE$ is the constant so $EF(E)dlogE = EF(E)dE/E = F(E)dE$

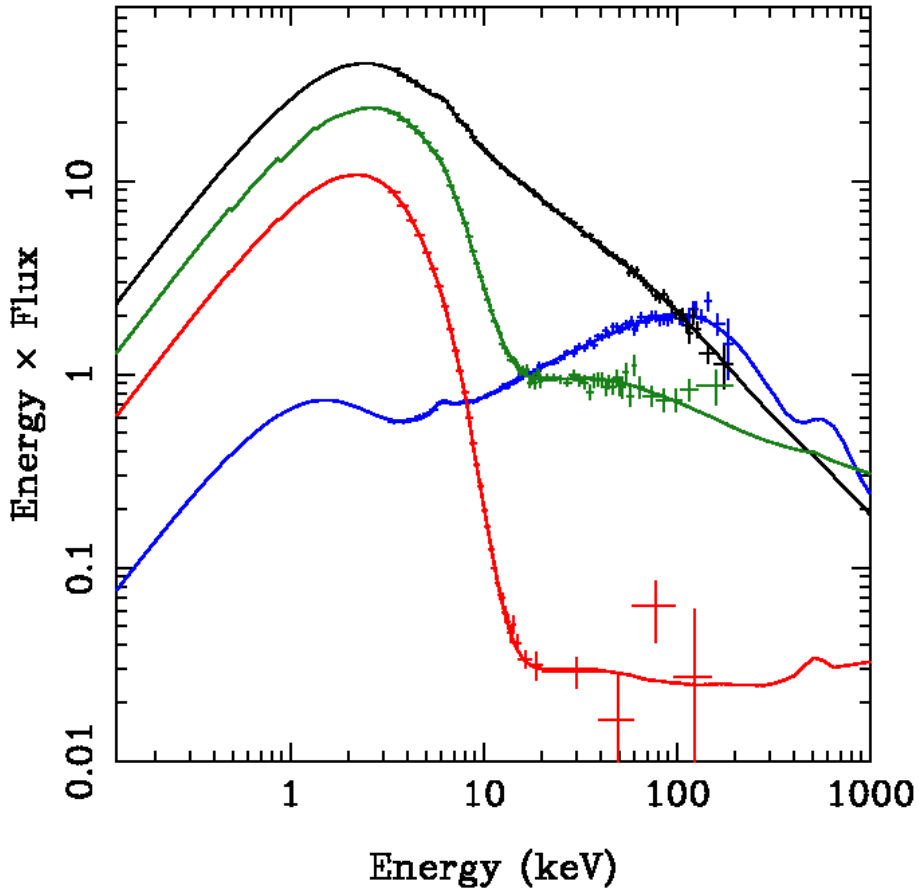

Figure 1.6: A selection of spectral states from the 2005 outburst of GRO J1655-40, as seen by *RXTE*. The blue line represents the low/hard state, the red line the high/soft state and the black and green lines represent the transition between the two (intermediate states).

reflection. The spectral states of neutron star binaries (NSBs) are complicated somewhat by the solid surface of the star (see chapter 3), but can also be modeled with the same contributing components. I will summarise these processes in the following sub-sections.

1.2.1 Quasi-thermal disc emission

The standard Shakura & Sunyaev (1973) disc solution consists of gas particles in nearly Keplerian orbits which are influenced only by the gravity of the central object (i.e. the disc has negligible self gravity). Angular momentum is slowly transported outwards by viscosity giving the gas a small inward velocity, $v_r << v_\phi$. The disc is geometrically thin (with aspect ratio $h/r \sim 0.01$) and optically thick meaning that liberated gravitational energy is radiated locally with a black body spectrum. If half of the liberated potential energy in an annulus of width dr is radiated (virial), then the luminosity from that annulus is

$$dL = \frac{GM\dot{M}}{2R^2}dR. \tag{1.2}$$

Each annulus radiates like a black body, so we can write $dL = A\sigma T^4 = 2\times 2\pi R\, dR\, \sigma T^4$ and re-arrange to obtain

$$T^4 = \frac{GM\dot{M}}{8\pi R^3\sigma}. \tag{1.3}$$

Here σ is the Stefan-Boltzmann constant. The total observed spectrum can be estimated simply by summing the black body contribution from each annulus, as is illustrated in Figure 1.7. Because the peak temperature of the contribution increases for smaller radii, this is called a 'multi-coloured' black body spectrum. Conserving angular momentum as well as energy gives

$$T^4 = \frac{3GM\dot{M}}{8\pi R^3\sigma}(1-\sqrt{R_{in}/R}). \tag{1.4}$$

This is the stress free inner boundary condition which arises because there is no viscosity interior to R_{in}. There are also some relativistic effects that must be considered (Novikov & Thorne 1973) but these are fairly small corrections. It is then possible to fit this predicted spectrum to HSS data in order to derive the position of the disc inner radius. If this is at the last stable orbit, the relation plotted in Figure 1.1 can therefore be used to measure the black hole spin (e.g. Kubota, Makishima & Ebisawa 2001; Gierliński & Done 2004; Middleton et al 2006; McClintock et al 2006; Kolehmainen & Done 2010).

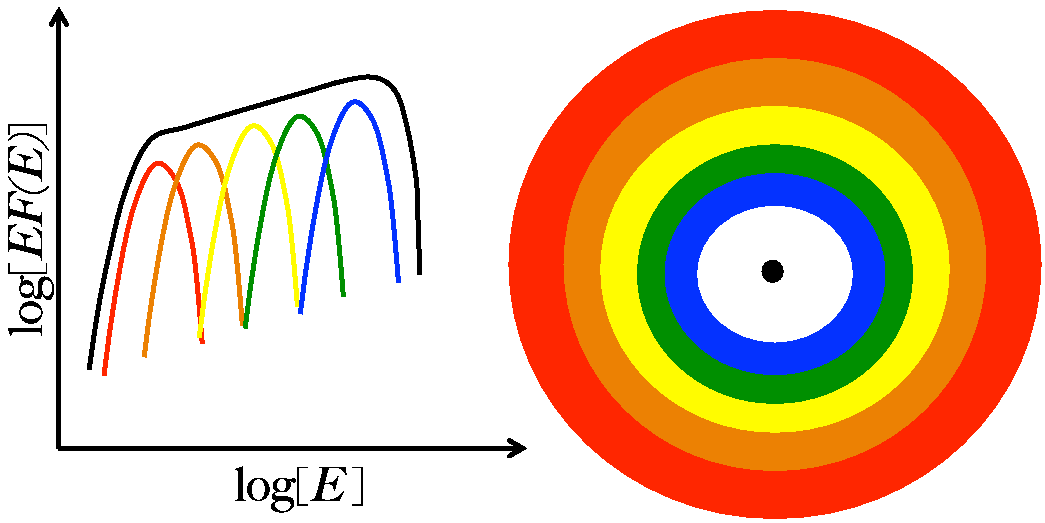

Figure 1.7: Schematic of a multi-coloured black body disc. Each annulus emits a black body with the peak temperature $T \propto r^{-3/4}$.

The nature of viscosity in the disc does not influence the emitted spectrum as long as the emission thermalises. Shakura & Sunyaev introduced the α prescription, whereby the radial viscous force is proportional to the pressure. This is equivalent to setting the kinematic viscosity to $\nu = \alpha c_s H$, where c_s is the sound speed, H is the disc semi-thickness and α is the dimensionless viscosity parameter. It is likely that the physical origin of this viscosity lies in the magneto rotational instability (MRI; Balbus & Hawley 1998). If different disc annuli are connected via magnetic fields, differential rotation will tangle up the field lines giving rise to the shearing force required for outward transport of angular momentum.

1.2.2 Comptonisation

Compton scattering is simply the transfer of energy between a photon and electron via a collision. Figure 1.8 illustrates a geometry whereby a photon with an energy ϵ_{in}

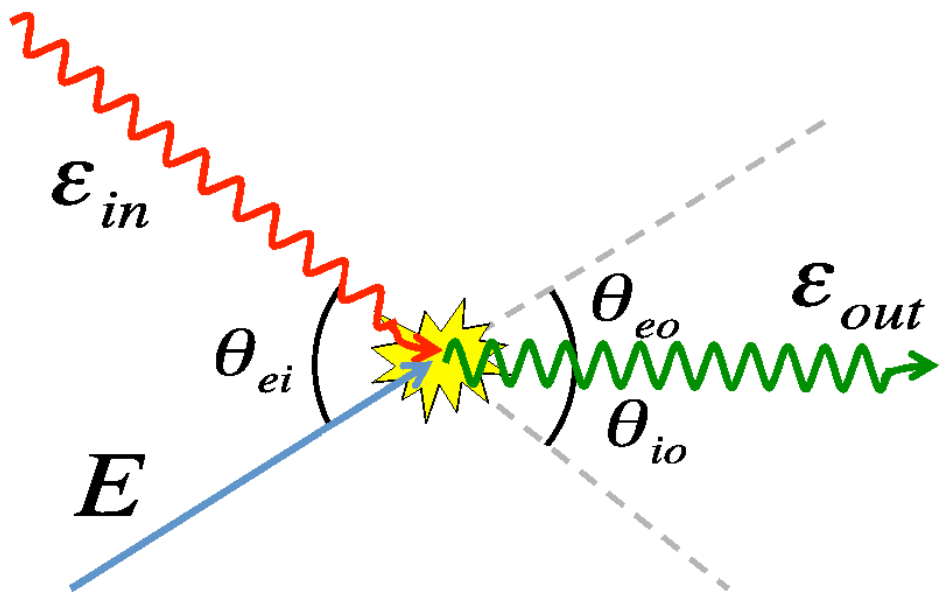

Figure 1.8: Schematic illustrating a collision between an electron with energy E and a photon with energy ϵ_{in}.

collides with an electron with velocity β and energy E. The photon recoils from the collision and its new energy is ϵ_{out}. Note the electron will also recoil but this is not pictured. The new photon energy is given by

$$\epsilon_{out} = \frac{\epsilon_{in}(1 - \beta\cos\theta_{ei})}{1 - \beta\cos\theta_{eo} + \epsilon_{in}/\gamma(1 - \cos\theta_{io})}. \tag{1.5}$$

Here, $\gamma = (1-\beta^2)^{-1/2}$ is the Lorentz factor, θ_{ei} is the angle between incident photon and (incident) electron, θ_{eo} is the angle between the output photon and the (incident) electron and θ_{io} is the angle between incident and output photons. Note that β is velocity in units of c and ϵ is represented as a fraction of the rest frame electron energy, $m_e c^2$. The energy of the electron is $E = (\gamma^2 - 1)^{1/2} m_e c^2$.

If the electron is at rest (i.e. $\beta = 0$) and $\epsilon_{in} << 1$ (the Thompson limit), equation

1.5 can be simplified using a binomial expansion to

$$\epsilon_{out} \approx \epsilon_{in}[1 - \epsilon_{in}(1 - \cos\theta_{io})]. \tag{1.6}$$

If we imagine many such collisions in an isotropic distribution of photons and electrons, the average output energy is $\epsilon_{out} \approx \epsilon_{in}[1 - \epsilon_{in}]$ (e.g. Rybicki & Lightman 1979). The average change in energy is therefore $\Delta\epsilon \approx -\epsilon_{in}^2$. The electron which was originally at rest has recoiled after the collision meaning that the photon has passed energy to the electron.

In a thermal distribution of electrons, the typical random velocity is $v^2 \sim 3kT_e/m_e$. The electron temperature can be re-written in dimensionless units as $\Theta = kT_e/m_ec^2$, meaning that the average electron velocity in the distribution is $\beta^2 = 3\Theta$. If the electron and photon distributions are again isotropic, in the limit of $\Theta << 1$ and $\epsilon_{in} << 1$, it can be shown using equation 1.5 (e.g. Rybicki & Lightman 1979)

$$\epsilon_{out} \approx (1 + 4\Theta + 16\Theta^2...)\epsilon_{in} \approx (1 + 4\Theta)\epsilon_{in}. \tag{1.7}$$

The average change in photon energy when a distribution of photons are scattered by a thermal distribution of electrons is therefore $\Delta\epsilon = 4\Theta\epsilon_{in}$ (for $\epsilon_{out} \lesssim 3\Theta$). Because the electrons pass energy to the photons, this process is called Compton up-scattering.

Because energy can only be exchanged in a collision, the total energy transferred depends on the likelihood of a collision. In the $\epsilon << 1$ Thompson limit, electrons have a cross section σ_T (the Thompson cross-section) for interaction with photons. A photon travelling a path length R sweeps out a volume $R\sigma_T$. The optical depth is defined as the number of electrons in this volume and so is given by

$$\tau = nR\sigma_T, \tag{1.8}$$

where n is the electron (volume) density. The scattering probability is $1 - e^{-\tau}$ which reduces to $\sim \tau$ for $\tau << 1$.

Therefore, if a distribution of seed photons are incident on some thermal cloud of electrons, a fraction $\sim \tau$ of these photons will be scattered up to an energy of $(1+4\Theta)\epsilon_{in}$. These output photons can also be scattered and the total number of scattering orders possible, N, is limited by the electron temperature such that $(1+4\Theta)^N \epsilon_{in} \sim 3\Theta$. Figure 1.9 illustrates that, because each scattering order is subject to the same fractional energy shift and the same fractional shift in flux, the output flux for $\epsilon_{in} < \epsilon < 3\Theta$ can be represented by a power law $F(\epsilon) \propto \epsilon^{-\alpha}$ where

$$\alpha \approx \frac{\log(\tau)}{\log(1+4\Theta)}. \tag{1.9}$$

The differential photon spectrum [2] is thus $N(\epsilon) \propto \epsilon^{-\Gamma}$ where $\Gamma = \alpha + 1$ is the photon index. Both functions will display low and high energy turn-offs at $\sim \epsilon_{in}$ and $\sim 3\Theta$ respectively.

Perhaps the most intuitive way to think of Compton scattering is in terms of the energetics. The electrons are being heated by gravitational collapse and so have a luminosity L_h. They are also being cooled by interactions with seed photons which have a luminosity L_s. The heating and cooling reach an equilibrium in order to maintain a temperature Θ for an optical depth τ. Pietrini & Krolik (1995) calculated the parameter dependencies numerically and recovered the simple empirical scaling relation

$$\alpha \approx 1.6 \left(\frac{L_s}{L_h}\right)^{1/4} \propto \frac{1}{\tau\Theta}. \tag{1.10}$$

This relation shows very clearly that, if the luminosity of seed photons illuminating the electron distribution (L_s) increases, this will cool the electrons and soften the output power law spectrum.

It is therefore possible to explain much of the observed spectral evolution of XRBs with a simple disc plus corona model in which the corona contains a population of thermal electrons which interact with seed photons provided by the disc. As the disc

[2] For a detector with a perfectly flat energy response, this is proportional to the count rate.

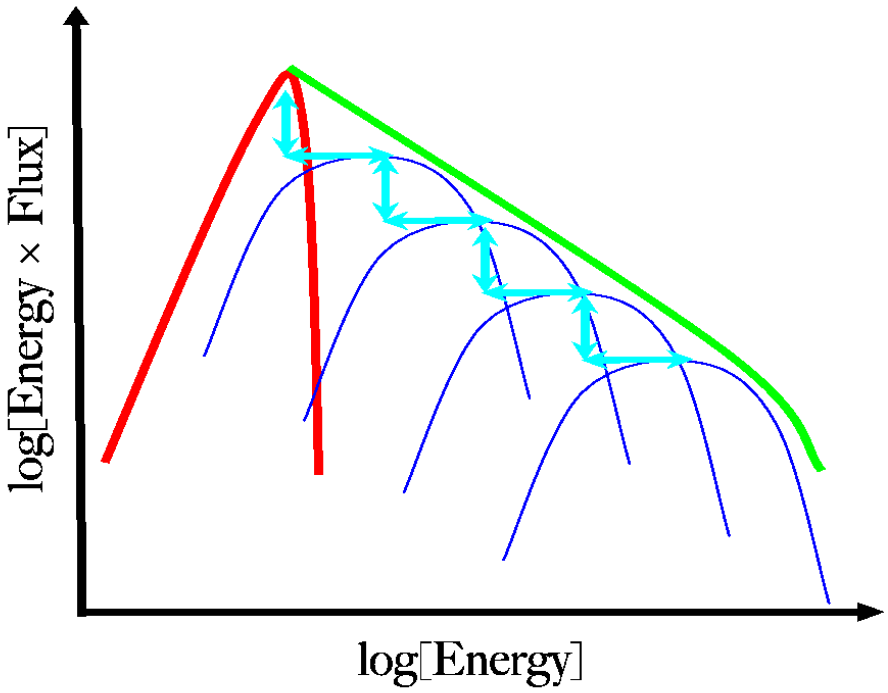

Figure 1.9: Schematic illustrating thermal Comptonisation. A population of seed photons (red) is incident on a population of thermally distributed electrons. The output spectrum can be approximated by a power law because each scattering order is subject to the same fractional energy shift and the same fractional shift in flux

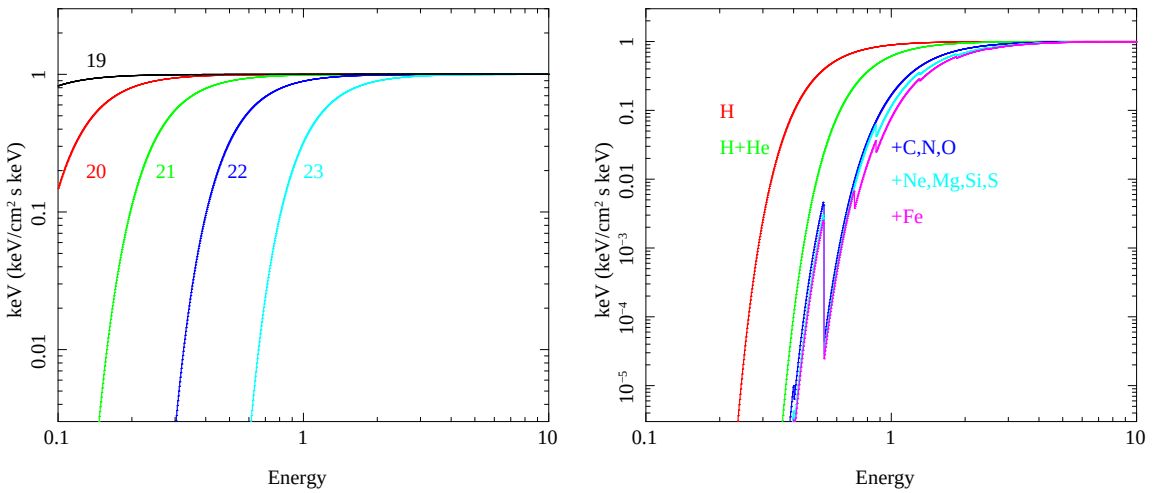

Figure 1.10: *Left:* A flat ($\Gamma = 2$) power law spectrum as observed through a cloud of hydrogen with column density $\log_{10} N_H = 19 - 23$. *Right:* The same intrinsic spectrum as seen through a cloud with $\log_{10} N_H = 22$ with progressively heavier elements being introduced to the column (with solar abundance) for each line.

luminosity increases, the luminosity of disc photons incident on the corona will naturally increase thus softening the resultant power law emission. This also cools the coronal electrons, leading to the high energy turn-off moving to lower energies, as observed (e.g. Ibragimov et al 2005).

1.2.3 Absorption

Intrinsic emission is modified by photo-electric absorption by material along the line of sight. This could be the interstellar medium of our galaxy (or the host galaxy for extra-galactic sources) or some kind of wind either from the accretion flow itself or the companion star. The amount of absorption is governed by the optical depth of the absorbing medium such that a fraction $e^{-\tau}$ of the intrinsic emission is transmitted. Whereas the interaction cross-section for free electrons (in the Thompson limit) is $\sigma(E) = \sigma_T$, the cross-section for bound atoms is much more complex. A hydrogen atom has one bound electron with binding energy 13.6eV. Since the atom can only absorb

photons with enough energy to un-bind the electron, the cross-section of hydrogen is zero below 13.6eV with a sharp edge at $E_{edge} = 13.6$eV and a slow decline going as $\approx (E/E_{edge})^{-3}$ above this. We can combine $nR = N_H$ (where n is now the *hydrogen atom* density) to make the column density. Figure 1.10 (left; reproduced from Done 2010) shows a flat ($\Gamma = 2$) power law spectrum as observed through a cloud of hydrogen with column density $N_H = 10^{19} - 10^{23}\mathrm{cm}^{-2}$ (black-cyan). A typical column through our galaxy has $N_H > 10^{20}\mathrm{cm}^{-2}$.

Heavier elements are also present, which have progressively larger binding energies. There are a number of energy shells, but the highest energy edge always results from an electron escaping from the innermost (K) shell. The total absorption cross-section is therefore a sum, weighted by relative abundances, of the cross-section for each element. Heavier elements have higher E_{edge} but lower abundance and therefore a smaller influence on the total absorption cross-section. Figure 1.10 (right; also reproduced from Done 2010) shows the transmitted emission from a flat power law through a $\log_{10} N_H = 22$ column. Different lines show the effect of adding progressively heavier elements, assuming solar abundances. The last astrophysically abundant element is iron, thus the magenta line shows the spectrum as observed through a neutral column with solar abundances.

Photo-electric absorption leaves an ion and a free electron. The remaining electrons in the ion are more tightly bound and thus have a higher binding energy. Figure 1.10 (right) effectively assumes that the free electrons always combine with the photo-ionised ions *before* the next absorption event. However, if the X-ray irradiation is very intense, there may on average be many absorption events by the time the ions recombine meaning that the cross-section is actually dominated by the collisions between photons and ions rather than collisions between photons and neutral atoms. The cross-section therefore depends on the balance between recombination and photo-ionisation. For higher ionisation states, more elements are, on average, completely stripped of

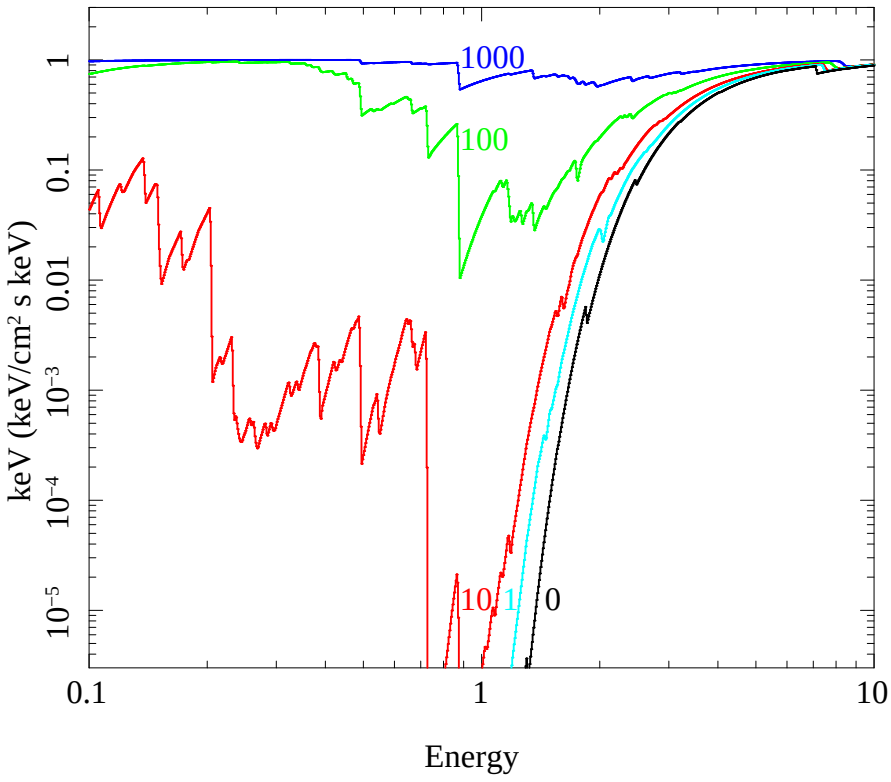

Figure 1.11: A flat power law spectrum as observed through a cloud with $\log_{10} N_H = 23$ with solar abundances and ionisation state ranging from $\log_{10} \xi = 0 - 1000$.

electrons meaning they do not contribute to the cross-section at all. Thus, the higher the ionisation state, the lower the total absorption cross-section. The ionisation state can be parametrised by the ionisation parameter $\xi = L/nc^2$, where L is the source luminosity (see e.g. Done 2010; Fabian et al 2000). Figure 1.11 (reproduced from Done 2010) shows the transmitted flux for a column density of $N_H = 10^{23}\text{cm}^{-2}$, with the number by each line representing $\log_{10} \xi$. We see that increasing ionisation does indeed reduce the overall absorption cross-section. Also, we can see for intermediate values of $\log_{10} \xi$, there are more edges than for neutral material. This is because, if there is not almost complete ionisation or neutrality, there are at least two relatively abundant ionisation states for each element.

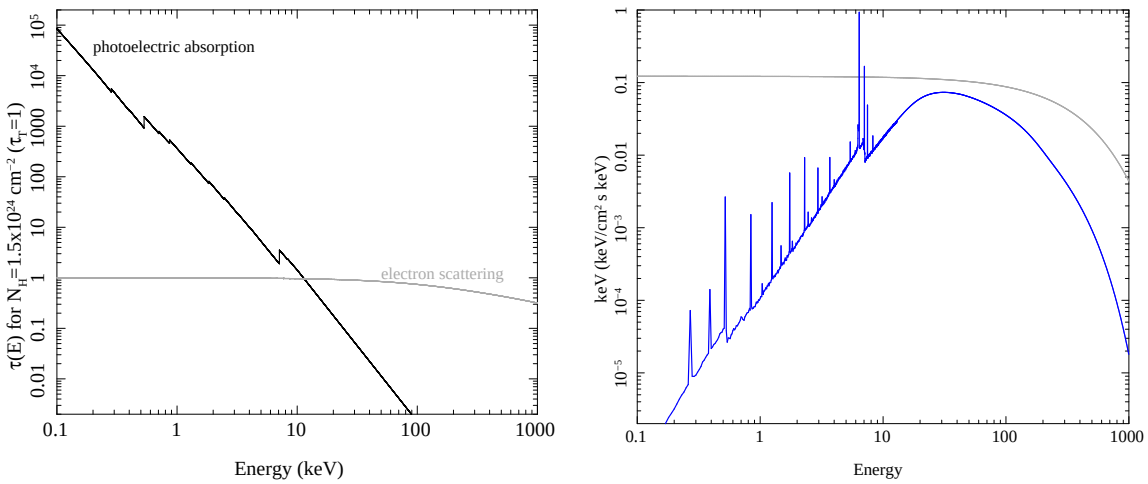

Figure 1.12: *Left:* Optical depth for neutral material with solar abundance and $N_H = 1.5 \times 10^{24}\mathrm{cm}^{-2}$ (black) together with the optical depth for electron scattering. *Right:* The corresponding reflection spectrum from such material. Both plots are reproduced from Done (2010).

1.2.4 Reflection

Some fraction of the flux emitted from the Comptonising corona will be incident on the disc and thus have some probability of scattering off electrons therein and being reflected into the line of sight. The reflection probability is set by the relative importance of scattering and photo-electric absorption. Figure 1.12 (left) shows the photo-electric absorption optical depth for neutral material (with the exception of hydrogen and helium which are fully ionised) with $N_H = 1.5 \times 10^{24}\mathrm{cm}^{-2}$ (black) along side the full (Klein-Nishima) electron scattering optical depth (grey) which drops-off from the Thompson limit for $E \sim 511$keV due to inelastic scattering. Thus we can see that photo-electric absorption will be important for $E \lesssim 10$keV because, the more photons are absorbed at a given energy, the fewer are available to scatter into our line of sight. Above ~ 10keV, electron scattering dominates. There will also be fluorescence lines resulting from an electron dropping to fill a lower shell thus emitting a photon

with energy equal to the difference in shell energies. The most common transition of this kind is the K_α line which results from an electron falling from the L ($n = 2$) shell down to the K ($n = 1$) shell.

Figure 1.12 (right) shows the reflection spectrum for a flat power law illuminating continuum, assuming all elements except for hydrogen and helium are bound (usually referred to as neutral reflection despite the assumed ionisation of hydrogen and helium). At low energies, we see that the reflection fraction increases with energy due to the reducing absorption cross-section. We also see many fluorescence lines with the most prominent being the iron K_α line. This is because the iron lines occur at the energy least suppressed by absorption, plus lighter elements are more likely to de-excite via Auger ionisation where an outer electron is lost instead of a photon being emitted. At high energies, the spectrum is dominated by inelastic electron scattering. High energy photons do scatter, but they lose a significant fraction of their incident energy from down-scattering. This bump at 20-50keV is often termed the reflection hump (George & Fabian 1991; Matt, Perola & Piro 1991).

Since the low energy reflection spectrum depends on absorption, reflection is sensitive to the ionisation state of the reflecting material. As Figure 1.11 shows, the absorption cross-section reduces with increased ionisation. This means that the total reflected flux increases with the ionisation parameter ξ. Figure 1.13 shows a reflection model which considers ionisation state and also calculates self-consistent fluorescence lines, for four different values of ξ. As expected, the $\lesssim$ 10keV spectrum increases in flux with ξ but the reflection hump, which is dominated by free electron scattering, is left largely unaffected by the change in absorption. Also the edges and emission lines are broader for higher ξ as free electron scattering becomes increasingly important with increasing ionisation.

Finally, we must consider that the disc is rapidly spinning. A non face-on observer will therefore see part of the disc moving rapidly towards them and the other side

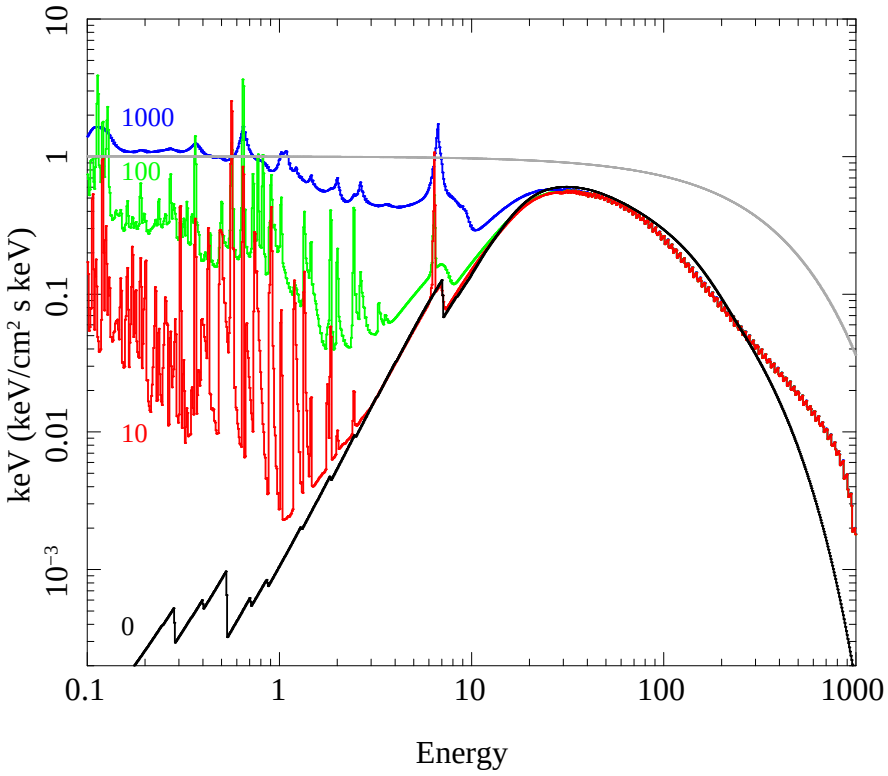

Figure 1.13: Reflection spectrum from a constant density slab including self-consistent line and and recombination continuum emission. Different lines represent different ionisation states with $\log_{10}\xi$ ranging from $0 - 1000$.

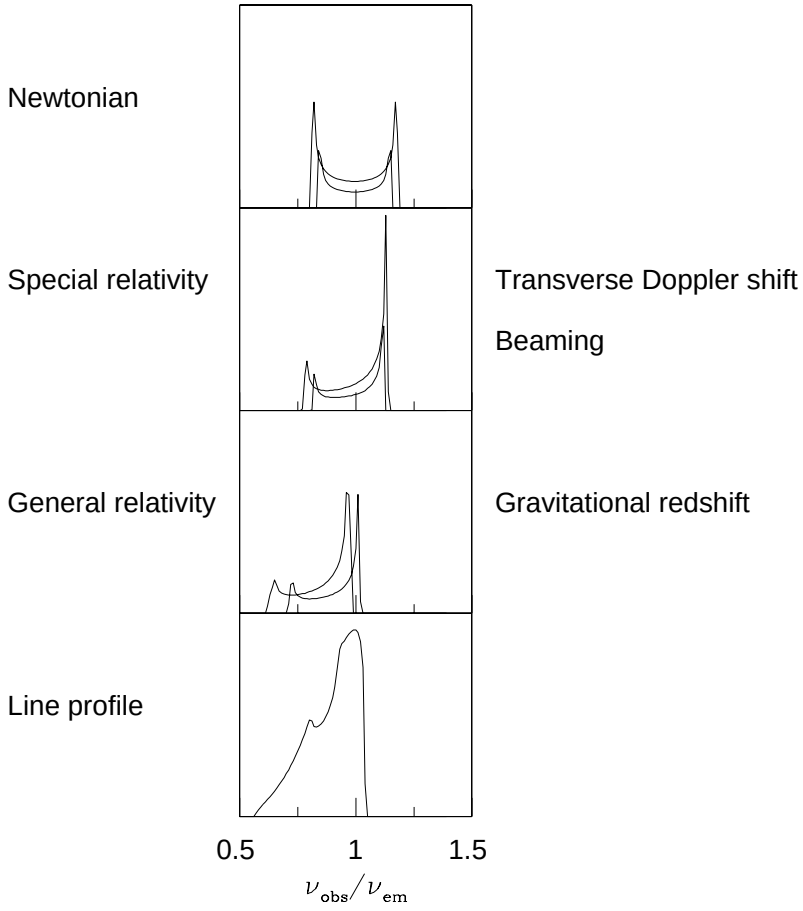

Figure 1.14: Observed line profile resulting from assuming the rest frame reflection spectrum to be a $\delta-$function iron K_α fluorescence line. Since the disc is spinning rapidly, a number of processes serve to broaden and skew the line meaning that the observer sees a broad line even if the rest frame line is very narrow.

rapidly away. This gives rise to a number of effects which are illustrated in Figure 1.14 (Fabian et al 2000) under the assumption that the rest frame reflection spectrum is simply a $\delta-$function iron fluorescence line. Emission from the approaching and receding sides is respectively blue and red shifted by the Doppler effect, giving rise to the 'two horn' profile pictured in the top plot. Doppler boosting of the blue wing plus length contraction in the line of sight lead to the skewed profile shown in the second plot down. Gravitational redshift also serves to move everything to a slightly lower energy. Since the final line profile includes all of these effects, it is relatively broad even if the line is very narrow in the rest frame. These effects provide a potentially very powerful diagnostic for the accretion flow because a smaller inner disc radius gives rise to more rapid rotation, thus greater smearing and skewing (e.g. Fabian et al 1989; 2000; Reis et al 2009; Miller et al 2006).

1.3 The truncated disc model

It is clear that a two component spectral model, in which a disc interacts with some Comptonising region, can explain much of the spectral behaviour of XRBs. It is, however, unclear what exactly this Comptonising region is. It could be a coronal layer covering the disc above and below the mid-plane (*sandwich model:* Haardt & Maraschi 1991; 1993). However, in this geometry the luminosity of disc photons intercepted by the coronal layer will be too large for the source to produce the hard power law emission observed in the LHS (Dove et al 1997; Gierliński et al 1997; Poutanen, Krolik & Ryde 1997); particularly when reprocessing of coronal emission in the disc is taken into account (Malzac, Dumont, & Mouchet 2005; Stern et al 1995). If, instead, the layer is only partially covering, it will be sufficiently starved of disc photons (*patchy corona:* Galeev, Rosner & Vaiana 1979; Haardt, Maraschi & Ghisellini 1994). Alternatively, the corona could be positioned above the black hole, in the form of a wind or the base of a jet (*lamp post model:* Markoff, Nowak & Wilms 2005; Miller et al 2006). However,

the corona in this geometry would also be prevented from emitting a hard spectrum due to the large incident luminosity of disc (plus reprocessed) photons. This can be remedied if the coronal region is assumed to be moving away from the disc (*outflowing corona:* Beloborodov 1999; Malzac, Beloborodov & Poutanen 2001). The picture I consider throughout this thesis is the *truncated disc model* (e.g. Esin, McClintock & Narayan; Done, Gierliński & Kubota 2007) whereby the thin disc truncates at some radius $r_o > r_{lso}$ and is replaced interior to this by some hot, optically thin accretion flow which acts as the Comptonising region.

The truncated disc geometry is illustrated in Figure 1.15. As the truncation radius moves in, the source transitions from the LHS, through the intermediate state, to the HSS. As this happens, the disc luminosity and temperature increase (as observed) and the luminosity of seed photons incident on the flow increases, thus cooling the electrons and softening the power law emission. The spectra can be fit if the truncation radius is assumed to move from $r_o \sim 60$ in the LHS to $r_o \approx r_{lso}$ in the HSS (e.g. Di Salvo et al 2001). The evolution of the reflection spectrum can also be interpreted in this picture. As r_o moves in, the luminosity of flow photons incident on the disc increases thus strengthening the appearance of reflection features in the spectrum and increasing the disc ionisation, as observed (e.g. Gierliński et al 1999). In addition to this, as r_o moves in, the amount of smearing and skewing of the iron line caused by increasingly rapid rotation of the inner disc should increase. There have been studies showing the data to be consistent with this picture (Gilfanov, Churazov & Revnivtsev 1999; Zdziarski, Lubinski & Smith 1999; Ibragimov et al 2005; Gilfanov 2010; Życki, Done & Smith 1999; Gierliński et al 1999) but there are also contradictory studies (Miller et al 2006; Miller et al 2009; Reis et al 2008; 2011) which have themselves been challenged on the grounds of both instrumental effects (Done & Diaz-Trigo 2010; Kolehmainen & Done 2010) and uncertainty over the detailed shape of the underlying continuum spectrum (Kolehmainen, Done & Diaz-Trigo 2011; 2012). Since there is thus no unambiguous

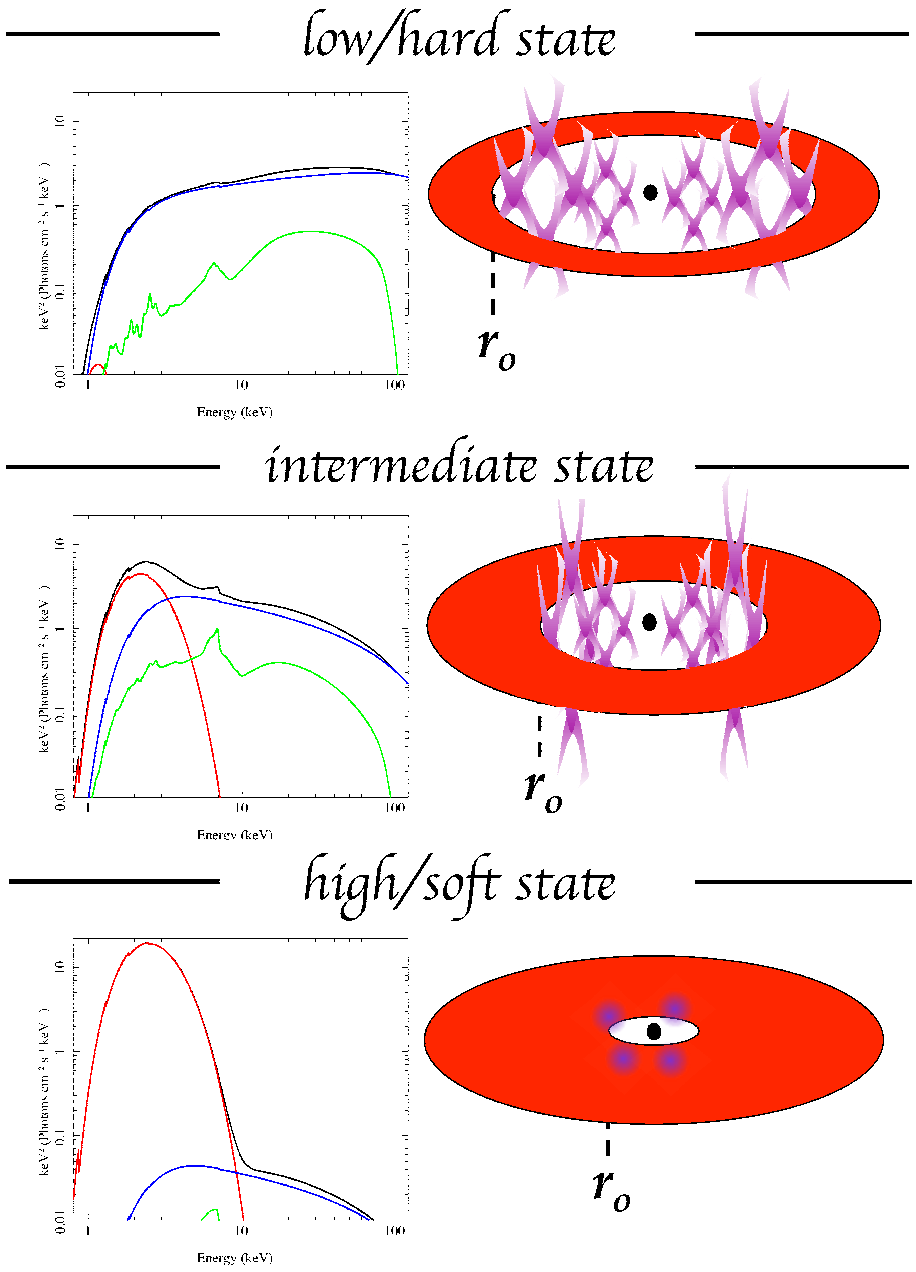

Figure 1.15: Schematic illustrating the truncated disc interpretation of the spectral state transitions.

evidence as yet to rule out the truncated disc model, and all alternative geometries (e.g. Markoff, Nowak & Wilms 2005; Miller, Homan & Miniutti 2006) run into other difficulties (Done, Gierliński & Kubota 2007), I use it as my framework in which to interpret the short timescale variability which forms the main subject of this thesis.

In this section, I will first discuss some of the physics associated with optically thin accretion flows and disc truncation before introducing short timescale variability. Analysis and modelling of this rapid variability holds the key to breaking the spectral degeneracy and resolving the contention in the literature over different accretion geometries because it provides us with vastly more information than simply considering the time averaged spectrum. The ultimate goal of this body of work is to explain the observed variability properties of XRBs in the context of the truncated disc model. In this section, I review the characteristic timescales we may expect to be associated with the accretion flow as a first step towards this goal.

1.3.1 Optically thin accretion flows

As discussed in section 1.2.1, the thin disc solution of Shakura & Sunyaev is based on the assumption that the disc is very optically thick. When the mass accretion rate is very low in quiescence, the density will be very low and this assumption breaks down. The disc no longer radiates like a black body and thus heats up (since black body radiation provides the most efficient cooling mechanism). This increases the internal (gas and radiation) pressure, causing the disc to expand vertically into a large scaleheight accretion flow. In such an optically thin, geometrically thick accretion flow, ions and electrons do not undergo enough collisions to thermalise (Stepney 1983; Shapiro, Lightman & Eardley 1976; Ichimaru 1977; Narayan & Yi 1995). The ions are hotter than the electrons because they hold all the gravitational energy, whereas Compton cooling is dominated by the electrons which have a far larger photon interaction cross-section. Another result of the sparsity of collisions is advective cooling and thus such accretion

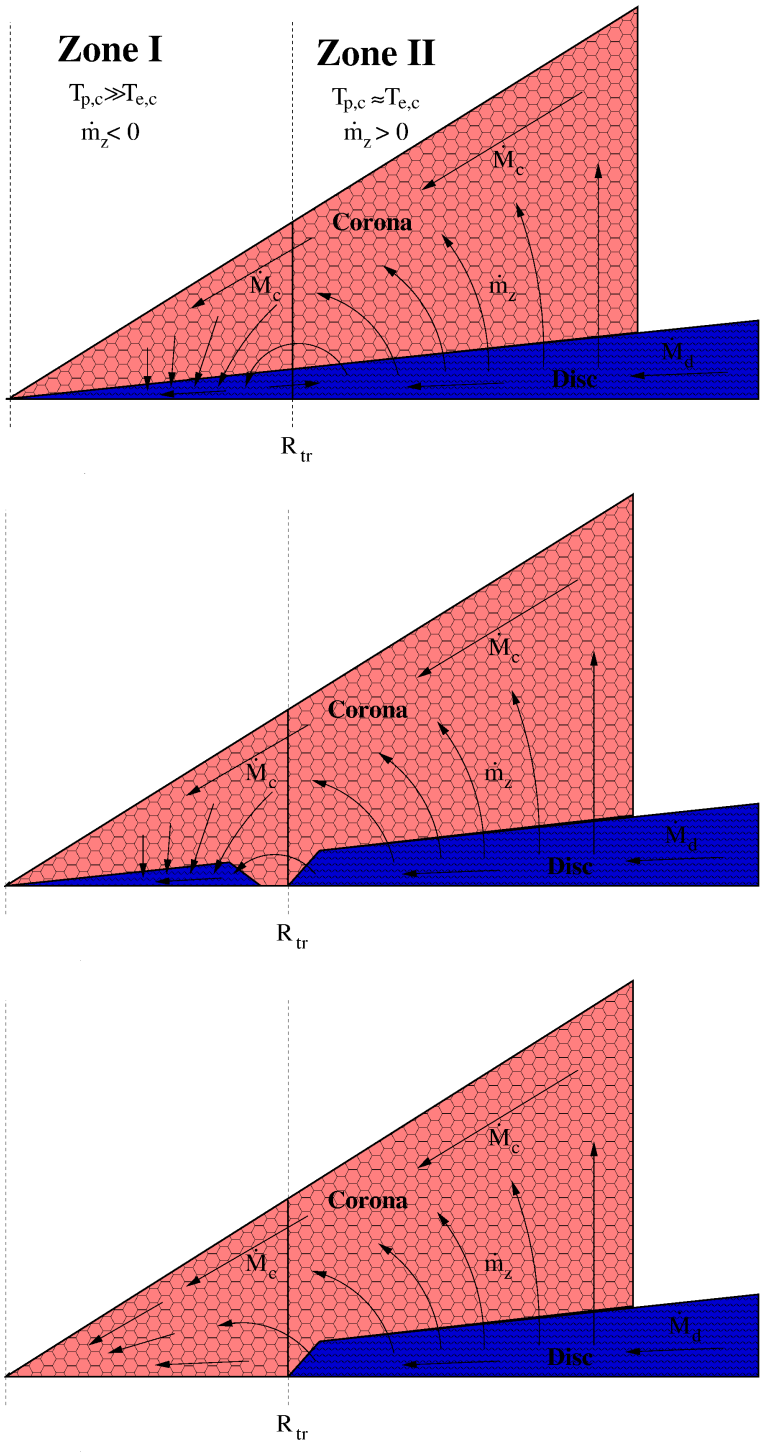

Figure 1.16: Schematic view illustrating the results of Mayer & Pringle (2007). The initial sandwich configuration (top; with only one side of the sandwich shown) is modified by mass transfer (arrows) between the disc (blue) and corona (red). Eventually, the inner regions of the disc evaporate and the outer regions condense.

flow solutions are often referred to as advection dominated accretion flows (ADAFs; Narayan & Yi 1995; also see Ichimaru 1977; Rees et al 1982).

The truncated disc model thus consists of a geometrically thin, optically thick disc (the disc) and a geometrically thick, optically thin flow (the flow), with some (poorly understood) transition at r_o which moves in as the mass accretion rate increases. It is possible to gain some understanding as to how such a two component accretion flow may form by considering the vertical density structure of the disc. If the disc is in hydrostatic equilibrium, the density will drop off from the midplane value at large z (Frank, King & Raine 1992). Consequently, the optical depth in these regions is lower than in the midplane and so a coronal layer could plausibly form on the top and bottom of the disc (i.e. a sandwich model geometry). Mayer & Pringle (2007) assume such a sandwich geometry and consider thermal interaction between the disc and coronal layer. They show that, after the system is left to evolve, the balance of heating and cooling leads to a truncated disc solution (the authors' schematic diagram is reproduced in Figure 1.16) where the disc evaporates interior to the truncation radius (labelled R_{tr}) and the flow condenses outside of some radius $> R_{tr}$ to form a truncated disc / hot inner flow configuration with an overlap region. In intuitive terms, they find that heating dominates for $R < R_{tr}$ and cooling dominates for $R > R_{tr}$. If the mass accretion rate through the disc were to increase, this would increase the disc luminosity meaning that cooling can dominate for a greater range of radii; i.e. the truncation radius moves in.

1.3.2 Short timescale variability

In addition to long term changes in mass accretion rate, XRBs also display variability on timescales far too short ($10^{-3} - 100$s) to result from global changes in accretion geometry. The properties and amplitude of this variability, as will be reviewed in section 1.4, are heavily dependent on spectral state. Figure 1.17 shows two light curves

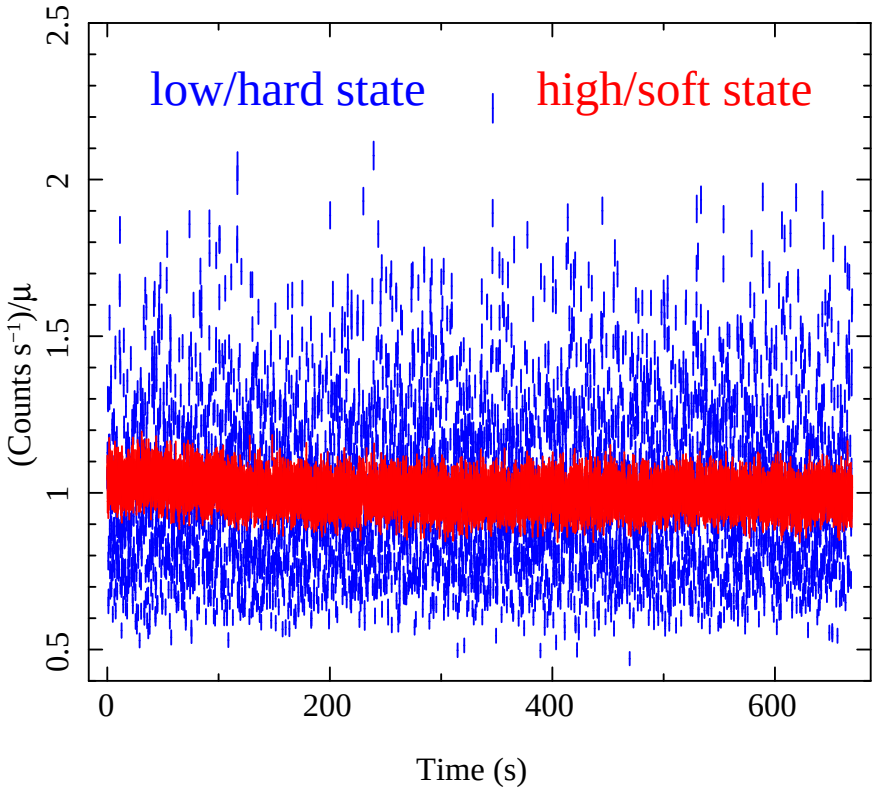

Figure 1.17: Count rate as a fraction of the mean plotted against time for XTE J1550-564 in the LHS (blue) and the HSS (red). We clearly see that the LHS light curve displays a far larger fractional variability than that of the HSS.

from XTE J1550-564 in both the HSS (red) and LHS (blue). We clearly see that the LHS light curve is far more variable than the HSS light curve on timescales $\sim$ 100s. Since the emission is stable when only a disc is present and variable when the flow is prominent, it may be inferred that the variability originates in the flow with the disc remaining fairly stable (e.g. Churazov, Gilfanov & Revnivtsev 2001)

The variability displayed in Figure 1.17 is aperiodic: there is strong variability on a range of timescales. In addition to this, a single timescale is often picked out by far more coherent quasi-periodic oscillations (QPOs). In Figure 1.18 I have plotted 3s of data from XTE J1550-564 in an intermediate state. The raw data (grey) display

variability on a range of timescales but it is just about possible to pick out a QPO with period $\sim 1/4$ s by eye. The short timescale noise in the raw light curve ($l_{raw}(t)$) can be smoothed out by averaging each point over the previous t_{short} seconds (so only variability on timescales longer than t_{short} remains), to create the function $l_{short}(t)$. This new light curve, however, still contains long time scale variability. Filtering the raw light curve on t_{long} seconds creates $l_{long}(t)$ which only contains the long term trends. I use $t_{short} \approx 0.18$s and $t_{long} \approx 0.39$s and calculate the light curve plotted in red by

$$l_{QPO}(t) = \sqrt{l_{short}(t)^2 - l_{long}(t)^2 + \mu^2}, \tag{1.11}$$

where μ is the average value of $l_{raw}(t)$. The QPO is now very clear and can be fit with a sine wave (black line) to show that it is coherent over the 3s duration plotted; i.e. the phase, amplitude and period stay fairly constant. The best fit sine wave has a period of $t_{QPO} = 0.256$s. Even the smoothed light curve is far from perfectly described by a sine wave: this is a quasi-periodic oscillation rather than simply a periodic one. As we will see later, the QPO period shortens as the spectrum softens and the truncation radius is inferred to move in.

Whereas the spectral properties of XRBs are fairly well understood, there is very little consensus in the literature as to the origin of the variability properties. There are, however, a few characteristic time scales which we may expect to be associated with the accretion flow. Simple consideration of these time scales forms the first step to building a model for the variability properties of XRBs.

1.3.3 Characteristic timescales of the accretion flow

The characteristic timescales of the accretion flow can be grouped into two classes: timescales associated with bound orbits in the Kerr metric (relativistic timescales) and timescales associated with the physics of the accretion flow itself (accretion timescales).

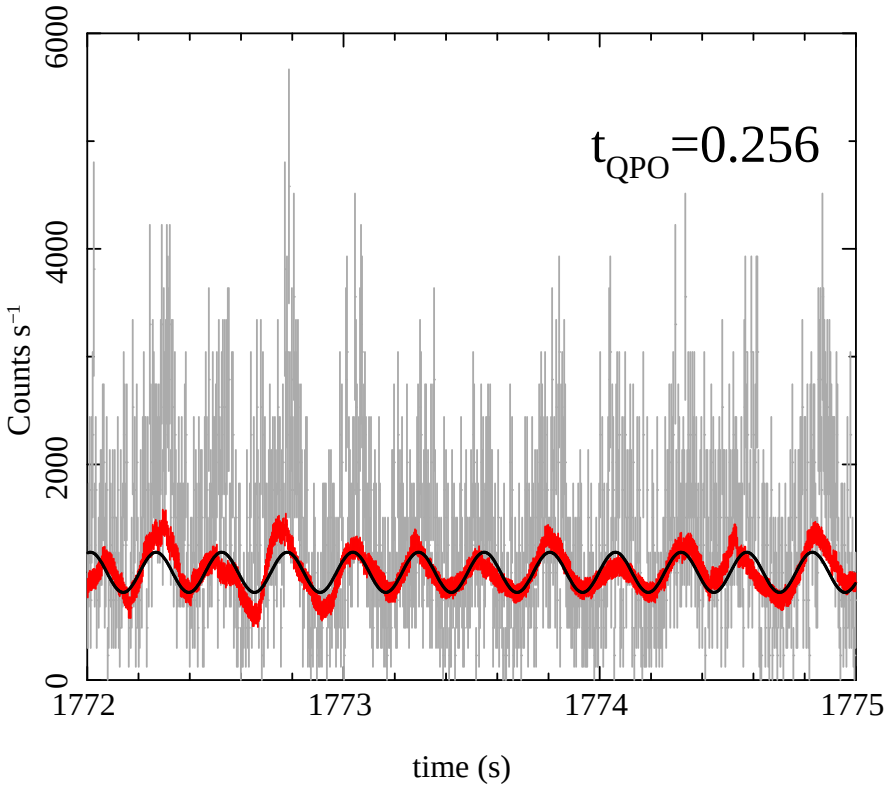

Figure 1.18: 3s light curve of XTE J1550-564 in an intermediate state (grey). This raw light curve can be filtered using equation 1.11 to produce the red line which has a clear periodicity. The black line is the best fitting sine wave which has a period of 0.256s.

Relativistic timescales

Relativistic bound orbits differ from those in Newtonian mechanics. I have already discussed the last stable orbit in section 1.1.1, the prediction of which is is one major difference between the Kerr metric and the flat metric always assumed in Newtonian mechanics. Figure 1.19 illustrates an elliptical orbit (blue dotted line) of a test particle around a massive object at the origin. This can be described by the three polar coordinates $\phi(t)$, $\theta(t)$ and $r(t)$. This is a closed orbit, meaning that the particle will keep following the same blue dotted line as it orbits the central object. Mathematically, we can say that each coordinate varies with an angular velocity Ω_ϕ, Ω_θ and Ω_r for the $\phi(t)$, $\theta(t)$ and $r(t)$ coordinates respectively (i.e. $\ddot{\phi(t)} = -\Omega_\phi^2\phi(t)$). In Newtonian mechanics, orbits always close and thus obey

$$\Omega_\phi = \Omega_\theta = \Omega_r = r^{-3/2}\frac{c}{R_g}. \tag{1.12}$$

A non-zero $\dot{r}(t)$ denotes an elliptical (as opposed to circular) orbit and a non-zero $\dot{\theta}(t)$ results from the $z-$axis not being orthogonal to the plane of the orbit (Figure 1.19).

However, if the central object is a spinning black hole with a spin axis aligned with the $z-$axis, it is possible to show from the Kerr metric (see e.g. Merloni et al 1999) that

$$\Omega_\phi \neq \Omega_\theta \neq \Omega_r. \tag{1.13}$$

Specifically

$$\begin{aligned}
\Omega_\phi &= \frac{r^{-3/2}}{1 + a_* r^{-3/2}}\frac{c}{R_g} \\
\Omega_\theta^2 &= \Omega_\phi^2\left[1 - \frac{4a_*}{r^{3/2}} + \frac{3a_*^2}{r^2}\right] \\
\Omega_r^2 &= \frac{r^2 - 6r + 8a_* r^{1/2} - 3a_*}{r^2(r^{3/2} + a_*)^2}\left(\frac{c}{R_g}\right)^2.
\end{aligned} \tag{1.14}$$

So the orbital motion in the ϕ direction departs from Newtonian mechanics only for the very inner regions of the accretion flow. When $\theta = \pi/2$, this reduces to the

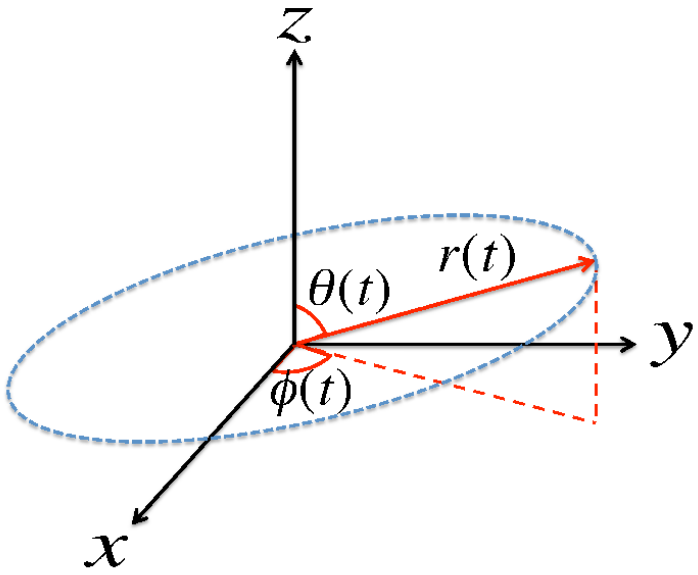

Figure 1.19: A bound elliptical orbit (blue dotted line), described by the three coordinates $\phi(t)$, $\theta(t)$ and $r(t)$. The orbit closes because all three coordinates vary with the same angular velocity.

$a_* = 0$ (Schwarzschild) case, giving $\Omega_\theta = \Omega_\phi = r^{-3/2}(c/R_g)$, which is consistent with classical mechanics. However, even in this limit, there is a small correction to $\Omega_r = r^{-2}\sqrt{r-6}(c/R_g)$ which only tends to the Newtonian case for $r >> 6$.

The non-degeneracy between coordinate velocities creates two effects. Perihelion precession is a rotation of the orbit's semi-major axis with an angular velocity $\Omega_{PP} = |\Omega_r - \Omega_\phi|$. This was observed in Mercury's orbit of the sun by Urbain le Verrier in 1859 (although it would be nearly 60 years before the observation could be correctly interpreted). Frame dragging is a slow rotation of the orbit's plane. This is also named Lense-Thirring precession after the authors who first derived it (Lense & Thirring 1918; although there is evidence that much of the merit for the derivation belongs to Einstein: Pfister 2007) and the angular velocity of precession is given by $\Omega_{LT} = |\Omega_r - \Omega_\phi|$. Relativistic corrections consistent with frame dragging were recently measured in the

orbit of Gravity Probe B around Earth (Everitt et al 2011), although there were high uncertainties in these measurements. However, this effect is much larger around a compact object because the curvature of space-time is so much greater near a black hole or neutron star. It is therefore possible that the observed variability in XRBs is some modulation of these orbital motions. In 1998-99, a slew of authors (Stella & Vietri 1998; Stella, Vietri & Morsink 1999; Merloni et al 1999; Markovic & Lamb 1998; Cui, Zhang & Chen 1998) noted that the QPO period is commensurate with the Lense-Thirring precession period at r_o, as estimated by spectral fitting. For example a moderate spin of $a_* = 0.5$ and a black hole mass of $10M_\odot$, gives a Lense-Thirring period of $t_{LT} = 2\pi/\Omega_{LT} \approx 0.26$s at a radius of $r \approx 9$. This is the same period as the QPO plotted in Figure 1.18, for which the truncated disc model estimates $r_o \sim 10$. As the truncation radius moves in, both $t_{LT}(r_o)$ and the QPO period decrease.

Accretion timescales

The time dependence of an accretion disc is described by the diffusion equation

$$\frac{\partial \Sigma}{\partial t} = \frac{3}{R}\frac{\partial}{\partial R}\left\{R^{1/2}\frac{\partial}{\partial R}(\nu \Sigma R^{1/2})\right\}, \tag{1.15}$$

which is derived using mass, angular momentum and energy conservation (see e.g. Frank, King & Raine 1992, equation 5.6). Here, Σ is the surface density and ν is the kinematic viscosity. Frank, King & Raine (1992) use an illustrative example with $\nu = constant$ to study how a ring of mass m and radius R_0 evolves with time. In this case, the initial surface density is

$$\Sigma(R, t = 0) = \frac{m}{2\pi R_0}\delta(R - R_0) \tag{1.16}$$

and it can be shown that the surface density at a position $x = R/R_0$ and time $t_* = 12\nu t/R_0^2$ is given by

$$\Sigma(x, t_*) = \frac{m}{\pi R_0} t_*^{-1} x^{-1/4} \exp\left\{-\frac{1 + x^2}{t_*}\right\} I_{1/4}(2x/t_*), \tag{1.17}$$

where $I_{1/4}(z)$ is a modified Bessel function. This is the Green's function which describes how the disc reacts to a perturbation in the surface density (or any related physical quantity).

Figure 1.20 shows that the Green's function causes the mass in the ring, which started out all at $x = 1$, to spread out with the peak of the distribution slowly drifting towards the compact object (i.e. the ring is being accreted). If we treat this initial ring of mass as a density perturbation, we can see that it is being damped out. From equation 1.17, we can see that damping occurs on a characteristic timescale given by setting the argument of the exponential term to unity. This is called the viscous timescale, obtained by setting $x^2 t_* \sim 1$ to get

$$t_{visc} \sim R^2/\nu. \tag{1.18}$$

By the same argument, the velocity of the radial drift illustrated in Figure 1.20 is given by

$$v_R \sim R/t_{visc}. \tag{1.19}$$

The disc therefore acts as a filter to fast variability. Perturbations in Σ on timescales shorter than t_{visc} will be strongly damped because the disc cannot react quickly enough.

We can use the α prescription ($\nu = \alpha c_s H$) to show

$$t_{visc} = \alpha^{-1}(h/r)^{-2} t_\phi. \tag{1.20}$$

This allows us to compare the viscous timescales of disc and flow assuming $\alpha \sim 0.1$ for both and $h/r \sim 0.01$ and ~ 0.2 for disc and flow respectively. This gives

$$t_{visc}(disc) \approx 450s\ (M/10M_\odot)(r/6)^{3/2} \tag{1.21}$$

and

$$t_{visc}(flow) \approx 1s\ (M/10M_\odot)(r/6)^{3/2}. \tag{1.22}$$

Therefore, the truncated disc model is consistent with Figure 1.17 which shows that the (disc dominated) HSS is stable on the $\sim$ 100s timescales on which the (flow dominated) LHS is highly variable.

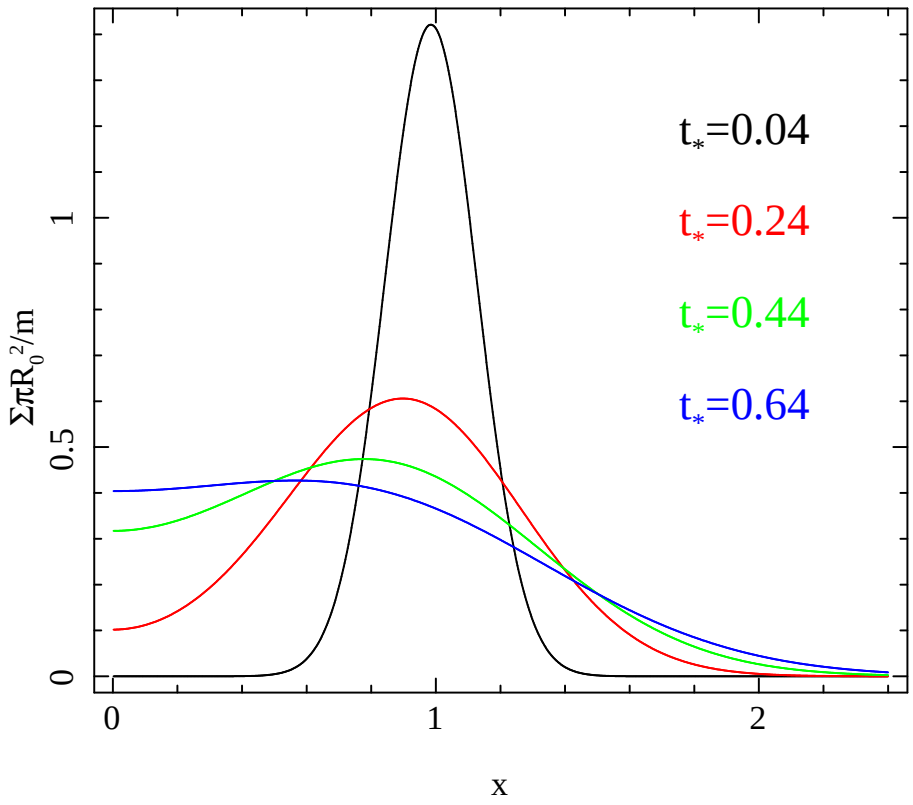

Figure 1.20: A ring of material starting at R_0 is spread out by the response of the disc with the peak of the distribution slowly moving towards the black hole (equation 1.17). The modified Bessel function in the Green's function is calculated using codes in Press et al (1992).

We also expect the amplitude of disc variability to be suppressed compared to the flow. This is because the disc has more independent regions per radial extent than the flow. To illustrate this, consider an accreting ring with constant h/r and width ΔR. We can model independent regions as spherical bubbles just small enough to fit in the ring. The bubbles therefore have a radius H, the ring width is $\Delta R = 2H$ and it is possible to fit $(2\pi R)/(2H)$ bubbles in the ring. There are therefore $N = \pi(h/r)^{-1}$ independent regions in the ring. Let us assume that each region generates fluctuations in, say, mass accretion rate to produce N uncorrelated $\dot{m}_n(t)$ functions with averages μ_n and variances σ_n^2. If the N regions all produce a similar amplitude of variability (i.e. $\mu_n \approx \mu$, $\sigma_n \approx \sigma$), the summed contribution of the ring has an average $\mu_{tot} \approx N\mu$ and variance $\sigma_{tot}^2 \approx N\sigma^2$. The fractional variability of the ring is therefore

$$\sigma_{tot}/\mu_{tot} \approx N^{-1/2}(\sigma/\mu) \propto (h/r)^{1/2}(\sigma/\mu), \tag{1.23}$$

and so we do indeed expect suppressed disc variability.

1.4 Spectral and timing properties of black hole binaries

The spectral and variability properties of XRBs are tightly correlated; thus a great deal of insight can be gained from considering their simultaneous evolution. The power spectrum provides a measure of the varability amplitude as a function of frequency (i.e. 1/timescale) and so is a useful tool in characterising variability. In this section, I first introduce the power spectrum before summarising the parallel evolution of the spectral and timing properties of BHBs.

1.4.1 The power spectrum

The power spectrum, or power spectral density (PSD; I will use the two terms interchangeably) is the modulus squared of the Fourier transform of a light curve. By definition, it is a continuous function and so the process of estimating the PSD from a discrete data set is not trivial.

The Fourier transform

The Fourier transform gives a decomposition of a signal $h(t)$ into sine waves. The contribution to the signal at a given frequency f is given by $a(f)\cos(2\pi ft - \phi(f))$. Every frequency therefore has an amplitude, $a(f)$, and a phase, $\phi(f)$. If $h(t)$ is infinitely long and continuous, it relates to its Fourier transform such that

$$\begin{aligned} H(f) &= \int_{-\infty}^{+\infty} h(t)e^{2\pi ift}dt \\ h(t) &= \int_{-\infty}^{+\infty} H(f)e^{-2\pi ift}dt. \end{aligned} \tag{1.24}$$

In general, both functions are complex but, since we will be considering it to be the observed signal, $h(t)$ is real. This means that the complex conjugate of $H(f)$ obeys the identity $H^*(f) = H(-f)$. Of course, we observe $h(t)$ neither continuously nor for an infinitely long time. We instead collect some number of X-ray photons in each time interval, dt, to record a (background subtracted) count rate, $h_k(t_k)$, at time $t_k = kdt$ where $0 \leq k \leq N-1$. The total duration of the light curve is therefore $T = Ndt$. The discrete Fourier transform of h_k is given by (e.g. Deeming 1975; Press et al 1992)

$$H_n(f_n) = \sum_{k=0}^{N-1} h_k(t_k)e^{2\pi ikn/N}, \tag{1.25}$$

where $f_n = n/(Ndt)$ for $1 \leq n \leq N/2$. This means that the lowest frequency we can study is $1/T$ and the highest is the Nyquist frequency, $1/(2dt)$. The frequency resolution available to us is $df = 1/(Ndt)$. Computing this is very expensive as it

requires $\sim N^2$ calculations. It is common to use the fast Fourier transform (FFT) algorithm which dramatically cuts this number to $\sim N \log_2 N$ (Press et al 1992). The way this algorithm works means that it requires N to be an integer power of 2. The FFT then gives us the amplitude a_k and phase ϕ_k as a function of frequency for a discretely sampled time series of finite length.

Estimating the power spectrum from discrete data sets

The power spectrum is given by

$$P(f) = |H(f)|^2 = a^2(f). \tag{1.26}$$

Since we do not have $H(f)$, we must estimate the power spectrum from $H_n(f_n)$. The periodogram is defined as

$$\mathcal{P}(f_n) = \frac{2T}{\mu^2 N^2}|H_n(f_n)|^2 = \frac{2T}{\mu^2 N^2}a_k^2 \tag{1.27}$$

where μ is the average (background subtracted) count rate. This normalisation means that the integral of $\mathcal{P}(f_n)$ over a range f_1 to f_2 gives the squared fractional rms over that frequency range. For this reason, I will always plot power spectra in units of frequency $\times$ power (i.e. units of fractional rms squared). The Poisson counting error on the count rate contributes a (approximately; see van der Klis 1989) constant power given by $P_{noise} = 2(\mu + B)/\mu^2$ for this normalisation, where B is the average background count rate. In order to consider the underlying variability independent from instrumental effects, we must therefore use the white noise subtracted periodogram, $\mathcal{P}(f_n) \rightarrow \mathcal{P}(f_n) - P_{noise}$.

The periodogram calculated for $h_k(t_k)$ only provides a poor estimate for the power spectrum of $h(t)$. The dispersion of the periodogram points is described approximately by a χ^2 distribution with 2 degrees of freedom meaning that the error on every periodogram point is $\sim \mathcal{P}(f_n)$ (e.g. van der Klis 1989; Papadakis & Lawrence 1993); i.e. 100% fractional error! A better estimate can be obtained using one or a combination

of two techniques. The first is ensemble averaging. This involves splitting the light curve into $\mathcal{M}$ intervals and averaging the periodograms from each interval; i.e.

$$\overline{P}(f_n) = \frac{1}{\mathcal{M}} \sum_{m=1}^{\mathcal{M}} \mathcal{P}_m(f_n) \tag{1.28}$$

with error

$$\overline{dP}(f_n) = \sqrt{\frac{1}{\mathcal{M}-1} \sum_{m=1}^{\mathcal{M}} (\mathcal{P}_m(f_n) - \overline{P}(f_n))^2}. \tag{1.29}$$

The second technique is geometric re-binning such that the (integer) number of points in the J^{th} frequency bin is

$$N_p(J) \leq c_0^J, \tag{1.30}$$

where c_0 is some constant larger than unity. The width of the J^{th} bin is therefore $\Delta f_J = df N_p(J)$ and the maximum frequency in the bin is

$$f_{max}(J) = \left[\sum_{j=1}^{J} N_p(j) + 1/2 \right] df. \tag{1.31}$$

The minimum frequency in each bin is simply $f_{min}(J) = f_{max}(J-1)$, meaning the frequency at the centre of each bin is $f(J) = (f_{max}(J) + f_{min}(J))/2$. For large values of J, the ratio f_J/f_{J-1} tends to a constant value (logarithmic re-binning), however for low J values, the bin spacing is wider than logarithmic to ensure that every bin contains at least one linearly spaced data point.

The estimated power in the bin is then

$$P_{bin}(f_J) = \frac{\sum_{nmin}^{nmax} \overline{P}(f_n)}{N_p(J)}, \tag{1.32}$$

where $nmin = 1 + \sum_{j=1}^{J-1} N_p(j)$ and $nmax = \sum_{j=1}^{J} N_p(j)$. If ensemble averaging has been carried out, the error can be estimated as

$$dP_{bin}(f_J) = \frac{\sqrt{\sum_{nmin}^{nmax} \overline{dP}(f_n)^2}}{N_p(J)}. \tag{1.33}$$

If no ensemble averaging has been carried out, the error estimate is given by the standard deviation around the mean power.

With enough smoothing, the power spectral estimate becomes well behaved such that $P_{bin}(f_J)$ belongs to a Gaussian distribution with width $dP_{bin}(f)$ and centre $P(f)$ meaning a model can be fit to the power spectrum by reducing χ^2. We do, however, lose information from this smoothing. Ensemble averaging reduces the duration, T, and therefore the lowest frequencies are lost. Binning clearly decreases the frequency resolution. All the results in this thesis are for XRBs which have low variability amplitude below ~ 0.01 Hz and so a typical observation of a few ks is easily long enough to do ensemble averaging without losing important information. I therefore use binned *and* averaged power spectral estimates throughout this thesis, referring to them hereafter simply as the power spectrum $P(f)$, with error $dP(f)$.

1.4.2 Power spectral properties of black hole binaries

In Figure 1.21, I plot 5 representative $\sim 3-31$keV PSDs from the 2002 outburst of GX339-4. We see that QPOs appear in the PSD as narrow peaks and aperiodic variability appears as broad band noise (BBN). The properties of these power spectral features vary dramatically during spectral evolution of the source.

PSDs 1 & 2: type-C QPO

PSDs 1 and 2 show strong BBN along with a QPO which is very weak in PSD 1 and dominant in PSD 2. Such QPOs which are present alongside strong BBN are classed as type-C QPOs (Casella, Belloni & Stella 2005). In the LHS, a QPO is often not observed, although it is likely that one is present but merely hidden by strong BBN. It is clear to see in PSD 2 that the QPO has a harmonic structure with peaks at the fundamental, $f_{QPO} \sim 5$Hz, along side a sub-harmonic at $1/2f_{QPO}$ and a second harmonic at $2f_{QPO}$ (a third harmonic is also often visible). These peaks are well described by Lorentzian

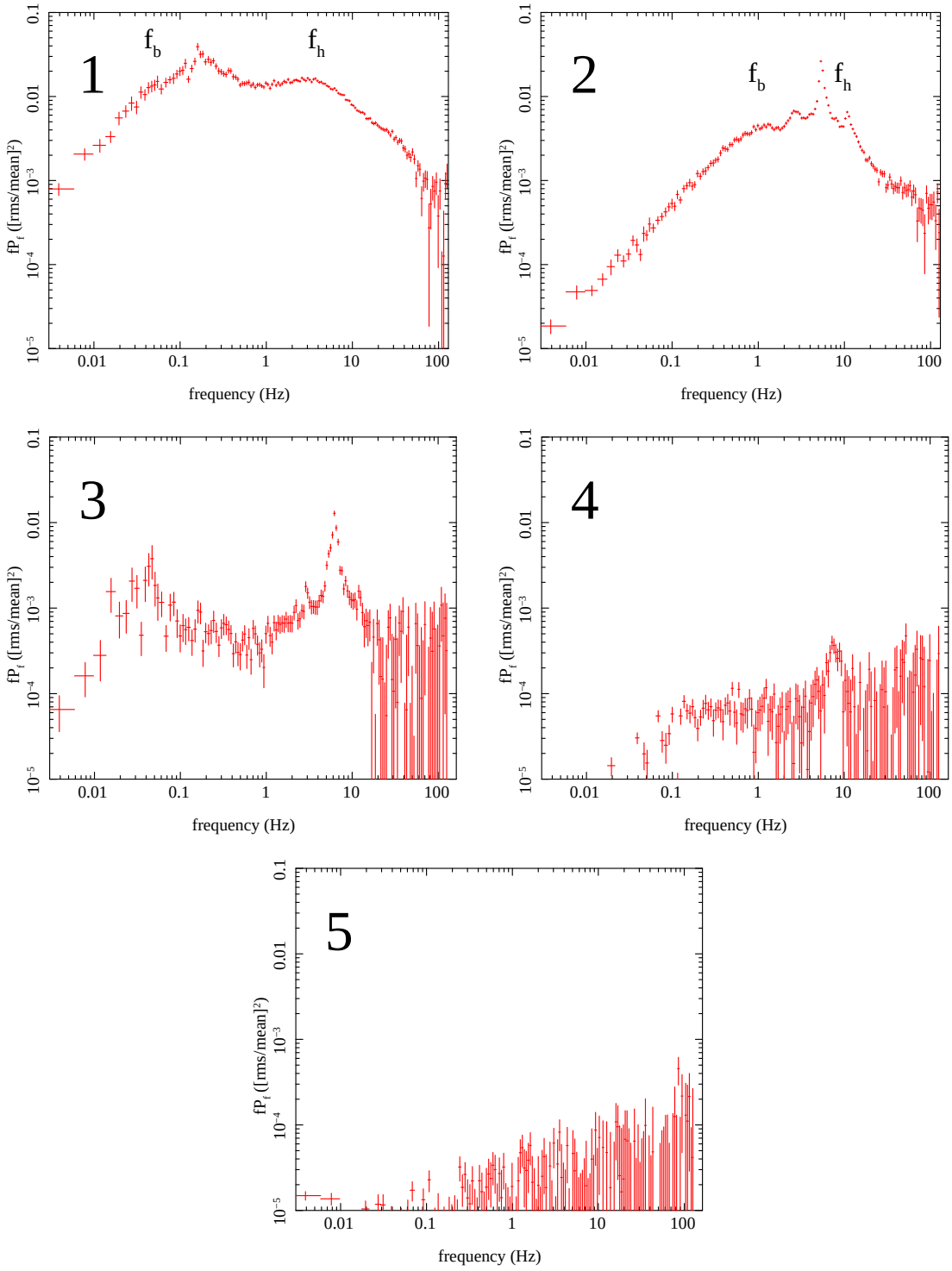

Figure 1.21: Five representative PSDs displaying type-C (1 and 2), type-B (3) and type-A (4) QPOs in addition to a typical HSS PSD displaying a low level of red noise (5).

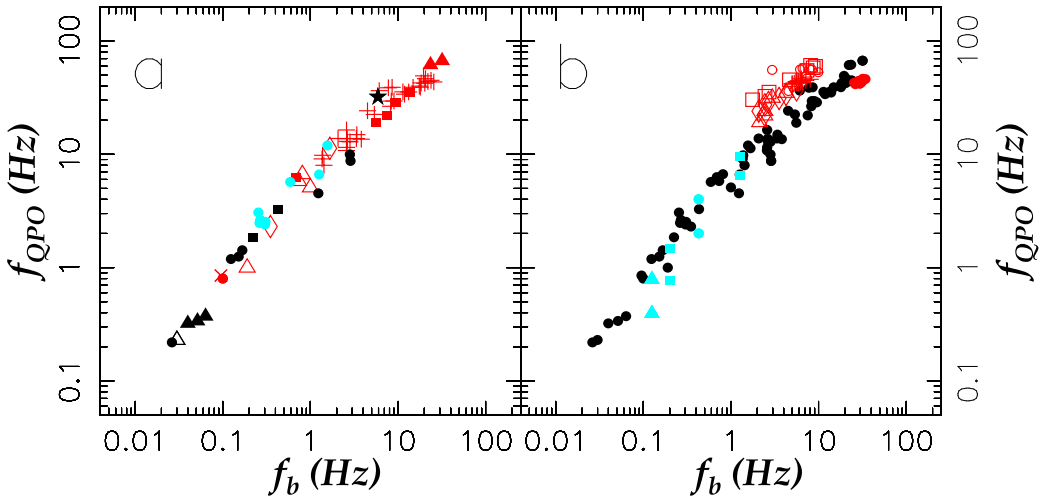

Figure 1.22: Low frequency break (f_b in the text, ν_b on the plot) plotted against QPO frequency (f_{QPO} in text, ν_{QPO} on the plot) for a number of different objects. In (a), the black points are BHBs, the red points are atolls and the blue points are a millisecond X-ray pulsar (see chapter 3). In (b), the black points are all the objects in (a), the red points are z-sources (again, see chapter 3) and the blue points are objects which display two QPOs. Different symbols correspond to different individual objects, see the original plot in Wijnands & van der Klis 1999 for details.

functions with three parameters: amplitude (i.e. integrated fractional rms), centroid frequency, f_c, and width, Δf. The width and centroid frequency can be combined into the quality factor, $Q = f_c/\Delta f$. For the hardest spectra, type-C QPOs are broad with $Q \sim 1 - 10$. As the source transitions through the intermediate state, the coherence increases before reaching a plateau at $Q \sim 10$ (e.g. Rao et al 2010). The Q of each harmonic is tied to the fundamental, except for the sub-harmonic which can sometimes be less coherent (Rao et al 2010). The BBN can be (roughly) fit with two Lorentzians with characteristic frequencies f_b and f_h which pick out low and high frequency breaks labelled in Figure 1.21.

During the rise to outburst, f_{QPO}, f_b and (to a far lesser extent) f_h increase with the amount of power above $\sim$ 10Hz remaining roughly constant (Gierliński, Nikołajuk & Czerny 2008). Figure 1.22, taken from Wijnands & van der Klis (1999), shows that f_{QPO} and f_b are tightly correlated (also see Klein-Wolt & van der Klis 2008). In this plot, only the black points are for black holes with all others being for neutron stars. I leave the details of NSBs to chapter 3 but we already see that the variability properties are similar for both objects in addition to the spectral properties. In BHBs, the type-C QPO frequency moves from $\sim$0.1-10 Hz.

The BBN can be interpreted in the truncated disc model as originating from turbulence stirred up by the inherently variable MRI (e.g. Balbus & Hawley 1998; Krolik & Hawley 2002). The disc and flow will respond to this turbulence by damping any fluctuations on frequencies greater than the local viscous frequency ($f_{visc}(r) = 1/t_{visc}(r)$). Due to the difference in scaleheight, the disc will damp these fluctuations more efficiently than the flow. The blue lines in Figure 1.23 illustrate that the noise from each radius in the flow will therefore peak at $f_{visc}(r)$ thus implying that $f_b \approx f_{visc}(r_o)$ and $f_h \approx f_{visc}(r_i)$, where r_i is the inner radius of the flow. As the truncation radius moves in, the regions of the flow fluctuating at low frequencies condense onto the disc and so this variability is lost. The inner radius of the flow, in contrast, hardly moves and thus

the power above $\sim$ 10Hz remains constant. If the QPO (black line) is some modulation of Lense-Thirring precession at the truncation radius, its centroid frequency will increase as the truncation radius moves in, as is observed.

PSDs 3-5: the rest

PSD 3 is significantly different from the first two. We still see a fairly strong QPO with harmonic structure but the BBN has almost completely disappeared. This is classed as a type-B QPO. PSD 4 is different again. This is a type-A QPO which is characterised as being very broad and weak (a very large integration time is needed to clearly pick the feature out), with no coincident BBN. It is unclear whether the three QPO types have a common physical origin. It is also unclear why the BBN disappears so suddenly. PSD 5 is for the HSS. The main characteristic of this is the low level of variability which is, of course, consistent with the HSS light curve shown in Figure 1.17 and easy to explain with a disc dominated accretion geometry. There are sometimes very weak QPOs observed during the HSS with $f_{QPO} > 10$ Hz for which the origin is, again, unclear.

1.4.3 Spectral evolution

The evolution of spectral and variability properties can be coupled together in a model independent fashion using hardness vs intensity diagrams (HIDs) and hardness vs rms diagrams (HRDs). In this case, the hardness ratio is defined as the 16-20/2-6 keV count rate and the intensity is defined as the PCU2 count rate (one of the proportional counter units of the proportional counter array; PCA). Figure 1.24 shows the HID and HRD for the 2002 outburst of GX339-4, adapted from Belloni (2010a). Following Belloni (2010), Motta et al (2011), Belloni et al (2005), I use this as a 'prototypical' outburst.

In Figure 1.24, consecutive observations are connected with a line showing that the

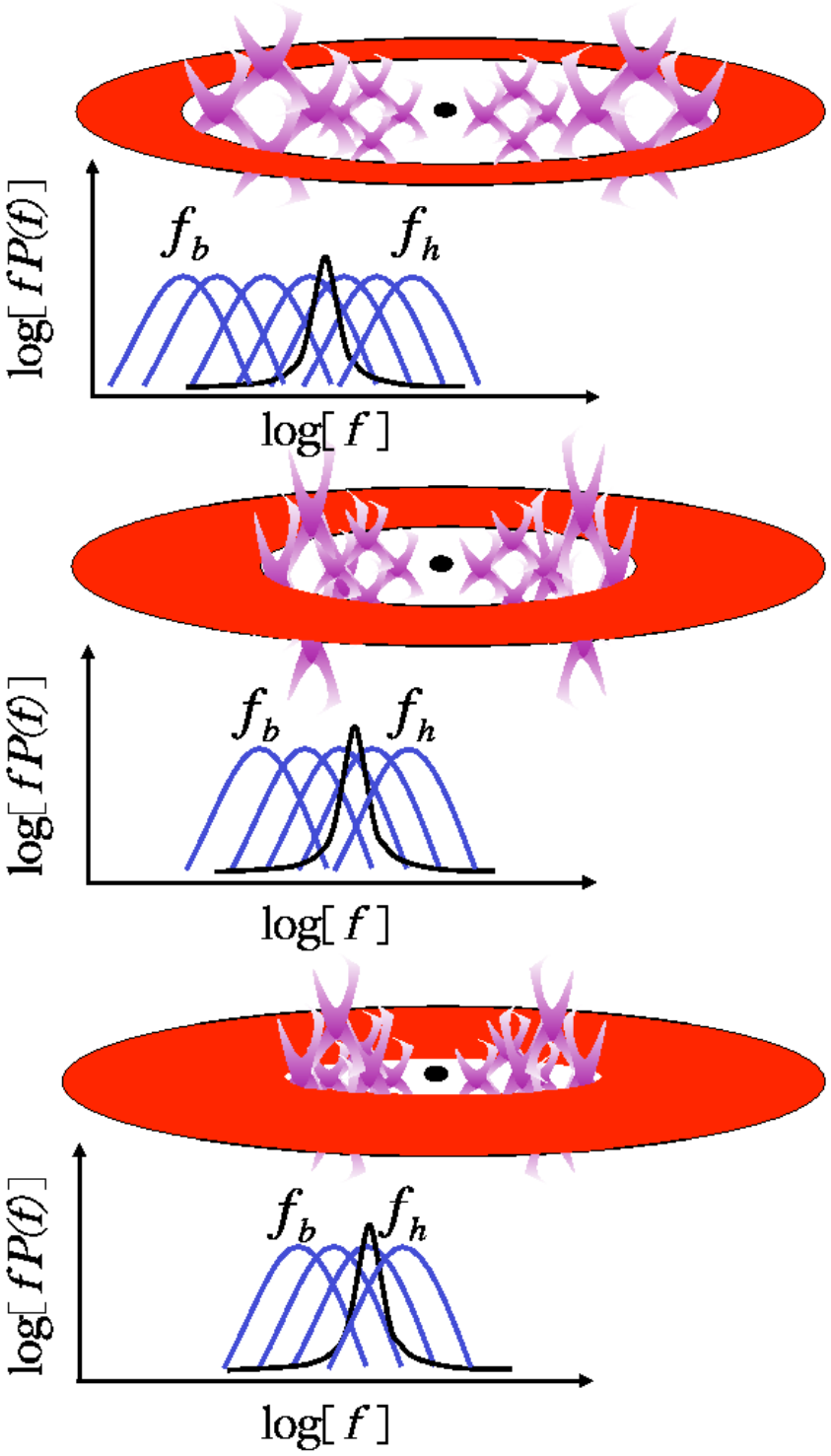

Figure 1.23: Schematic illustrating how the truncated disc model can qualitatively explain the evolution of the BBN. The variability generated in each region of the flow peaks at the local viscous frequency. As the truncation radius moves in, low frequency power is lost.

source follows a characteristic 'q' shaped track. The direction of motion is always anti-clockwise. Plainly, LHS observations are all on the far right of the diagram because the spectrum is dominated by a hard power law and HSS observations reside on the far left because the spectrum is dominated by a disc component. We can now clearly see that the fall back to quiescence happens at lower flux than the rise to outburst. For this reason, it seems best to define the state transitions by the spectral hardness rather than count rate (e.g. Belloni 2010).

We can also use variability properties to differentiate between spectral states. The 5 different kinds of marker in this Figure represent the 5 different varieties of PSD illustrated in Figure 1.21. Filled circles correspond to PSD 1 (weak type-C QPO), open circles to PSD 2 (strong type-C QPO), filled stars to PSD 3 (type-B QPO), open stars to PSD 4 (type-A QPO) and crosses to PSD 5 (very weak red noise). Remarkably, *all* of the observations with type-A and B QPOs occur over a very narrow range of hardness during both the rise and the fall. This implies that there is something unique about this hardness range and so the intermediate state is split up into the hard intermediate state (HIMS), with type-C QPOs, and the soft intermediate state (SIMS), with type-A and B QPOs. This is illustrated at the bottom of the Figure where the type of QPO present for a given range of hardness is labelled.

Radio observations also point to the existence of a collimated jet which displays a connection with the X-ray states and transitions. A compact and mildly relativistic jet is observed in the LHS and HIMS but not in the HSS (Fender, Belloni & Gallo 2004). The transition between these two regions marks the ejection of a fast relativistic jet, observed as a bright radio flare. Fender, Belloni & Gallo (2004) dub the narrow region on the HID at which this occurs the 'jet line' and remark that it coincides with the transition between HIMS and SIMS (which they dub the 'QPO line'). This leaves open the possibility that the material responsible for the BBN is being ejected in the jet thus naturally explaining the transition from type-C to type-B QPOs. However,

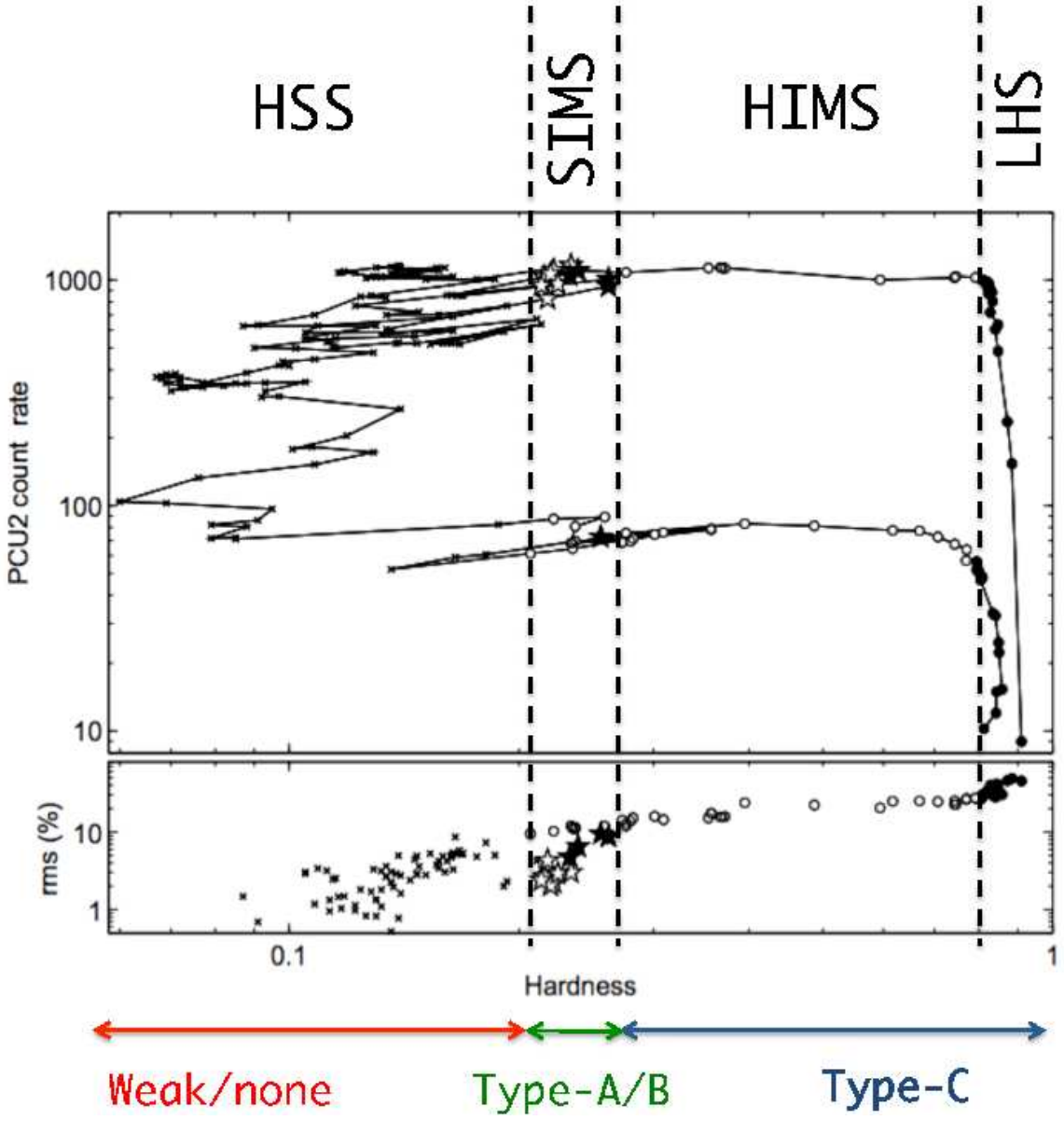

Figure 1.24: HID and HRD of the 2002/2003 outburst of GX339-4. The four state classifications are labelled at the top with the different varieties of QPO labelled at the bottom.

Fender, Belloni & Gallo (2005) use a bigger sample to show that the lines do not always coincide but are always close.

Whereas the HID is q shaped, the HRD follows a linear track with only the SIMS observations falling below the trend line (mainly because of the lack of BBN in the PSD). This, again, can be interpreted with a moving truncation radius. As Figure 1.23 illustrates, the radial extent of the variable flow governs the range of frequencies at which significant variability is present. Since the hardness is ultimately governed by the luminosity of disc photons seen by both the observer and the flow, both the hardness and rms are driven by the position of the truncation radius.

1.5 Higher order statistics

Statistical techniques which compare how timing properties depend on energy band provide the most powerful tools to derive the underlying physics driving the emission in XRBs. In this section, I summarise some of these techniques.

1.5.1 Frequency resolved spectroscopy

Frequency resolved spectroscopy involves comparing the variability amplitude of different energy bands. Figure 1.25 shows PSDs from GX339-4 (reproduced from Wilkinson & Uttley 2009) in the LHS for 0.5-1keV (solid red line) and 2-10keV (dotted blue line) energy bands. It is clear that the two PSDs have different shapes. It is also possible to see that there is more integrated power in the soft (0.5-1keV) band compared with the hard (2-10keV) band.

Integrating the PSD for each energy band over only a narrow frequency range (rather than over all frequencies) isolates the fractional variability amplitude as a function of energy *and* frequency. Multiplying the fractional variability through by the average count rate in that energy band, $\mu(E)$, gives the *absolute* variability as a

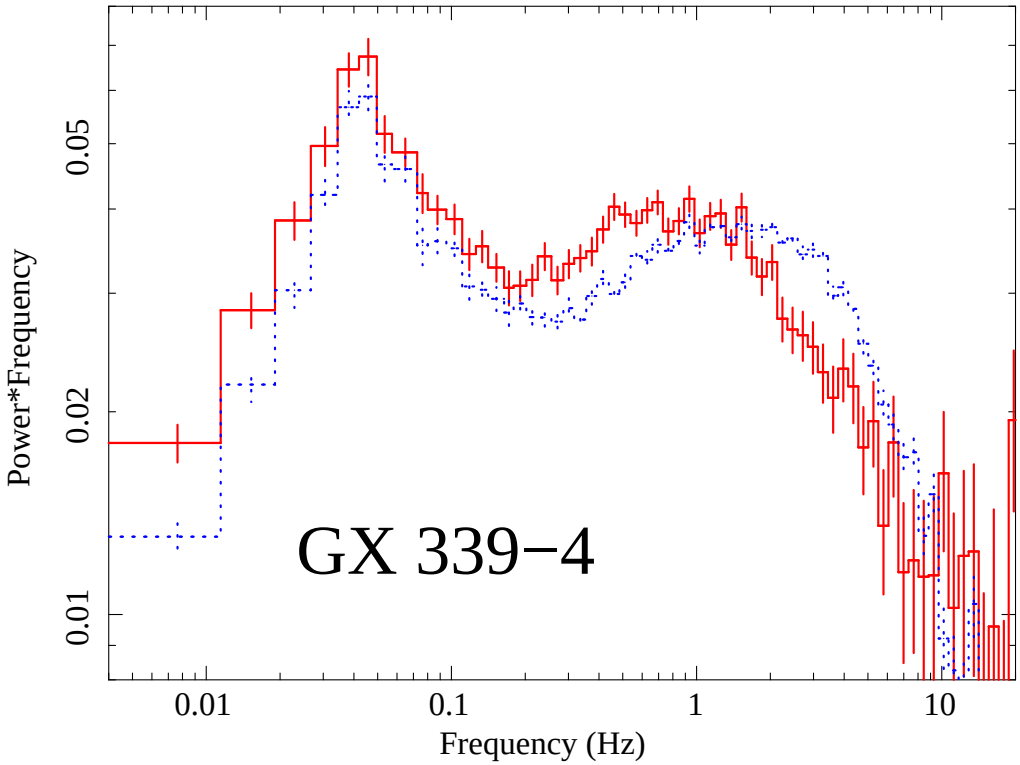

Figure 1.25: Soft and hard band PSDs for GX339-4, as seen by *XMM Newton* (reproduced from Wilkinson & Uttley 2009). The solid red line is for 0.5-1keV and the dotted line is for 2-10keV. Note, the $y-$axis is plotted on a linear scale.

function of energy and frequency. The spectrum which varies in the frequency range $f - \Delta f/2$ to $f + \Delta f/2$ is therefore given by

$$S(E, f) = \mu(E)\sqrt{P(E, f)\Delta f}. \tag{1.34}$$

This is extremely useful because it is in units of count rate and so spectral components can be recognised in the data.

The right hand panel of Figure 1.26 is taken from Revnivtsev, Gilfanov & Churazov (1999) and shows the spectrum of Cygnus X-1 in the LHS for three different frequency ranges, plotted as a ratio to a power law with $\Gamma = 1.8$. It is clear that the power law is harder and the reflection features are weaker for higher frequencies. The first (and to date only) intuitive explanation for this in the literature, offered in Ingram & Done

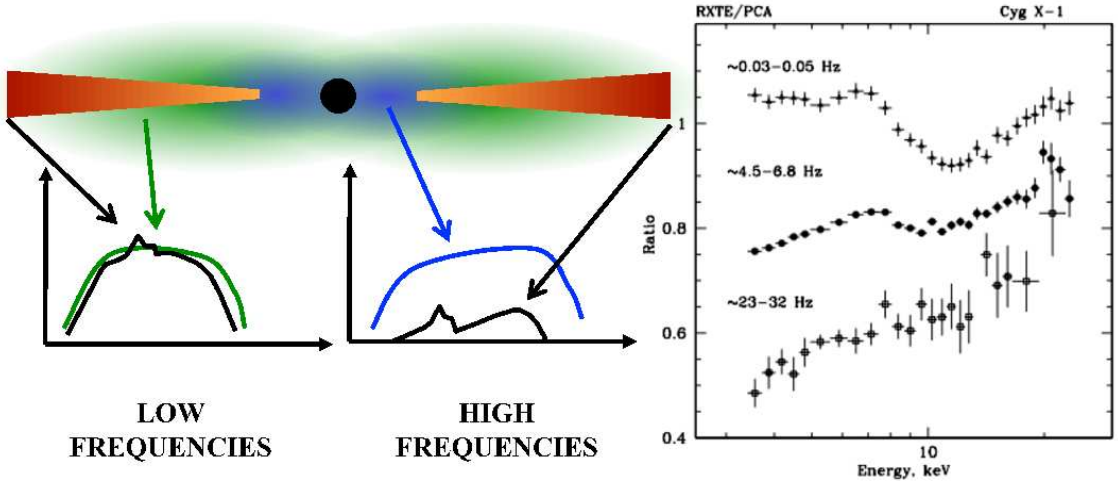

Figure 1.26: *Right:* Frequency resolved spectra for Cygnus X-1 in the LHS (Revnivtsev, Gilfanov & Churazov 1999). The slow variability displays a softer spectrum and stronger reflection features than the fast variability. *Left:* The interpretation of this in a truncated disc geometry (see text).

(2011; 2012) which form the basis for Chapters 4 and 5 of this thesis, is demonstrated by the schematic in Figure 1.26 (left). This shows a truncated disc geometry, in which the inner regions vary more rapidly than the outer regions because of the difference in local viscous timescale. Because the outer regions are closer to the disc, electrons there will see a greater flux of disc seed photons and therefore will be cooler than those in the inner regions. Therefore the inner regions emit the hardest spectrum (the blue line in the cartoon) and dominate the high frequency spectrum. By much the same argument, the disc sees a greater flux of Comptonised photons from the (closer by) outer regions than from the inner regions, meaning that the slowly varying spectrum from the outer region displays stronger reflection features. We therefore see that this technique effectively probes the spectrum as a function of *radius*, since all characteristic frequencies of the accretion flow have a radial dependence.

1.5.2 Correlated variability

A ubiquitous property of emission from accreting objects is the strong correlation observed between different energy bands. Figure 1.27 is taken from Churazov, Gilfanov & Revnivtsev's (2001) study of Cygnus X-1 in the HIMS. The left hand panel shows the count rate in a soft (< 3.3keV) energy band, $S(t)$, plotted against the corresponding count rate in a hard (> 9.4keV) energy band, $H(t)$. Each point is averaged over 16s and so the highest variability frequency visible is 0.03125Hz. It is clear that the two correlate, with the points being well described by the straight line, $S(t) = A + B\ H(t)$ where $A > 0$. This shows that the spectrum varies in *shape* as well as intensity (as we already know from frequency resolved spectroscopy). The authors find a similarly good linear relation between the count rate in each energy channel, $C(E,t)$, and the hard band such that $C(E,t) = A(E) + B(E)\ H(t)$. $A(E)$ and $B(E)$ therefore represent the constant and variable components of the spectrum respectively. In the right hand panel of Figure 1.27, both components are unfolded around the PCA response using a $\Gamma = 2.5$ power law model and plotted in units of energy $\times$ flux. $A(E)$ (which is in absolute units) is represented by the open circles and $B(E)$ (which has an arbitrary normalisation) is represented by the filled circles. Clearly the shape of the constant component is well described by the multi-coloured disc black body model (with peak temperature $kT_{bb} = 0.5$keV) shown in yellow whereas the variable component looks like Comptonisation plus reflection. Finally, the solid square points are selected for high and low flux intervals of $H(t)$. The green lines approximate these points reasonably well using a model $M(E) = A(E) + I\ B(E)$, where I is the only free parameter. Thus the stable disc / variable corona picture is appropriate, at least for the SIMS.

Another manifestation of the correlated nature of XRB variability is the linear rms-flux relation. This can be calculated by splitting the light curve into ~ 3s segments and finding the mean (flux) and standard deviation (σ) in each segment before plotting σ against flux. Figure 1.28, from Uttley & McHardy (2001) shows that, after binning, the

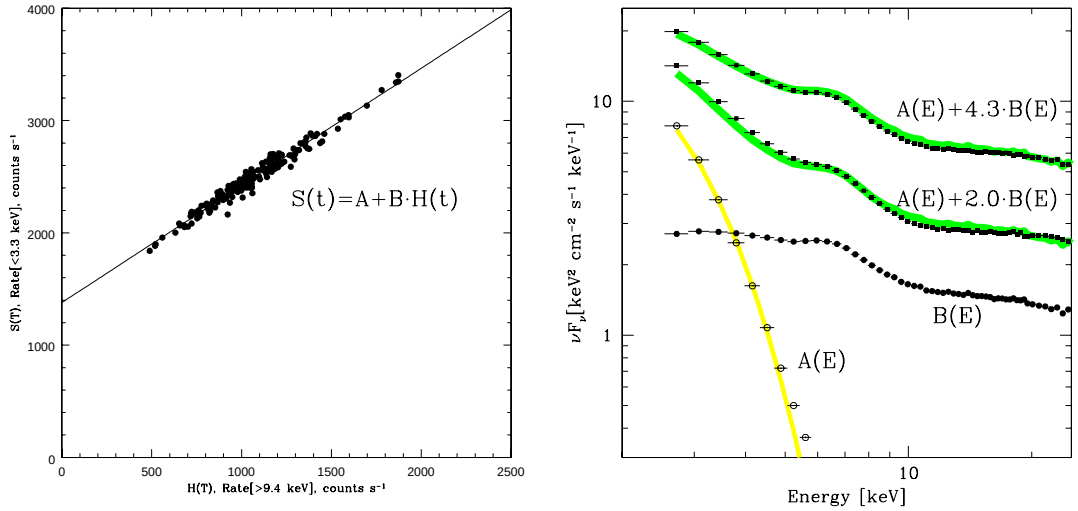

Figure 1.27: *Left:* Soft band ($<$ 3.3keV) count rate plotted against hard band ($>$ 9.4keV) count rate for Cygnus X-1 in the SIMS (Churazov, Gilfanov & Revnivtsev 2001). The two correlate and the points can be fit with the straight line $S(t) = A + B.H(t)$. *Right:* This relation can be used (see text) to define constant, $A(E)$ and variable, $B(E)$, components shown in the right hand plot. The constant component is the shape of a disc spectrum whereas the variable component contains power law and reflection components.

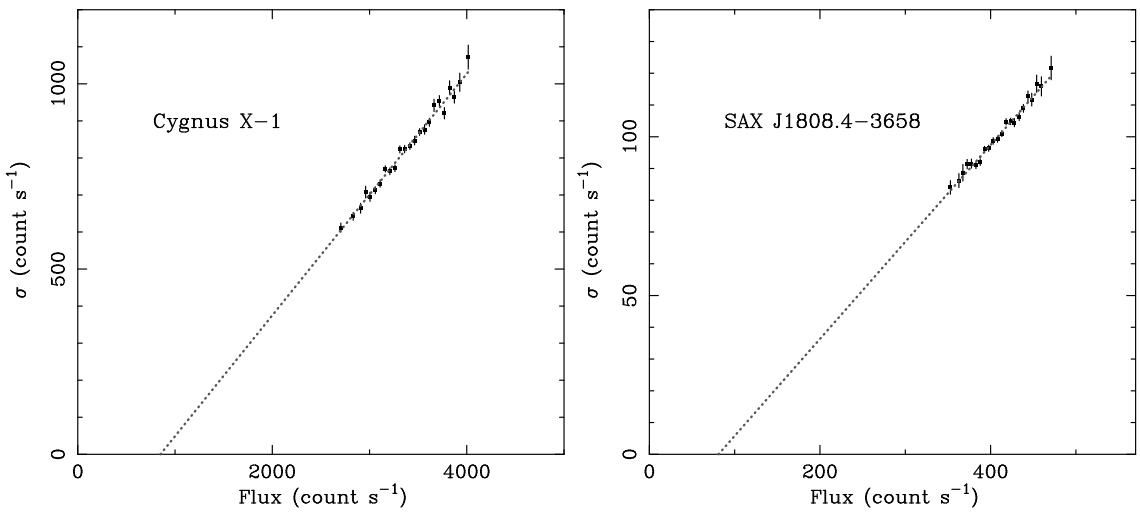

Figure 1.28: The rms-flux relation for the BHB Cygnus X-1 and the accreting millisecond X-ray pulsar SAX J1808.4-3658 (Uttley & McHardy 2001).

relation is clearly linear both for the BHB Cygnus X-1 and the atoll source (millisecond X-ray pulsar) SAX J1808.4-3658. This is seemingly a ubiquitous property of emission from accretion. Linear rms-flux relations have been observed in BHBs, NSBs, an active galactic nucleus (AGN) and an ultra luminous X-ray (ULX) source (Uttley & McHardy 2001; Uttley 2004; Gaskell 2004; Uttley, McHardy & Vaughan 2005, Heil & Vaughan 2010; Heil, Vaughan & Uttley 2011; 2012).

The fact that the different energy bands and timescales are correlated tells us that, in a picture where different frequencies are generated in different regions of the flow, these regions must be in causal connection (Uttley, McHardy & Vaughan 2005). The truncated disc interpretation of the PSD is consistent with this as long as we consider the mass accretion rate fluctuations stirred up in each region of the flow to *propagate* towards the compact object (Lyubarskii 1997). As I show explicitly in Chapters 4 and 5, the linear rms-flux relation (and the linear relation between $S(t)$ and $H(t)$; Kotov, Churazov & Gilfanov 2001) can be reproduced once we consider propagation (Arévalo & Uttley 2006).

1.5.3 The cross spectrum

The cross spectrum is particularly useful for studying accreting objects because it picks out correlated variability. Moreover, unlike the power spectrum, the cross spectrum contains information on both variability *amplitude* and *phase*. If we imagine measuring light curves from a range of subject bands, $s(E,t)$, and a reference band, $r(t)$, the cross spectrum is

$$C(E,f) = S^*(E,f)R(f). \tag{1.35}$$

This is a complex function and so has real and imaginary parts given by

$$\begin{aligned}
\Re[C(E,f)] &= \Re[S(E,f)]\Re[R(f)] + \Im[S(E,f)]\Im[R(f)] \\
&= |C(E,f)| \cos\Delta(E,f) \\
\Im[C(E,f)] &= \Re[S(E,f)]\Im[R(f)] - \Im[S(E,f)]\Re[R(f)] \\
&= |C(E,f)| \sin\Delta(E,f).
\end{aligned} \tag{1.36}$$

where $\Delta(E,f)$ is the frequency dependent phase lag of the subject band (centred at E) with respect to the reference band (so $\Delta > 0$ is for the subject band lagging the reference band). We now hit the same problem we encountered for the power spectrum: we cannot measure continuous and infinite functions, only finite and discretely binned light curves. This problem can be solved by separately smoothing the real and imaginary parts of the cross spectrum in the same way as described for the power spectrum in section 1.4.1. After this smoothing has been performed (which is hereafter assumed rather than written explicitly), we can recover the value of the phase lag

$$\tan\Delta(E,f) = \frac{\Im[C(E,f)]}{\Re[C(E,f)]}, \tag{1.37}$$

and the associated time lag

$$t_{lag}(E,f) = \frac{\Delta(E,f)}{2\pi f}. \tag{1.38}$$

The left hand panel of Figure 1.29, from Nowak et al (1999), shows the time lag of the 8.2-14.1keV band with respect to the 0.0-3.9keV band for Cygnus X-1 in the LHS,

as seen by the *RXTE* PCA. We see that the hard lags the soft with the amplitude of the lag reducing with increasing frequency. The right hand panel, taken from Kotov, Churazov & Gilfanov (2001), shows the time lag, again for Cygnus X-1, for a frequency bin centred on 2.5Hz as a function of energy (the reference band is trivially where the lag is zero). We see that the lag amplitude increases with subject band energy.

As shown by Kotov, Churazov & Gilfanov (2001) and Arévalo & Uttley (2006), this can be explained in the propagating mass accretion rate fluctuations model of Lyubarskii (1997) if the outer regions emit a softer spectrum than the inner regions. Consider a perturbation at large r which modulates the soft spectrum immediately. It will take some time to propagate to the inner regions where it is emitted in the hard spectrum. The larger the separation between energy bands, the further the perturbation has to travel to get to the hard emitting region. Also, all regions in the flow can vary slowly but only the inner regions can vary quickly. Therefore a slow perturbation is more likely to have travelled a long distance than a fast perturbation which must have originated at small r. Such a model, using propagating fluctuations in an inhomogeneous emitting region, was used to create the red line in the right hand panel (Kotov, Churazov & Gilfanov 2001). The model I consider in this thesis is naturally consistent with this reasoning because the outer regions of the flow see more seed photons and are therefore cooler than the inner regions. This assumption is, of course, also consistent with the results of frequency resolved spectroscopy.

The cross spectrum can also be used to study the amplitude of correlated variability. The covariance spectrum, which is analogous to the power spectrum is given by

$$Cov(E, f) = \frac{|C(E, f)|^2}{|R(f)|^2}, \tag{1.39}$$

where $|R(f)|^2$ is the white noise subtracted power spectrum of the reference band. If a normalisation analogous to equation 1.27 is used, integrating $Cov(E, f)$ from f_1 to f_2 gives the (squared) correlated fractional variability amplitude of the subject band in that frequency range. In XRBs, the intrinsic variability is highly correlated and so

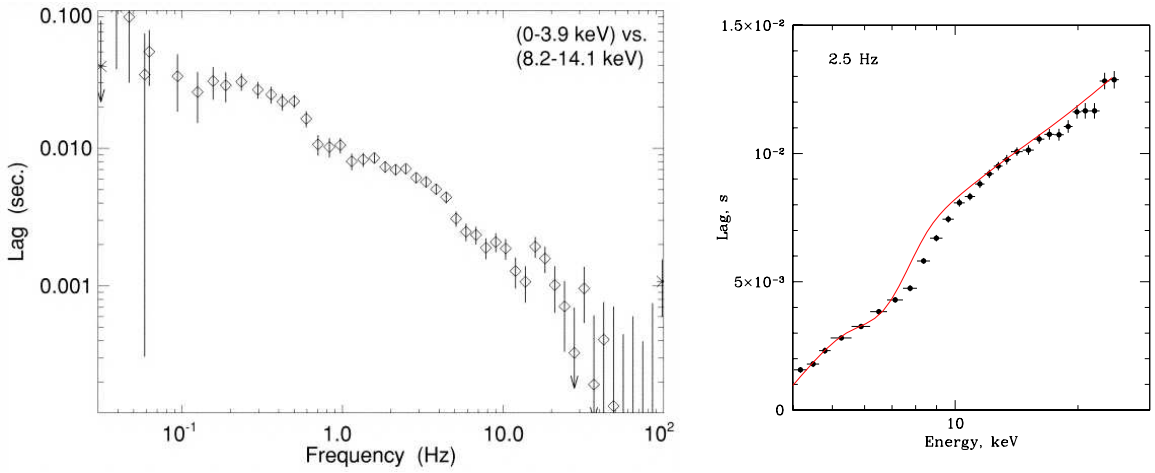

Figure 1.29: *Left:* Time lag of hard (8.2-14.1keV) emission with respect to soft (0-3.9keV) emission in Cygnus X-1, plotted as a function of frequency (Nowak et al 1999). *Right:* Time lag of the subject band with respect to a reference band centred on ∼3keV, plotted as a function of subject band energy for Cygnus X-1 (Kotov, Churazov & Gilfanov 2001).

$Cov(E, f)$ provides an estimate of the subject band power spectrum except the white noise in the subject band automatically cancels and so does not need to be subtracted. The reference band white noise still has to be subtracted but it is selected as the band with the highest signal to noise so as to reduce errors. Therefore, the formula

$$S(E, f) = \mu(E)\sqrt{Cov(E, f)\Delta f}, \tag{1.40}$$

gives the frequency resolved spectrum but with much smaller errors, particularly for high energies and high frequencies where the signal to noise is generally poor (Wilkinson & Uttley 2009).

Figure 1.30, reproduced from Wilkinson & Uttley (2009), shows the unfolded frequency resolved spectrum of SWIFT J1753.5-0127 in the LHS, calculated using this method. The green line is the mean spectrum, the red line is for 'slow' variability ($\sim 0.004 - 0.4$Hz) and the blue line is for 'fast' variability ($0.25 - 10$Hz). These data

are from the *XMM Newton* European Photon Image pn Camera (EPIC-pn) which has much better low energy coverage than the *RXTE* PCA. This means that the disc peak energy is within the observable band pass. The authors fit all three spectra with an absorbed disc plus power law model. If the disc were completely stable, the disc normalisation would drop to zero for the red and blue lines. We see that this is not the case and thus this is the first (and only) proof that the disc varies in the LHS. It is not clear from this exactly what variability amplitude the disc contributes relative to the power law because decomposing a frequency resolved spectrum into additive spectral components is formally inappropriate if those components are correlated with one another. Since the disc and power law *do* correlate, a disc, $d(E,t)$, plus power law, $pl(E,t)$, spectral model has a power spectrum

$$\begin{aligned} P(E,f) &= |D(E,f)|^2 + |PL(E,f)|^2 \\ &\quad +2|D(E,f)||PL(E,f)|\cos\Delta(E,f). \end{aligned} \tag{1.41}$$

Since the cross term does not vanish (at least not for low frequencies), we cannot trust the quantitative information provided by the fit in Figure 1.30. We can, however, see that there *is* disc variability which (unsurprisingly) peaks at lower frequencies. More work is needed to quantitatively ascertain how important disc variability is in the LHS.

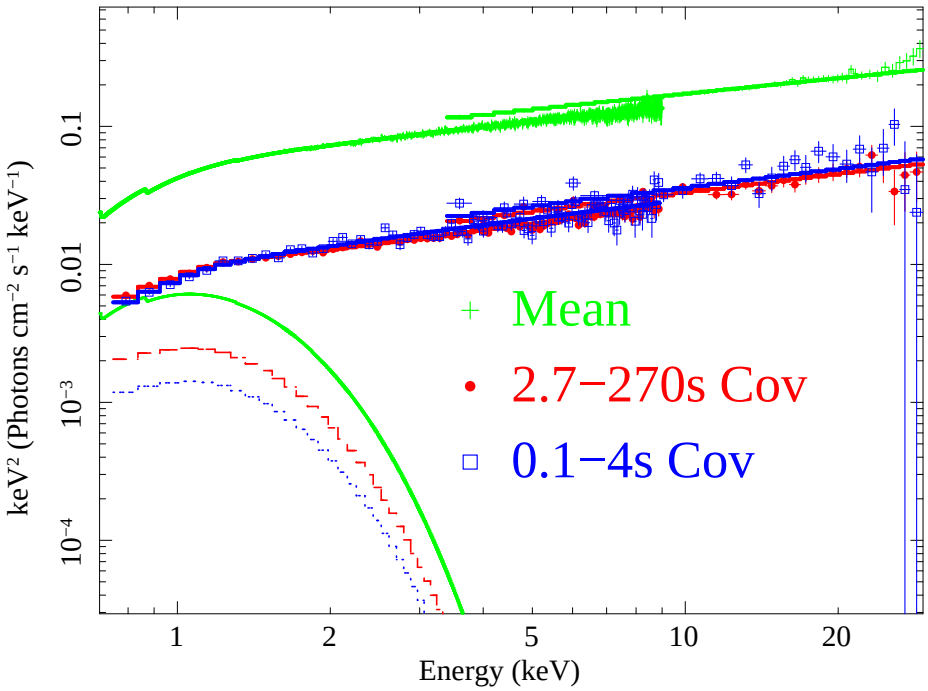

Figure 1.30: Frequency resolved spectrum for SWIFT J1753.5-0127 in the LHS, calculated using the covariance spectrum (Wilkinson & Uttley 2009). The mean spectrum is in green, the fast variability in blue and the slow variability in red. We clearly see that disc emission *does* contribute the the variability in the LHS.

Chapter 2

Low frequency QPO spectra and Lense-Thirring precession

2.1 Introduction

Relativistic precession models associate the low frequency QPO (LF QPO) with the Lense-Thirring precession frequency at the truncation radius (Stella & Vietri 1998; Stella et al 1999; Psaltis & Norman 2000, Fragile et al 2001). In this picture, a moving truncation is responsible both for the changing spectral shape *and* the moving QPO frequency. However, there are several problems with such an identification. Firstly, this associates the frequency with the inner edge of the thin (cool) disc, yet the QPO (and all the rapid variability) is associated with the Comptonised emission, not the disc (Churazov et al 2001; Sobolewska & Życki 2006; Belloni et al 1997; Cui et al 1999; Casella et al 2004). Secondly, and more fundamentally, it requires that all BHB are spinning. Given their birth in the collapsing core of a massive star this is not surprising, with estimates of $a_* < 0.8 - 0.9$ (Gammie, Shapiro & McKinney 2004). However, this allows for a *range* of spins in BHBs, as is also suggested by observations (Davis, Done & Blaes 2006; Shafee et al 2006). The Lense-Thirring precession timescale depends strongly on spin, so predicts that the same truncation radius in BHBs of different spin

should give different QPO frequencies. Yet observations seem to show little difference in QPO frequencies from object to object (Sobczak et al 2000; Pottschmidt et al 2003, Kalemci et al 2004, Belloni et al 2005). This makes any Lense-Thirring model appear uncomfortably fine-tuned, especially in the light of tight correlation between the low frequency break in the power spectrum and QPO frequency which extends across both black holes *and* neutron stars (Wijnands & van der Klis 1999). The low frequency break is most plausibly from the viscous timescale at r_o (Psaltis & Norman 2000; DGK07), so does not depend on spin, unlike a Lense-Thirring model for the QPO. Any range in spin between different objects (and neutron star spins are *known* to range between $a_* = 0.2 - 0.4$, while the black hole spins can plausibly be significantly larger) should then give rise to a large dispersion in the break-QPO relation, yet the data limit this to less than a factor of 2 (Klein-Wolt & van der Klis 2008).

This chapter is adapted from Ingram, Done & Fragile (2009) in which we show how Lense-Thirring models can match the observations by considering the physical interpretation of recent numerical simulations. Specifically, we suggest that the *shape* of the warped, geometrically thick accretion flow which fills the region inside r_o affects the frequency at which it precesses. We discuss how this precession can modulate the hard X-ray emission in order to produce the observed energy dependence as well as frequency behaviour of the QPO.

2.2 Predictions for low frequency QPO spectra from Lense-Thirring precession

2.2.1 Point particle

The Lense-Thirring precession frequency for prograde orbits in the limit of a small perturbation with respect to the equatorial plane is

$$f_{LT} = |f_\phi - f_\theta| = f_\phi \left[1 - \sqrt{1 - \frac{4a_*}{r^{3/2}} + \frac{3a_*}{r^2}}\right] \quad (2.1)$$

where $f_\phi = c/[2\pi R_g(r^{3/2} + a_*)]$, a_* is the dimensionless spin per unit mass and r is the dimensionless orbital radius (in units of $R_g = GM/c^2$).

We assume a black hole mass of $10M_\odot$ throughout this paper. Figure 2.1 shows the precession frequency for a variety of black hole spins from $0.3 < a_* < 0.998$ as a function of radius down to the last stable orbit, r_{lso}. This clearly shows that the highest frequency predicted is heavily dependent on spin, and that these are well in excess of the ~ 10Hz maximum observed QPO frequency for $a_* > 0.3$. The corresponding Keplerian frequencies (upper lines) plotted for comparison trace out even higher values.

2.2.2 Solid disc with inner radius at the last stable orbit

The simple estimates in the previous section assumed single particle orbits at the truncation radius of the thin disc, r_o. However, the energy dependence of the QPO clearly associates it with the hot flow rather than the disc. Thus we consider Lense-Thirring precession of the geometrically thick, hot flow interior to the truncated disc as illustrated in Figure 2.2. Fragile et al. (2007) estimate the associated frequency assuming that the black hole torque from the misalignment makes the entire flow precess as a solid body between an inner and outer radius, r_i and r_o (again scaled in

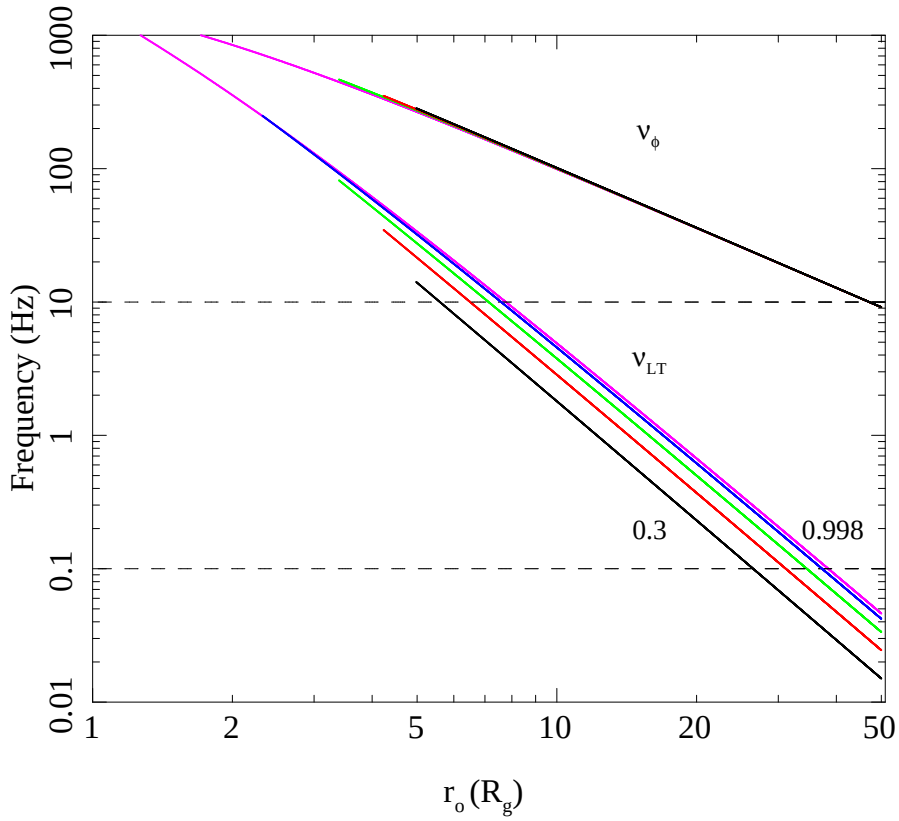

Figure 2.1: Lense-Thirring precession frequency for a point particle and Keplerian orbital frequency plotted against orbital radius. The solid black, red, green, blue and magenta lines depict $a_* = 0.3$, $a_* = 0.5$, $a_* = 0.7$, $a_* = 0.9$ and $a =_* 0.998$ respectively. The dashed lines represent the limits of the observed range. Although Lense-Thirring precession gives predictions closer to observation than Keplerian frequencies, the peak frequency and a_* dependence do not match observation.

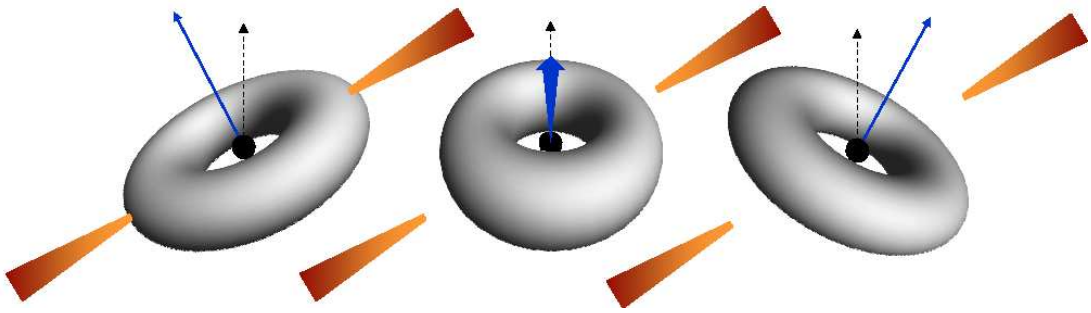

Figure 2.2: Schematic diagram of the geometry considered. The inner flow (grey with blue angular momentum vector) precesses about the black hole angular momentum vector whilst the outer disc (red/orange) remains aligned with the binary partner. The flow extends between r_i and r_o.

units of R_g to make them dimensionless). This gives

$$f_{prec} = \frac{(5-2\zeta)}{\pi(1+2\zeta)} \frac{a_*[1-(r_i/r_o)^{1/2+\zeta}]}{r_o^{5/2-\zeta} r_i^{1/2+\zeta}[1-(r_i/r_o)^{5/2-\zeta}]} \frac{c}{R_g} \tag{2.2}$$

where the moment of inertia of the disc is calculated assuming a surface density of the form $\Sigma = \Sigma_o(r/r_i)^{-\zeta}$. Classical advection dominated accretion flows give $\zeta = 0.5$, while thin discs have $\zeta \sim -0.5$, and the numerical simulations give $\zeta \sim 0$. We choose $\zeta = 0$, but note this makes less than a factor of 2 difference from the other prescription for the resultant QPO frequency even at the largest radii, and that this difference decreases monotonically as r_o decreases.

Figure 2.3 shows the precession frequency plotted against r_o for a number of spins with $r_i = r_{lso}$. These frequencies are always higher at a given r_o as the effective radius is a surface density weighted average from r_i to r_o We still, however, see the same two problems encountered in section 2.2.1, namely, that the peak frequency is too high and varies too strongly with spin.

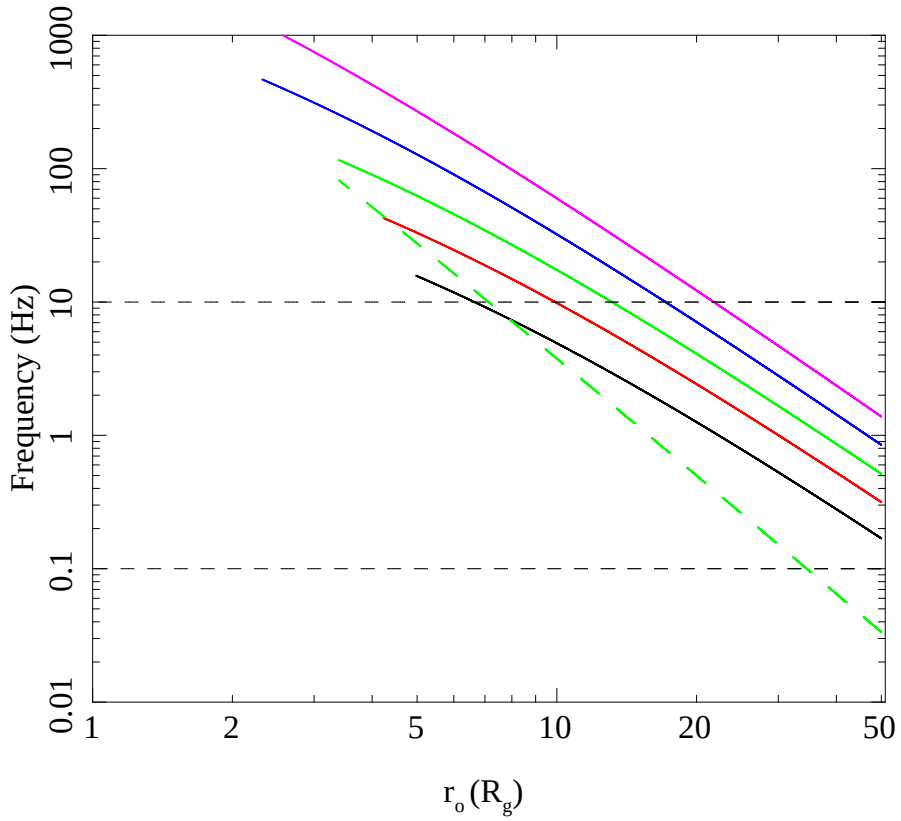

Figure 2.3: Precession frequency of an inner flow of varying outer radius. The solid black, red, green, blue and magenta lines represent spin values of $a_* = 0.3$, $a_* = 0.5$, $a_* = 0.7$, $a_* = 0.9$ and $a_* = 0.998$ respectively. The green dashed line represents a point particle for $a_* = 0.7$. The minimum radius is the last stable orbit as a function of spin. We see that, as in the case of point particle Lense-Thirring, the peak frequency is both higher than observed values and has too strong a spin dependence.

2.2.3 Inner radius

So far we have considered a flow with its inner radius at the last stable orbit. Instead, the precession timescale is set by where the surface density drops significantly, as the region interior to this will not contribute significantly to the moment of inertia. Full general relativistic simulations of the magneto-rotational instability (MRI, the underlying source of the stresses which transport angular momentum) show that this drops sharply at around $1.5 \times r_{lso}$ (e.g. Fig 4. in Krolik, Hawley & Hirose 2005) for thick flows aligned with the black hole spin.

However, we are considering Lense-Thirring precession so the key issue is that the flow is *misaligned*. The extra torques on the flow give extra contributions to the stresses. Simulations (e.g. Fragile et al 2007) have shown this to increase the inward velocity, and therefore decrease the density of the flow. Figure 2.4 shows the surface density profile obtained from two simulations, both of a flow misaligned by 15^o but with differing black hole spin. The blue points are for $a_* = 0.9$ (Fragile et al 2007) and the red points are for $a_* = 0.5$ (Fragile et al 2009). We have fit the data with a smoothly broken power law function $\Sigma_o x^\alpha/(1+x^\gamma)^{(\zeta+\alpha)/\gamma}$ where $x = r/r_i$. This gives x^α and $x^{-\zeta}$ for $r << r_i$ and $r >> r_i$, respectively, while γ controls the sharpness of the break. We fix $\zeta = 0$ (see Section 2.2.2) and obtain $r_i \sim 9$ for $a_* = 0.9$ and $r_i \sim 8$ for $a_* = 0.5$, both of which are significantly larger than $r_{lso} - 1.5\ r_{lso}$ for untilted flows.

Ideally, we would now like to re-plot Figure 2.3 using the inner radius for a misaligned flow. However, we only have two simulation points for r_i which is clearly inadequate for our purposes. We therefore make an analytical approximation in the next section in order to address this point.

Solid flow with inner radius set by bending waves

The additional torques will be strongest where the flow is most misaligned, so these should track the *shape* of the flow. This is set by bending waves, which communicate

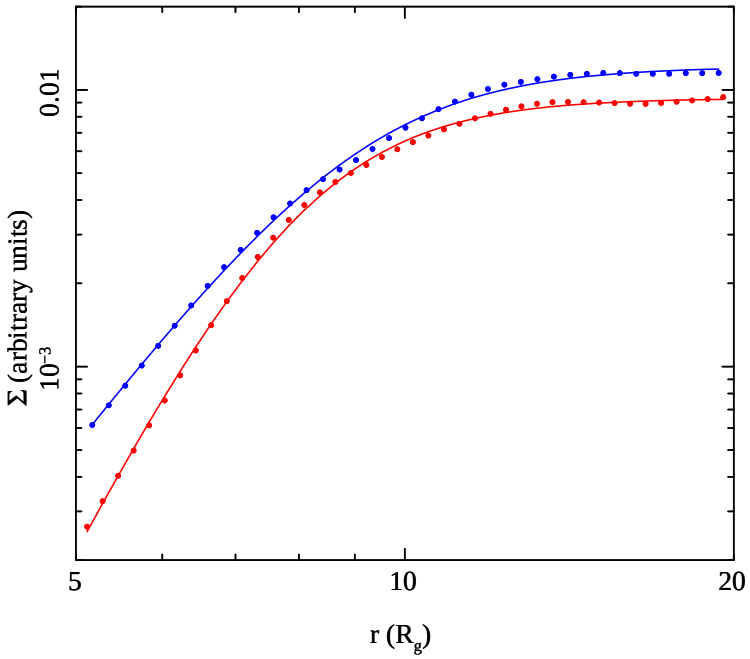

Figure 2.4: Surface density as a function of radius recovered from numerical simulations of a misaligned flow (Fragile et al 2007) with $a_* = 0.5$ (red) and $a_* = 0.9$ (blue). Data points have been fit by a double law which breaks at r_i. We find $r_i(a_* = 0.5) \sim 8$ and $r_i(a_* = 0.9) \sim 9$.

the warp and twist in initially circular and coplanar orbits, against viscous damping. Analytic approximations to the resulting shape can be calculated assuming linear perturbations in an initially thin disc (e.g. Ferreira & Ogilvie 2008). The global structure then depends on the ratio of the viscosity parameter, α, relative to the disc semi-thickness, $H = hR_g$. For $\alpha > h/r$, warped disturbances via Lense-Thirring precession are propagated by viscous decay which eventually drags the inner disc into alignment with the black hole spin, while the outer disc aligns with the orbital plane of the companion star (Bardeen & Peterson 1975, King et al 2005). The Bardeen-Petterson transition radius can be roughly defined as the point where viscosity can no longer propagate warps in the disc outward quickly enough to prevent a twisting of the disc due to differential precession.

However, we are considering instead a hot inner flow which is geometrically thick so $\alpha < h/r$. In this case, the warp is propagated via bending waves. The local sound crossing timescale is shorter than the precession timescale throughout the flow allowing the material to be strongly coupled by pressure waves. Consequently, the flow precesses as a solid body (Fragile et al 2007) with its shape influenced by the bending waves (Ferraria & Ogilvie 2008; Pringle 1992, Lubow et al. 2002). Undamped bending waves have a characteristic wavelength of

$$\lambda \sim \frac{\pi r^{9/4}}{(6a_*)^{1/2}}\Big(\frac{h}{r}\Big). \tag{2.3}$$

These waves are, therefore, smooth at large radii and oscillatory at small radii due to the strong r dependence of the wavelength. Figure 12 in Fragile et al (2007) and Figure 10 in Fragile et al (2009) show the tilt angle of the flow at varying radii for $a_* = 0.9$ and 0.5, respectively. This tilt angle increases dramatically at small radii in a manner similar to that of the bending waves. It could be that this rapid change in disc tilt gives rise to additional stresses which lead to the observed drop off in surface density. It is encouraging that Figure 13 in Fragile et al (2007) seems to support this assertion as it shows that the viscosity parameter of the disc, α, increases rapidly at small radii.

The largest radius at which the rate of change of disc tilt is significant is $r \sim \lambda/4$ i.e. at $r_i \sim 2.5(h/r)^{-4/5}a_*^{2/5}$ (using equation 2.3) as this is the first point at which the bending waves have room to turn over. A more rigorous treatment by Lubow et al (2002) gives $r_i \sim 3.0(h/r)^{-4/5}a_*^{2/5}$. Both of these expressions give ~ 10 and 8 for $a_* = 0.9$ and 0.5, respectively, for $h/r = 0.2$, in agreement with the simulations (see Section 2.2.3).

Figure 2.5 shows the precession frequency recalculated assuming the inner radius as above. We see that the expected decrease in QPO frequency with spin is offset by the increase in inner radius with spin. Counter-intuitively, the QPO probes smaller radii in the flow for lower black hole spins! Figure 2.5 is in fact remarkably like the observed data in that it predicts a maximum frequency of ~ 10 Hz for all spins considered here

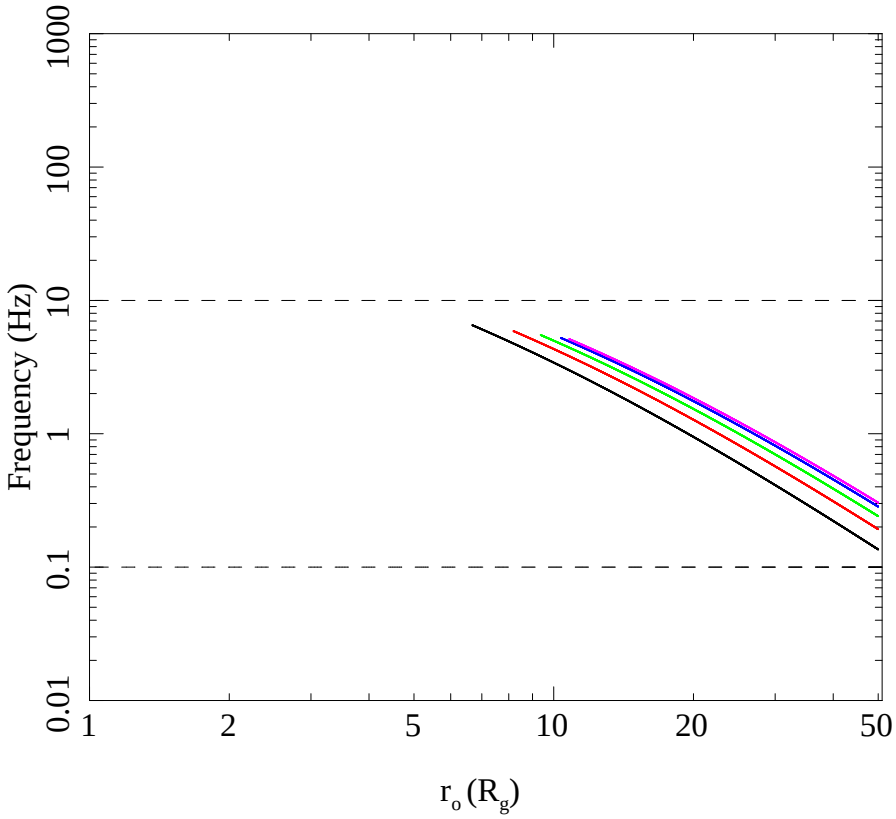

Figure 2.5: Precession frequency versus outer radius of a hot flow with scale height $h/r = 0.2$ and inner radius set by the bending wave region $r_i = 3.0(h/r)^{-4/5}a_*^{2/5}$ (Lubow et al 2002) for spins of $a_* = 0.3$ (black), $a_* = 0.5$ (red), $a_* = 0.7$ (green), $a_* = 0.9$ (blue) and $a_* = 0.998$ (magenta). The expected increase in QPO frequency with a_* is mostly cancelled out by the increased radial extent of the bending wave region, and the maximum QPO frequency is $\sim 10Hz$, as observed.

($a_* > 0.3$). It also predicts the frequency to be mostly dependent on the outer radius of the flow, not spin, which allows the QPO frequency to tightly correlate with any other frequency picked out by this radius, e.g. the low frequency break in the broad band power spectrum (Psaltis et al 1999; Wijnands & van der Klis 1999; Psaltis & Norman 2000).

This is a very encouraging result, but we caution that many more simulations are

needed to quantify the behaviour the inner radius as a function of spin, and to assess the effect of misalignment angle (both current simulations are for 15°). Such simulations also mean that the simplified form of the surface density profile in equation 2 can be replaced by the *observed* precession frequency of the flow. However, the two current simulations show the drawback of this approach as this is also sensitive to the *outer* boundary condition. Our model sets the outer radius of the precessing flow by the inner edge of the truncated disc. The flow can only freely precess in the region where there is no thin disc blocking the mid-plane. Instead, the current simulations only include the hot flow, and its effective outer radius is larger for the $a_* = 0.5$ run than in the $a_* = 0.9$ and the precession frequency directly observed from the simulations is roughly a factor of two higher for $a_* = 0.9$ than for 0.5. Thus the simulations need also to include an outer boundary condition in order to properly explore parameter space, and to consider the additional torque on the flow from the interaction between the thin disc and hot flow which adds a great deal of complexity.

2.3 Discussion

The Lense-Thirring frequency of the inner flow precessing as a solid disc does not match observed LF QPO frequencies if we assume the inner radius of the flow is set by the last stable orbit. However, recent numerical simulations show that the surface density profile of a misaligned flow drops substantially at radii which are significantly larger than r_{lso} for $a_* = 0.9$ and $a_* = 0.5$. We postulate that this radius is set by the shape of the bending waves which distort the disc. This radius increases with a_* in a way that counteracts most of the expected increase in QPO frequency with spin at a given r_o. This results in a maximum value of $\sim 5 - 10$Hz for a $10M_\odot$ black hole of almost any spin, as observed.

Clearly this conclusion depends on the outcome of future numerical simulations. It also depends on the flow being misaligned! The Bardeen-Peterson effect dictates that

a misaligned thin disc will gradually align with the black hole at small enough radii (Bardeen & Peterson 1974). Most analytical estimates predict that the disc should be more or less aligned at typical values of the truncation radius (e.g. Fragile et al 2001). This, therefore, implies that the flow should be aligned if most of the material for the hot flow accretes through the outer disc which, in turn, implies that it shouldn't precess! However, the thin disc alignment should be rather different for a truncated thin disc. We intend to explore this effect in future work.

These caveats aside, we have a very attractive model for the origin of the low frequency QPO in black hole binaries. This is made even more compelling as it ties the QPO to the hot flow, so should directly modulate the Comptonised tail, as observed, even though the outer radius r_o is determined by the thin disc.

There are several processes which can imprint the modulation on the spectrum. The flow is translucent (optical depth, $\tau \sim 1$) so there can be weak projected area effects. More importantly, the flow can self-occult causing a dip in the flux of maximum depth $exp(-\tau)$ when the flow is aligned with the observer's line of sight. There should also be a variation in the number of seed photons from the disc irradiating the flow which, for example, will give maximum flux when the flow is maximally misaligned with the disc. Relativistic effects can also contribute to the modulation (Schnittman, Homan & Miller 2006; Schnittman & Rezzolla 2006)

These effects will give a stronger modulation for higher inclination angles, and higher optical depth. There is observational evidence for both of these, with a compilation of BHB showing that the maximum QPO r.m.s. strength increases with inclination, and with mass accretion rate i.e. optical depth of the hot flow (Schnittman, Homan, & Miller 2006). This can also explain why the QPOs appear stronger on the hard–to–soft transition during the rapid rise to outburst than on the soft–to–hard transition on the decline. The hysteresis effect (plausibly caused by the rapid rise driving the disc into a non-steady state configuration: Done, Gierliński & Kubota 2007) means

that the luminosity during the rise is higher, so the mass accretion rate through the hot flow and hence its optical depth are both also larger, giving stronger modulation.

This all fits well with the observations that broader, weaker QPOs are seen in the low inclination systems such as 4U 1543-47 (Schnittman, Homan & Miller 2006). Our model also *predicts* that Cyg X-1 should have the weakest QPOs, as observed, as it is both at low inclination *and* is stable to the hydrogen ionisation instability which drives the enhanced optical depth seen during hysteresis (DGK07).

The physical processes in our model are scale invariant, so predict that the frequencies for a given black hole spin, a_*, depend linearly on mass, as generally assumed (Vaughan & Uttley 2005; Gierlinski et al 2008; Middleton et al 2008). The BHB alone probably span $6 - 14 M_\odot$ (Remillard & McClintock 2006), so this predicts a factor of 2.3 variation in frequency which may be detectable.

2.4 Conclusions

Lense-Thirring precession of a radially extended section of the hot inner flow in the truncated disc models can match the properties of the low frequency QPO in BHB. The outer radius of the precessing flow is set by the truncation radius of the cool disc. This sweeps inwards as the source makes a transition from the low/hard to high/soft state (DGK07). The surface density of a misaligned flow drops off at an inner radius greater than the last stable orbit (Fragile et al 2007). The expected increase in QPO frequency with spin is mostly counteracted by the increasing inner radius in our (albeit speculative) models for r_i. This gives a maximum predicted QPO frequency of 6-10 Hz irrespective of spin, as observed in all BHB. Thus while the QPO mechanism fundamentally depends on black hole spin, the behaviour of the inner radius of the hot flow means that it does *not* give a simple diagnostic of a_*.

The QPO arises from the hot flow, so naturally modulates the hard X-ray flux through a combination of self occultation, projected area and relativistic effects. These

become stronger as a function of inclination and optical depth, as observed.

This gives the first mechanism for the QPO which predicts both its frequency and spectral behaviour, and embeds it firmly in the models for the accretion flow and associated jet. If confirmed by further numerical simulations, this solves the 20 year mystery of how these characteristic frequencies arise in the accretion flow.

Chapter 3

A physical interpretation of the variability power spectral components in accreting neutron stars

3.1 Introduction

Neutron star binaries (NSBs) can be distinguished into two sub-types: the Z-sources and the atoll sources, so named after the shape they trace out on an X-ray colour-colour diagram. The Z-sources are the most luminous ($L/L_{Edd} > 0.5$) while the atolls are seen over the same range of Eddington fractions ($\sim 10^{-3} - 1$) as BHBs (see e.g. van der Klis 2006; 1997). Since BHBs and atolls are both powered by accretion in a similar gravitational potential, it should be possible to apply the ideas developed thus far for BHBs to atoll sources.

The spectral evolution of atolls is often studied using a colour-colour diagram (CD). Figure 3.1 shows a CD for 5 outbursts of the transient atoll source Aquila X-1, reproduced from Reig et al (2004). Here, hard colour is (9.7-16keV counts)/(6.0-9.7keV counts) and soft colour is (3.5-6.0keV counts)/(2.0-3.5keV counts). This can be split into 3 states: the extreme island state (EIS), the island state (IS) and the banana

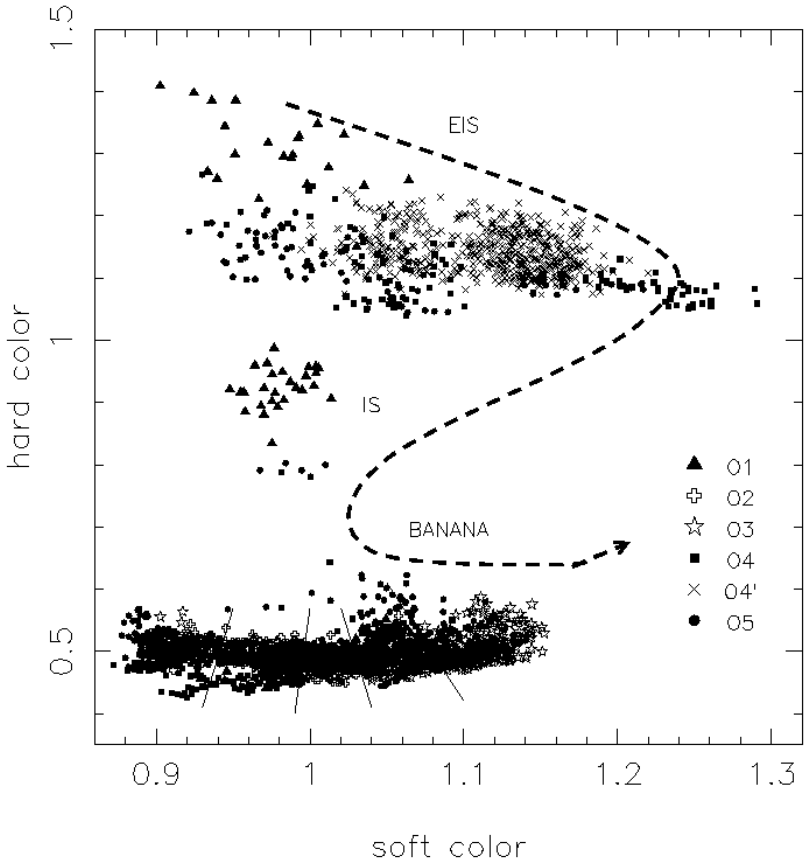

Figure 3.1: Colour-colour diagram for the atoll source Aquila X-1 for 5 different outbursts (reproduced from Reig et al 2004). Hard colour is defined as (9.7-16keV counts)/(6.0-9.7keV counts) and soft colour as (3.5-6.0keV counts)/(2.0-3.5keV counts). The source traces out a characteristic C or atoll shape which can be split into the extreme island state (EIS), island state (IS) and banana branch. The dashed arrow illustrates increasing X-ray luminosity.

branch. The dashed line points out increasing X-ray luminosity.

The main spectral differences between atolls and BHBs can be attributed to the solid neutron star surface. For example, coherent pulses are caused by hotspots forming on the neutron star surface, either due to larger scale magnetic fields (the atoll subclass know as millisecond accreting X-ray pulsars; Gierlinski & Done 2002a; Wilkinson et al 2011; Liu et al 2007) or nuclear burning (X-ray bursts; Strohmayer & Bildsten 2006). Both processes give an excellent estimate of the neutron star spin frequency with X-ray bursts in the millisecond X-ray pulsars SAX J1808.4-3658 and XTE J1814-338 occurring at identical frequencies to the corresponding pulses within an error of ~ 1 Hz (Chakrabarty et al 2003; Strohmayer & Bildsten 2003).

These spin constraints tell us that even the most rapidly spinning neutron stars are only rotating at approximately half the Keplerian rotational frequency (at $r \sim 6$). As remarked in section 1.2.1, Newtonian gravity predicts that half of the rest mass energy of the accretion flow is locked up in the kinetic energy of the accreting gas particles. Material accreting onto the neutron star surface must therefore slow down to the spin frequency of the neutron star and so a boundary layer forms in which the lost kinetic energy is liberated as radiation. In General Relativity, the energy of the boundary layer is even larger (Sunyaev & Shakura 1986; Sibgatullin & Sunyaev 2000) giving it a comparable luminosity to the rest of the accretion flow. This will plainly affect the spectrum, as will direct thermal emission from the surface due to irradiation and/or conduction.

Figure 3.2 (reproduced from Done, Gierlinski & Kubota 2007) shows unfolded, unabsorbed spectra for the atoll 4U 1705-44 (a) in the IS and (b) on the banana branch with the model extrapolated beyond the low energy band pass of the PCA. We see that, as for BHBs, the spectrum can be fit with disc (red), Comptonisation (blue) and reflection (green) components. However, there are differences. The low energy turn-off of the Comptonised emission is not tied to the disc temperature because the

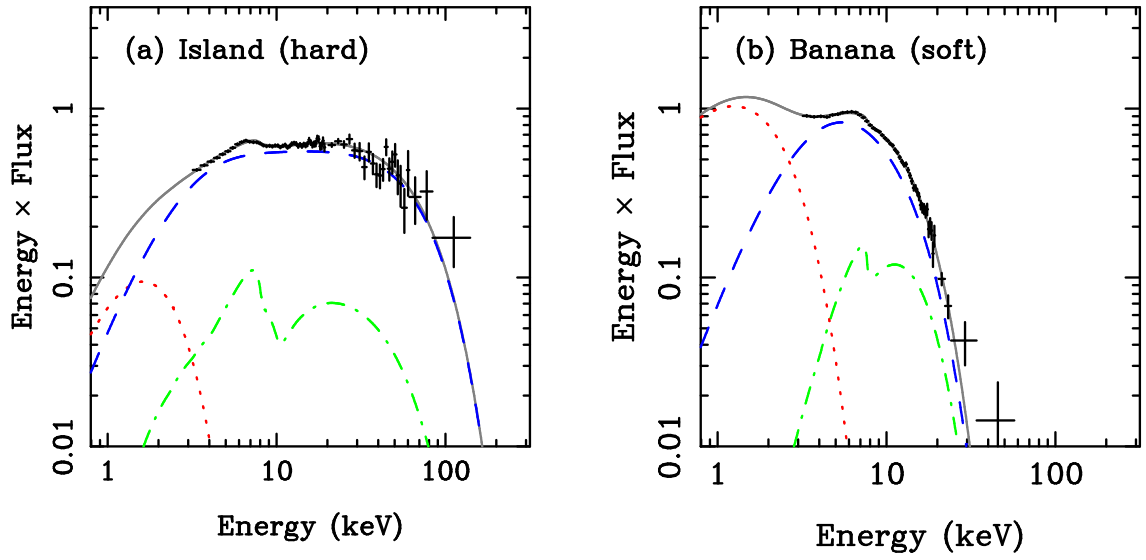

Figure 3.2: *RXTE* spectra of the atoll 4U 1705-44 (a) in the IS and (b) on the banana branch, reproduced from DGK07. The spectra have been unfolded and unabsorbed and the best fitting models have been extrapolated below the PCA bandpass (3keV). Spectrum (a) is fit with a blackbody (red), its thermal Comptonisation (blue) and reflection (green). Spectrum (b) is fit with a disc blackbody (red), Comptonisation seeded by the (unseen) emission from the NS surface and reflection (green).

dominant source of seed photons is the thermal emission from the neutron star surface. Also, we see that the Comptonised spectrum in (b) is so optically thick that it is nearly thermal. It is possible to explain the different tracks followed by BHBs and atolls on a CD by considering these extra processes (Gierlinski & Done 2002b; Done & Gierlinski 2003; Done, Gierlinski & Kubota 2007).

There are also comparisons to be drawn between the PSDs of black hole and neutron star binaries. Atoll power spectra can also be approximately described as broad band noise, characterised by low and high frequency breaks at f_b and f_h respectively, with a LF QPO superimposed. Whereas f_h remains roughly constant, f_b moves with the QPO frequency, f_{QPO}. We can see by turning back to Figure 1.22, which shows f_b plotted

against f_{QPO} for both black holes and neutron stars, that power spectral evolution is very similar for both classes of object. In (a), the black points are for BHBs with the red and blue points for atolls (the blue points are millisecond pulsars). In (b), the black points are all of the points from (a), the red points are Z-sources and the blue points are for objects which display two QPOs. It is clear that all of these objects (except for possibly the Z-sources) lie on the same relation with the factor ~ 10 difference in average frequency between black holes and neutron stars consistent with a factor ~ 10 mass scaling. This strongly implies that common processes give rise to these features in both object classes (Wijnands & van der Klis 1999; Klein-Wolt & van der Klis 2008).

We can therefore interpret the power spectral evolution of atolls in the picture developed thus far for BHBs, with the LF QPO produced by Lense-Thirring precession of the entire hot inner flow. Numerical simulations show that angular momentum transport in the accretion flow takes place via stresses (a.k.a. 'viscosity') generated by the magneto rotational instability (MRI: Balbus & Hawley 1998). This process generates fluctuations in all quantities (e.g. Krolik & Hawley 2002). However, the mass accretion rate at any given radius cannot change faster than the local viscous timescale, so fluctuations at each radius are damped on this timescale (Lyubarskii 1997; Psaltis & Norman 2000; also see Titarchuck & Osherovich 1999; Misra & Zdziarski 2008 for a slightly different approach). As illustrated in Figure 1.23, this gives rise to self-similar fluctuation power between the viscous timescale at the inner and outer radii of the flow. (Lyubarskii 1997; Churasov et al 2001; Nowak & Wagoner 1995; King et al 2004). The inner radius of the flow is now presumably the neutron star surface, thus giving rise to a constant component at f_h. The evolution of the continuum power spectrum can therefore determine the inner and outer radii of the flow, and these can be used to *predict* the LF QPO frequency, to compare with that observed.

Atoll power spectra also display a pair of kHz QPOs, a feature not (unambiguously) observed in BHB power spectra. The peak frequency of both the upper, f_{ukHz}, and

lower, f_{lkHz}, QPO is seen to increase as the source spectrum softens such that it correlates with the break frequency and the LF QPO. (see e.g. the reviews by van der Klis 2005, hereafter vdK05; McClintock & Remillard 2006, hereafter MR06; and Done, Gierlinski & Kubota 2007, hereafter DGK07). Relativistic precession models (Stella & Vietri 1998; 1999) identify f_{ukHz} and f_{lkHz} respectively as some modulation of the orbital, $f_\phi(r_o)$, and the perihelion precession, $f_{pp}(r_o)$, frequencies, both evaluated at the truncation radius.

This chapter is adapted from Ingram & Done (2010). In this paper, we studied atolls with well constrained spins using the assumption that $f_{ukHz} = f_\phi(r_o)$ in order to give an accurate determination of the truncation radius. This identification independently constrains a key parameter of the LF QPO model. Hence we used the atolls to outline a self-consistent model for *all* the observed components in the power spectrum.

3.2 The origin of the broad band power spectrum

We choose atoll sources with multiple observations showing the power spectral evolution so as to test the model over a wide range of r_o. We consider only low spin systems ($a_* < 0.3$), because higher spins lead to an equatorial bulge of the neutron star which distorts space-time from being well described by the Kerr metric (Miller et al 1998). This leads us to pick the atoll systems 4U 1728-34 and 4U 0614+09 (van Straaten et al 2002), both of which have spin $a_* \sim 0.2$ and (assumed) mass $M \sim 1.4 M_\odot$. Typical power spectra of 4U 1728-34 and 4U 0614+09 are shown in the top and bottom panels respectively of Figure 3.3. We see that the QPOs can be fit with narrow Lorentzians with the broad band noise requiring a number of broad Lorentzians (although note that the Lorentzian labelled L_h is sometimes referred to as the hectohertz QPO; e.g. van Straaten 2002; van Straaten et al 2003; Di Salvo et al 2001).

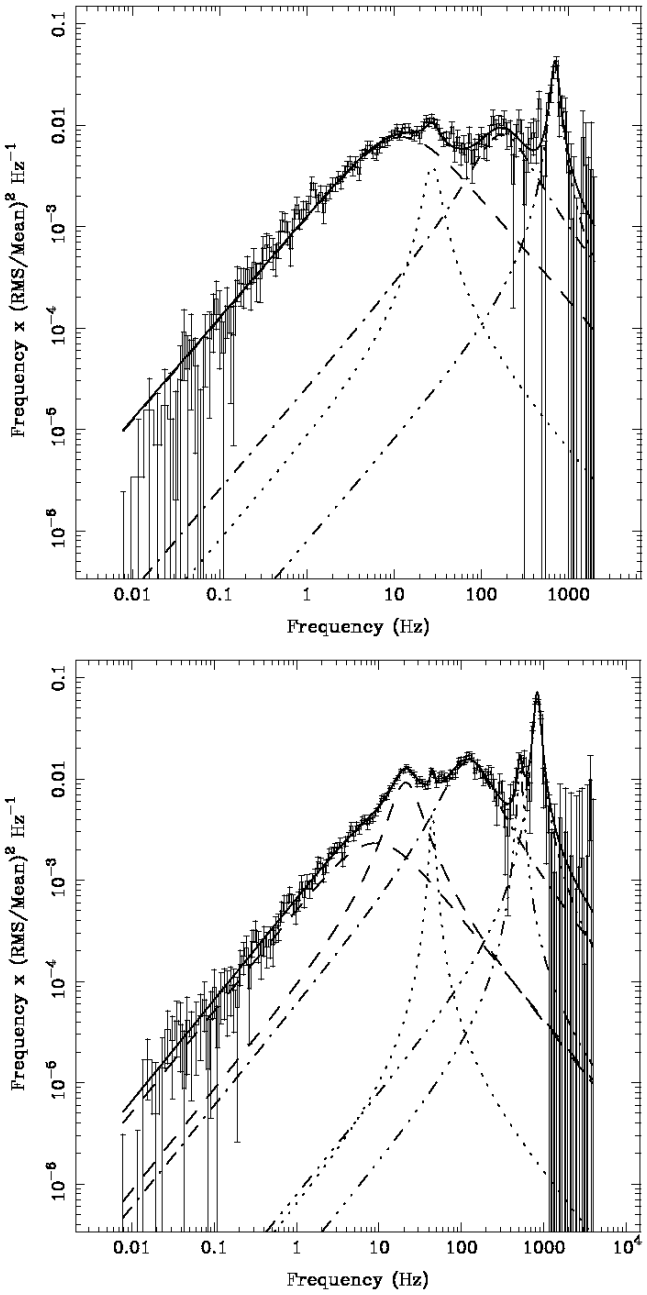

Figure 3.3: Power spectra and fit functions for 4U 1728-34 (top) and 4U 0614+09 (bottom), reproduced with the permission of van Straaten et al (2002) and the AAS. Lorentzians represent the following components: the low frequency Lorentzian L_b (peaking at f_b; dashed line), the LF QPO (peaking at f_{QPO}; dotted line), the high frequency Lorentzian (peaking at f_h; dot-dashed line) and the kHz QPOs (peaking at f_{lkHz} and f_{ukHz}; triple dot-dashed). When there are two dashed lines present, as in the bottom panel, we will refer to the left hand one as L_{b2} and the right hand one as L_{VLF} with one assumed to be a continuation of L_b.

3.2.1 Outer radius

The evolution of the high and low frequency breaks can be qualitatively explained in the truncated disc/hot inner flow model. The inner radius of the flow remains constant at the neutron star radius, so giving the constant high frequency power, while the outer radius sweeps inwards, leading to the progressive loss of low frequency components (Gierlinski, Nikolajuk & Czerny 2008). Quantitatively this can be modelled by each radius generating noise power as a zero-centred Lorentzian with width $\Delta f = f_{visc}$. The viscous frequency $f_{visc} = 1.5\alpha(h/r)^2 f_\phi$, where α is the Shakura-Sunyaev viscosity parameter, h/r is the disc semi-thickness and f_ϕ is the rotational frequency of fluid particles within the flow. However, none of these are necessarily straightforward to define. MRI simulations of black hole accretion flows show that α and h/r vary with radius (e.g. Fragile et al 2007, 2009). Additionally, h/r should change during state transitions as the hot inner flow collapses. In neutron stars especially, this collapse marks the transition from the hard X-ray emission region being an extended optically thin boundary layer which merges smoothly onto the hot inner flow, to a much more compact boundary layer. As well as the impact of such a transition on h/r, the viscosity mechanism in the boundary layer may well be very different to that of the standard MRI, and the azimuthal velocity field is dominated by that of the star rather than being Keplerian.

This makes neutron stars somewhat more complex than black holes. However, their saving grace is that we can use their additional kHz QPOs to independently determine r_o assuming that $f_{ukHz} = f_k(r_o) = c/[2\pi R_g(r_o^{3/2} + a_*)]$ (it should be safe to assume f_ϕ at the inner edge of the *disc* to be Keplerian). The blue triangular points in Figure 3.4 show that this requires r_o to decrease from $20 - 8R_g$, consistent with the expected change in radius from the spectral softening seen from the island state to the lower banana branch (Barret 2001).

The square magenta points in Figure 3.4 show the high frequency break (hectohertz)

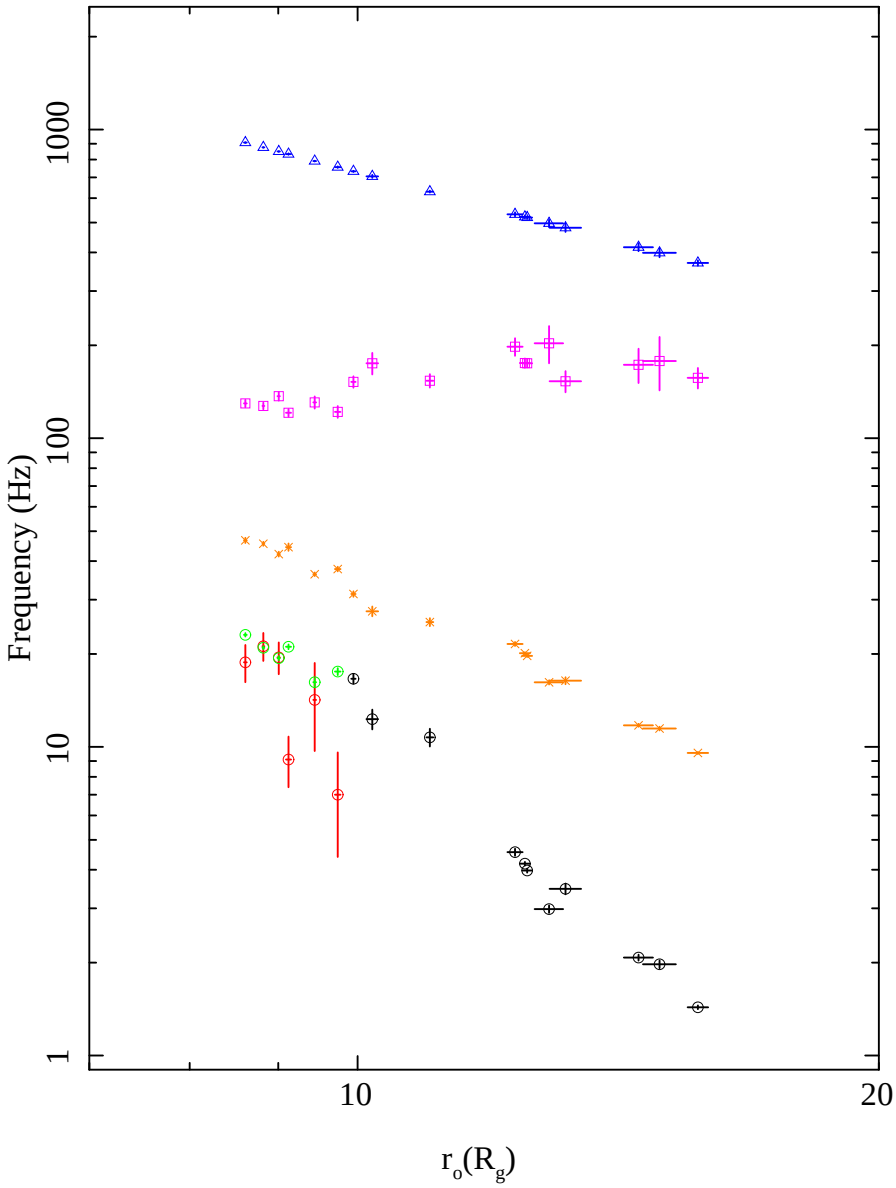

Figure 3.4: Plot of characteristic frequencies plotted against r_o as inferred from the assumption $f_{ukHz} = f_k(r_o)$. The blue triangular points represent f_{ukHz} and the square magenta points represent f_h. The orange crossed points represent the LF QPO frequencies and the circular points the low frequency break. The black points are for power spectra where there is no ambiguity over what the break frequency is whereas the red points are for $f_b = f_{b2}$ and the green points for $f_b = f_{VLF}$.

frequency, which remains approximately constant as discussed earlier and the crossed orange points show the LF QPO frequency. This correlates with the low frequency break (e.g. Wijnands & van der Klis 1999), which is represented by the circular points. Of these, the black points represent data where f_b is unambiguously identified in the power spectra. However, this becomes difficult at the highest ukHz QPO frequencies (i.e. smallest radii) as there is an additional component observed in the low frequency power spectrum e.g. the lower panel of Figure 3.3, where two low frequency Lorentzians are required. It is not immediately clear which one of these corresponds to f_b e.g. van Straaten et al (2002) refer to the lowest frequency Lorentzian as L_b and call the other L_{VLF} while Altamirano et al (2008) put L_b on the right and term the other L_{b2}. Here we only use L_b where this break is unambiguously determined by the data. Where there are two competing low frequency components we refer to the lowest frequency one as L_{b2} and the other as L_{VLF}. The green points in Figure 3.4 represent f_{VLF} whereas the red points represent f_{b2}. The green points connect smoothly onto the black points where f_b is unambiguously determined, while the red points do not. Thus it seems most likely that the higher of the two low frequency components represents the continuation of the break frequency determined by r_o.

Of these 6 points with a split break frequency, 4 are from observations of 4U 1728-34 and 2 from 4U 0614+09. If we analyse the colour-colour diagram of 4U 1728-34 (Di Salvo et al 2000), we see that these 4 observations (9-12 of 19) occur just before the transition between the island state and the banana branch. Intriguingly, the geometry inferred from models of the spectral evolution require an *overlap* between the hot flow and truncated disc close to the transition. The splitting of the break frequency then has an obvious interpretation with the outer radius of the hot flow being larger than the inner radius of the thin disc. The hot flow in this overlap region will have smaller scale fluctuations, as the size scale of the magnetic field is limited by the thin disc in the mid plane. Thus f_{b2} can be interpreted as the viscous frequency at the edge of the

corona with f_{VLF} being the viscous frequency at the truncation radius.

3.2.2 Inner radius

We assume that the lower break frequency, f_b is identified with $f_{visc}(r_o)$, and we use the independent constraints on r_o from the ukHz QPO above to track out the unknown variation in f_{visc} ($\propto \alpha(h/r)^2 f_\phi(r)$). We parameterise this as a power law, so that $f_b = f_{visc}(r_o) = A r_o^{-\gamma}$. We then use the best fit values of A and γ derived from the low frequency break to determine $r_i = [(A f_h)]^{1/\gamma}$ assuming that the high frequency break in the noise power (hectohertz component) is the viscous frequency at r_i.

However, as discussed in the previous section, we do not necessarily expect this power law representation of $f_{visc}(r)$ to stay constant as the truncation radius sweeps in and the source spectrum softens due to the collapse of the more extended hot flow into the boundary layer, with its potentially very different viscosity and azimuthal velocity. Instead we split the radial range in r_o into four groups of points, each described by a different best fit power law. The top panel of Figure 3.5 shows this best fit power law relation for each group of points, with a clear change in both slope and normalisation as the truncation radius moves inwards. Quantitatively, the inferred value of γ moves from 3.25 (blue), 3.02 (magenta), 2.88 (green) to 2.69 (red). We can now use our moving power law representation in order to extrapolate values for $r_i = [(A f_h)]^{1/\gamma}$ taking care to use the correct values of γ and A for a given value of f_h.

The lower plot of Fig. 3.5 shows the derived values for r_i with error bars including the systematic error in determining the best fit values of A and γ. We infer from this that the radius of the neutron star lies at $r_i \approx 4.5 \pm 0.04 \approx 9.2 \pm 0.1$ km. This would mean that the neutron star is slightly smaller than its own last stable orbit (5.3 R_g for $a_* = 0.2$), indicating a soft equation of state, but we caution that the exact value depends on the accuracy of our assumed power law representation of the viscous frequency with radius. Any more complex form will extrapolate to a different inner

radius, and the value of this radius may also be affected by time dilation. Nonetheless, the remarkable constancy of the derived inner radius gives some confidence in our approach, and the value of 9.2 km is very close to the 'canonical' assumption of 10 km for a $1.4M_{\odot}$ neutron star.

3.3 Testing Lense-Thirring in atolls

Now we have both the inner and outer radius for the hot flow, we can directly calculate the predicted Lense-Thirring precession frequency. However, there is one additional free parameter which is the mass distribution in the hot flow, which can be parameterised by ζ, the radial dependence of the surface density, $\Sigma = \Sigma_i(r/r_i)^{-\zeta}$ (see IDF09 and Fragile et al 2007). The LF QPO frequency is then *predicted* to be

$$f_{prec} = \frac{(5-2\zeta)}{\pi(1+2\zeta)} \frac{a_*[1-(r_i/r_o)^{1/2+\zeta}]}{r_o^{5/2-\zeta} r_i^{1/2+\zeta}[1-(r_i/r_o)^{5/2-\zeta}]} \frac{c}{R_g} \tag{3.1}$$

Simulation data for black holes shows $\zeta \sim 0$ (e.g. Fragile et al 2007) but neutron stars have a solid surface which could give a rather different situation where the flow is increasingly concentrated on the neutron star surface as the accretion rate increases. Nonetheless, assuming $\zeta = 0$, and taking r_i fixed at 4.5 (see previous section) gives quite a good fit (grey line) to the observed LF QPO (black circles) as shown in Fig 3.6.

The fit can be made even better by allowing ζ to vary. As r_o decreases the expectation is that the flow goes from being similar to the BH case, to being more and more concentrated in the boundary layer i.e. we expect an increase in ζ as the dense boundary layer begins to dominate the surface density of the flow. Such an increase in the surface density profile is also implied by the change in viscous frequency implied from the previous section, since surface density is inversely proportional to the radial velocity $v_r = Rf_{visc}$. We fit our Lense-Thirring model to the four different sets of points from before and obtain excellent agreement with observation if ζ takes the values -0.7 (blue), -0.3 (magenta) 0.6 (green) and 2.7 (red) i.e. ζ increases with decreasing r_o

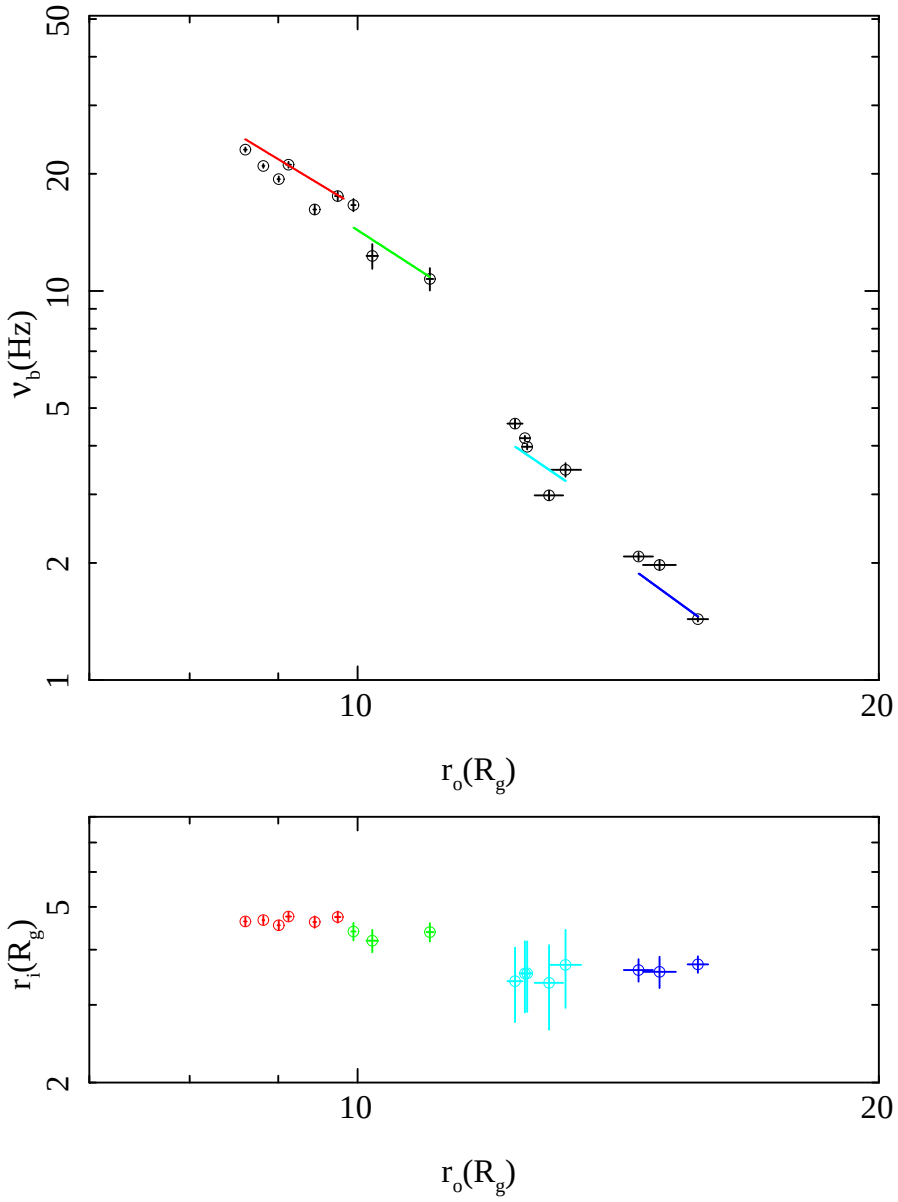

Figure 3.5: *Top panel:* Break frequency plotted against truncation radius, r_o, with four separate power law fits: $\gamma = 3.25$ (blue), 3.02 (magenta), 2.88 (green) and 2.69 (red). This treatment assumes that the viscous frequency is given by a power law, the index of which becomes less negative as r_o reduces. f_b is then $f_{visc}(r_o)$ and r_i is the value of r that gives $f_{visc}(r) = f_h$. *Bottom panel:* Inferred values for r_i plotted against r_o.

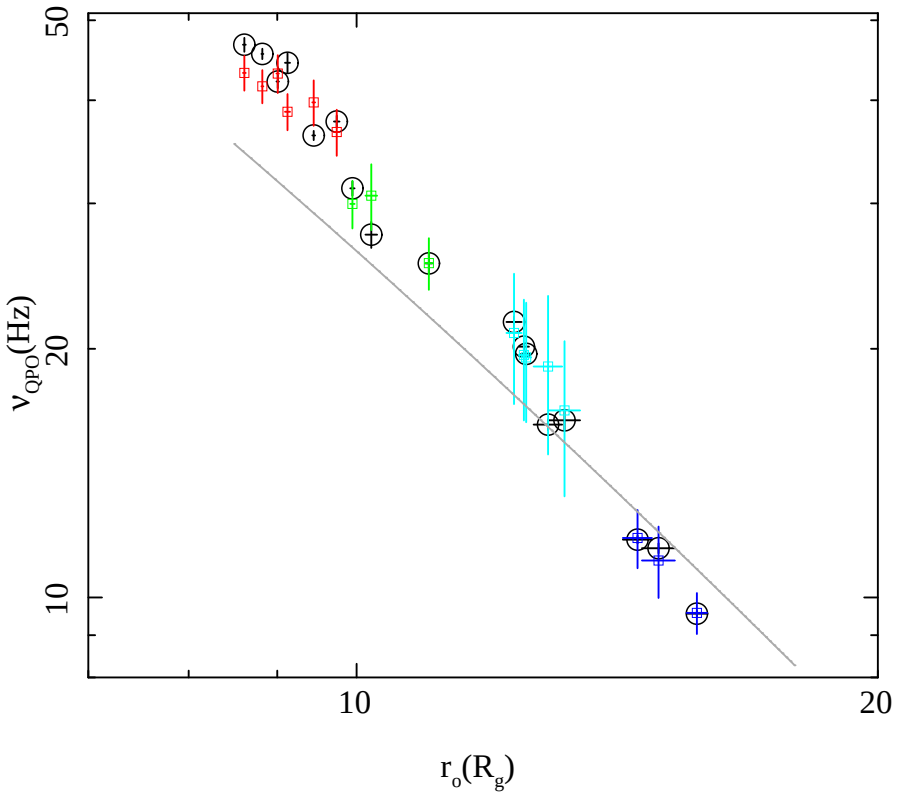

Figure 3.6: LF QPO frequency plotted against truncation radius (black circles). The grey line tracks Lense-Thirring precession frequency of the inner flow with $r_i = 4.5$ and $\zeta = 0$. The blue, magenta, green and red squares are for $\zeta = -0.7$, -0.3, 0.6 and 2.7 respectively and use the r_i values from the bottom plot of Figure 3.5.

as expected. However, a quantitative understanding of how these parameters should interact in neutron stars is a very difficult goal as the boundary conditions associated with accreting neutron stars are so poorly understood.

3.4 Conclusions

We show that the broadband continuum noise power and LF QPO seen in atolls and BHB can be self-consistently explained in the *same* truncated disc/hot inner flow model which describes their spectral evolution. We test this on the atoll systems, as these have strong kHz QPOs which most probably pick out the truncation radius of the thin disc, r_o, so this key parameter is known independently. Using the standard assumption that the upper of the two kHz QPOs marks the Keplerian frequency gives that r_o decreases from $20 - 8\ R_g$ during the marked spectral transition seen in atolls from the hard (island) state to soft (banana branch) spectra.

The low frequency break seen in the noise power is then consistent with being the viscous timescale of the hot flow at r_o. All smaller radii in the hot flow contribute to the noise power, giving the broad band continuum power spectrum. The highest frequency noise component marks the viscous timescale at the inner edge of the hot flow, r_i. We use our parameterisation of f_{visc} to calculate r_i and find that this remains remarkably constant at $r_i \sim 4.5 \equiv 9.2$ km for a $1.4 M_\odot$ neutron star.

The truncated disc model also gives a physical interpretation for the observed 'splitting' of the lowest frequency noise component seen close to the spectral transition. At this point the spectral models predict that the disc overlaps the hot flow, so there is a component which tracks turbulence in the hot flow *within* the disc inner radius, and another component which tracks the true outer edge of the hot flow which extends over the disc.

With all of the parameters of the truncated disc geometry constrained, we are then able to test the Lense-Thirring precession model for the LF QPO presented in IDF09.

This gives a fairly good match to the data at large truncation radii, but increasingly underestimates the QPO frequency as r_o decreases. Nonetheless, it still only 25 per cent too low even at the smallest r_o. However, there is still one additional free parameter which is the radial dependence of the surface density of the hot flow. Allowing this to change so that the flow becomes increasingly concentrated towards r_i as the truncation rate decreases, as expected from the collapse of a hot flow into the boundary layer, gives an excellent match to the data. However, we caution that the expected evolution of the surface density is not well understood quantitatively for neutron stars.

It must also be noted that considering the whole flow to precess removes a previous objection to Lense-Thirring precession as the origin of the LF QPO. If the LF QPO is produced by Lense-Thirring at r_o then this implies the moment of inertia of the neutron star is too large (Markovic and Lamb 1998). Instead, in our model the LF QPO is produced at some mass weighted radius between r_o and r_i with the weight increasingly towards r_i for softer spectra (higher frequencies). Thus for the lowest values of $r_o \sim 8.5$, the LF QPO is predominantly produced by material at $r_i = 4.5$ rather than at r_o, so the moment of inertia is correspondingly reduced.

Overall, we present a model of the power spectrum in which both broad band continuum and LF QPO components are interpreted physically. This forms a framework in which the characteristic frequencies in the power spectrum can be used as a diagnostic of the properties of the accretion flow in strong gravity.

Chapter 4

A physical model for the continuum variability and QPO in accreting black holes

4.1 Introduction

Despite being known about for ~ 25 years (e.g. van der Klis 1989), there is still no consensus in the literature as to the origin of the QPO and broad band variability observed in the PSD of black hole and neutron star binaries. There are multiple potential models for the LF QPO which fall into 2 main categories: those associated with a geometrical misalignment of the accretion flow and black hole spin (Stella & Vietri 1998; Fragile, Mathews & Wilson 2001; Schnittman 2005; Schnittman et al 2006; Ingram, Done & Fragile 2009, hereafter IDF09), and those associated with wave modes of the accretion flow (Wagoner et al 2001; Titarchuk & Oscherovich 1999; Cabanac et al 2010). Most of these concentrate on matching the QPO frequency, but the spectrum of the QPO gives additional constraints. This is similar to that of the spectrum of the broadband variability, showing that they both arise predominantly from the Comptonising region rather than the disc (e.g Gilfanov et al 2003; Sobolewska & Życki 2006), favouring models in which the modulation arises directly from the Comptonised emission e.g. IDF09, where the QPO is set by Lense-Thirring (vertical) precession of the entire hot

inner flow interior to the disc truncation radius at r_o, or by a mode of the hot inner flow (Cabernac et al 2010).

The physical origin for the viscosity of the flow is the Magneto-Rotational Instability (MRI: Balbus & Hawley 1991). This is inherently variable, with large fluctuations in all quantities, both spatially and temporally (Krolik & Hawley 2002), making it a natural origin for the broad band noise (Noble & Krolik 2009; Ingram & Done 2010; Dexter & Fragile 2011). However, these fluctuations also effectively shred any coherent wave modes in the flow (see e.g. Reynolds & Miller 2009; Henisey et al 2009). This casts doubt on trapped wave propagation as the origin of the LF QPO, leaving Lense-Thirring precession as the most likely candidate. As shown in the two previous chapters, precession of the entire hot flow from r_o to r_i can match the observed LF QPO frequency in both BHBs (IDF09) *and* neutron stars (NS; Ingram & Done 2010), and provides a clear mechanism to match the spectrum as this is a modulation of the Comptonising region.

Thus the entire power spectrum can be explained by MRI fluctuations in a hot flow, which is also precessing around the black hole. However, the power spectrum does not represent all the information contained in the variability, as it uses only Fourier amplitudes, not phases. This is important as the light curves contain additional correlations which give a linear rms-flux relation (Uttley & McHardy 2001). This is equivalent to the flux on these timescales having a log-normal distribution (Negoro et al 2000), and rules out simple models of the variability where the light curve is made from adding together multiple, uncorrelated events (Uttley & McHardy 2001; see also DGK07). Instead, this can be produced if the light curve is made from a multiplicative process, rather than an additive one. Again, the MRI in the hot flow gives a physical interpretation to this. The MRI at large radii produces intrinsic fluctuations in the density of the flow. These fluctuations propagate down to smaller radii on a viscous timescale, so all higher frequency fluctuations are smoothed out. These smoothed and

lagged fluctuations in mass accretion rate modulate the MRI fluctuations produced by the next radius, and so on, down to the smallest radii in the flow (Luybarski 1997: hereafter L97). This naturally produces a light curve which has an rms-flux relation/log-normal flux distribution (Uttley, McHardy & Vaughan 2005; Kotov et al 2001: hereafter K01; Arevalo & Uttley 2006: hereafter AU06; also see Misra & Zdziarski 2008).

This chapter is adapted from Ingram & Done (2011) in which we use these ideas to build a model for the entire power spectrum, where the broadband noise arises from propagation of MRI fluctuations through the hot flow from r_o to r_i and the LF QPO arises from Lense-Thirring precession *of the same hot flow*.

4.2 The simplified model

We first introduce the simplified toy model considered in IDF09 and Ingram & Done (2010), whereby the low frequency break, f_b, occurs at the viscous frequency of the truncation radius and the QPO frequency, f_{QPO}, is the precession frequency of the flow. Using the Shakura Sunyaev (1973) viscosity prescription, $f_b = f_{visc}(r_o) = \alpha(h/r)^2 f_k(r_o) = -v_r(r_o)/R_o$ where α is the viscosity parameter, h/r the flow semi-thickness, f_k the Keplerian frequency and v_r is the infall velocity. The Lense-Thirring precession frequency is then a weighted average of the point particle precession frequency at each radius in the hot flow, so

$$f_{prec} = f_{QPO} = \frac{\int_{r_i}^{r_o} f_{LT} f_k \Sigma r^3 dr}{\int_{r_i}^{r_o} f_k \Sigma r^3 dr} \tag{4.1}$$

(Liu & Melia 2002) where r_i is the innermost point of the flow (i.e. the surface density is negligible interior to this), Σ is the surface density and

$$f_{LT} = f_k \left[1 - \sqrt{1 - \frac{4a_*}{r^{3/2}} + \frac{3a_*}{r^2}} \right] \tag{4.2}$$

is the point particle Lense-Thirring precession frequency for a dimensionless spin parameter a_* (Merloni et al 1999). Here, r is dimensionless, expressed in units of

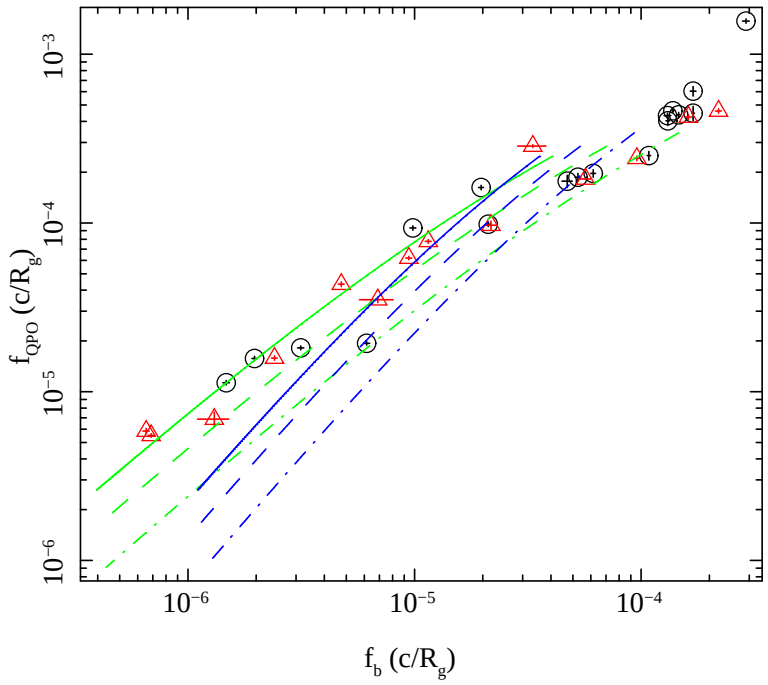

Figure 4.1: The QPO-break relation plotted in dimensions of c/R_g for a fiducial mass of 10 and $1.4M_\odot$ for black holes (black circles) and neutron stars (red triangles) respectively. The fact that these frequencies lie on the same relationship for the two objects implies a common physical origin. The lines are predictions of the simplified model for spins of $a_* = 0.2$ (dot-dashed), 0.5 (dashed) and 0.998 (solid) with r_o ranging from r_i to 100 and $r_i = r_{bw}$. For the blue lines, we assume the viscous frequency to be proportional to the Keplerian frequency. For the green lines, we assume $f_{visc} = Br^{-m}f_k$ where $B = 0.03$ and $m = 0.5$ and find good agreement with the trend in the data.

$R_g = GM/c^2$. In the weak field limit ($a_* << 1$ and/or $r >> 1$), equation 4.2 reduces to

$$f_{LT} \approx f_{nodal} = \frac{a_*}{\pi r^3}\frac{c}{R_g}, \tag{4.3}$$

(e.g. van der Klis 2006; Stella & Vietri 1998). An analytic form for the integrals in equation 4.1 can therefore be obtained in the weak field limit if we assume $\Sigma \propto (r/r_i)^{-\zeta}$ between an inner and outer radius for the hot flow r_i and r_o (Fragile et al 2007, IDF09). This gives

$$f_{QPO} = \frac{(5-2\zeta)}{\pi(1+2\zeta)}\frac{a_*[1-(r_i/r_o)^{1/2+\zeta}]}{r_o^{5/2-\zeta}r_i^{1/2+\zeta}[1-(r_i/r_o)^{5/2-\zeta}]}\frac{c}{R_g}. \tag{4.4}$$

Hence this model predicts the relation between f_{QPO} and f_b which can be compared to the multiple observations of these frequencies in both black holes and neutron stars (e.g. Wijnands & van der Klis 1999; Klein-Wolt & van der Klis 2008). The observed relation is continuous, implying that these frequencies show the same behaviour in both sources, i.e. that neither can depend strongly on any property of the neutron star surface but are instead set by the accretion flow itself. We re-plot this data in Figure 4.1, normalising the frequencies by mass for a fiducial mass of 1.4 and $10M_\odot$ for neutron stars (red triangles) and black holes (black circles), respectively. This shows even more clearly that the two different types of object show the same observed relation between these frequencies as they now occupy the same range.

The blue lines show the prediction of the toy model, where the hot flow has constant $\alpha = 0.2$ and $h/r = 0.2$, surface density constant with radius (i.e. $\zeta = 0$: Fragile et al 2007) between r_o and r_i, where r_i is given by the bending wave radius. Warps in a large scale height flow are communicated via bending waves which have wavelength $\lambda \propto r^{9/4}$ and so are smooth at large r and oscillatory at small r. The bending wave radius ($r_i = 3.0(h/r)^{-4/5}a_*^{2/5}$; Fragile et al 2007; 2009; Fragile 2009; IDF09) marks the transition between the two regimes. We show $a_* = 0.2$ (dot-dashed), $a_* = 0.5$ (dashed) and $a_* = 0.998$ (solid). While this very simple model predicts frequencies which are fairly close to the observations, it is clear that the gradient of this model in log space

is different from that observed.

Plainly the assumptions above are very simplistic. Global analytic models of the hot flow with a standard α viscosity do not have $f_{visc} \propto f_K$ as they depart from the self-similar solutions at $r < 100$ due to the requirement that the flow becomes supersonic (Narayan, Kato & Honma 1997; Gammie & Popham 1998). Full numerical simulations also show that α is not constant (e.g. Fragile et al 2007; 2009). Ingram & Done (2010) also suggest that ζ can change in neutron stars as the material piles up onto a boundary layer. However, the similarity between the mass scaled frequencies seen in neutron stars and black holes shown in Fig. 4.1 make this now seem unlikely to be an important effect as it would not affect the black holes.

Here then we simply assume that $\alpha(h/r)^2$ is a power law function of radius, so that $f_{visc} = Br^{-m} f_K$. We choose values for B and m which allow us to match the data in Figure 4.1. We see good agreement with the observations for $B = 0.03$ and $m = 0.5$ (green lines), again for $a_* = 0.2$ (dot-dashed), $a_* = 0.5$ (dashed) and $a_* = 0.998$ (solid). We use this specific prescription for the viscous frequency in the following section.

4.3 The full model

We consider a model where local fluctuations in the mass accretion rate of the flow propagate down towards the central object (e.g. L97; K01). Our method mainly follows that of AU06, with a few small differences.

We split the flow into annuli, characterised by a radius r_n and width dr_n, with logarithmic spacing so dr_n/r_n is a constant for all annuli from r_o to r_i. We assume that the generated power spectrum of mass accretion rate fluctuations at radius r_n is given by a zero centred Lorentzian cutting off at the viscous frequency

$$|\tilde{\dot{m}}(r_n, f)|^2 \propto \frac{1}{1 + (f/f_{visc}(r_n))^2} \tag{4.5}$$

where $f_{visc} = -\frac{1}{R_g} v_r/r = Br^{-m} f_K$ as discussed at the end of section 4.2 and a tilde

denotes a Fourier transform. This approximates the MRI generating a white noise of variability power which is then damped by the response of the flow on timescales shorter than $t_{visc}(r)$. Note that magnetic fields can also affect the mass accretion rate by driving direct angular momentum loss through an outflow (jet/wind). This process is damped, not on the viscous timescale, but on the time it typically takes for magnetic field fluctuations to randomly align over enough neighbouring annuli to drive significant angular momentum loss (t_{mag}; King et al 2004). We ignore this effect here .

We start at the outermost annulus, so $r_1 = r_o$, and generate the time dependent fluctuations in mass accretion rate, $\dot{m}(r_1, t)$, from equation 5.4 using the method of Timmer & Koenig (1995). We normalise each $\dot{m}(r_n, t)$ to have a mean of unity and fractional variability $\sigma/I = F_{var}\sqrt{N_{dec}}$ where F_{var} is the fractional variability per decade in radial extent and N_{dec} is the number of annuli per decade in radial extent. Thus the mass accretion rate across the first annulus is $\dot{M}(r_1, t) = \dot{M}_0\dot{m}(r_1, t)$ where $\dot{M}_0$ is the mean mass accretion rate. This then propagates inward to the second annulus, travelling a distance dr_1, which takes a time $t_{lag} = R_g\ dr_1/v_r(r_1)$. When it arrives at r_2, it has been filtered by the response of the flow which we take from Psaltis & Norman (2000) to get

$$\tilde{\dot{M}}_f(r_n, f) \propto \frac{\tilde{\dot{M}}(r_n, f)}{\sqrt{1 + [(dr_n/r_n)(f/f_{visc}(r_n))]^2}}. \tag{4.6}$$

The mass accretion rate at the n^{th} annulus is then given by

$$\dot{M}(r_n, t) = \dot{M}_f(r_{n-1}, t - t_{lag})\dot{m}(r_n, t) \tag{4.7}$$

where $t_{lag} = R_g\ dr_n/v_r(r_n)$. However, equation 4.6 only filters out fluctuations on much shorter timescales (by a factor dr/r) than the typical timescales generated in the annulus (equation 5.4) and so we can say $\tilde{\dot{M}}_f(r_n, f) \approx \tilde{\dot{M}}(r_n, f)$ to a very good approximation. The mass accretion rate at the n^{th} annulus is therefore given by

$$\dot{M}(r_n, t) = \dot{M}(r_{n-1}, t - t_{lag})\dot{m}(r_n, t), \tag{4.8}$$

until the $N^{\rm th}$ annulus which is r_i.

To transform this into a light curve requires an emissivity, $\epsilon(r)$ such that the luminosity from each annulus is given by $dL(r,t) = 1/2\ \dot{M}(r_n,t)\epsilon(r)r_n dr_n c^2$ where we assume the emissivity $\epsilon(r) \propto r^{-\gamma} b(r)$ where $b(r)$ is a boundary condition. For a Newtonian thin disc, $\gamma = 3$ and we have the stress free inner boundary $b(r) = 3(1 - \sqrt{r_i/r_n})$ but we note that the large scale magnetic fields present in the large scale height flow can give a stressed inner boundary condition $b(r) = 1$ (Agol & Krolik 2000; Beckwith Hawley & Krolik 2008). Also γ is, in general, a free parameter since the emission need not exactly follow the radial dependence of gravitational energy release as long as the *total* energy release is gravitational. A different emissivity for different energy bands gives a way for the model to predict frequency dependent time lags between hard and soft X-ray bands (K01; AU06).

4.4 The fiducial model

Figure 4.2b shows 20s of the resulting light curve for a fiducial set of input parameters for a black hole mass of $M = 10M_\odot$ and a spin of $a_* = 0.5$. We assume $r_i = 2.5$, $r_o = 20$, $F_{var} = 0.4$, $B = 0.03$, $m = 0.5$, $\gamma = 4.5$ with a stressed inner boundary condition (see Section 4.2). We calculate the light curve with 2^{22} time points, corresponding to $\sim$ 4096 s (a typical length for an RXTE observation) of data on a time binning of 0.00097 s, and 30 radial bins per decade in radius.

Figure 4.2a (red) shows the PSD of this light curve, while the black and green points show the effect of changing the number of radial bins per decade to $N_{dec} = 10$ and $N_{dec} = 50$, respectively. Clearly, the high frequency power is not well resolved with only 10 radial bins per decade, while the difference between 30 and 50 is very small. Hence we use $N_{dec} = 30$ for the fiducial model. For all PSDs, we use a combination of ensemble averaging and geometric rebinning. Each periodogram is calculated for 128s of data. Since we simulate 4096s of data, we can average over $\mathcal{M} = 32$ realisations. Geometrical rebinning is always carried out using a rebinning constant of $c_0 = 1.05$.

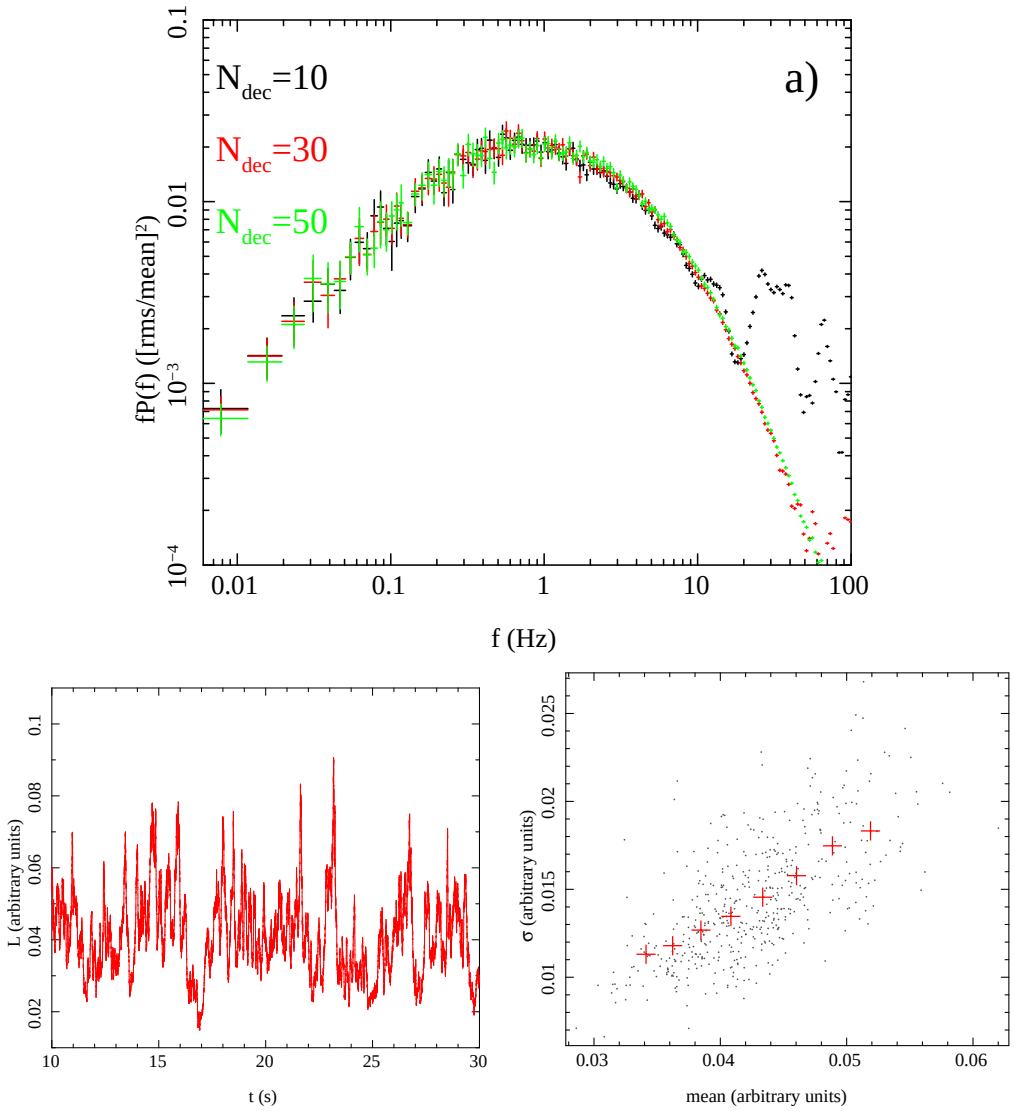

Figure 4.2: *Top (a):* The simulated power spectral density calculated using 10 (black), 30 (red) and 50 (green) radial bins per decade. We see that 10 bins is not enough to resolve the high frequency power but 30 bins is a good approximation. *Bottom left (b):* A 20 second section of the simulated light curve (using 30 radial bins per decade). *Bottom right (c):* The rms-flux relation for the light curve shown. We see that this is linear as observed.

The PSD shows the same characteristic broadband noise features as are seen in the power spectra of black hole binaries, namely band limited noise, with low and high frequency breaks, peaking between 0.1-10 Hz. Figure 4.2c shows the rms-flux relation for the fiducial light curve, derived from splitting this into 4s segments. As with the data (Uttley & McHardy 2001), we see a large scatter before binning (grey points) but, after binning (red crosses), we retrieve a linear flux-rms relation (AU06).

4.5 The truncated disc/hot inner flow model

The major prediction of the truncated disc/hot inner flow model is that the spectral softening as the source brightens from a low/hard through to intermediate states is caused by the truncation radius of the thin disc moving inwards (e.g. DGK07; Gierlinski, Done & Page 2008). This radius also sets the outer edge of the hot flow, so this predicts that r_o decreases also.

Figure 4.3 shows the predicted PSD for $r_o = 50$, 20 and 10, as required to match the energy spectral evolution (and low frequency QPO: IDF09), with all other parameters held constant at the fiducial model values described above. The model *predicts* that decreasing the outer radius of the hot flow leads to less low frequency power, while the high frequency power remains constant. This is precisely what is seen in the PSD of the data (DGK07; Gierlinski, Nikolajuk & Czerny 2008).

This is the first physical model of the power spectral behaviour which naturally reproduces the observations. The low frequency break is close to the frequency of the viscous timescale at r_o, as proposed by e.g. Churazov et al (2001); Gilfanov & Areief (2005); DGK07; Ingram & Done (2010). However, the high frequency break is *not* at the viscous frequency at r_i. We explore the origin of the high frequency break below.

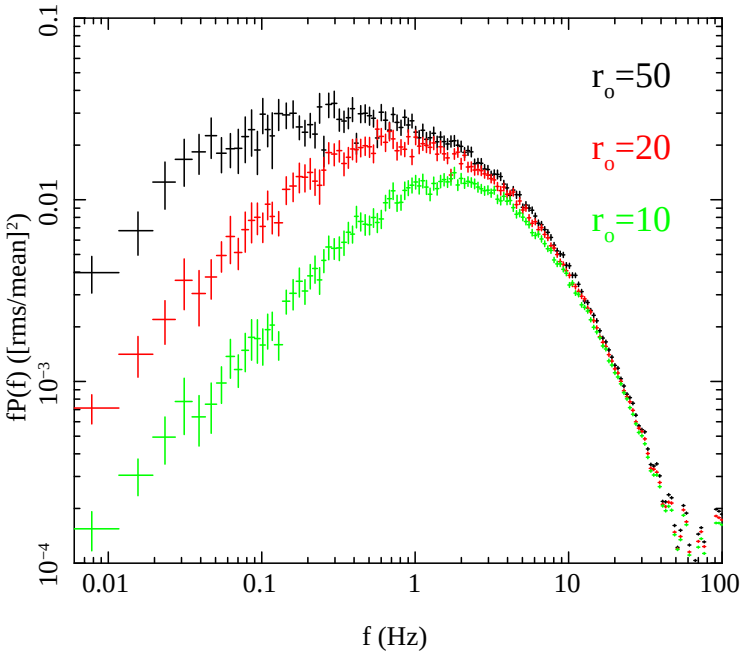

Figure 4.3: PSD calculated using the fiducial parameters with $r_o = 50$ (black), 20 (red) and 10 (green) with total fractional variability generated per decade in radius, F_{var}, held constant. This has the same characteristics as the observed PSD of the data as the source softens from a low/hard to intermediate state, namely that the low frequency power drops while the high frequency power remains constant.

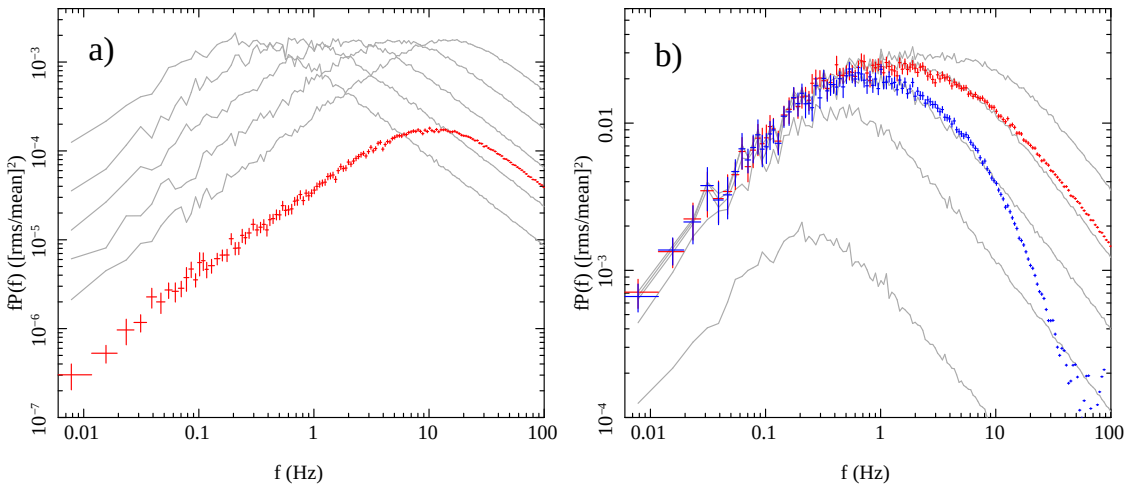

Figure 4.4: *Left (a):* The grey lines are the power spectra of 5 simulated $\dot{m}(r_n, t)$ functions. We simulate 30 of these functions but, for clarity, only plot 5 without showing the errors. The red line is the PSD of the light curve created by assuming there to be no propagation (i.e.$\dot{M}(r_n, t) = \dot{m}(r_n, t)$) and an emissivity index of 4.5. Because the functions we sum over are uncorrelated, the PSD of the light curve looks like the (weighted) sum of the 100 PSDs with the only difference being the normalisation. *Right (b):* The grey lines are now the power spectra of $\dot{M}(r_n, t)$ functions, i.e. we now allow propagation. These are correlated at low frequencies but not at high frequencies allowing the model to reproduce the observed linear sigma-flux relation. The red line is the PSD of the light curve if we do not consider the propagation time between annuli (i.e. $t_{lag} = 0$) and the blue line results if we do consider the propagation time. We see that the red line differs from the top plot in 2 ways: the normalisation is much higher and high frequency noise is lost. However, much more high frequency noise is lost for the blue line indicating that considering lags reduces high frequency noise. These plots illustrate that the prediction from shot noise models such as the top plot that the observed high frequency break is the viscous frequency at the inner radius breaks down once we consider a more advanced model capable of reproducing other observational properties.

4.5.1 Effect of propagation on the PSD shape

Figure 4.4a shows a model where the variability at each radius is a Lorentzian at the local viscous frequency (see equation 5.4), but with no propagation so there is no causal connection between annuli. We show the PSD of the resulting $\dot{m}(r_n, t)$ functions from 5 of the 25 individual radial annuli (rings 1,7,13,19 and 25), from r_o to r_i as the grey lines on Figure 4.4a. These peak, as expected, at $f_{visc}(r_o)$ and $f_{visc}(r_i)$. The total variability (red) is an emissivity weighted sum of these fluctuations, but since they are uncorrelated, the effect of this is to strongly dilute the total variability seen. This total PSD does have $f_h \approx f_{visc}(r_i) \sim 12$Hz as our emissivity weighting strongly favours the smallest radii, but $f_b > f_{visc}(r_o)$ (~ 10Hz and ~ 0.3Hz respectively). In fact, to achieve $fP_f \propto f^0$ as observed, we would have to assume a completely flat emissivity profile, which seems very unlikely. More fundamentally, such uncorrelated fluctuations *cannot* reproduce a linear rms-flux relation.

This is in sharp contrast to a model where fluctuations propagate down in radius. The resulting PSD from the same set of radii are shown in Figure 4.4b, where the power in each annulus increases strongly with radius as the MRI power generated in each annulus is modulated by the propagating fluctuations from all radii prior to it. The red line shows the resulting emissivity weighted power spectrum from the total flow assuming that time lags between radii are negligible. This preserves the maximum correlation between variability at different annuli i.e. gives the least dilution between fluctuations in different annuli. This is very different to that in Figure 4.4a, both in normalisation and shape. The normalisation is dramatically enhanced because the long timescale fluctuations are correlated together, so at low frequencies the power from different radii add together as they are in phase. This gives $f_b \approx f_{visc}(r_o) \sim 0.3$Hz as the correlated variability weighting to larger radii is stronger than the emissivity weighting to smaller radii. However, at the fastest timescales, the power is mainly generated at the smallest radii, so it does not correlate with any other fluctuations generated at

larger radii, so is not enhanced in the same way.

The blue line shows how time delays dramatically change the high frequency break as the propagation time prevents the mass accretion rate from two consecutive annuli from being correlated on time scales shorter than t_{lag}. This reduces the correlation between the fastest timescale variability, strongly suppressing high frequency power. Thus in the propagating fluctuation model, the low frequency break is $f_b \approx f_{visc}(r_o)$ but $f_h << f_{visc}(r_i)$, which appears to be consistent with the King et al (2004) model for the case $t_{mag} >> t_{visc}$ (see Figure 3b therein). This makes intuitive sense, since this limiting case prevents angular momentum loss driven directly by magnetic field fluctuations from significantly affecting the short timescale variability, effectively aligning their assumptions with ours.

4.5.2 Emissivity and boundary condition

We use an emissivity to translate the fluctuations in mass accretion rate to a luminosity. This emissivity is in two parts, firstly a power law dependence in radius, and secondly a boundary condition. Our fiducial model parameters have $\gamma = 4.5$ and a stressed boundary condition, $b(r) = 1$. This emissivity peaks at r_i, so fluctuations from the very smallest radii are given most weight.

Figure 4.5 compares this (black line) with results using the same power law radial dependence, but with a stress-free inner boundary condition (red line), $b(r) = 3(1 - \sqrt{r_i/r})$. This emissivity goes to zero at the innermost radius, so the highest frequency fluctuations are strongly suppressed. However, this also has a more subtle effect on the region between the two breaks, as there is a gradual decrease in weighting of fluctuations below $r = 2r_i$, and a stronger weighting to the fluctuations at larger radii, giving the tilt between f_b and f_h.

This effect is similar to that of changing the radial dependence of the emissivity. The green line shows $\gamma = 3$ with a stress-free boundary condition, showing an even

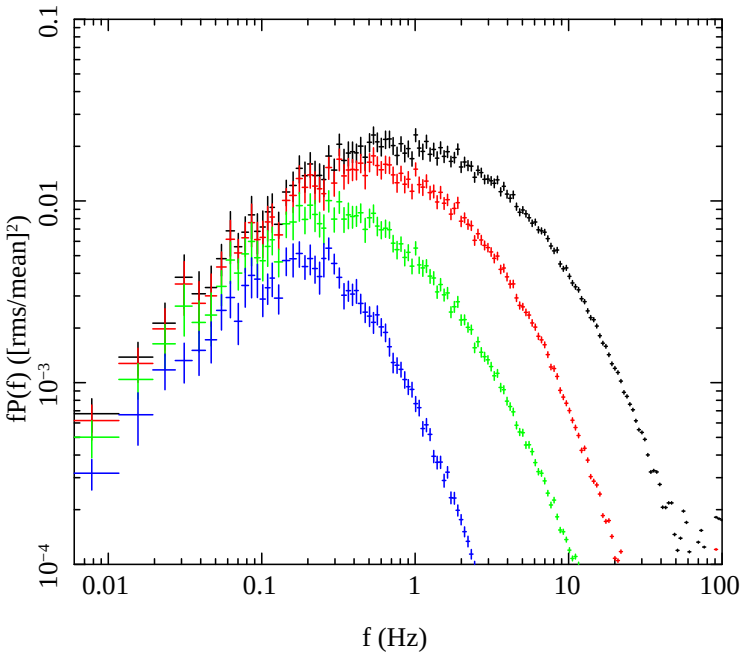

Figure 4.5: The PSD calculated assuming $b(r) = 1$ and $\gamma = 4.5$ (black), $b(r)$ =stress free and $\gamma = 4.5$ (red), $b(r)$ =stress free and $\gamma = 3$ (green), all with $r_i = 2.5$. The blue points are for $b(r)$ =stress free, $\gamma = 3$ and $r_i = 6$. This illustrates that we can reduce the predicted high frequency noise by changing boundary condition, emissivity index or inner radius.

stronger tilt to the PSD between f_b and f_h (green). However, it is also similar to changing the inner radius of the flow. The blue line in Figure 4.5 shows the resulting PSD from $\gamma = 3$ and a stress-free inner boundary condition with $r_i = 6$. Thus there are degeneracies between the two parts to the emissivity and the inner radius, making it unlikely that they can all be uniquely constrained by the observed PSD.

It is clear from this analysis that while the low frequency break is fairly strongly linked to the viscous timescale of the outer radius of the hot flow (as assumed in section 4.2), the high frequency break is rather more complex, depending on propagation correlations, emissivity, boundary condition and inner radius in addition to the viscous timescale. This makes it difficult to directly associate the high frequency break with any physical parameter of the models. Instead, we now use the additional information from the QPO to remove some of the degeneracies inherent in this model for the broadband noise.

4.6 The QPO: Precession and surface density

For our fiducial model, we used the observed relation between the low frequency break and LF QPO to set the radial dependence of the viscous timescale, assuming that the low frequency break was set by the viscous timescale at r_o and that the QPO was Lense-Thirring precession of the entire hot flow from r_o to r_i (Section 4.2). This assumed that the surface density of the hot flow, $\Sigma = \Sigma_0(r/r_i)^{-\zeta}$ between r_o and r_i, with $\zeta = 0$. However, the broadband noise model described above *calculates* a self-consistent surface density as mass conservation implies

$$\dot{M}(r_n, t) = -2\pi r_n v_r(r_n)\Sigma(r_n, t), \tag{4.9}$$

(Frank, King & Raine 1992) where v_r is now expressed in units of c, $\dot{M}$ in units of $\dot{M}_0$, Σ in units of $\dot{M}_0/(cR_g)$ and r in units of R_g. Using our velocity prescription, we can

then easily show

$$\Sigma(r_n, t) = \frac{\dot{M}(r_n, t) r^{m-1/2}}{B}. \tag{4.10}$$

This means that, for the time averaged surface density, $\zeta = 1/2 - m$ giving extra physical motivation for the parameters used in section 4.2 ($\zeta = 0$ and $m = 1/2$). Note that equation 4.10 results from assuming the angular momentum loss from outflows to be negligible (Pringle 1981; Livio & Pringle 1992).

Figure 4.6 shows $\Sigma(r_n)$ plotted at a number of different times $(0, 256, 512, ..., 1792\ s)$ along with the corresponding $\dot{M}(r, t)$ function. $\dot{M}(r, t)$ is quite clearly more variable at small r. This is because we have assumed the variability *generated* in each logarithmic annulus to be the same but annuli at smaller radii include also the fluctuations that have propagated down from large r and so the *emitted* variability is greater (see Figure 4.4b). We do not see a drop off in surface density at the bending wave radius like that seen in simulations (e.g. Fragile 2009) because we assume that the infall velocity can be given by a power law. It is clear that, for the surface density drop off at a given point, the infall velocity must accelerate at that point. In a future paper, we will investigate this model with a more advanced velocity prescription.

Therefore the broadband noise model above, set by r_i, r_o and F_{var} *predicts* the QPO frequency at any point in time. The fluctuations in surface density with time *predict* that the QPO frequency changes, i.e. it is quasi–periodic rather than truly periodic. However, the precession frequency will not respond instantaneously to these changes, as their effect is only communicated across the entire hot flow by bending waves. These travel at the sound speed, faster by a factor $\sim \alpha$ than the viscous timescale across the region, so we calculate the QPO frequency every ~ 4 s rather than at every point. We then average these values to get the predicted QPO frequency (by combining equation 4.1 and equation 4.2 numerically rather than assuming the weak field limit as before) and use the dispersion around this to set the *r.m.s.* variance of these QPO frequencies, σ_{QPO}.

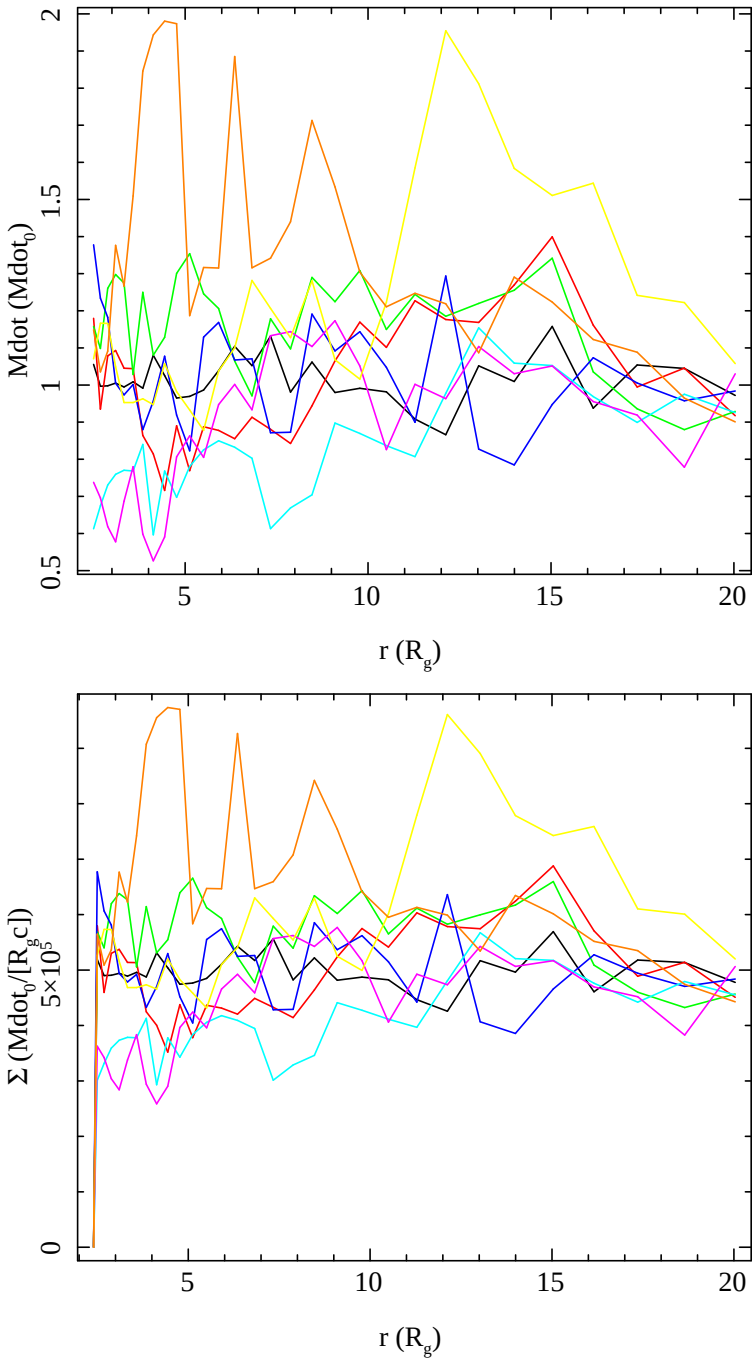

Figure 4.6: *Top:* Mass accretion rate as a function of radius shown here at a number of different times. *Bottom:* Surface density as a function of radius shown at the same times as the lines of corresponding colour in the top plot. This is calculated by applying mass conservation in the flow.

Fig. 4.7 shows σ_{QPO}/f_{QPO} as a function of f_{QPO} as r_o varies from 300–10 in the fiducial model. This decrease in r_o not only leads to an increase in QPO frequency, but also to a decrease in the QPO width, or equivalently, an increase in its coherence/quality factor $Q = f_{QPO}/\sigma_{QPO}$. An increase in QPO coherence during the transition from low/hard state to hard intermediate state is commonly observed in BHBs (although Q tends to plateau at ~ 10 for $f_{QPO} \gtrsim 1$; Belloni, Psaltis & van der Klis 2002; Rao et al 2010). Our model provides the first physical explanation for this effect as the smaller the radial extent, the higher the QPO frequency, but also the smaller the fluctuation power, giving smaller jitter in frequency. The red squares in Fig 4.7 show the *observed* frequency and width of the QPO from data from the 1998 rise to outburst of the BHB XTE J1550-564 (see section 7). The model matches the trend in the data fairly well, and forms a lower limit to the width of the QPO. However, other effects such as the on-time of the QPO (see Lachowicz & Done 2010) can decrease the coherence of the signal, so our model only predicts an upper limit for the quality factor, Q, of the QPO.

The model also predicts another correlation, one between the QPO frequency and flux on short timescales. The top plot of Figure 4.8 shows this for the fiducial model (i.e. $r_o = 20$), with precession frequency calculated every 4s together with the instantaneous luminosity at that time. After binning (red crosses), there is a clear linear relation between the two. This happens because both the QPO frequency and the luminosity depend on the mass accretion rate fluctuations. A perturbation in mass accretion rate at large r will lead to a perturbation in the surface density. This will reduce the precession frequency but will have little effect on the luminosity because the emissivity is quite steeply weighted towards small r. Later on, this perturbation will have propagated inwards to small r where it has the effect of increasing the precession frequency, but now also has much more of an effect on the luminosity. Heil, Vaughan & Uttley (2011) have recently discovered this correlation in data from the 1998 rise to outburst of XTE J1550-564 (a similar correlation was previously discovered for a

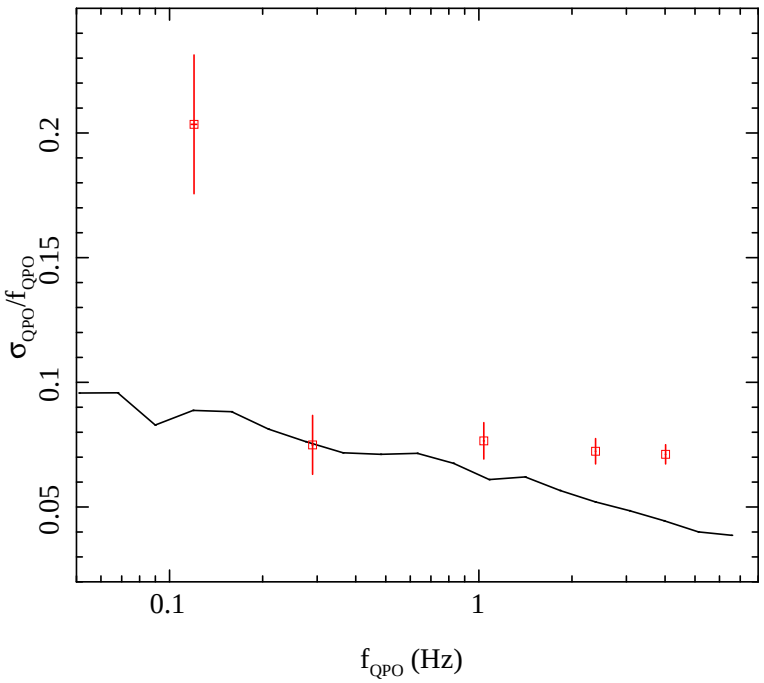

Figure 4.7: Fractional variability of the precession frequency plotted against the average precession frequency (black line). These are calculated by measuring the precession frequency every 4s for a number of different truncation radii, ranging from $300 - 10$, and taking the average and standard deviation over a 2048s duration. The red squares show the observed QPO width and frequency in data from the 1998 rise to outburst of XTE 1550-564. We see broad agreement with the data, however, other effects such as on-time of the QPO can decrease the coherence of the signal so we note that we are only able to predict a lower limit for the width of the QPO

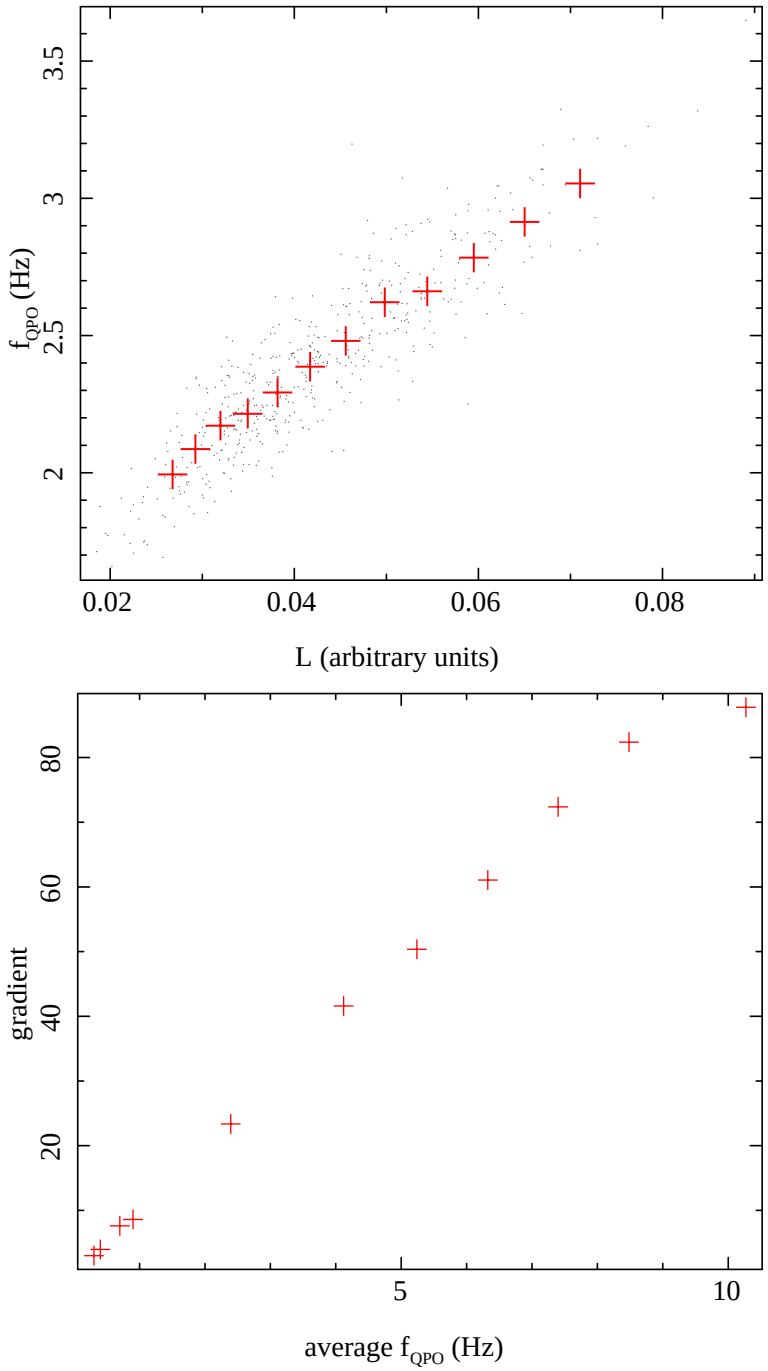

Figure 4.8: Precession frequency plotted against luminosity, where both are calculated at 4s intervals using the fiducial model parameters (grey points). After binning (red crosses), we clearly see a linear relationship between the two quantities. This relationship has recently been discovered in data from the 1998 rise to outburst of XTE J1550-564 (Heil, Vaughan & Uttley 2011), demonstrating the substantial predictive power of this model.

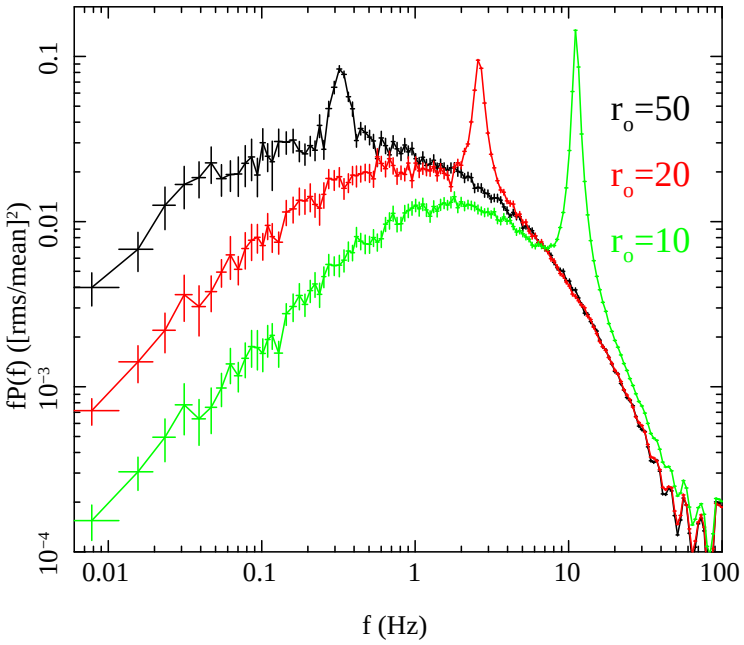

Figure 4.9: The full PSD calculated using the fiducial model parameters with $r_o = 50$ (black), 20 (red) and 10 (green). Here, the QPO is represented by a Lorentzian centred at the precession frequency with the width set by the r.m.s variance in precession frequency (see text).

type-B QPO by Nespoli et al 2003). They also find that the gradient of this relation is steeper for observations with a higher QPO frequency. This is also predicted by the model as illustrated in the bottom plot of Figure 4.8 where we have measured the gradient of the f_{QPO}-L relation and the average QPO frequency for 11 different r_o values. There is clearly a very strong correlation as is seen in the data. This is because an *absolute* change in precession frequency depends on a *fractional* change in mass accretion rate whereas an *absolute* change in luminosity depends on an *absolute* change in mass accretion rate. The same absolute change in mass accretion rate at a given radius and time constitutes a larger *fractional* change for small r_o than for high r_o. Therefore the luminosity will experience exactly the same change in both instances but the precession frequency will undergo a larger change when r_o is smaller. The

fact that these are *predicted* properties of the model constitutes strong support for its validity.

To include the QPO into our power spectral model, we must predict a *shape* for the QPO light curve as well as a frequency. The data show that the QPO has a power spectrum which can be represented by a Lorentzian at the fundamental frequency, f_{QPO}, together with its second and third harmonic and sub-harmonic i.e. at $2f_{QPO}$, $3f_{QPO}$ and $1/2f_{QPO}$ (e.g. Belloni, Psaltis & van der Klis 2002). Our model for the QPO in terms of Lense-Thirring precession *predicts* the shape of the modulation of the emission from the hot flow via variation of projected area, self-occultation and seed photons (IDF09). We will explore this further in a later paper (Ingram, Done & $\dot{Z}$ycki in prep), but here we simply assume that all the harmonics have the same quality factor, Q, and allow the power in each harmonic to be a free parameter. We then generate a QPO light curve, L_{QPO}, using these narrow Lorentzians as input to the Timmer & Koenig (1995) algorithm, and add this to the light curve already created for the broadband noise.

We show an example of the final predicted PSD in Figure 4.9, using the fiducial model parameters with $r_o = 50$ (black), 20 (red) and 10 (green). For clarity, we have set the normalisation of all the harmonics other than the fundamental to 0, set the width of the QPO using the model prediction of σ_{QPO}/f_{QPO}, and set its rms power to be constant across the three simulations. These PSD show all the main features seen in the data during spectral transitions of BHB (Gierlinski, Nikolajuk & Czerny 2008).

4.7 Conclusions

The truncated disc/hot inner flow model designed to describe the spectral evolution of BHB can also give a self consistent geometry in which to model the correlated evolution of the power spectrum. Propagating fluctuations through a hot flow which extends from and outer to inner radius, $r_o - r_i$, can produce the band limited noise characteristic

of the continuum power spectrum, as well as producing the rms-flux relation (L97; K01; AU06). Lense Thirring precession of this *same* hot flow can produce the QPO, with frequency set by the *same* parameters of r_o and r_i, together with the surface density of the flow (IDF09). The surface density is itself given self consistently by mass conservation from the propagating fluctuations. This predicts that the surface density fluctuates, so predicts that the QPO frequency will vary on short timescales (i.e. that it is a quasi rather than true period). These fluctuations set an upper limit to the coherence of the QPO, and this increases (i.e. width decreases) as r_o decreases. This is due to the decrease in fluctuation power due to the smaller range of radii from which to pick up variability. All these features are well known properties of the data (e.g. Remillard & McClintock 2006; DGK07): this model gives the first quantitative description of their origin. The fluctuations also predict that the flux and QPO frequency are correlated on short timescales, as a perturbation in the surface density at large radii leads to a longer QPO frequency but has little effect on the luminosity. As this propagates down, it weights the mass distribution to smaller radii, increasing the QPO frequency but also increasingly contributing to the luminosity due to the centrally peaked emissivity. This behaviour has also recently been observed (Heil, Vaughan & Uttley 2011).

The model also gives a framework in which to interpret some otherwise very puzzling aspects of the energy dependence of the variability seen in BHB. The extended emission region can be inhomogeneous, with different parts of the flow producing a different spectrum. The outermost parts of the flow are closest to the cool disc, so will intercept more seed photons and have a softer spectrum than that produced in the more photon-starved inner part of the flow (Kawabata & Mineshige 2010; Makishima et al 2008; Takahashi et al 2008). This implies that a larger fraction of the lower energy Compton scattered photons come from larger radii in the flow than the higher energy ones. The higher frequency variability is preferentially produced at the smallest radii, where

the spectrum is hardest. The flow at these small radii is also furthest from the cool disc, so has little reflection spectrum superimposed on the Compton continuum. Thus the model predicts that the fastest variability has the hardest spectrum and smallest reflected fraction, while slower variability has a softer spectrum and larger reflected fraction. This trend is also observed in the data (Revnivtsev et al 1999), and is very difficult to interpret in any other geometric picture as the inner disc edge cannot change in radius on even the longest timescale (few seconds) over which this relation is seen.

Similarly, the propagating fluctuations model means that a fluctuation starts at larger radii and then accretes down to smaller radii. Thus the fluctuation first affects the region producing a softer spectrum, then propagates down to smaller radii which produce the harder spectrum, so the hard band lags the soft band. The size of this lag depends on the frequency of fluctuations considered. Slow fluctuations (low frequencies) are produced at the outermost radius, so have the longest propagation time down to the innermost radius. High frequencies are produced only close to the inner radius, so only have a short distance to travel and hence have shorter lags. This gives rise to the frequency dependent time lags seen in the spectrum (Miyamoto & Kitamoto 1989; Revnivtsev et al 2001; K01; AU06). The precession model for the QPO also predicts harmonic structure. As the flow precesses, Comptonised emission is modulated by self occultation in the observer's line of sight and variation in seed photons from the changing projected area of the disc. In general this predicts non-sinusoidal variability, with the harmonic structure of the QPO being dependent on the details of the geometry of the flow. This gives rise to the prospect of actually using the PSD of BHBs to probe the geometry of the flow in detail.

While the many successes of the model are clearly evident, it is also clear that it is still far from complete. The most obvious outstanding issues are of the interaction of the hot flow with the truncated disc. The mechanism by which the cool disc truncates is not well established, though evaporation powered by thermal conduction between the

two different temperature fluids almost certainly plays some role in this (Liu et al 1997; Rozanska & Czerny 2000; Mayer & Pringle 2007). Whatever the mechanism, it seems physically unlikely that this will give a smooth transition between a cool thin disc and the hot flow. Any inhomogeneities will probably also be amplified by the difference in velocity between the disc and flow (discs are close to Keplarian, while the hot flow is strongly sub Keplarian) so there will be a shearing turbulent layer formed between them. Recent results show that there is variability associated with the truncated disc at a few 10s of seconds in the low/hard state of the bright BHBs GX339-4 and SWIFT J1753.5-0127 (Wilkinson & Uttley 2009), suggesting that there is considerable complexity in the disc truncation (see also Chiang et al 2010). Full numerical simulations of the MRI in a composite truncated disc/hot inner flow geometry are probably required in order to show the effect of these. However, such simulations are way beyond current computer capabilities. A more tractable issue is the effect of relativity on the propagating fluctuations. Near the black hole, light bending and time dilation should be important and consequently future versions of this model need to take these effects into account. The final goal should of course be the creation of a fully relativistic model which can produce a Fourier resolved spectrum with both energy and time dependence such that we can test it against observations such as the PSD, the energy spectrum, the lag spectrum, the cross spectrum etc. This is of course very ambitious but it is the only way we can genuinely achieve a full theoretical understanding of what drives mass accretion and emission in BHBs.

Chapter 5

Modelling variability in black hole binaries: linking simulations to observations

5.1 Introduction

In the previous chapter (based on Ingram & Done 2011; hereafter ID11), we explored a model to explain the PSD of BHBs in the truncated disc / hot inner flow geometry initially proposed to explain the observed spectral transitions. Here the QPO is driven by Lense Thirring precession of the entire hot flow (as considered in Chapter 2) and the broad band variability is a result of propagating mass accretion rate fluctuations in the same hot flow. Crucially, these two processes are linked such that a few physical parameters (inner and outer radius of the hot flow, surface density of the hot flow) set both the QPO *and* broad band noise properties. Precession of the fluctuating flow modulates its observed emission, imprinting the QPO on the broad band noise, while fluctuations in the flow cause fluctuations in the precession frequency, making a quasi-periodic rather than periodic oscillation.

This chapter is adapted from Ingram & Done (2012a), in which we develop a more advanced version of the model which is in better agreement with the results of General Relativistic Magnetohydrodynamic (GRMHD) simulations. We fit the model to data

from the 1998 outburst of XTE J1550-564, allowing us to directly compare the results of simulations with observations of BHBs. This model is now publically available within the spectral fitting package XSPEC (Arnaud et al 1996) as a local model, PROPFLUC.

5.2 The model

As in ID11, the model consists of fluctuations in mass accretion rate which propagate towards the black hole (following Lyubarskii 1997, Kotov et al 2001 and AU06) within a flow that is precessing. Here we develop the model to include a number of improvements which allow us to gain more physical insight from the best fit parameters. Most significantly, we change our underlying assumption about the viscous frequency $f_{visc}(r)$. In ID11 we assumed that this was a power law between r_i and r_o, the inner and outer radius of the precessing hot flow. Here we have it be a smoothly broken power law, with the radius of the break being the bending wave radius, r_{bw}, expected from a misaligned flow. The viscous frequency is related to the surface density profile, Σ via the radial infall velocity $v_r(r)$ as $f_{visc}(r) = -v_r(r)/R$ and mass conservation sets $\dot{M} \propto \Sigma 2\pi r v_r$. Hence we can use the surface density profiles from the GRMHD simulations to derive $f_{visc}(r)$, which is especially important as the QPO frequency is dependent on $\Sigma(r)$.

We also change the assumed emissivity from ID11, where $\epsilon \propto r^{-\gamma} b(r)$ (where $b(r)$ was an unknown boundary condition) to $\epsilon \propto r^{-\gamma}\Sigma(r)$ i.e. we tie the emission to where the mass is in the flow. We describe the details of the model below, mainly focusing on these improvements made since ID11. Note that we assume a 10 solar mass black hole throughout.

5.2.1 Steady state properties

The surface density of the flow sets the QPO frequency by global precession as

$$f_{prec} = \frac{\int_{r_i}^{r_o} f_{LT} f_k \Sigma r^3 dr}{\int_{r_i}^{r_o} f_k \Sigma r^3 dr} \tag{5.1}$$

where f_k is the Keplerian orbital frequency and f_{LT} is the point particle Lense-Thirring precession frequency (equation 4.2).

We use the GRMHD simulations of tilted flows to guide our description of $\Sigma(r)$ (Fragile et al 2007; 2009; Fragile 2009). These can be well fit by a smoothly broken power law function

$$\overline{\Sigma(r_n, t)} = \frac{\Sigma_0 \dot{M}_0}{c R_g} \frac{x^\lambda}{(1+x^\kappa)^{(\zeta+\lambda)/\kappa}}. \tag{5.2}$$

(IDF09), where $x = r/r_{bw}$ is radius normalised to the bending wave radius $r_{bw} = 3(h/r)^{-4/5} a_*^{2/5}$, Σ_0 is a dimensionless normalisation constant and $\dot{M}_0$ is the average mass accretion rate which we will assume stays constant over the course of a single observation. This gives $\Sigma \propto r^\lambda$ for small r and $\Sigma \propto r^{-\zeta}$ for large r, where κ governs the sharpness of the break. The bending wave radius occurs at radii larger than the last stable orbit because there are additional torques created by the misaligned black hole spin which result in additional stresses i.e. enhanced angular momentum transport. The material in falls faster, so its surface density drops.

Mass conservation then sets the viscous frequency as

$$f_{visc}(r_n) = \frac{\dot{M}_0}{2\pi R^2 \overline{\Sigma(r,t)}} = \frac{1}{2\pi r_{bw}^2 \Sigma_0} \frac{(1+x^\kappa)^{(\zeta+\lambda)/\kappa}}{x^{\lambda+2}} \frac{c}{R_g}, \tag{5.3}$$

such that $f_{visc} \propto r^{\zeta-2}$ for large r and $f_{visc} \propto r^{-(\lambda+2)}$ for small r.

5.2.2 Propagating mass accretion rate fluctuations

As in ID11 (and AU06), we start by splitting the flow up into N annuli of width dr_n such that $r_1 = r_o$ (the truncation radius) and $r_N = r_i + dr_n \approx r_i$ (the inner radius of the

flow). We assume that the power spectrum of variability generated in mass accretion rate at the n^{th} annulus is given by a zero centred Lorentzian cutting off at the local viscous frequency

$$|\tilde{\dot{m}}(r_n, f)|^2 \propto \frac{1}{1 + (f/f_{visc}(r_n))^2} \tag{5.4}$$

where a tilde denotes a Fourier transform and $f_{visc}(r_n)$ is derived from Equation 5.3.

We use the method of Timmer & Koenig (1995) to generate mass accretion rate fluctuations, $\dot{m}(r_n, t)$, which satisfy equation 5.4. These are normalised to have a mean of unity and fractional variability $\sigma/I = F_{var}/\sqrt{N_{dec}}$ where, unlike ID11, F_{var} and N_{dec} are the fractional variability and number of annuli per decade in *viscous frequency* rather than radius. These two descriptions are exactly equivalent where f_{visc} is a power law function of radius as in ID11, as $df_{visc}/f_{visc} = dr/r$. However, the more physical smoothly broken power law form for f_{visc} does not retain this property. We choose to parametrise the noise power in terms of df_{visc}/f_{visc} and discuss the implications of this in section 5.2.3.

The mass accretion rate through the outer annulus is given by $\dot{M}(r_1, t) = \dot{M}_0 \dot{m}(r_1, t)$. Variability is generated in every other annulus according to Equation 5.4, but this is also accompanied by the noise from the outer regions of the flow which propagates inwards. Thus the mass accretion rate at the n^{th} annulus is given by

$$\dot{M}(r_n, t) = \dot{M}(r_{n-1}, t - t_{lag})\dot{m}(r_n, t), \tag{5.5}$$

where $t_{lag} = -R_g dr_n/v_r(r_n) = dr_n/(r_n f_{visc}(r_n))$ is the propagation time across the n^{th} annulus and $v_r(r_n) = -R_g r_n f_{visc}(r_n)$ is the infall velocity.

To convert these mass accretion rate fluctuations into a lightcurve, we assume that the luminosity emitted from the n^{th} annulus is given by

$$dL(r_n, t) = \eta/2 \ \dot{M}(r_n, t)c^2 \epsilon(r_n) r_n dr_n, \tag{5.6}$$

where the (dimensionless) emissivity is given by

$$\epsilon(r_n) = \epsilon_0 r_n^{-\gamma} b(r_n), \tag{5.7}$$

and γ is the emissivity index, η the emission efficiency (this may be smaller than unity due to e.g. advection), $b(r)$ the boundary condition and ϵ_0 is a normalisation constant. In ID11, we considered two boundary conditions: the 'stress free' boundary condition $b(r) = 3(1 - \sqrt{r_n/r_i})$ and the 'stressed' boundary condition $b(r) = 1$. Here, however, we make the intuitive and physical assumption that the boundary condition is set by the surface density such that $b(r) \propto \overline{\Sigma(r_n, t)}$ where $\overline{\Sigma(r_n, t)}$ is the *time averaged* surface density. This allows the model to link the emission with the amount of material in a particular annulus.

The fluctuating mass accretion rate will also have an effect on precession because mass conservation needs to hold on short time scales as well as long time scales, which gives $\dot{M}(r_n, t) \propto \Sigma(r_n, t) 2\pi r^2 f_{visc}$. This means that the surface density at time t is given by

$$\Sigma(r_n, t) = \frac{\Sigma_0 \dot{M}(r_n, t)}{cR_g} \frac{x^\lambda}{(1 + x^\kappa)^{(\zeta+\lambda)/\kappa}}, \tag{5.8}$$

which trivially averages to equation 5.2 on long time scales. Because the surface density sets the precession frequency (equation 5.1), we see that the fluctuations in mass accretion rate cause the precession frequency to vary, thus allowing the model to predict a quasi-periodic oscillation rather than a purely periodic oscillation.

5.2.3 Surface density profile

In ID11, we parametrised the viscous frequency with a power law. The fiducial model parameters therein gave $f_{visc} = 0.03 r^{-0.5} f_k$, corresponding to a surface density profile $\Sigma(r) = constant$ between the inner and outer radii which were set to $r_i = 2.5$ and $r_o = 50$ respectively. By comparison, the GRMHD titled flow simulations of Fragile et al (2009) also give $\Sigma(r) = constant$ at large radii, but then smoothly break at the bending wave radius to a much steeper dependence. The most relevant simulation to this paper is the case with $a_* = 0.5$ as this is likely closest to the spin of XTE J1550-564 (e.g. Davis, Done & Blaes 2006; Steiner et al 2011). This has surface

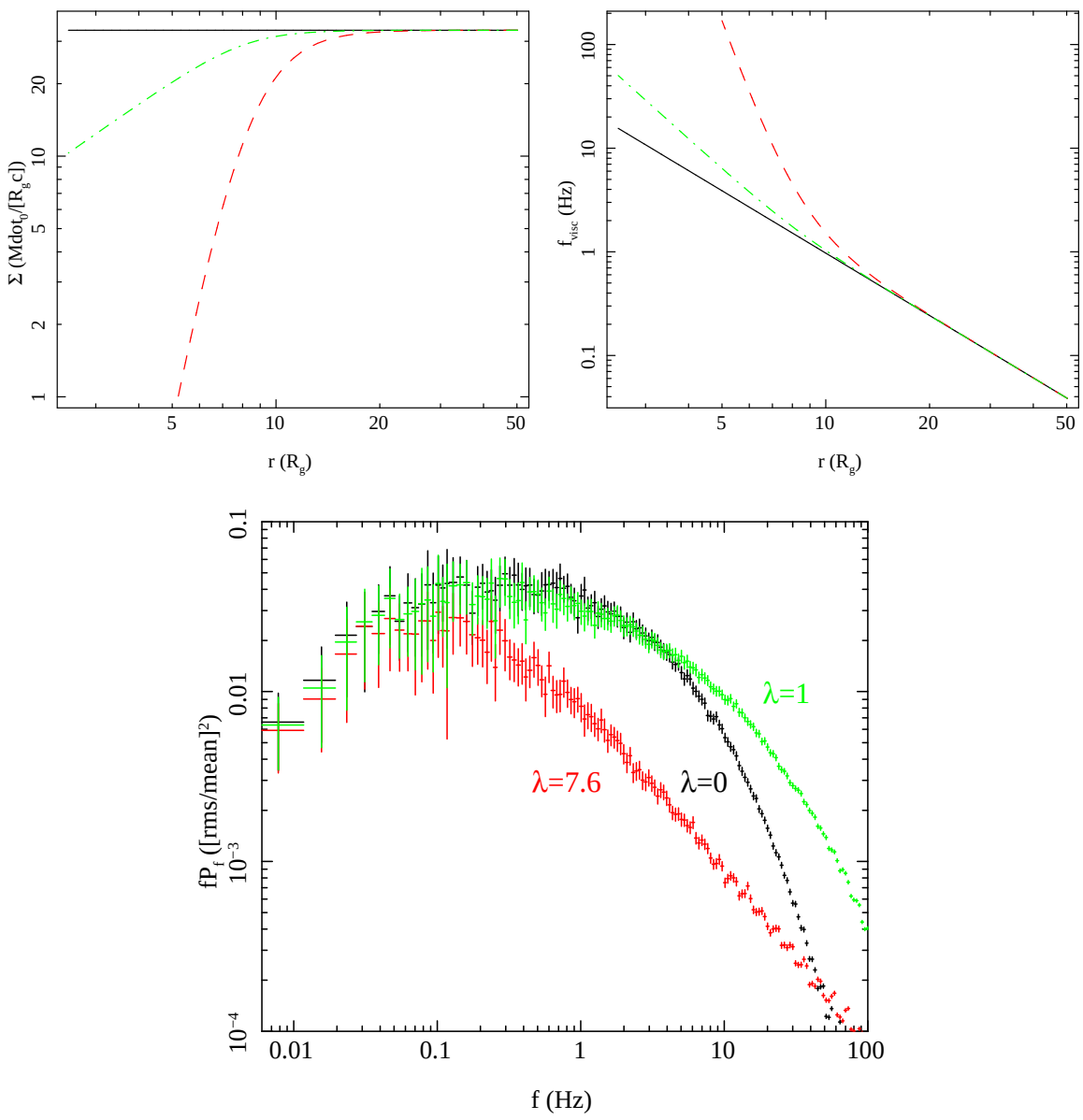

Figure 5.1: *Top left:* Surface density as a function of radius for the fiducial model parameters in ID11 (solid black line), simulations of a misaligned accretion flow around a 10 solar mass black hole with $a_* = 0.5$ (red dashed line) and the fiducial model parameters we choose for this paper (green dot-dashed line). The red dashed line is calculated using equation 5.2 with $\lambda = 7.6$, $\kappa = 5$, $\zeta = 0$ and $r_{bw} = 8.08$ (the parameters which best fit the simulation data). For the dot-dashed green line, $\lambda = 1$ with all other parameters the same. *Top right:* The viscous frequency as a function of radius resulting from assuming the surface density to be given by the corresponding line in the top panel. *Bottom:* The PSD predicted using the surface density given by corresponding lines in the top panel.

density parameters (Equation 5.2, see Figure 4 in IDF09) of $r_{bw} = 8.1$ (corresponding to $h/r = 0.21$), $\kappa = 5$, $\lambda = 7.6$ and $\zeta = 0$.

In the top of Figure 5.1, we plot these two different surface density prescriptions (top left) and their resulting viscous frequencies (top right), with the power law shown by the black solid line and the broken power law shown by the red dashed line. In the case of the broken power law, we choose the normalisation $\Sigma_0 = 33.3$ to ensure that both assumptions become consistent with one another at large radii. The bottom plot of Figure 5.1 shows the PSD resulting from the two different prescriptions. The new (and more physically realistic) surface density prescription predicts much less noise at high frequencies than the previous model, where the surface density remained constant down to the innermost radii.

To retrieve sufficient high frequency power in order to match the data requires $\lambda = 1$ rather than 7.6 (green dot-dashed lines in the top plots of Figure 5.1). This gives a more gradual drop-off in surface density, leading to a less severe transition in viscous frequency at the bending wave radius and hence more high frequency power (green points in the bottom plot of Figure 5.1). We discuss the physical implications of this in more detail in Section 6.2.1. For now, however, we use $\lambda = 1$ for our fiducial model.

We can also use the fiducial model parameters to explore the significance of assuming $df_{visc}/f_{visc} = constant$ (hereafter df/f for simplicity). From equation 5.3, df/f and dr/r are related as

$$(df/f) = (dr/r)\left[\frac{\zeta + \lambda}{x^{-\kappa} + 1} - (\lambda + 2)\right], \tag{5.9}$$

where we employ the convention $df/f < 0$ and $dr/r > 0$ (since f_{visc} is higher for smaller r). Since, by definition, each ring generates the same fractional variability, each must contain the same number of independent regions, implying $(dr/r) = A(h/r)$. Here, A is a constant which sets the resolution ($A = 2$ means each independent region covers the whole vertical extent of the flow). We can therefore rearrange equation 5.9 to obtain

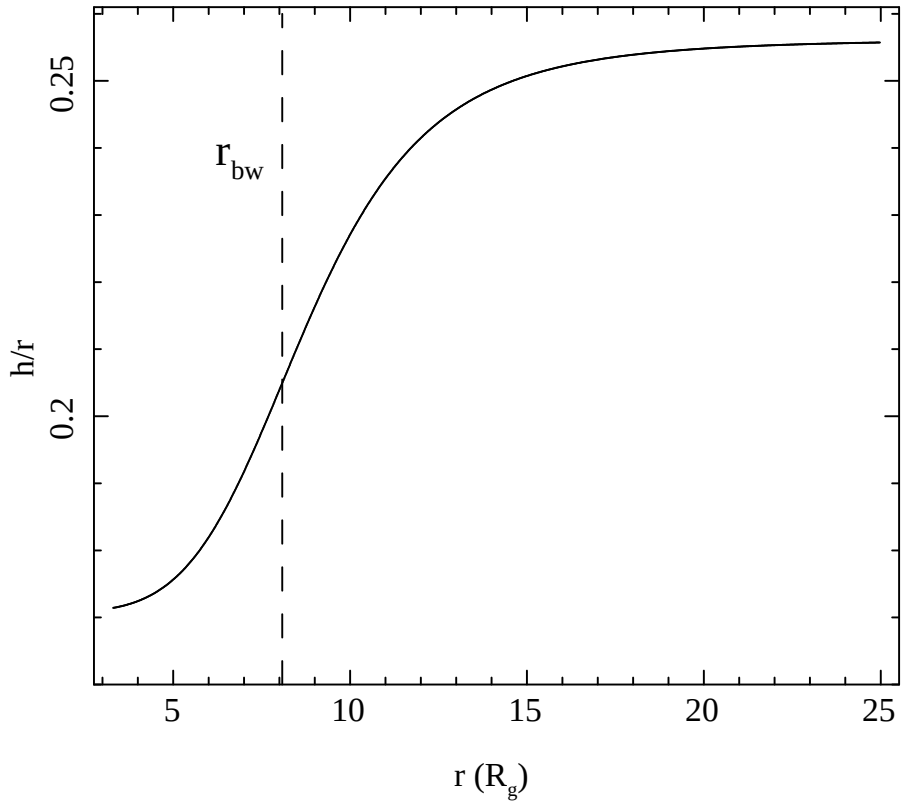

Figure 5.2: Flow scale height as a function of radius as predicted by the fiducial model. The dotted line represents the bending wave radius which sets the break in the function.

an expression for the flow scale height

$$(h/r) = \frac{(df/f)}{A}\left[\frac{\zeta+\lambda}{x^{-\kappa}+1} - (\lambda+2)\right]^{-1}. \tag{5.10}$$

The formula linking the bending wave radius with the scale height (evaluated at the bending wave radius) can then be used to show $(df/f)/A = (3)^{5/4} a_*^{1/2} r_{bw}^{-5/4}(\zeta/2 - \lambda/2 - 2)$. Figure 5.2 shows the scale height as a function of r for the fiducial parameters. We see that our $df/f = constant$ assumption means we predict the scale height to drop off at small radii, consistent with simulation results (Figure 13 in Fragile et al 2007).

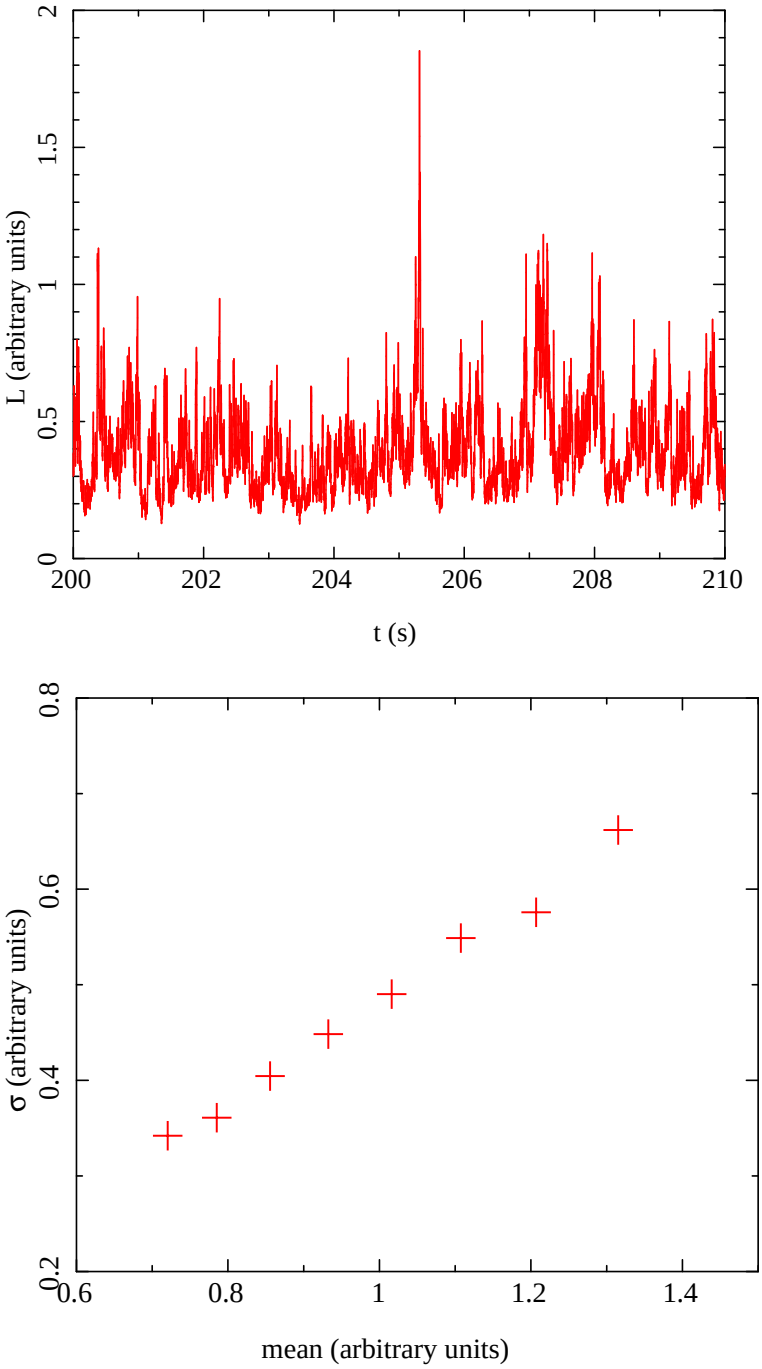

Figure 5.3: *Top:* A 10s segment of the light curve calculated using the fiducial model parameters and $r_o = 50$. *Bottom:* The sigma-flux relation for the above light curve. We see this is linear as is seen in the data.

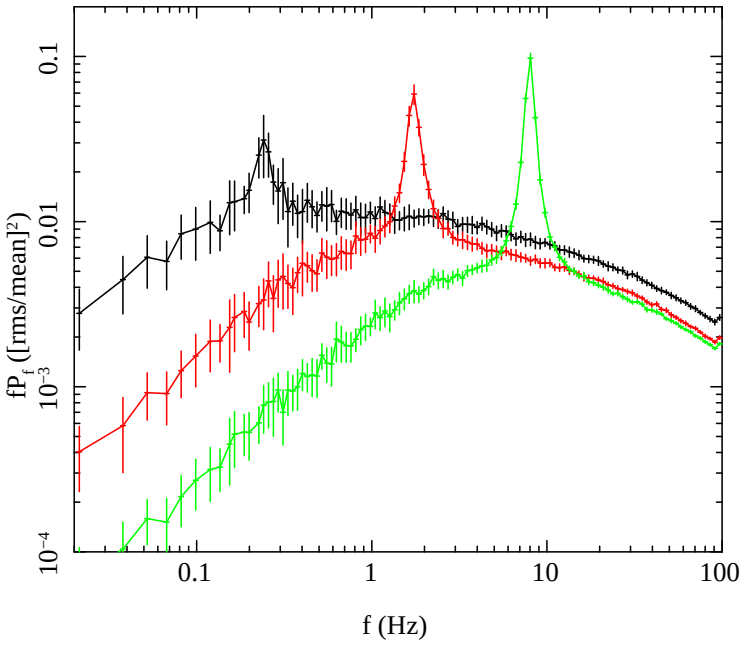

Figure 5.4: The predicted PSD for the fiducial model parameters with $r_o = 50$ (black), 20 (red) and 10 (green). For clarity the normalisation of the fundamental is set to increase as r_o reduces and all the other QPO components are normalised to zero.

5.2.4 The fiducial model

Following the discussion in section 5.2.1, we use model parameters $\Sigma_0 = 33.3$, $r_{bw} = 8.1$, $\kappa = 5$, $\lambda = 1$ and $\zeta = 0$. We also set $r_i = 2$ and $\gamma = 4$ but note that the new assumptions for surface density coupled with the new boundary condition mean the model is now much less sensitive to the parameter r_i than its predecessor in ID11. Figure 5.3 (top) shows a 10s segment of the light curve created using these assumptions and with $r_o = 50$. We use $N_{dec} = 15$ (i.e. 15 annuli per decade in viscous frequency) with 2^{22} time steps, giving a duration of $4096s$ (similar to a typical *RXTE* observation) for a time bin of $dt = 9.7 \times 10^{-4}$. Figure 5.3 (bottom) confirms that this light curve has the linear sigma-flux relation implied by its skewed nature. The PSD of this light curve is represented by the red points in Figure 5.1 (bottom).

We calculate the QPO as in ID11, but we briefly summarise this here for complete-

ness. The QPO fundamental frequency is set to the average (over the 4096s duration) precession frequency calculated from Equation 5.1. In principle we can calculate the width of the QPO from the fluctuations in frequency which result from fluctuations in surface density. However, these only set a lower limit to the width of the QPO since it can also be broadened by other processes (ID11), so we leave this as a free parameter. We can in principle predict the harmonic structure in the QPO lightcurve by a full Comptonisation calculation of the angle dependent emission from a precessing hot flow (Ingram, Done & Zycki in preparation). Until then, we simply allow the normalisations of the harmonics to be a free parameter but fix their width so that they have the same quality factor as the fundamental (apart from the sub-harmonic which is free: Rao et al 2010). We use the method of Timmer & Koenig (1995) to generate a light curve from these narrow QPO Lorentzians and add this to the light curve already created for the broad band noise.

Figure 5.4 shows the full PSD given by the fiducial model parameters with $r_o = 50$ (black), $r_o = 20$ (red) and $r_o = 10$ (green). For clarity we set the normalisations of the QPO harmonics to zero, and increase the normalisation and quality factor of the fundamental as r_o decreases to match with the data. This captures the essence of the observed evolution of the PSD in terms of a decreasing truncation radius.

5.3 Fitting to data

We use *RXTE* data from the 1998 outburst of XTE J1550-564 (Remillard et al 2002; Sobczak et al 2000; Rao et al 2010; Wilson & Done 2001; Altamirano 2008). We look at 5 specific observations with observational IDs: 30188-06-03-00, 30188-06-01-00, 30188-06-01-03, 30188-06-05-00 and 30188-06-11-00; hereafter observations 1-5 respectively. We only consider energy channels 36-71 (corresponding to 13.36-27 keV) in order to avoid disc contamination.

For all PSDs, we use a combination of ensemble averaging and geometric rebinning.

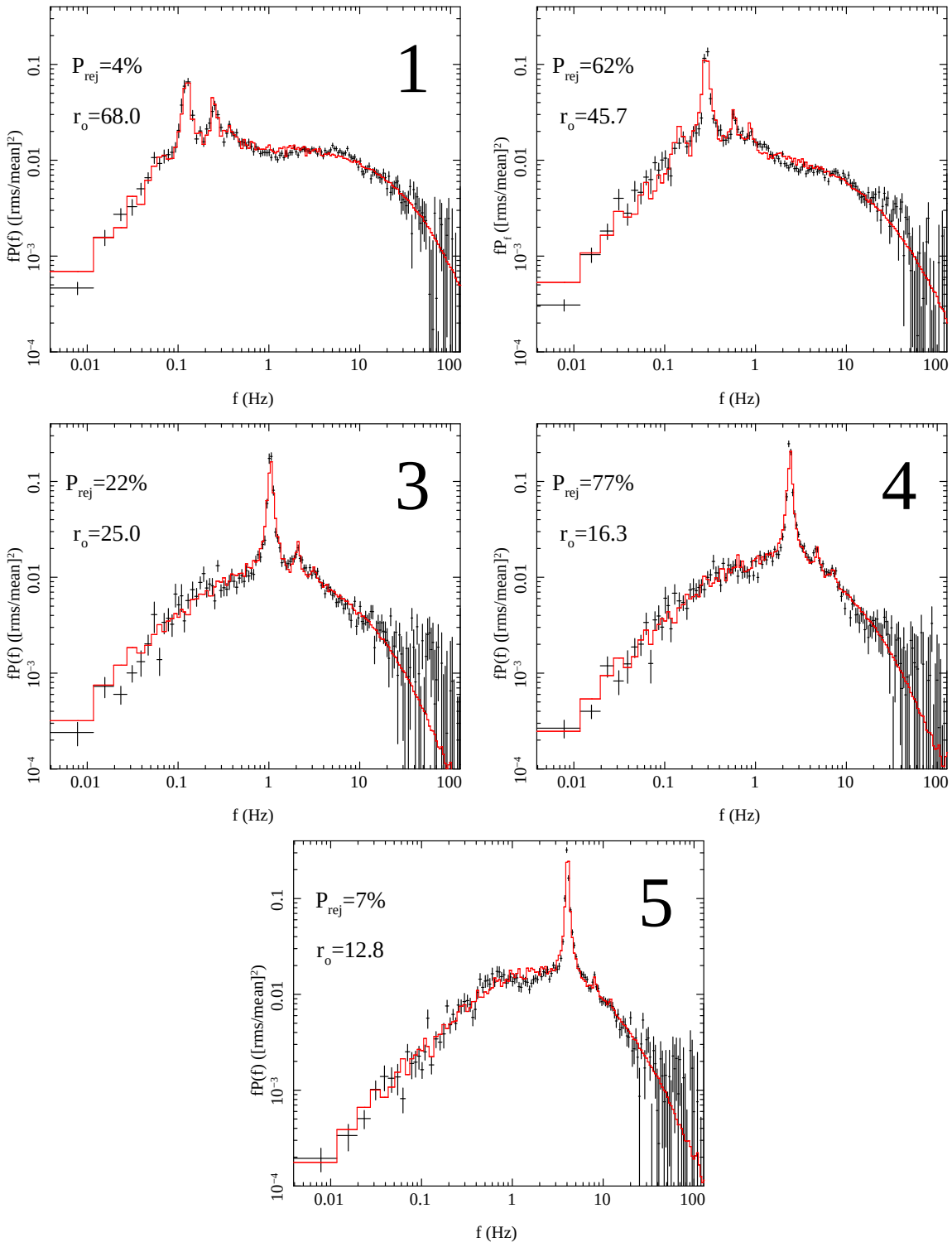

Figure 5.5: Best fit PSDs along with data points for observations 1-5. The rejection probability, P_{rej}, and truncation radius, r_o, are included in each plot. The rest of the best fit physical parameters are included in table 5.1.

Each periodogram is calculated for 128s of data. Since we simulate 4096s of data, we can average over $\mathcal{M} = 32$ realisations. For the observed data, the duration of the observation limits us to $\mathcal{M} = 41,\ 26,\ 13,\ 14$ and 14 for observations 1-5 respectively. Geometrical rebinning is always carried out using a rebinning constant of $c_0 = 1.05$. Since this smoothing should lead to statistically well behaved PSDs with Gaussian error distributions (for both observed *and* simulated data), we carry out the fit using a χ^2 minimization test. However, to test our assumption of Gaussian errors, we do *a posteriori* checks on the goodness of fit using the rejection probability method of Uttley et al (2002) and Markewicz et al (2003). This involves comparing the agreement between data and model with the agreement between the model and alternative realisations which use the same parameters. The minimized χ^2 value is calculated as

$$\chi^2 = \sum_J \frac{(P_{mod}(f_J) - P_{obs}(f_J))^2}{dP^2_{mod}(f_J) + dP^2_{obs}(f_J)}. \tag{5.11}$$

We then simulate many more (1000) realisations with the same model parameters (i.e. we change the seed for the random number generator) in order to calculate many values of

$$\chi^2_k = \sum_J \frac{(P_{mod}(f_J) - P_k(f_J))^2}{dP^2_{mod}(f_J) + dP^2_k(f_J)}, \tag{5.12}$$

where $P_k(f_J)$ is the PSD of the k^{th} realization. The rejection probability, P_{rej}, is given by the percentile of χ^2_k values which are smaller than χ^2. This method therefore asseses the likelihood that $P_{obs}(f_J)$ does not belong to the distribution that $P_{mod}(f_J)$ and each $P_k(f_J)$ belong to *without* making any assumptions about the shape of that distribution.

We incorporate our model for the power spectrum into XSPEC, using the local model functionality. This is now available publically as PROPFLUC, described in detail in the appendix. Our model outputs a PSD rather than the more familiar flux as a function of energy. We fit each observed PSD to derive the parameters of the smoothly broken power law surface density. We assume that the shape of the surface density stays constant across all datasets, but its normalisation Σ_0 can change. We also allow the

Obs	Σ_0	ζ	λ	κ	r_i	r_o	h/r (r_{bw})	F_{var}	γ
1	5.43					68.0	0.41 (4.6)	0.32	
2	10.48					45.7	0.27 (6.5)	0.31	
3	21.73	$\equiv 0$	$\equiv 0.9$	$\equiv 3.0$	$\equiv 3.3$	25.0	0.21 (8.0)	0.36	5.28
4	30.03					16.3	0.13 (12.03)	0.43	
5	30.36					12.8	0.12 (12.1)	0.48	

Table 5.1: Best fit physical parameters for observations 1-5. A $\equiv$ symbol indicates that the parameter has been fixed.

bending wave radius to be a free parameter, $r_{bw} = 3(h/r)^{-4/5}a_*^{2/5}$ (where h/r is the scaleheight of the flow). As we have fixed the spin, the best fit value of r_{bw} gives us an estimate of the scale height of the flow which may change through the transition due to the increase in seed photons from the disc cooling the flow. The inner radius of the flow is tied across all the data sets, and we fit for r_o. The remaining free parameters which determine the broadband noise are the level of MRI fluctuations generated over each decade in frequency, F_{var}, and the emissivity index, γ (held constant across all 5 observations).

While XSPEC can fit the model to the 5 PSD simultaneously, this is very slow. Instead, we used trial and error to set values of the parameters which are tied across all the datasets and then fix these to fit the remaining parameters for each PSD individually.

5.3.1 Fit results

The data and best fit model PSD are shown in Figure 5.5. These give a reduced χ^2 value of 1.09 (764.6 for 704 degrees of freedom). We calculate the rejection probability to be $P_{rej} = 4\%$, 62%, 22%, 77% and 7% for observations 1-5 respectively. The lowest values of P_{rej} obviously imply a very good fit but even the higher values are still acceptable.

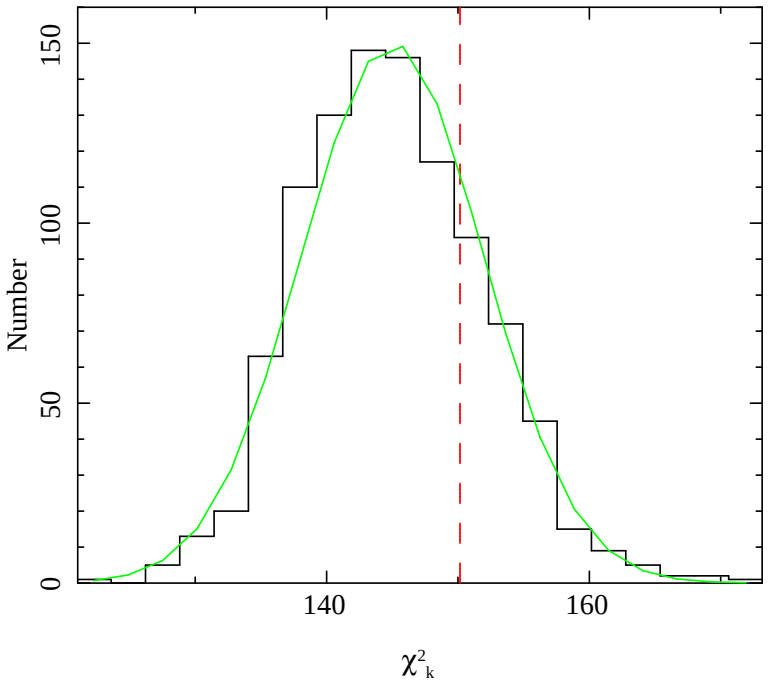

Figure 5.6: Distribution of χ^2_k values calculated using the best fit model parameters for observation 4. The green line illustrates that this is a nearly Gaussian distribution. The red dashed line picks out the χ^2 value for this observation and we see that, although it is larger than the mean χ^2_k value, it still lies believably within the distribution meaning we can be confident that the model fits.

Figure 5.6 shows the distribution of χ^2_k values from the P_{rej} calculation (black stepped line) using the best fit parameters for observation 4. The red dashed line shows the χ^2 value for this observation and we see that, although it is larger than most χ^2_k values, it still lies believably within the distribution. We also plot (green solid line) a Gaussian with the same mean, standard deviation and normalisation as the distribution and we see very good agreement between the two. This confirms that the PSD estimate we use does indeed give (approximately) Gaussian errors and therefore χ^2 is a reliable measure of goodness of fit.

Table 5.1 shows all of the best fit physical parameters. The truncation radius moves from $r_o = 68 - 13$, while F_{var} increases throughout the transition. In addition, our new parametrisation means that we can directly explore the change in bending wave radius, r_{bw}, and surface density normalisation, Σ_0. The bending wave radius increases, implying that the flow scaleheight, h/r, is collapsing. This makes sense physically as the decreasing truncation radius means that the flow is cooled by an increasing number of seed photons, so the electron temperature decreases. The spectra also show that the optical depth increases (as is also implied by the increasing surface density normalisation). This increases the coupling between electrons and ions so the ion temperature also decreases (Malzac & Belmont 2009). The flow is held up (at least partly) by ion pressure so the scale height of the flow collapses.

Note that, in our model, the characteristic frequency $f_{visc}(r_{bw})$ *decreases* as the other characteristic frequencies increase. This at first seems to contradict the results of Lorentzian fitting which always show the high frequency break, f_h, to increase. This apparent contradiction occurs due to the effect of propagation on the PSD shape as discussed in ID11. As the truncation radius moves in and the range of frequencies produced by the flow narrows, the highest frequencies become less affected by destructive interference and thus, even though the *generated* variability peaks at a lower frequency as the r_o moves in, the *emitted* variability actually peaks at higher frequencies, as

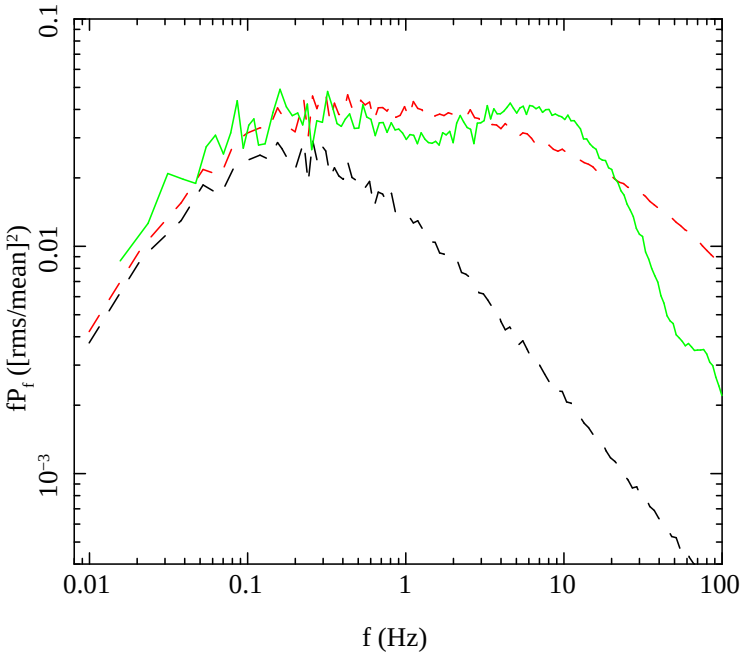

Figure 5.7: The red dashed line is the PSD predicted using the fiducial model parameters with $r_o = 50$ (i.e. $\lambda = 1$) whereas the black dashed line is for $\lambda = 7.6$ with all other parameters the same. For the green solid line, we use the same parameters as used for the black line but we have changed the model by assuming the annulus containing r_{bw} to be more variable than the other annuli. We see we can recover the amount of high frequency power required to match the observations using this assumption.

observed.

5.4 Discussion

We have improved upon the model of ID11 by including a surface density profile which has the same shape as predicted by GRMHD simulations. We obtain an excellent fit to data for five observations and the evolution of the best fit parameters is self-consistent. However, we require the surface density interior to the bending wave radius to drop-off as r^λ with $\lambda \sim 1$, where as the simulations predict $\lambda \approx 7$ (see Figure 5.1). A possible

reason for this apparent discrepancy is that the torque created by the misalignment between flow and black hole angular momenta not only creates a drop-off in surface density but also generates extra turbulence which we do not account for in our model. Because the surface density sets the emissivity, we can still reproduce the observations by over predicting the surface density at small r to compensate for under predicting the intrinsic variability. In Figure 5.7, we re-plot the predicted PSD for $\lambda = 7.6$ (dashed black line) and $\lambda = 1$ (dashed red line) without errors for clarity. For the green solid line, also plotted without errors, we have changed the model slightly. We again set $\lambda = 7.6$ but now the fractional variability in the annulus containing r_{bw} is higher (by a factor of 10) than that at all other annuli so as to approximate the additional turbulence created by the bending waves. We see that it is possible to qualitatively reproduce the shape of the broad band noise using a surface density profile consistent with simulations if we include this extra assumption.

It is interesting that the green line in Figure 5.7 does not have a flat top between low and high frequency breaks as the model generally predicts, but rather has a 'bump' at $\sim$ 7Hz and another at $\sim$ 0.15Hz. There are actually many observations of bumpy power spectra such as this which cannot be well described by the model in its current state (e.g. Axelsson et al 2006; Wilkinson & Uttley 2009). In fact, even the data considered here show evidence that a double hump is a more appropriate description than flat top noise (especially observations 1 and 5). It therefore looks likely that the variability generated by the MRI is not as uniform as we naively assume and actually some regions produce more variability than others thus giving rise to a bumpy power spectrum such as the green line in Figure 5.7.

5.5 Conclusions

We have made some improvements to a model designed to predict the power spectral behaviour of BHBs in the context of a truncated disc / hot inner flow geometry which

can also explain the energy spectral evolution. The model uses simple, theoretically motivated assumptions in order to reproduce the shape and evolution of the broad-band noise with the extra requirement that the QPO is generated by Lense-Thirring precession of the entire hot inner flow. Because the model now assumes a surface density profile consistent with that predicted by GRMHD simulations, we can now gain more physical insight from the evolution of best fit parameters which reproduce the observed evolution of the PSD. A coherent picture is now emerging: as the truncation radius, r_o, moves inwards, the increased number of seed photons incident on the flow cool it, thus reducing both the electron and ion temperatures, T_e and T_i respectively. The Comptonised emission from the flow is therefore softer and, in addition to this, the lower ion temperature gives rise to a lower pressure meaning that the scale height of the flow, h/r, should collapse. The bending wave radius, which sets the shape of the surface density, is given by $r_{bw} = 3(h/r)^{-4/5}a_*^{2/5}$ and therefore increases as h/r collapses. Also, because the volume of the flow is reducing, the surface density must increase and, by mass conservation, the infall velocity decreases. When we fit the model to five observations of XTE J1550-564, we see all of these trends: r_o reduces and r_{bw} increases as does Σ_0, the normalisation of the surface density (and also the inverse of the normalisation of the infall velocity).

Since the model has the capability to reproduce other higher order statistical properties seen in the data such as time lags and the frequency resolved spectrum, it is very attractive. However, although we believe the *trends* in best fit parameter values to be reliable, their *absolute* values should not be taken too seriously. This is because there are a few complexities not currently included in the model. For example, we currently effectively assume that the disc is stable which is not true, at least in the low/hard state (Wilkinson & Uttley 2009). Although we only consider energies at which the Comptonized emission dominates, the disc is feeding the flow and therefore disc variability should propagate to the flow and modulate the hard emission. This means that

the lowest frequencies in the PSD are actually being generated in the disc and not in the flow, meaning we over predict the truncation radius, r_o. In fact, it could be that the entire low frequency Lorentzian in the PSD is generated in the disc (perhaps from the presumably turbulent process of disc truncation) before propagating to the flow, with the MRI only generating the high frequency Lorentzian. This would provide an alternative explaination for the double humped nature of the observed BHB PSD.

The main uncertainty associated with the model is that it is unclear exactly how the disc and flow couple together. Although the most likely truncation mechanism is evaporation via thermal conduction (e.g. Liu, Meyer & Meyer-Hofmeister 1997; Różańska & Czerny 2000; Mayer & Pringle 2007), the details of this process are still far from well understood and, in particular, numerical simulations of a truncated disc / hot inner flow configuration are far beyond current computing capabilities. Whatever the specific nature of the coupling, it seems very likely that the disc will exert a torque on the flow, especially in a region where the flow overlaps the disc, which would slow down precession. This means that r_o would need to be smaller in order for the model to reproduce both the QPO *and* the broad band noise. For this reason, we see our best fit values of r_o as upper limits rather than definitive measurements.

Still, it is extremely encouraging that this model can produce a good fit to PSD data whilst also having the potential to qualitatively reproduce many other properties seen in the data.

5.6 Appendix: Using propfluc

This model is publically available as the XSPEC local model, PROPFLUC. Here we include some tips for anyone wanting to use the model.

5.6.1 Data

We use `powspec` from XRONOS in order to create a power spectrum from the observed light curve. We set `norm=-2`, which means white noise will be subtracted and choose the minimum lightcurve time step, which is $dt_{obs} = 0.390625 \times 10^{-2} s$ for *RXTE* data. We set the number of time steps per interval to $2^{15} = 32768$, meaning that the duration of an interval is $2^{15} dt_{obs} = 128 s$. This means that a periodogram will be calculated for each interval with minimum frequency 1/128Hz and maximum (Nyquist) frequency $1/(2dt_{obs}) = 128$Hz. The number of intervals per frame should be set to maximum so that powspec averages over as many intervals as the length of the observation allows and we use a geometric re-binning with a constant factor of 1.045, resulting in 150 new bins. The resulting binned power spectrum can then be written to a data file in the form

$$f,\ df,\ P,\ dP.$$

XSPEC, however is expecting to recieve data in the form

$$E_{min},\ E_{max},\ F(E_{max} - E_{min}),\ dF(E_{max} - E_{min})$$

where E_{min} and E_{max} are the lower and upper bounds of each energy bin and F is the flux. It is therefore neccessary to create a data file with inputs

$$f_{min},\ f_{max},\ P(f_{max} - f_{min}),\ dP(f_{max} - f_{min}) \tag{5.13}$$

where f_{min} and f_{max} are the lower and upper bounds of each frequency bin. As f marks the centre of a bin and df is defined such that $f_{max} = f + df$ and $f_{min} = f - df$, this equation can be re-written as

$$f - df,\ f + df,\ 2Pdf,\ 2dPdf.$$

We then use `flx2xsp` in order to convert this into a `.pha` file and also generate a diagonal response function. The data can now be loaded into XSPEC and, eventhough

the axis on the plots are by default labeled as flux and energy, it is in fact reading in a power spectrum as a function of temporal frequency (i.e the command `ip euf` will show frequency multiplied by power plotted against frequency for both data and model).

5.6.2 Model

The model consists of a FORTRAN program, `propfluc.f`, and a data file `lmodel_pf.dat`. These two files are all that is needed to load the model using the local model functionality. The model has 18 parameters, summarised in table 5.2, plus XSPEC always includes a 19^{th} normalization parameter which must be set to (and fixed at) unity. The simulated light curve is generated using a time step of $dt = dt_{obs}/4 = 9.76562 \times 10^{-4}s$. It is important that this time step is short because the Nyquist frequency must be higher than the highest frequency at which significant variability is generated. The final power spectrum is calculated using 2^{17} steps per interval, meaning that each interval is $2^{17}dt = 2^{17}dt_{obs}/4 = 2^{15}dt_{obs} = 128s$. The simulated power spectrum is then binned into the same frequency bins used for the observed power spectrum. For this reason, it is vital that the periodograms are calculated on the same interval (i.e. 128s) for both model and data, the use of two different intervals could result in empty bins in the simulated power spectrum which doesn't help χ^2! In table 5.2 we see that it is possible for the user to decide on the length of simulated light curve (parameter 17). Since the interval length is fixed, this dictates how many intervals the power spectrum is averaged over. We recommend $nn = 22$ (32 intervals) for fitting but this does make the code very slow. Preliminary fitting is best done with $nn = 20$ (8 intervals) as this is faster but provides a good enough PSD estimate to work with. It should be noted that this setting slightly under predicts the power but it is a constant offset and so the best fit found using $nn = 20$ has a higher value for F_{var} than that found using $nn = 22$ but the other parameters are largely unaffected. The main advantage of using $nn = 22$

is that χ^2 gives a much more reliable estimate of goodness of fit.

The model is difficult to fit, partly because of the stochastic nature of the power spectrum and partly because of the complicated relationship between parameters. We recommend finding a good fit by eye first and fixing a few key parameters before fitting. We set XSPEC to calculate the gradient in χ^2 numerically rather than analytically and set the critical $\Delta\chi^2$ value to 0.1 rather than the default 0.01. Finally, the third column of table 5.2 shows all of our best fit model parameters for observation 1, with a $\equiv$ symbol indicating that the parameter is fixed.

	Parameter	Comments	Obs 1
1	`Sigma0`	Normalization of surface density.	5.43
2	`rbw`	Bending wave radius - dictates where $\Sigma(r)$ breaks.	4.60
3	`kappa`	Dictates sharpness of the break.	$\equiv 3.0$
4	`lambda`	Dictates $\Sigma(r)$ for $r < r_{bw}$.	$\equiv 0.9$
5	`zeta`	Dictates $\Sigma(r)$ for $r > r_{bw}$.	$\equiv 0.0$
6	`Fvar`	Intrinsic amount of variability generated per decade in f_{visc}.	0.32
7	`fbmin`	This is $f_{visc}(r_o)$. It is much easier to set this instead of r_o.	0.129
8	`ri`	Inner radius	$\equiv 3.3$
9	`sig_qpo`	QPO width (fundamental). Width of higher harmonics is tied to this.	0.0226
10	`sig_subh`	Width of the subharmonic. This can have a different Q value to the other harmonics.	0.0283
11	`n_qpo`	Normalization of fundamental.	0.244806
12	`n_h`	Normalization of second harmonic.	0.1706
13	`n_3h`	Normalization of third harmonic.	0.1018
14	`n_subh`	Normalization of sub-harmonic.	0.0967
15	`em_in`	Emissivity index (i.e. γ).	5.281
16	`dL`	The model gives the option to generate a Gaussian error on each point of the simulated lightcurve, thus creating white noise. To match a typical *RXTE* observation, this needs to be $dL \sim 0.8$, however we recommend setting this to zero and using white noise subtracted data.	$\equiv 0.0$

Table 5.2: Summary of model parameters.

	Parameter	Comments	Obs 1
17	`nn`	Sets the number of time steps in the simulated light curve (i.e. the light curve has a total duration of of $2^{nn}dt$). This must be an integer because the model uses a fast fourier transform algorithm (Press et al 1992). The PSD estimate of the model must be calculated on the same interval as the data (128s) and therefore the value of nn used dictates how many intervals are averaged over.	$\equiv 22.0$
18	`Ndec`	Sets the radial resolution. If this is particularly high, the code is very slow! $N_{dec} = 15$ should be sufficient. The total number of annuli used is sufficient. The total number of annuli used is calculated from this.	$\equiv 15.0$

Table 5.3: Table 5.2 continued.

Chapter 6

The effect of frame dragging on the iron K_α line in X-ray binaries

6.1 Introduction

Over the course of the previous chapters, I have presented evidence that the spectral and timing properties of XRBs can be self-consistently explained with a truncated disc / hot inner flow accretion geometry, with the entire hot inner flow precessing due to the relativistic effect of frame dragging. In our model, it is this precession which gives rise to the low frequency QPO in XRBs. This is not the first model to associate the QPO with Lense-Thirring precession. Stella & Vietri (1998) and Stella, Vietri & Morsink (1999) showed that the Lense-Thirring precession frequency of a test mass at the truncation radius is broadly consistent with the QPO frequency. Schnittman (2005) and Schnittman, Homan & Miller (2006) developed this into a fully relativistic description of a misaligned ring, showing that its direct emission and iron line signature should be modulated on the precession frequency, which could be somewhat higher than observed. However, the real problem with these models is that the energy spectrum of the QPO is dominated by the Comptonised emission (Sobolewska & Zycki 2006; Rodriguez et al 2004), requiring that the QPO mechanism predominantly modulates the hot flow rather than the disc (although the variability could be produced elsewhere before propagating into the flow; Wilkinson 2011). Since our model considers the entire

hot flow to globally precess, it naturally explains the QPO spectrum. Such global precession has been seen in recent numerical simulations (Fragile et al 2007, Fragile 2009). I show in chapter 2 of this thesis (based on Ingram, Done & Fragile 2009) that the predicted frequency range is completely consistent with the type-C QPO in BHBs and also in NSBs (chapter 3 based on Ingram & Done 2010).

There are other more subtle properties that are naturally explained by the precessing flow model. In chapter 4 (based on Ingram & Done 2011), I show that the correlation between QPO frequency and total flux observed on short time scales (Heil, Vaughan & Uttley 2011) is predicted by the model presented in this thesis. This is because the propagating fluctuations in mass accretion rate which give rise to the broad band noise (e.g. Lybarskii 1997; Arevalo & Uttley 2006) will affect the moment of inertia of the flow leading the precession frequency to fluctuate. The linear relation with flux then occurs because both the flux *and* the precession frequency depend on mass accretion rate. Although it is very encouraging that this property is predicted by the model, we still do not have unambiguous proof that the flow precesses - a QPO produced from any mode of the hot flow will also couple to fluctuations propagating through the hot flow, and should give an f_{QPO}-flux relation.

The interpretation of the QPO as vertical precession requires a truncated disc as otherwise the flow could not cross the equatorial plane. The issue of whether or not the disc truncates is still somewhat controversial. Nowak et al (2011) show that the broad iron line in a low/hard state of Cyg X-1 can be variously interpreted as implying a disc anywhere from $6-32R_g$ (for their Obs 4) depending whether the continuum is thermal Comptonisation, non-thermal Comptonisation, multiple Compton components or includes a jet contribution. Fabian et al (2012) show another deconvolution of a similarly shaped spectrum from Cyg X-1, where the spectrum below 10 keV is dominated by highly ionised, highly smeared reflection, with a very small inner radius of $\sim 1.3R_g$ and a very steep emissivity profile (a.k.a. the lightbending model). However, this

lightbending geometry seems to be inconsistent with the independent requirement on the un-truncated disc geometry that the source is beamed away from the disc in order to produce an intrinsically hard spectrum (Malzac, Beloborodov & Poutanen 2001).

Although the only models for rapid spectral variability currently in the literature involve inhomogeneous emission in an extended Comptonising region (Kotov, Churazov & Gilfanov 2001; Arevalo & Uttley 2006; this thesis) where the line profile is consistent with a truncated disc (Makishima et al 2008), the issue is clearly still very controversial. This chapter is adapted from Ingram & Done (2012b) in which we use the truncated disc geometry in order to propose a distinctive test of a *vertical precession* origin of the QPO. As a tilted flow precesses, the illumination pattern on the disc rotates. The resulting iron line is boosted and blue shifted at a time when the flow illuminates the approaching side of the disc, and red shifted when the flow illuminates the receding side of the disc. Since this periodic rocking of the iron line is a requirement of the Lense-Thirring QPO model, this also offers a potentially unambiguous test of disc truncation. Our geometry differs from the Schnittman, Homan & Miller (2006) model, where a precessing inner disc ring produces the iron line and continuum. Instead, we have a hot inner flow replacing the inner disc to produce the continuum, and precession of the entire hot flow produces a rotating illumination pattern which excites the iron line from the outer thin disc.

6.2 Model geometry

In this section, we outline the geometry used for our QPO model. We assume that the spin axis of the compact object is misaligned with that of the binary system as may be expected from supernova kicks (Fragos et al 2010). Due to frame dragging, the orbit of an accreting particle from the binary partner will precess around the spin axis of the compact object. The effect of frame dragging on an entire accretion flow depends on the dynamics of the flow. A thin accretion disc being fed by a binary partner out

of the spin plane of the compact object will form a Bardeen Petterson configuration (Bardeen & Petterson 1975) where the outer regions align with the binary partner and the inner regions align with the spin of the compact object, with a transition between the two regimes at r_{BP}. The value of r_{BP} is not well known, with analytical estimates ranging from $\sim 10-400\ R_g$ (see e.g. Bardeen & Petterson 1975; Papaloizou & Pringle 1983; Fragile, Mathews & Wilson 2001). In the thin disc regime, warps caused by the misaligned black hole propagate in a viscous manner. This means that the time scale on which a warp is communicated is much longer than the precession period and therefore a steady configuration forms. In contrast, warps in a large scale height accretion flow are communicated by bending waves (see e.g. Lubow, Ogilvie & Pringle 2002; Fragile et al 2007) which propagate on approximately the sound crossing timescale which is *shorter* than the precession period. For this reason, the hot flow can precess as a solid body with the precession period given by a surface density weighted average of the point particle precession period at each radius (Liu & Melia 2002), while a cool disc forms a stable warped configuration. This solid body precession of a hot flow has been seen explicitlly in recent numerical simulations (Fragile et al 2007) for the special case of a large scale height flow which we consider here.

The key aspect is that the flow angular momentum has to be misaligned with the black hole spin. Yet the outer thin disc will warp into alignment with the black hole at r_{BP}. Since this radius is poorly known, there are two possible scenarios. Firstly r_{BP} may be small enough for the outer thin disc to still be aligned with the binary partner at the truncation radius. In this case, the hot flow is misaligned with the black hole spin by the intrinsic misalignment of the binary system which will naturally lead to solid body precession of the entire flow. Secondly, if r_{BP} is large, the disc and hence hot flow are intrinsically aligned with the black hole spin. However, precession may be possible. The flow has a large scale height, so is sub-Keplerian. At the truncation radius it overlaps with the Keplerian disc, so this overlap layer is probably Kelvin-Helmholtz

unstable, producing turbulence. Clumps forming from random density fluctuations in regions high above the midplane could temporarily mis-align the flow leading to intermittent precession. This predicted intermittency has the advantage of naturally explaining the observed random jumps in QPO phase (Miller & Homan 2005; Lachowicz & Done 2010).

Here we assume the first geometry i.e. assume that r_{BP} is very small. However, the effect of rotating illumination on the iron line is qualitatively the same in the second geometry, differing only in the details. In the next section, we outline the geometry used. We work under the assumption that the central object is a black hole, but the geometry is valid for neutron stars also.

6.2.1 Disc

The geometry we consider for the two component accretion flow is illustrated in Figure 6.1. We assume that the disc has angular momentum vector set by the binary system, $\underline{\hat{J}}_{BS}$, and that this is misaligned with the spin axis of the black hole (the z-axis) by an angle β. The flow angular momentum vector, $\underline{\hat{J}}_{flow}$, precesses around the z-axis with phase given by the precession angle, γ. The plane of the disc is the plane orthogonal to $\underline{\hat{J}}_{BS}$, while the plane of the flow is orthogonal to $\underline{\hat{J}}_{flow}$. In this coordinate system, the binary partner will orbit in the 'disc' plane. The observer's position is described by an inclination angle, θ_i, and a viewer azimuth, ϕ_i, which can take the range of values $0 \leq \theta_i \leq \pi/2$ and $0 \leq \phi_i \leq 2\pi$. Here, θ_i is defined with respect to the binary (i.e. the disc) angular momentum vector and ϕ_i is defined with respect to the x-axis.

The flow then precesses around a circle centred on the black hole spin axis, from being aligned with the disc when $\gamma = 0$, to being misaligned by angle 2β with respect to the disc when $\gamma = \pi$. We can define a vector $\underline{\hat{r}}_d$ which points from the black hole to any point on the disc plane. If the top of the flow is its brightest part, the region of the disc most strongly illuminated by the flow for a given γ is where the

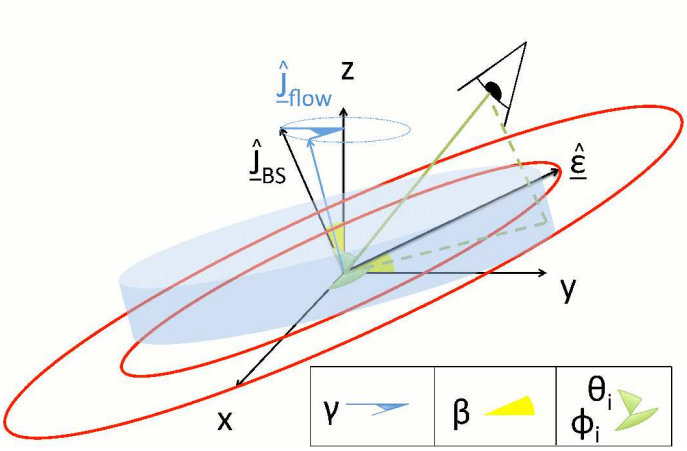

Figure 6.1: Schematic diagram illustrating the coordinate system we are considering. The black hole is at the origin and the black hole angular momentum vector is aligned with the z-axis. See text for details.

angle between $\hat{r}_d$ and $\hat{J}_{flow}$ is smallest. The smallest this angle can ever be is for $\hat{r}_d = \hat{\epsilon}$ when $\gamma = \pi$; i.e. this is the most that the flow angular momentum vector ever aligns with any azimuth of the disc plane. $\hat{\epsilon}$ therefore defines the azimuth of the disc which sees the maximum illumination from the flow. Material in the disc is spinning rapidly and, because precession is prograde, this orbital motion is anti-clockwise for our geometry. The viewer azimuth ϕ_i therefore specifies the direction with respect to the viewer in which disc material in the maximally illuminated region (i.e. on the $\hat{\epsilon}$ axis) is moving. For $\phi_i = 0$, the receding part of the disc is most strongly illuminated as the flow precesses. Instead, for $\phi_i = \pi/2$ the maximum illumination is on the patch directly in front of the black hole. For $\phi_i = \pi$ the maximum illumination is on the approaching side of the disc, while for $3\pi/2$ it it for the patch directly behind the black hole. We assume that the disc is razor thin and flat (i.e. no flaring). The mathematical definitions for the geometry we use are outlined in the appendix (section 6.7.1).

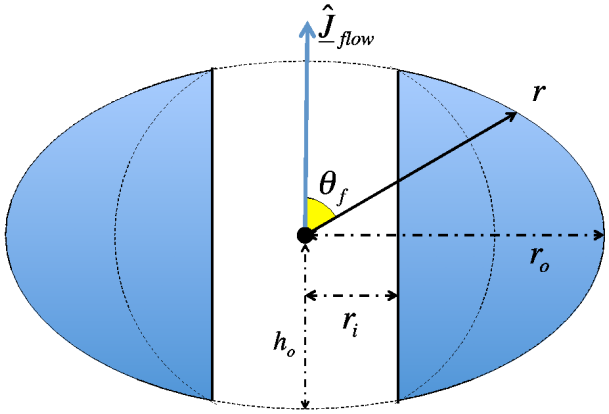

Figure 6.2: Schematic diagram illustrating the cross section of the flow. See text for details.

6.2.2 Flow

Unlike the disc, the flow has volume and scale height, so we must make some assumptions about its shape. We assume that it is a crushed sphere; i.e. viewed from above it is circular but it has an elliptical cross section as illustrated in Figure 6.2. The semi-major axis of the ellipse is r_o and the semi-minor axis is h_o. We choose to parametrise this by defining a scaleheight, h/r, such that $h_o = (h/r)r_o$. Figure 6.2 also shows that we set an inner radius, r_i, such that the core of the quasi-spherical flow is missing. This is to incorporate a flavour of the numerical simulations which show that shocks (at the bending wave radius) can truncate the inner region of the hot flow (Fragile et al 2007). Any point on the flow surface is then a distance r away from the black hole, where r is a function of the angle θ_f. We assume that each radius of the surface radiates the gravitational potential energy released at that radius (i.e. we use a surface rather than a volume emissivity). This gives a simple analytic model where the central parts of the flow (outside of r_i) are brighter than the outer parts, but that these bright regions are near the poles which gives a reasonable reflection fraction, $(\Omega/2\pi)$ while

also giving a reasonable precession frequency (set by r_i, r_o, M, the surface density profile which we assume to be constant, and a_*, where a_* is the dimensionless spin parameter: equation 1 in Ingram, Done & Fragile 2009). Note that, even though this is a simplified prescription, the most influential aspect of the flow geometry is where the brightest region lies. In nearly all imaginable geometries, this point lies at the pole of the flow (as it does for our geometry). Thus our mathematically convenient assumptions for flow geometry should provide us with results not materially different from a far more difficult calculation assuming a geometry identical to the Fragile et al (2007) simulation. More details of the flow geometry are presented in the appendix (section 6.7.1).

Fundamentally, the precession frequency modulates the continuum as the pole moves in and out of sight. The QPO maximum occurs when the pole faces the observer and the minimum when it faces away. Thus the region of the disc preferentially illuminated is in front of the black hole (from the point of view of the observer) at the QPO maximum and behind for a QPO minimum. Because precession is prograde, this means that the flow illuminates the approaching disc material during the rise to a QPO maximum (because the pole has to first move towards us in order to face us) and the receding material on the fall to a QPO minimum. Below we calculate the self-consistent illumination pattern for the disc as a function of QPO phase for our assumed geometry.

6.3 Implications of a precessing flow

6.3.1 Disc irradiation

Each flow surface element will radiate a luminosity dL over a semi-sphere (because the element radiates *away* from the black hole). A disc surface element with area dA_d will intercept some fraction of this luminosity. This fraction can be calculated

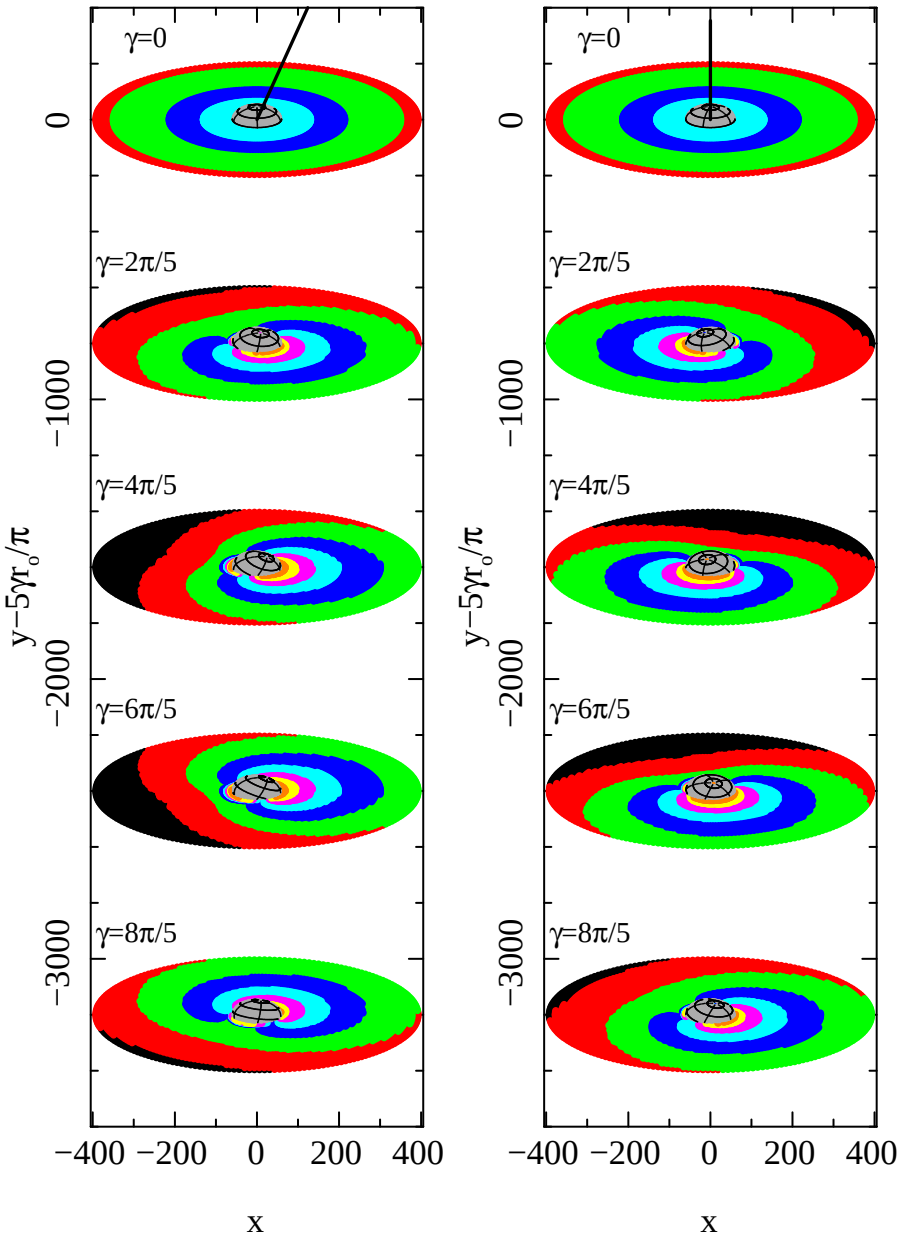

Figure 6.3: Disc irradiation by the flow as seen by a viewer with $\theta_i = 60^o$ and $\phi_i = 0^o$ (left) or $\phi_i = 90^o$ (right). The flow is shown in grey with black gridlines for clarity. The truncation radius is $r_o = 60$. The luminosity incident on the disc is grouped into 8 bins with black, red, green, blue, cyan, magenta, yellow and orange representing the dimmest to brightest patches on the disc. The solid black line in the top picture of each plot indicates the black hole spin axis. Flow precession causes the characteristic illumination pattern to rotate around the disc.

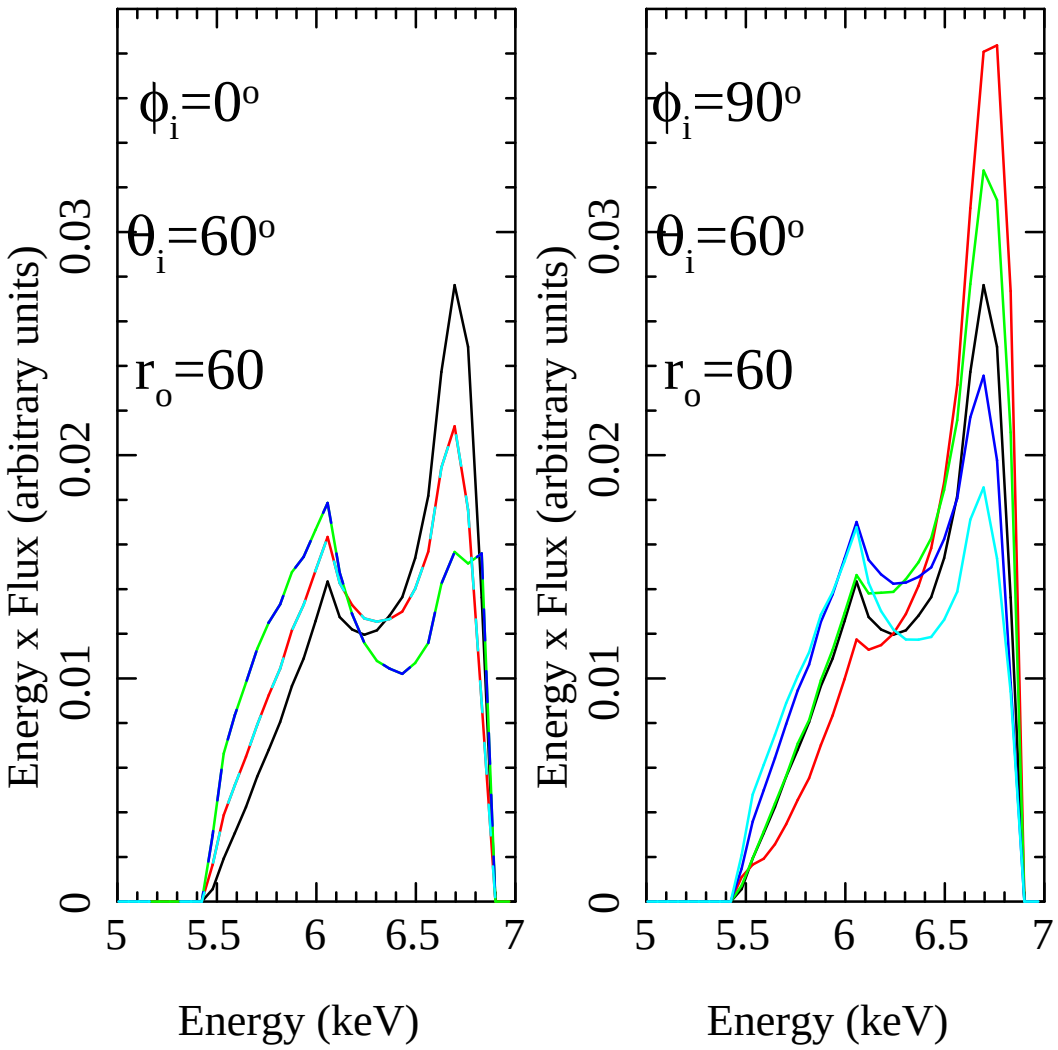

Figure 6.4: The iron line profile as seen by a viewer with $\theta_i = 60^o$ and $\phi_i = 0^o$ (left) or $\phi_i = 90^o$ (right). The rest frame iron line profile is assumed to be a $\delta-$function at 6.4 keV and the truncation radius is $r_o = 60$ as in Figure 6.3. Different colours represent different snapshots in time with black, red, green, blue and cyan representing the top to bottom snapshots pictured in Figure 6.3. The rotation of the illumination pattern causes the iron line profile to rock from red to blue shift.

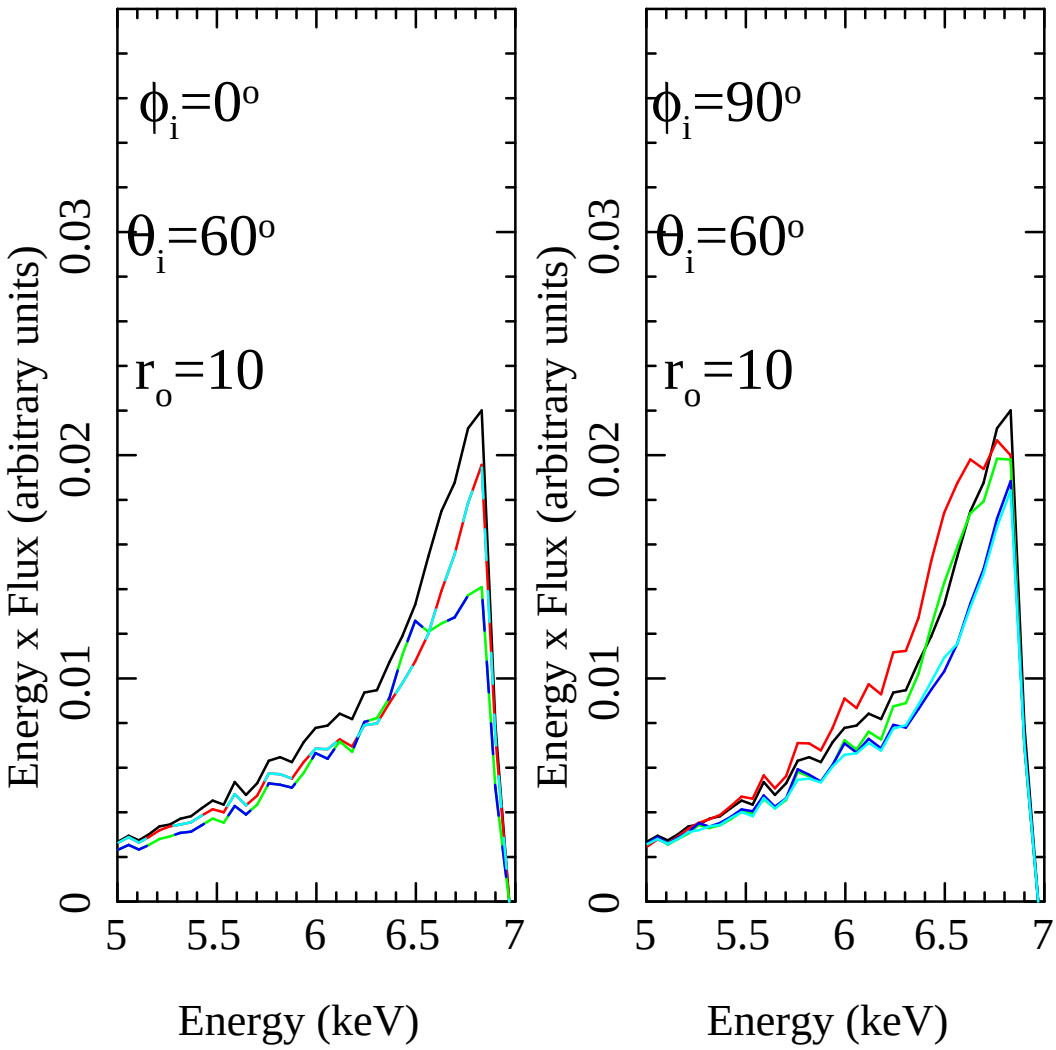

Figure 6.5: The iron line profile as seen by a viewer with $\theta_i = 60^o$ and $\phi_i = 0^o$ (left) or $\phi_i = 90^o$ (right). The rest frame iron line profile is still assumed to be a $\delta-$function at 6.4 keV but the truncation radius is now $r_o = 10$. The different colours represent the same snapshots in time as in Figure 6.4. We see the motion of the iron line is different here compared to Figure 6.4. Due to stronger Doppler (and relativistic) boosting in the inner disc, the red wing never dominates in the $E < 6.4$ keV region.

self-consistently from the projected area of the disc element. The disc element will not intercept any of the luminosity from the flow element if it makes an angle greater than $\pi/2$ with a vector which is orthogonal to the flow element and points away from the black hole (i.e. if it is not in the unit semi-sphere of the flow element). Also, as observers with $\theta_i \leq 90^o$, we only observe reflected photons which are intercepted by the *top* of the disc.

The total incident luminosity on the disc surface element is calculated by integrating over the surface of the entire flow. We do this calculation for every disc surface element over a full range of precession angles ($0 \leq \gamma < 2\pi$) in order to build a picture of disc irradiation as a function of precession angle (and therefore time). The details of this calculation are presented in the appendix (section 6.7.2). For simplicity, we use a Euclidean metric i.e. assume that light travels in straight lines. This should be a fairly reasonable approximation because we assume a fairly large value of r_i throughout the paper (following Dexter & Fragile 2011; Ingram & Done 2012a; Fragile 2009) and so lightbending is not very significant (e.g. Fabian et al 1989).

Throughout the paper, we will use the values $r_i = 7$, $\beta = 15^o$ and $h/r = 0.9$ (we discuss our reasoning for these fiducial values in section 6.3.3). Figure 6.3 shows the resulting illumination pattern with $r_o = 60$, with snapshots taken at five different values of precession angle γ for an inclination angle of $\theta_i = 60^o$. The left hand plot shows the pattern as seen by an observer at $\phi_i = 0^o$, whereas the right hand plot shows this for $\phi_i = 90^o$. The luminosity is grouped into bins of equal logarithmic size with black, red, green, blue, cyan, magenta, yellow and orange representing the dimmest to brightest bins respectively. The flow is shown in grey with black gridlines included for clarity. In the top picture of each plot, we also include a straight black line to illustrate the orientation of the black hole spin axis. This is misaligned with $\underline{\hat{J}}_{BS}$ by $\beta = 15^o$ but, as Figure 6.3 demonstrates, the apparent misalignment between these two vectors depends on the viewing position. We clearly see the flow precess, with the pole of the

flow moving in a circle around the black hole spin axis. As it does, the brightest part of the disc is always the region closest to the pole of the flow meaning that it *rotates* around the disc. Because of our asymmetric geometry, the flow starts off aligned with the disc, is misaligned by 2β when $\gamma = \pi$ before aligning again for $\gamma = 2\pi$. For $\phi_i = 0$, the maximum misalignment (giving the maximum illumination of the disc) is on the right hand (receding) side of the disc, while for $\phi_i = 90$ it is directly in front of the black hole, but in both cases the illumination pattern rotates. In the next section, we will discuss how this will affect the observed iron K_α line.

6.3.2 Effect on the iron K_α line profile

When the flow emission irradiates the disc, bound atoms in the disc will fluoresce to produce emission lines, the most prominent being the iron K_α line at ~ 6.4 keV (George & Fabian 1991; Matt, Perola & Piro 1991). However, this line is in the rest frame of the disc which is rotating rapidly meaning that a non face-on observer will see some regions of the disc moving towards them and others receding. Doppler shifts mean that emission from the approaching side is blue shifted while that on the receding side is red shifted. Also, length contraction along the line of motion beams the emission in that direction. Thus the blue shifted emission from the approaching side is also boosted in comparison to the red shifted emission, leading to a broadened and skewed iron line. An additional energy shift is provided by time dilation and also gravitational redshift which combine to broaden the line even further (Fabian et al 1989; 2000). Figure 6.3 clearly shows that, according to this model, the disc irradiation pattern *rotates* around the disc meaning that sometimes the brightest region of the disc is receding (e.g. the $\phi_i = 0^o$, $\gamma = 4\pi/5$ scenario in Figure 6.3), and sometimes the brightest region is approaching (e.g. the $\phi_i = 90^o$, $\gamma = 2\pi/5$ scenario in Figure 6.3). Therefore, as the flow precesses, the iron line will periodically rock between red and blue shift. In this example, the material in the disc and the irradiation pattern are both rotating

anti-clockwise. In general, they they could both be moving clockwise but the resulting pattern is the same (maximum blueshift, QPO maximum, maximum redshift, QPO minimum). Lense-Thirring precession is prograde, so the disc and flow will never be rotating in opposite directions, making this periodic shifting of the iron line profile a unique prediction of the model.

We use the illumination pattern on each surface element of the disc to set the amount of intrinsic iron line emission. We assume that this is a $\delta-$function at $E_0 =$ 6.4keV and then use the radius and azimuth of the surface element of the disc and the inclination of the observer to calculate the shifted line emission (see the appendix; section 6.7.4).

Figure 6.4 shows the iron line profile at five snapshots of time with black, red, green, blue and cyan lines corresponding to $\gamma = 0$, $2\pi/5$, $4\pi/5$, $6\pi/5$ and $8\pi/5$ respectively. We use the same parameters as for Figure 6.3. The details of this calculation are presented in the appendix (section 6.7.4). For simplicity, we do not include light bending but this should not be a large effect for the comparatively large radii we consider. The left hand plot is for $\phi_i = 0^o$, $r_o = 60$ (i.e. corresponding to the left plot of Figure 6.3) and we see that the iron line does indeed rock between red and blue shift as the illumination pattern rotates. Note that, for these parameters, the 2nd and 5th snapshots have an identical iron line profile, as do the 3rd and 4th snapshots. The right hand plot is for $\phi_i = 90^o$, $r_o = 60$ (i.e. corresponding to the right hand plot in Figure 6.3). We see that the periodic rocking has a different phase and the peak flux of the blue wing is much larger. This is because, for the $\phi_i = 0^o$ case, the approaching side of the disc is never the brightest part, whereas this does happen for the $\phi_i = 90^o$ case. This movement of the iron line is obviously a very distinctive model prediction and so could provide a detectable, unambiguous signature of a vertically tilted, prograde precessing flow i.e. a clean test of a Lense-Thirring origin of the QPO.

Figure 6.5 shows the same thing but now $r_o = 10$. We see that Doppler (and

relativistic) boosting of the blue wing is now such a large effect that the red wing never dominates even when the flow is preferentially illuminating the receding material. As such, the motion of the iron line is different. Crucially, although the exact shape of the iron line depends on the illumination pattern and thus the details of the assumed flow geometry, this dependence on truncation radius is really quite robust to changes in flow geometry. The differences between Figures 6.4 and 6.5 are driven primarily by the difference in disc angular velocity (i.e. the position of the truncation radius) and not the details of the modelling. Thus this effect could provide a robust diagnostic for the accretion flow geometry.

6.3.3 Modulation of the continuum

As the flow precesses, the luminosity seen by the observer will change periodically giving rise to a strong QPO (with the quasi-periodicity provided by frequency jitter among other processes; Ingram & Done 2012a; Heil, Vaughan & Uttley 2011; Lachowicz & Done 2010). This is because the total surface area of the flow viewed by the observer changes and, also, some regions of the flow are brighter than others meaning that a trough in the light curve would typically occur when the brightest regions of the flow (i.e. the poles) are hidden. The calculation for this process is similar to that performed in section 6.3.1. Each flow surface element emits a luminosity dL. The observer at θ_i, ϕ_i will see no luminosity from this surface element if they are not within the unit semi-sphere of the element, and we also remove luminosity from lines of sight which are obstructed by the disc. We can then integrate over every flow element to calculate the observed luminosity as a function of precession angle.

The blue lines in Figure 6.6 show the observed luminosity expressed as a fraction of the total luminosity, L_{tot}, plotted against precession angle. We use the fiducial parameters $r_i = 7$, $\beta = 15^o$ and $h/r = 0.9$ and consider the $r_o = 60$ example. The solid line is for $\phi_i = 0^o$ and the dashed line represents $\phi_i = 90^o$. As expected, the

observed luminosity varies with precession angle and the phase depends on ϕ_i. The fractional rms is 8.4% and 4.2% for $\phi_i = 0^o$ and $\phi_i = 90^o$ respectively. These values are lower than the observed QPO rms values of $\sim 10 - 15\%$. However, the predicted values would be higher if we were to consider that the flow is fed by disc photons, the flux of which incident on the flow will change periodically as the flow precesses. We ignore this process here because it will affect the direct and reflected emission equally and so will not contribute to the rocking iron line effect.

For the green line, we plot the total luminosity incident on the disc (which determines the iron line / reflected flux) as a function of precession angle. Because the disc is flat, this does not depend on ϕ_i. This effectively tracks the misalignment between flow and disc with the minimum reflection occurring when the flow is aligned ($\gamma = 0$) and the maximum when the flow is misaligned by 2β ($\gamma = \pi$). Hence the direct and intercepted emission are generally out of phase. The black lines show the reflection fraction (intercepted/direct) with the solid and dashed lines representing $\phi_i = 0$ and 90^o respectively. This corresponds to the solid angle of the disc, and the time averaged ratio for $\phi_i = 0^o$ is $\Omega/2\pi = 0.263$, and with $\Omega/2\pi = 0.238$ for the $\phi_i = 90^o$ case. These values are fairly representative of those observed for the low/hard state (e.g. Gierlinski et al 1999; Zycki, Done & Smith 1998; Gilfanov 2010).

Note that a large value of h/r gives a reasonable reflection fraction but under predicts the QPO rms. If we had considered, for example, an overlap region between disc and flow, disc flares or a small disc scale height, we could have achieved a reasonable reflection fraction *and* the correct QPO rms (for this we would also need to consider the variation in disc seed photons) for a far lower value of h/r. However, these effects are all very difficult to model and our assumed geometry should not significantly affect the final results. Thus we choose the fiducial parameter values to give reasonable results for a simplified geometry.

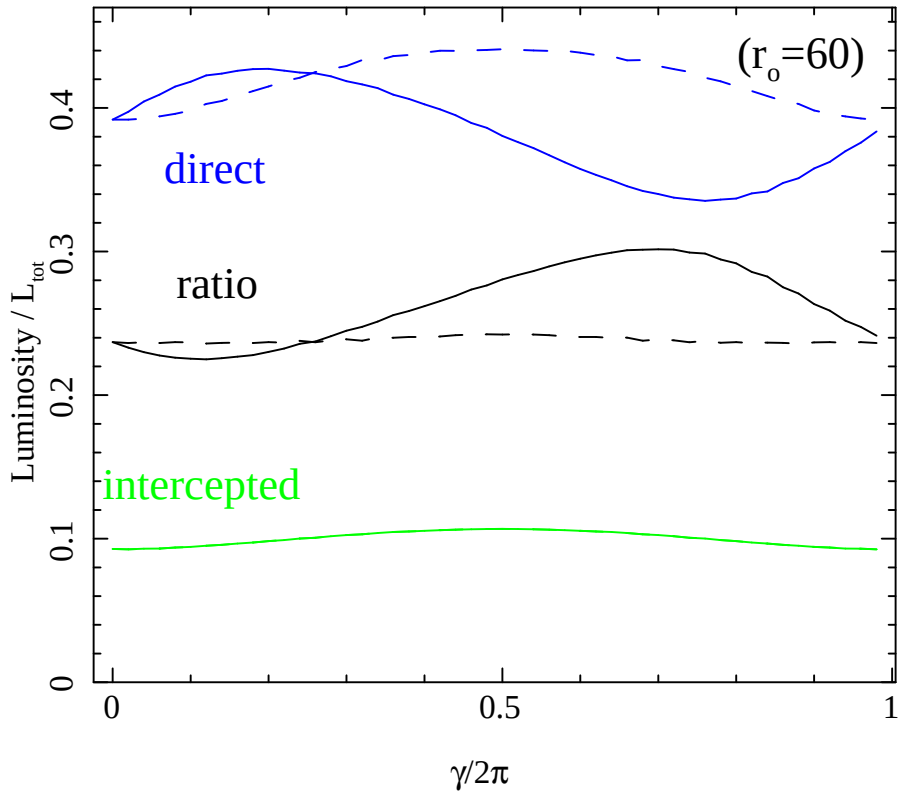

Figure 6.6: Emission as seen by a viewer at $\theta_i = 60^o$ and $\phi_i = 0^o$ (solid lines) or $\phi_i = 90^o$ (dashed lines). The blue line represents emission directly observed from the flow. We see that precession of the flow introduces a strong periodicity. The green line represents the total luminosity intercepted by the disc. This also has a periodicity because the misalignment between disc and flow changes as the precession angle, γ, evolves. It does not, however, depend on the position of the observer. The black line is the ratio between direct and reflected (intercepted) light, $(\Omega/2\pi)$.

6.4 Spectral modelling

We now use a full reflected spectrum rather than just a line, and recalculate the effect of the rotating disc illumination pattern and varying effective area of the flow for this more realistic scenario. We consider the same two values of truncation radius as those considered previously, $r_o = 60$ and $r_o = 10$. These values correspond to precession frequencies of $f_{QPO}(r_o = 60) = 0.145$ Hz and $f_{QPO}(r_o = 10) = 5.36$ Hz for the fiducial parameters, a spin of $a_* = 0.5$ and a mass of $M = 10M_\odot$ (i.e. 2.9 and 107.1 $a_*(M_\odot/M)$ Hz). They also correspond to different spectral states, with $r_o = 60$ giving rise to a low/hard state (LHS) spectrum and $r_o = 10$ leading to a soft intermediate state (SIMS) spectrum. The QPO in the LHS spectrum will be of type-C whereas it will be of type-B for the SIMS spectrum.

6.4.1 Method

For both the LHS and SIMS spectra, we include quasi-thermal disc emission, Comptonised flow emission and a reflection spectrum. We use XSPECv12 (Arnaud 1996) throughout. We describe the disc with DISKBB (Mitsuda et al 1984), and for simplicity we assume that this spectrum is constant. This is not strictly true. Figure 6.3 shows that the inner disc is periodically obstructed by the flow, giving a small periodicity in the hottest part of the disc emission. Also, the non-reflected photons which illuminate the disc will thermalise and add to the intrinsic disc emission, and this additional thermal emission will vary in intensity, being stronger when the flow is at its maximum misalignment angle to the disc, and weakest when the flow is aligned with the disc. This additional thermal emission is also periodically redshifted/blueshifted in the same way as the line. However, these effects should be small as they are diluted by the much larger constant flux from the disc. We will investigate this in a future paper, as evidence for this may have been observed (Wilkinson 2011). However, here we are interested in the iron line region and so ignore this potential contribution to the QPO

in the disc spectrum.

For the flow we assume that every element emits the same spectrum, meaning that the periodicity is in the normalisation of the flow spectrum. We describe the spectrum by the Comptonisation model NTHCOMP (Zdziarski, Johnson & Magdziarz 1996; Zycki, Done & Smith 1999) which produces a power law spectrum with high and low energy cut-offs governed by the electron temperature and disc photon temperature (kT_{bb} tied to the disc temperature) respectively. We fix the normalisation of this by the angle averaged flux from the flow (L_{tot}), to set the flux from each surface element of the flow. We then use the method described in section 6.3.3 to determine the modulation of the observed continuum, to calculate the factor by which to multiply the normalisation of NTHCOMP as a function of phase angle.

We use the method described in section 6.3.2 to calculate the illuminating flux from the flow at each surface element in the disc, and use this to set the normalisation of the illuminating NTHCOMP model. We describe the shape of the resulting reflected emission by RFXCONV (Ross & Fabian 2005; Done & Gierlinski 2006; Magdziarz & Zdziarski 1995; Kolehmainen, Done & Diaz Trigo 2011). This is similar in form to the IREFLECT model in XSPEC but replaces the very approximate ionisation balance incorporated in this model with the much better Ross & Fabian (2005) calculations. This outputs a partially ionised (parametrised by $\log_{10}\xi$) reflection spectrum, including the self consistent emission lines, for a general illuminating spectrum. We fix the inclination angle of the reflector at θ_i and abundances at solar. We calculate the reflected emission from this illuminating flux assuming $\Omega/2\pi = 1$. This is an underestimate as RFXCONV assumes that the disc is illuminated isotropically, whereas in our geometry the illumination is preferentially at grazing incidence. However, the amount of reflection is also set by the unknown details of the shape of the flow, so this approximation is good enough to demonstrate the general behaviour of the model.

The reflected emission from each surface element is shifted in energy depending on

		LHS	SIMS
PHABS	N_h (cm^{-2})	1×10^{22}	1×10^{22}
DISKBB	kT_{bb} (keV)	0.1	0.5
	norm	1×10^8	5×10^4
NTHCOMP	kT_{bb} (keV)	0.1	0.5
	kT_e (keV)	100	60
	Γ	1.7	2.4
	norm	5	4
RFXCONV	$\Omega/2\pi$	1	1
	$\log_{10}\xi$	2.4	3
	norm	5	4
QPO	r_o (R_g)	60	10
modulation	β (degrees)	15	15
&	r_i (R_g)	7	7
smearing	h/r	0.9	0.9

Table 6.1: Summary of the parameters used for both the LHS and SIMS spectral models.

the radius and azimuth (see the appendix; section 6.7.4). We sum the reflected emission from all the disc elements to derive the total reflected emission for each phase. This gives the correct relative normalisation of the continuum and reflected flux, and how this changes as a function of precession phase angle γ for a given set of model (r_o, r_i, β, h/r, θ_i, ϕ_i) and spectral (kT_{bb}, Γ, $\log\xi$, kT_e) parameters.

6.4.2 Phase resolved spectra

The parameters used for each state are shown in Table 6.1. We assume that kT_{bb}, Γ and disc ionisation increase as the rise to outburst continues whereas kT_e decreases,

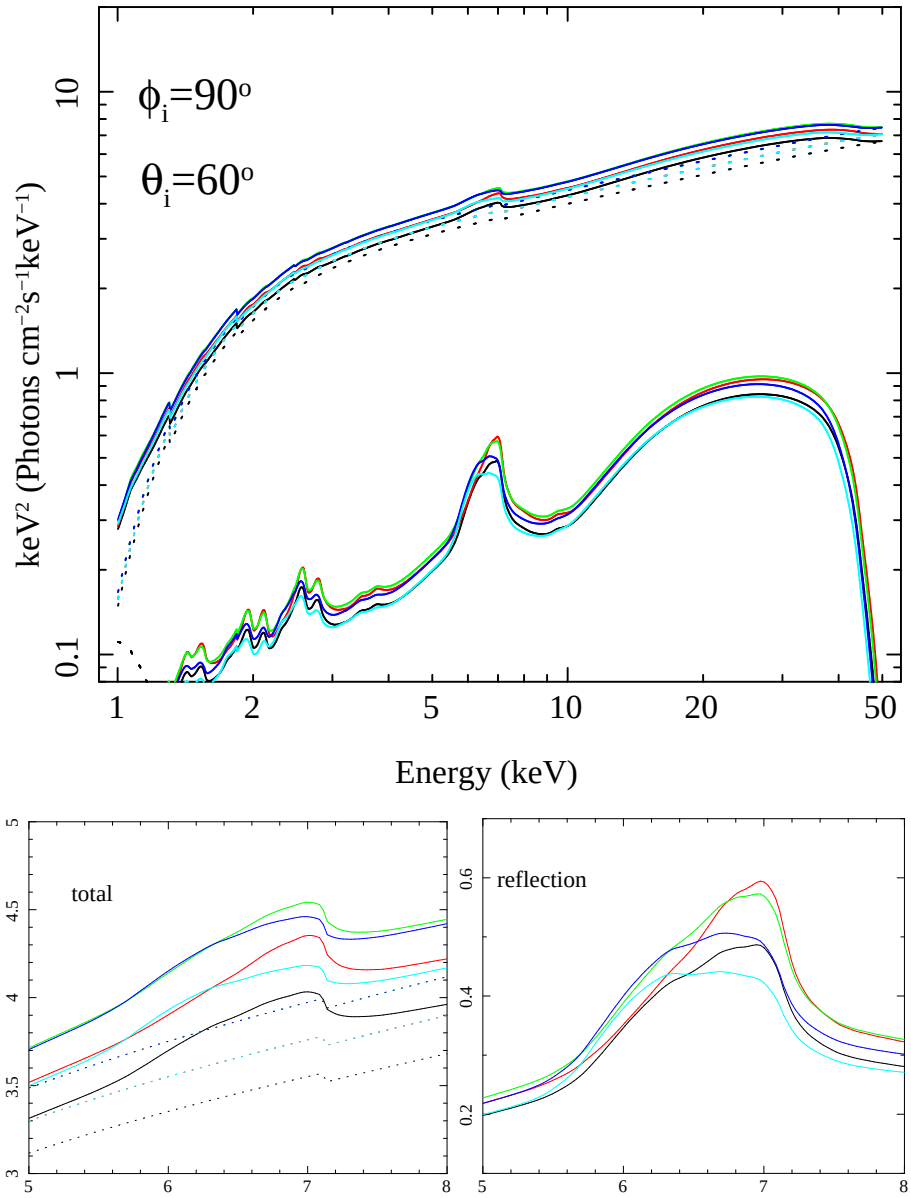

Figure 6.7: LHS spectrum for five snapshots in time calculated using the model described in the text, using the parameters listed in Table 6.1. We use the same convention as for Figures 6.4 and 6.5 with black, red, green, blue and cyan representing the first to last snapshots. The top plot is a broadband spectrum with all of the components. The disc and Comptonisation components are both represented by dotted lines and the total spectrum as well as the reflection component are represented by solid lines. The bottom right plot zooms in on the intrinsic iron line and the bottom left plot zooms in on the iron line region of the total spectrum. We see that the motion of the iron line is still present but dilution from the continuum makes the effect much more subtle in the total spectrum.

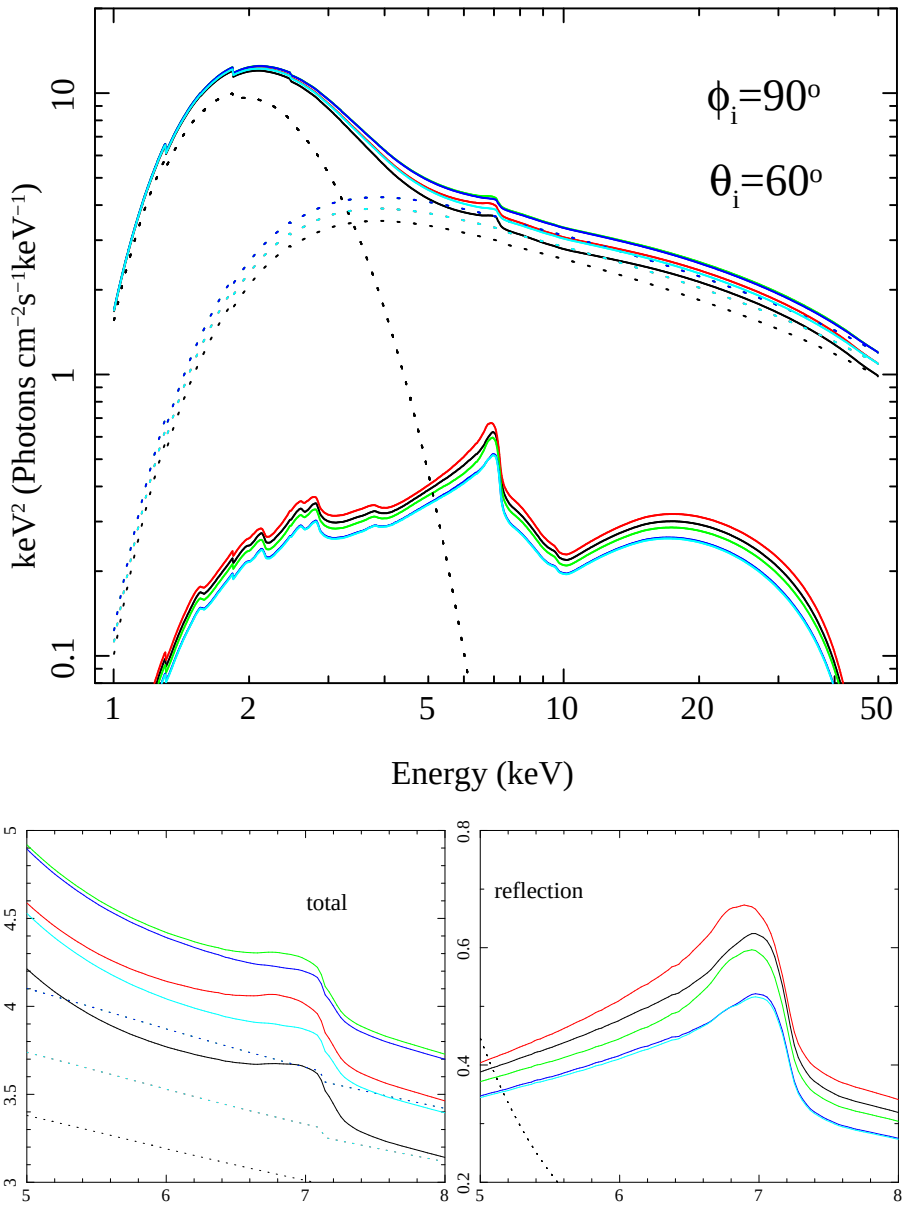

Figure 6.8: SIMS spectrum for five snapshots in time calculated using the model described in the text, using the parameters listed in Table 6.1. We use the same conventions as for Figure 6.7. We see that, as for the $\delta-$function calculation, the movement of the iron line is characteristically different for the SIMS compared with the LHS.

as is commonly observed. The resultant time averaged LHS ($r_o = 60$) spectrum has a $2 - 10$ keV flux of ~ 0.3 Crab and $\Omega/2\pi = 0.24$ (or iron line equivalent with of 150 eV when fit by a diskline profile rather than a full reflected spectrum). For the SIMS ($r_o = 10$) spectrum, the flux is ~ 0.66 Crab and the reflection has $\Omega/2\pi = 0.42$ (iron line equivalent width of $\sim$ 240 eV) with a much steeper continuum. These values are typical of those observed in the relevant states for fairly bright BHBs (e.g. GRS1915+104 in its QPO state: Ueda et al 2010, and the intermediate state of GX339-4; Tamura et al 2012), justifying our choice of parameters.

Figure 6.7 shows the LHS spectrum as viewed from a position with $\phi_i = 90^o$ and $\theta_i = 60^o$ at five different snapshots in time. We use the same convention as for Figures 6.4 and 6.5 with black, red, green, blue and cyan representing $\gamma = 0$, $2\pi/5$, $4\pi/5$, $6\pi/5$ and $8\pi/5$ respectively. The top plot shows the total spectrum (upper solid lines) and its components, the constant disc (black dotted line just seen in the lower left hand corner of the plot), variable flow (dotted continuum lines just underneath the total spectra - the symmetry means that the red dotted line is the same as the cyan, while the green is the same as the blue) and reflected spectra (lower solid lines). We clearly see the flow continuum oscillate while the reflection spectrum rocks between red and blue shift, as well as changing in normalisation. The reflection spectrum is in phase with the continuum in this example because $\phi_i = 90^o$ (see Figure 6.6) but, in general, there is a phase difference between the two components. The lower left plot zooms in on the iron line region in the total spectrum, while the lower right plot shows the changes in the reflected emission. We see that the reflected spectrum displays similar behaviour to the corresponding $\delta-$function (right hand plot of Figure 6.4). The rocking movement in the underlying reflection spectrum is still visible in the total spectrum, though somewhat diluted by the changing continuum level.

Figure 6.8 shows the same thing but for the SIMS. As for the $\delta-$function iron line profile in section 6.3.2, we see that the major effect is now the strength and position of

the blue wing rather than a rocking motion from blue to red due to the much stronger Doppler boosting in the inner disc. Nonetheless, there is still a clear periodic shift in the line shape with QPO phase, although the pronounced rocking of the iron line peak energy predicted for the LHS provides more of a 'smoking gun' for the Lense-Thirring model.

6.5 Observational predictions

In this section, we consider how this effect may be best observed. One potential method is to look at phase lags between different energy bands. We could define a red wing energy band (say $5.4 - 6.4$keV) and a blue wing energy band (say $6.4 - 7.4$keV) and look for a phase lag between the two. However, Figures 6.7 and 6.8 show that, due to dilution from the periodically varying continuum, the energy shifting of the iron line is very subtle in the total spectrum. This means that the phase lag between red and blue wings is very small ($2 - 6 \times 10^{-2}\pi$) for our model and, consequently may be difficult to observe. Instead, we consider phase resolved spectroscopy.

6.5.1 Phase binning

The random phase jumps and varying period characteristic of QPO light curves make phase resolved spectroscopy difficult. Naively folding the light curve on the QPO period is not appropriate. It is, however, possible to isolate the maximum and minimum phase bins of the QPO by averaging over the brightest and faintest points in the light curve. Miller & Homan (2005) did this for two GRS 1915+105 light curves, both containing a strong type-C QPO. This allowed them to compare the spectra corresponding to the QPO peak and trough. This analysis can be taken a step further because a rise will always follow a trough and a fall will always follow a peak. This simple phase binning can therefore provide four phase bins as opposed to two. Crucially, our model

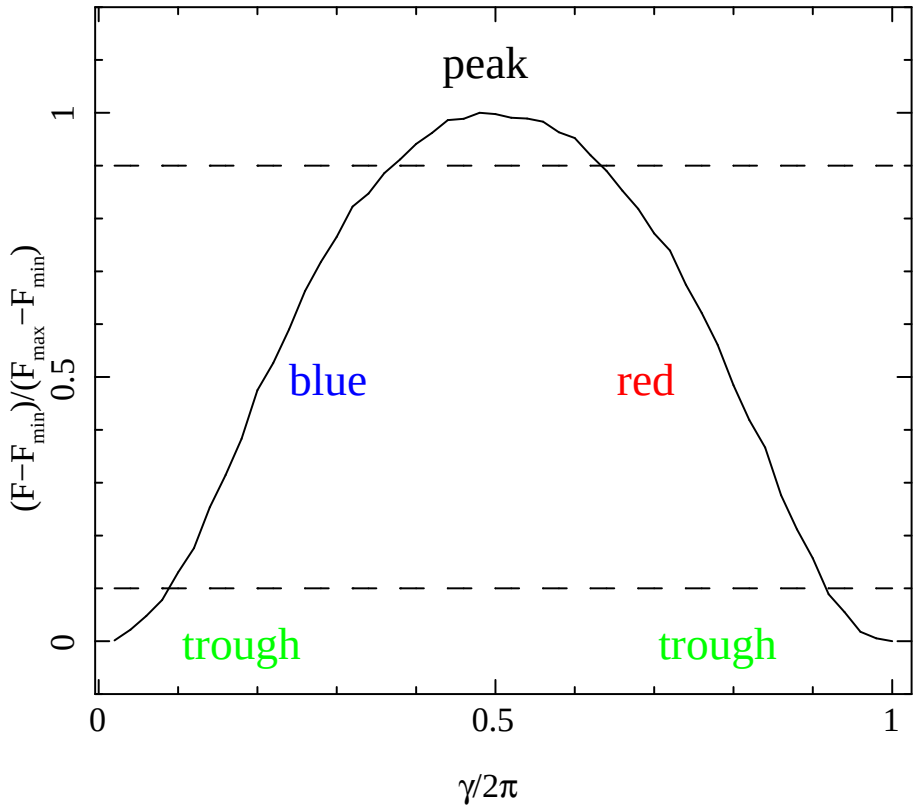

Figure 6.9: The 2-20 keV integrated flux of the LHS model with $\phi_i = 90^o$ and $\theta_i = 60^o$ plotted against precession angle. The dashed lines are flux thresholds. Intervals of the light curve above the top dashed line are considered to be the QPO peak, intervals below the bottom dashed line are considered to be the trough. The rising section which will always follow a trough will have the bluest iron line profile. The falling section which always follows the peak will have the reddest iron line profile.

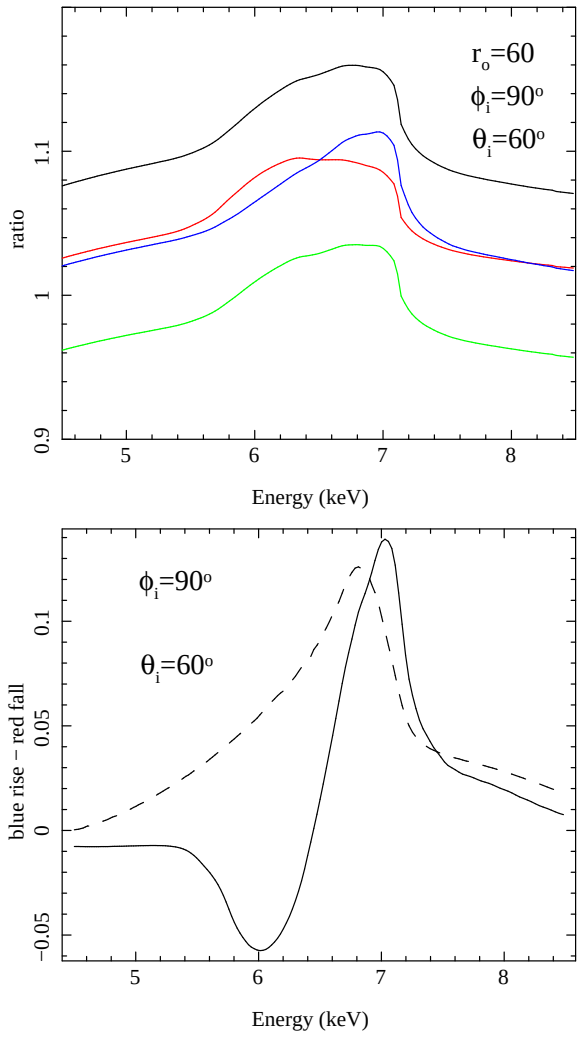

Figure 6.10: *Top:* Phase binned spectra calculated assuming $r_o = 60$, $\phi_i = 90^o$ and $\theta_i = 60^o$ plotted as a ratio to a power law with photon index $\Gamma = 1.6$. These four phase bins are for the QPO minimum (green), rise (blue), maximum (black) and fall (red). As expected, the rise has the most heavily blue shifted iron line and the fall has the most heavily red shifted iron line. *Bottom:* The red fall spectrum subtracted from the blue rise spectrum. The solid line is for the $r_o = 60$ example shown in the top plot and the dashed line is for $r_o = 10$. The shape of this difference spectrum is different for the two truncation radii. There is no negative section in the dashed line because strong Doppler boosting in the inner disc prevents the red wing from dominating.

predicts that the maximum red shift *always* follows the QPO peak and the maximum blue shift *always* follows the QPO trough. This is because the pole of the flow (which is the brightest region) faces us, then is moving away from us, then faces away from us, then is moving towards us (before facing us again). Therefore the flow illuminates the observer, then the receding (red shift) part of the disc, then the region hidden to the observer then the approaching (blue shift) part of the disc.

Figure 6.9 shows the 2-20keV light curve of our LHS model with $\phi_i = 90^o$ and $\theta_i = 60^o$. We define a peak as the brightest 10% of the light curve and a trough as the faintest 10%. These thresholds are shown as dashed lines. We can therefore isolate the trough, the blue rise, the peak and the red fall. This flux selection means that the majority of the counts lie in the more interesting rise and fall sections as opposed to the peak and trough (unlike the flux selection of Miller & Homan who were interested in the peak and trough spectra). Figure 6.10 (top) shows the result of averaging spectra belonging to each of these four phase bins. The green line is the trough spectrum, the blue line is the rise spectrum, the black line is the peak spectrum and the red line is the fall spectrum. All are plotted as a ratio to a power law with photon index $\Gamma = 1.6$. We use this photon index rather than $\Gamma = 1.7$ because the reflection hump makes the total spectrum harder than the underlying Comptonisation. As expected, the rise spectrum contains the most heavily blue shifted iron line and the fall spectrum contains the most heavily red shifted iron line. Because we tie the normalisation of the power law across the four spectra, we can see that the peak spectrum has the highest flux, the trough spectrum has the lowest and the rise and fall have comparable flux.

In the bottom plot of Figure 6.10, we plot the red fall spectrum subtracted from the blue rise spectrum. We use the absolute spectrum in units of energy $\times$ flux rather than a ratio to a power law. The solid line is for the example shown in the top plot where $r_o = 60$ and the dotted line is for $r_o = 10$. When $r_o = 60$, the red wing of the iron line dominates during the fall meaning that the solid line in the bottom plot dips below

zero for $5.4 \gtrsim E \gtrsim 6.4$. During the fall, the blue wing dominates which gives rise to the hump in the $6.4 \gtrsim E \gtrsim 7.4$ region. Due to relativistic boosting, the blue hump is larger than the red dip. When $r_o = 10$, the inner regions of the disc are moving much faster than the $r_o = 60$ case and therefore the Doppler boosting is a much more significant effect. So much so, in fact, that the red wing of the iron line never dominates over the blue wing, even during the fall. The dotted line in the bottom plot therefore contains no red dip but only a blue hump. The peak of the blue hump is lower for $r_o = 10$ than for $r_o = 60$ but the area under the line is greater. This is because the iron line is more heavily smeared in the $r_o = 10$ case, again due to faster orbital motion closer to the black hole.

For both the LHS and the SIMS, the difference in iron line profile between the QPO rise and the QPO fall is significant, offering the possibility of direct observation for a range of spectral states. Note that this association of the rise with the bluest profile and the fall with the redest profile is robust as long as we are confident that the top (pole) of the flow is brighter than the sides. Because type-B QPOs provide a far cleaner signal than type-C QPOs, which are always coincident with broad band variability, it will be easier to observe this effect for a source in the SIMS. However, the QPO phase dependence of the iron line is particularly distinctive for the LHS model. An enhanced blue wing on the QPO rise, as predicted for the SIMS model, may feasibly be produced by some other process. A dominant red wing on the QPO fall and an enhanced blue wing on the rise, as predicted for the LHS model, can only realistically be produced by precession and a large truncation radius. Moreover, an observation showing that the difference spectrum *changes* between states as we predict (i.e. the bottom plot of Figure 6.10) would surely provide excellent evidence, not only of the precession model, but also that the truncation radius moves between the LHS and the SIMS. In the next section, we assess the likelihood of achieving such observational confirmation.

6.5.2 Simulated observations

We test the feasibility of observation directly by simulating phase resolved spectra using the FTOOL FAKEIT. This adds Poisson noise to a model before subtracting a representative background and deconvolving around a given response matrix. We simulate LHS spectra for 50 phase bins evenly spaced in precession phase angle, γ. We assume 100s exposure for each phase bin. This corresponds to $50 \times 100\text{s} = 5\text{ks}$ of good time. We sort the simulated data into four phase bins just as we did with the model. For the simulated data, there is just one QPO cycle with a long exposure but, for observational data there will be many short exposure QPO cycles to average over. As long as any fluctuations in the accretion geometry over this time are varying around an average value, the two processes should be equivalent to a good approximation.

The top left plot in Figure 6.11 shows the result of simulating the response of the Rossi x-ray timing explorer (*RXTE*) proportional counter array (PCA; top layer, detector 2). We unfold the spectrum around a flat power law and, as for the model, take the ratio to a power law with photon index $\Gamma = 1.6$. We use the same model as that shown in the top plot of Figure 6.10; i.e. $r_o = 60$, $\phi_i = 90^o$, $\theta_i = 60^o$. Again, the green points are the trough, the blue points are the rise, the black points are the peak and the red points are the fall. Although a shift in line energy is visible between the rise and fall spectra, it is unlikely to be statistically significant due to a high noise level and low spectral resolution. The two observations of GRS 1915+105 studied by Miller & Homan (2005) were both seen with *RXTE* and, as such, the data were of a comparable quality to our simulation. They fit the QPO peak and trough spectra with a simple continuum model plus a Gaussian function for the iron line. When allowed to be free in the fits, the centroid energy of the Gaussian was higher for the trough spectrum than for the peak spectrum in both observations. However, they were also able to achieve statistically acceptable results by fixing the centroid energy to the value measured for the total spectrum. Therefore, although there is some evidence that the

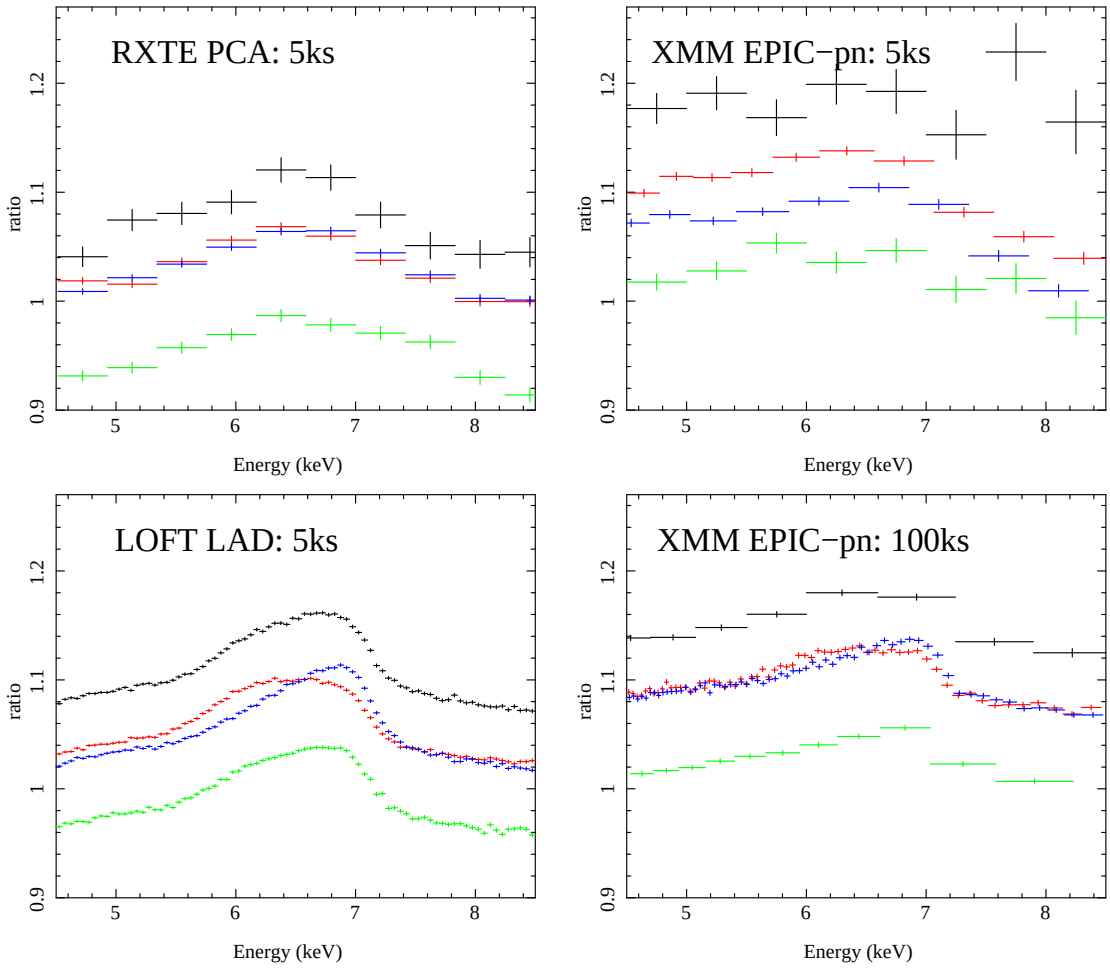

Figure 6.11: Simulated observations of the phase binned spectra shown in Figure 6.10 with $r_o = 60$, $\phi_i = 90^o$ and $\theta_i = 60^o$. These spectra are unfolded around a flat power law and plotted as the ratio to a power law with $\Gamma = 1.6$ and unity normalisation. Again the four phase bins are for the QPO minimum (green), rise (blue), maximum (black) and fall (red). Observed with the *RXTE* PCA or the *XMM Newton* EPIC-pn for 5ks, it is difficult to see by eye the difference in iron line peak energy between different phase bins. In contrast, a 100ks EPIC-pn exposure recovers the model well and the *LOFT* LAD does so with an exceptionally high precision for a 5ks exposure.

line energy shifts, it is by no means statistically significant. It should be possible to achieve a slightly more significant result with *RXTE* data by comparing the rise and fall phases rather than the peak and trough, but this is always marginal in practice due to the limited energy resolution of *RXTE* fast timing modes.

The top right plot of Figure 6.11 shows the same thing but for the *XMM Newton* European photon imaging pn camera (EPIC-pn). The Poisson noise level seems to be marginally worse compared with the simulated PCA data. Although the spectral resolution of the EPIC-pn is far better than that of the PCA, its effective area is less ($\sim 0.05\mathrm{m}^2$ compared with $\sim 0.12\mathrm{m}^2$) meaning that we require a very heavy re-binning to get a reasonable signal to noise. Therefore, it may prove difficult to observe this effect using either *RXTE* or *XMM Newton*. However, the number of counts in the rise and fall phase bins could be maximised by halving the peak and trough phase bins and adding them to either the rise or the fall (i.e. the first half of the peak phase becomes part of the rise and the second half becomes part of the fall).

A longer exposure is required to reduce the counting errors. In the bottom right hand panel of Figure 6.11, we plot the result of assuming a 100ks exposure for the EPIC-pn. Encouragingly, we see that the dominant red wing in the falling phase is indeed resolved. However, over such a long exposure time, parameters such as r_o may have systematically moved and so care must be taken to take this into consideration.

The size of the effect is also dependent on our assumptions. A smaller flow scale-height would increase the size of this effect because the flux emitted from the poles of the flow would be an even greater fraction of the flux emitted from the entire flow. Frame dragging could therefore have a larger effect on the iron line than we predict here making it easier to observe with current instruments than our simulations imply. However, it also must be noted that the continuum will be more complicated than we assume here with some QPO phase dependent spectral pivoting resulting from a variation in the flux of disc photons incident on the flow. This will make observation

harder.

The bottom left hand plot of Figure 6.11 shows the potential impact of the proposed mission *LOFT* (the large observatory for x-ray timing). We use the 'required' response of the large area detector (LAD), which is the principle instrument of the mission. Because the LAD has an exceptionally large effective area (10-12m^2), the results are far clearer than those provided by current missions. In fact, the noise level is so low with *LOFT*, it would be possible to constrain spectra for far more than four phase bins. We could also constrain these spectra for less than 5ks good time, meaning that we could conduct detailed studies of the evolution of the phase resolved spectra.

6.5.3 RMS spectum

Since we calculate 50 spectra for both the LHS and SIMS models, it is simple to calculate the rms spectrum of the QPO. This is simply the standard deviation of each energy channel in absolute units (i.e. not divided through by the average). Figure 6.12 shows this for the LHS model (top) and the SIMS model (bottom) with the mean spectrum plotted in black and the QPO spectrum plotted in red. Since the QPO spectrum is fairly sensitive to model assumptions, it provides a good way to constrain model parameters against observation. For the models we use here, the misalignment angle β is large and thus we see reflection features in the LHS QPO spectrum as the amount of reflection changes with QPO phase.

By contrast, in the SIMS, the extent of the flow is so small ($r_i = 7$ and $r_o = 10$) that even this large misalignment angle does not give rise to significant variability in the total reflection fraction. Previous rms spectral analyses of the QPO have not looked at this in detail (e.g. Sobolewska & Zycki 2006). We plan to address this issue in a future work (Axelsson et al in preparation).

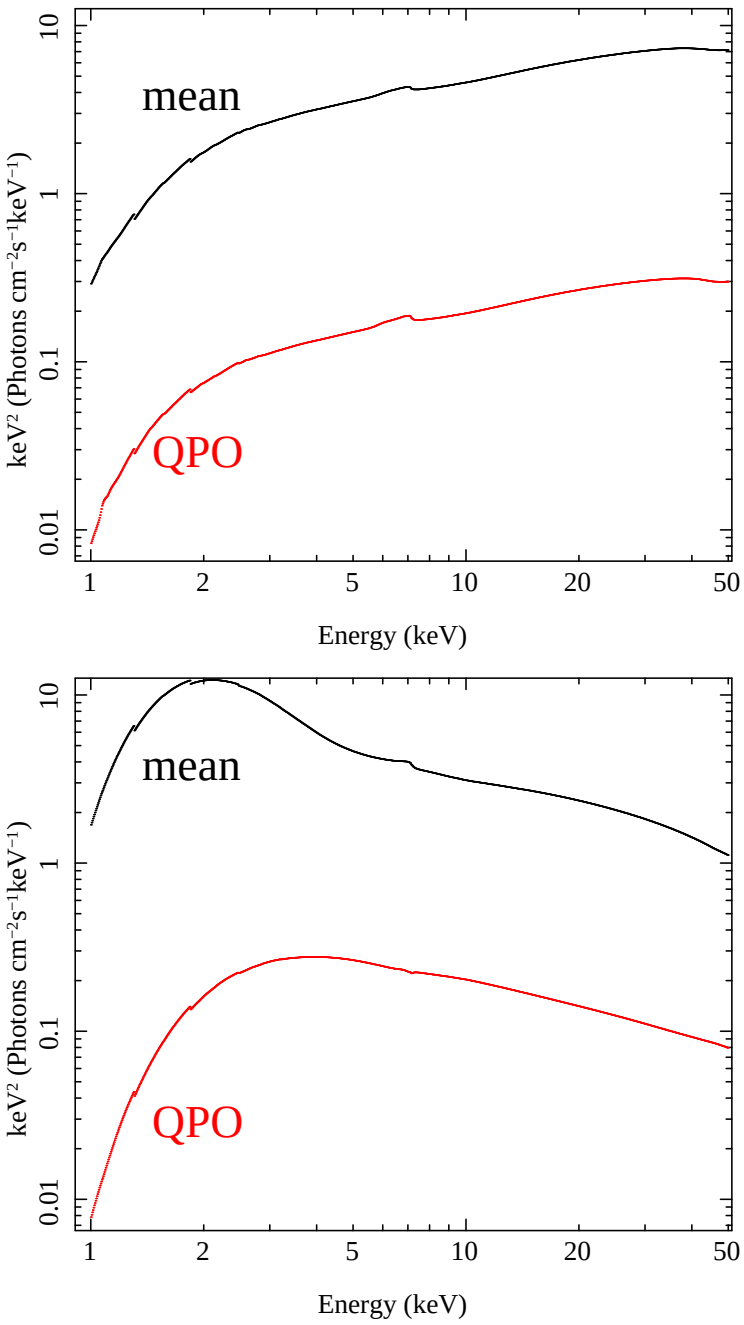

Figure 6.12: Mean and QPO spectra for the LHS (top) and SIMS (bottom) models. The QPO spectum is calculated by measuring the standard deviation of each energy channel around the mean value across 50 values of precession angle.

6.6 Conclusions

The truncated disc / precessing inner flow model for the spectral timing properties of XRBs predicts a QPO phase dependence of the iron line profile. This results from the inner flow preferentially illuminating different regions of the disc as it precesses. When the brightest region of the disc is moving towards us, the iron line will be blue shifted and boosted. When the brightest region is receding, the iron line will be red shifted. As the illumination pattern rotates around the disc, the iron line rocks between blue and red shift. This process always happens in a particular order with the most heavily blue shifted iron line profile following the QPO trough and the most heavily red shifted iron line profile following the QPO peak. It is possible to isolate the peaks and troughs in a light curve using a simple flux selection. The rising phase, which follows the trough, is predicted to have the bluest iron line and the falling phase, which follows the peak, is predicted to have the reddest iron line.

We predict this QPO phase dependence of the iron line profile to be present for a large range of spectral states (and therefore truncation radii). This means that it may be best to search for the effect in spectra containing type-B QPOs which have very little broad band variability associated with them and therefore provide a much cleaner signal than type-C QPOs. However, the nature of the iron line phase dependence changes with truncation radius. When it is large, the red wing can dominate over the blue wing during the fall from QPO peak to trough. When it is small, Doppler boosting from the rapidly moving inner regions of the disc means that the red wing can never dominate over the blue wing. The characteristic shape of the difference spectrum between rise and fall should therefore change as the spectrum evolves from the LHS to the SIMS. The dominant red wing of the QPO fall spectrum in the LHS (the 'red dip' in the difference spectrum) is the most unique model prediction but if we wish to observe this, we must disentangle the underlying QPO signal from the broad band noise. This will be the subject of a future paper. An observation of the effect in both states, along

with confirmation that the difference spectrum *changes* with state, would constitute excellent evidence, not only of the precession model, but also that the truncation radius moves between the LHS and the SIMS.

Quasi-periodic shifting of the iron line peak energy is a unique prediction of the Lense-Thirring precession model for the low frequency QPO in XRBs. We have shown that it may be possible to observe such an effect with current missions, but that *LOFT* will be able to measure this with precision, enabling us to place accurate constraints on the accretion geometry.

6.7 Appendix

6.7.1 Geometry

In order to perform our calculations, we must define some vectors using the coordinate system outlined in Figure 6.1. We represent the x, y and z axes with the standard $\hat{\underline{i}}$, $\hat{\underline{j}}$ and $\hat{\underline{k}}$ unit basis vectors. It then follows from Figure 6.1 that

$$\begin{aligned} \hat{\underline{J}}_{BS} &= -\sin\beta\ \hat{\underline{j}} + \cos\beta\ \hat{\underline{k}} \\ \hat{\underline{\epsilon}} &= \cos\beta\ \hat{\underline{j}} + \sin\beta\ \hat{\underline{k}}. \end{aligned} \tag{6.1}$$

The three vectors $\hat{\underline{i}}$, $\hat{\underline{\epsilon}}$ and $\hat{\underline{J}}_{BS}$ therefore form a right handed Cartesian coordinate system: the disc basis vectors. We can define a vector, $r_d\ \hat{\underline{r}}_d$, which points from the origin (the black hole) to any point on the disc where

$$\hat{\underline{r}}_d = \cos\phi_d\ \hat{\underline{i}} + \sin\phi_d\ \hat{\underline{\epsilon}}. \tag{6.2}$$

Note, because the disc is razor thin, there is no $\hat{\underline{J}}_{BS}$ component (i.e. $\hat{\underline{J}}_{BS}.\hat{\underline{r}}_d = 0$) and ϕ_d is simply the angle between $\hat{\underline{r}}_d$ and the x-axis. We also define a vector pointing from the origin to the observer using the disc basis vectors

$$\hat{\underline{S}} = \sin\theta_i\cos\phi_i\ \hat{\underline{i}} + \sin\theta_i\sin\phi_i\ \hat{\underline{\epsilon}} + \cos\theta_i\ \hat{\underline{J}}_{BS}. \tag{6.3}$$

In order to describe points on the surface of the flow, we must define flow basis vectors. The 'z-axis' of this right handed coordinate system is $\underline{\hat{J}}_{flow}$ which precesses around $\underline{\hat{k}}$ as illustrated in Figure 6.1. The other two basis vectors, $\underline{\hat{x}}_f$ and $\underline{\hat{y}}_f$, must therefore also precess with the flow. We use

$$\begin{aligned} \underline{\hat{x}}_f &= \cos\gamma\ \underline{\hat{i}} + \sin\gamma\ \underline{\hat{j}} \\ \underline{\hat{y}}_f &= -\cos\beta\sin\gamma\ \underline{\hat{i}} + \cos\beta\cos\gamma\ \underline{\hat{j}} + \sin\beta\ \underline{\hat{k}} \\ \underline{\hat{J}}_{flow} &= \sin\beta\sin\gamma\ \underline{\hat{i}} - \sin\beta\cos\gamma\ \underline{\hat{j}} + \cos\beta\ \underline{\hat{k}}, \end{aligned} \tag{6.4}$$

such that $\underline{\hat{x}}_f = \underline{\hat{i}}$ when $\gamma = 0$ but, as the precession angle unwinds, the axes move. We can then specify a point in the flow with the vector $r_f\ \underline{\hat{r}}_f$ where

$$\underline{\hat{r}}_f = \sin\theta_f\cos\phi_f\ \underline{\hat{x}}_f + \sin\theta_f\sin\phi_f\ \underline{\hat{y}}_f + \cos\theta_f\ \underline{\hat{J}}_{flow}. \tag{6.5}$$

Here, θ_f is the angle between $\underline{\hat{r}}_f$ and $\underline{\hat{J}}_{flow}$ and ϕ_f is the angle between $\underline{\hat{r}}_f(\theta_f = \pi/2)$ and $\underline{\hat{i}}$.

Because our flow is elliptical with semi-minor axis in the $\underline{\hat{J}}_{flow}$ direction and semi-major axis in the $\underline{\hat{a}} = \cos\phi_f\ \underline{\hat{x}}_f + \sin\phi_f\ \underline{\hat{y}}_f$ direction, the distance from the origin to any point on the surface is

$$r_f(\theta_f) = \frac{r_o h_o}{\sqrt{(h_o\sin\theta_f)^2 + (r_o\cos\theta_f)^2}}. \tag{6.6}$$

Because r_f is uniquely determined by θ_f, we can define $dr = |r(\theta_f) - r(\theta_f + d\theta_f)|$.

We need to be able to write down the unit vector normal to the flow surface. We can do this using a few identities. Imagine a triangle drawn between the two focuses of the ellipse, F_1 and F_2, and any point on the circumference of the ellipse, P. We know that the distance from the origin to either focus is $f = \sqrt{r_o^2 - h_o^2}$ and also that the three sides of the triangle add up to $2r_o + 2f$. We can define the angle between the line from P to F_1 ($P\ F_1$) and the line from P to F_2 ($P\ F_2$) as ψ. We know that the surface area unit vector, $\underline{\hat{A}}$, goes directly between these two lines such that the angle

between $-\underline{\hat{A}}$ and each line is $\psi/2$. We can say that $\underline{\hat{A}}$ points from some point x_o $\underline{\hat{a}}$ to the point on the flow surface, P, in such a way that this condition is satisfied. Say that d is the distance from P to F_2 and Ω is the angle between the lines F_2 F_1 and F_2 P. We can use the cosine rule a few times to show that $d = \sqrt{f^2 + r_f^2 - 2fr_f \sin\theta_f}$ and $\cos\Omega = (f^2 - r_o^2 + r_o d)/(f\ d)$. It is then possible to show that

$$\underline{\hat{A}} = \frac{r_f\ \underline{\hat{r}}_f - x_o\ \underline{\hat{a}}}{\sqrt{x_o^2 + r_f^2 - 2x_o r_f \sin\theta_f}} \tag{6.7}$$

where

$$\cos\psi = \frac{2r_o^2 + d^2 - 2r_o d - 2f^2}{d(2r_o - d)} \tag{6.8}$$

and

$$x_o = f - \frac{d\sin(\psi/2)}{\sin(\pi - \psi/2 - \Omega)}. \tag{6.9}$$

We will also need to define a vector which points from a given point on the flow to a given point on this disc. This can be written as

$$\zeta\ \underline{\hat{\zeta}} = -r_f\ \underline{\hat{r}}_f + r_d\ \underline{\hat{r}}_d. \tag{6.10}$$

From this, it is simple to show that the distance between the two points is

$$\zeta^2 = r_f^2 + r_d^2 - r_f r_d\ \underline{\hat{r}}_f.\underline{\hat{r}}_d. \tag{6.11}$$

All of these vectors will become very useful for the following sections.

6.7.2 Disc irradiation calculations

So, we need to calculate what luminosity a disc element with surface area $dA_d = r_d d\phi_d dr_d$ will intercept from a flow surface element emitting a luminosity dL over a semi-sphere (because it only emits *away* from the rest of the flow). We can then integrate over all flow elements to work out the total flow luminosity that the disc element intercepts. For the disc patch to see anything at all from a given flow element,

it must pass two tests. First, does it lie in the unit semi-sphere of the flow element; i.e. is $\hat{\underline{A}}.\hat{\underline{\zeta}} > 0$. Also, because we are viewing the top of the system ($\theta_i \leq 90^o$), we only see luminosity which has reflected off the *top* of the disc. Therefore, we only count luminosity incident on the top of the disc in our integral. This means we require $\hat{\underline{\zeta}}.\hat{\underline{J}}_{BS} < 0$. If one of these conditions isn't met, the luminosity intercepted by the disc element is $dL_r = 0$. If both are, we have

$$dL_r = \frac{(-\hat{\underline{\zeta}}.\hat{\underline{J}}_{BS})dA_d}{2\pi\zeta^2} dL. \tag{6.12}$$

We see that, the amount of luminosity intercepted depends on the projected area of the disc patch as seen by the flow element. If the patch is face-on as seen by the flow, $\hat{\underline{\zeta}}.\hat{\underline{J}}_{BS} = 1$ and the projected area is dA_d. This area reduces as the patch turns away from the emitting flow element. The total luminosity incident on a disc patch is calculated by adding up the contribution from every flow element.

6.7.3 Flow modulation calculations

We now need to calculate how much luminosity a telescope with effective area A_{eff} will intercept from a given flow element in order to again integrate over the whole flow. For the telescope to see any luminosity at all, two tests must again be passed. First of all, the viewer must be in the unit semi-sphere of the flow element. This means we require $\hat{\underline{A}}.\hat{\underline{S}} > 0$. We also won't see anything if the emission is blocked by the disc. We know the emission definitely won't be blocked by the disc if the flow element is above the disc; i.e. $\hat{\underline{r}}_f.\hat{\underline{J}}_{BS} > 0$. Even if the element is below the disc plane, we still might be able to see through the hole in the centre of the disc. So, imagine a point on the flow which is below the disc plane, emitting along the vector $\hat{\underline{S}}$. At some point it will intercept the disc plane. The distance between the flow element and the point where the vector crosses the disc plane is ζ. This point will be a distance r_d from the origin. We can write

$$\zeta\hat{\underline{S}} = -r_f\ \hat{\underline{r}}_f + r_d\ \hat{\underline{r}}_d. \tag{6.13}$$

Dotting both sides with $\underline{\hat{J}}_{BS}$ and rearranging gives

$$\zeta = \frac{-r_f \ \underline{\hat{r}}_f . \underline{\hat{J}}_{BS}}{\cos\theta_i}. \tag{6.14}$$

We then know that

$$r_d^2 = \zeta^2 + r_f^2 + 2\zeta r_f \underline{\hat{S}} . \underline{\hat{r}}_f. \tag{6.15}$$

If $r_d^2 < r_o^2$, we still see the flow element through the hole in the disc. If not, it is hidden by the disc.

So, if the unit-sphere and disc obstruction tests are not passed, the luminosity intercepted by the telescope is $dL_{obs} = 0$. Otherwise, this is

$$dL_{obs} = \frac{A_{eff} \ dL}{2\pi D^2}, \tag{6.16}$$

where D is the distance to the source. Note, because the telescope is so far away and is pointed straight at the black hole, we can say that the projected area of the telescope as seen by any flow element is A_{eff}. We then just set $A_{eff}/(2\pi D^2) = 1$, because it only tells us about normalisation, and sum up the contribution from each flow element.

6.7.4 Iron line profile calculations

A disc element at $r_d \ \underline{\hat{r}}_d$ is rotating with Keplerian velocity v_k. An observer at θ_i, ϕ_i then sees the disc patch travelling towards them at a velocity of $v = v_k \sin\phi \sin\theta_i$ where $\phi = \phi_i - \phi_d$. The tangent points of the disc will therefore travel towards the observer at a velocity of $\pm v_k \sin\theta_i$. This means that a photon emitted will energy E_{em} with be red shifted by

$$E_{em}/E_{obs} = (1 - 3/r_d)^{-1/2} \left[1 + \frac{\cos\alpha}{[r_d(1 + \tan^2\xi_o) - 2]^{1/2}} \right], \tag{6.17}$$

where

$$\begin{aligned} \cos\alpha &= \sin\phi \sin\theta_i (\cos^2\theta_i + \cos^2\phi \sin^2\theta_i)^{-1/2} \\ \tan\xi_o &= \cos\phi \sin\theta_i (1 - \cos^2\phi \sin^2\theta_i)^{-1/2}, \end{aligned} \tag{6.18}$$

(Fabian et al 1989; 2000).

For a given precession angle, γ, the flow luminosity incident on a disc patch described by r_d and ϕ_d is $L_r(r_d, \phi_d)$. If this luminosity were all emitted at energy E_{em}, the observer would see a luminosity, all at E_{obs}, of

$$dL_{obs} \approx L_r(r_d, \phi_d)(E_{obs}/E_{em})^3 \cos\theta_i. \tag{6.19}$$

Here, the approximations come from assuming light to travel in a straight line. Throughout this paper, we ignore gravitational light bending thus taking these to be good approximations. This should be apropriate since the inner radius of the flow is assumed to be $r_i = 7$ throughout and light bending effects outside of this radius will be minimal. The total observed luminosity as a function of energy is calculated by summing the contribution from each disc patch. As the flow precesses and the function $L_r(r_d, \phi_d)$ evolves, the observed iron line profile will change.

Chapter 7 | *Concluding remarks*

In this thesis, over the course of 5 papers, I have investigated a model intended to quantitatively explain the spectral and variability properties observed for XRBs. Set in the framework of the truncated disc model which was originally designed to explain the long term spectral transitions with a moving truncation radius, the first premise of the variability model is that, as the truncation radius moves in, all characteristic frequencies associated with that radius increase and thus the characteristic frequencies measured in the PSD also increase. Following authors such as Stella & Vietri (1998) and Marković & Lamb (1998), I associate the low frequency QPO with Lense-Thirring precession. However, in our model the entire inner accretion flow precesses as a solid body as has been seen in the recent numerical simulations of Fragile et al (2007; 2009). This extra step allows the model to reproduce the observed QPO frequency range in both BHBs (Ingram, Done & Fragile 2009) and NSBs (Ingram & Done 2010) with the extra advantage of predicting a QPO in the Comptonised emission rather than the disc, as is observed (Sobolewska & Życki 2006, Rodriguez et al 2004). Fluctuations in mass accretion rate driven by the intrinsically variable MRI (Balbus & Hawley 1998) but damped on the local viscous timescale in the accretion flow (Psaltis & Norman 2000; Churasov, Gilfanov & Revnivtsev 2001; Lyubarski 1997) can then produce the broad band noise observed in the PSD. In our model, the disc is stable and the flow is variable with the variability amplitude from a given annulus of the inner flow peaking at the local viscous timescale. Thus the low frequency variability is produced in the

outer flow and the high frequency variability in the inner part. As the truncation radius moves in, the lowest frequency noise is lost and the low frequency break in the power spectrum moves to higher frequencies.

The two processes can be tied together simply by imposing mass conservation. This allowed us to define a model for the QPO *and* broad band noise which uses only one set of parameters. We were thus able to fit the model to a series of observed PSDs (Ingram & Done 2011; Ingram & Done 2012a). Since this is a physical model, we can gain insight from the evolution of best fit parameters values which imply that the flow scale height collapses as the truncation radius moves in, consistent with the gas pressure reducing with temperature in the flow. Mass conservation also implies that the mass accretion rate fluctuations will drive fluctuations in the surface density and, consequently, the precession frequency, giving rise to a quasi-periodic oscillation rather than a pure periodicity. Since the total variability amplitude of the mass accretion rate fluctuations reduces as the truncation radius moves in, we naturally predict the QPO to be less coherent in the LHS than in the HIMS, as is observed (Rao et al 2010; Belloni 2010).

Also, one of the key predictions of this model is the short timescale QPO-flux correlation (Heil, Vaughan & Uttley 2011). Since the flux and precession frequency are both sensitive to the mass accretion rate fluctuations, the two correlate on short time scales ($\sim$3s). This was discovered in *RXTE* data from XTE J1550-564 *after* I wrote the original PROPFLUC code. When we looked for this property in the simulated data, it was present and, in fact, a necessary consequence of the assumptions we had already made. In addition to this, since the outer regions of the flow see a greater luminosity of seed photons than the inner regions and contribute slower variability, the frequency resolved spectrum (Revnivtsev, Gilfanov & Churazov 1999) can naturally be explained, at least qualitatively. This also allows the model to reproduce the observed phase lags between energy bands (Arévalo & Uttley 2006; Kotov, Chirazov & Gilfanov 2001).

Although this is encouraging, it by no means constitutes unambiguous proof for the model. Chapter 6 summarises our latest paper (Ingram & Done 2012b) in which we suggest a potentially unambiguous test for the precession model. As the flow precesses, the patch of the disc preferentially illuminated by the flow rotates such that a non face on observer sees a quasi-periodic shift between blue and red shift in the iron K_α line. We use a spectral model in order to predict the spectral shape as a function of QPO phase and simulate observation with *RXTE*, *XMM Newton* and the proposed ESA mission *LOFT*. We find that it may be difficult to constrain the spectral shape sufficiently with archival *RXTE* or *XMM Newton* data (consistent with Miller & Homan 2005). This could perhaps be solved with a very long *XMM Newton* observation. However, the effect will be clearly observable using *LOFT*, should it fly.

For all the successes of the model, there are weaknesses. Our assumption of a completely stable disc conflicts with observation (Wilkinson & Uttley 2009). Future versions of the model must incorporate disc variability. This could solve two other problems highlighted in chapter 5. Firstly, the model always predicts flat top noise whereas the observed PSD always has a 'double hump' shape that only approximates to flat top noise. Secondly, in order to achieve a fit to the PSD, we had to assume a surface density profile with a much more gradual drop-off at small radius than that predicted by the simulations (Fragile 2009; Ingram, Done & Fragile 2009). Perhaps the low frequency hump is actually generated in the inner few R_g of the outer disc (before propagating into the flow) and the flow only generates the high frequency hump. Since we will not then need the flow to produce variability on such a wide frequency range, it will be possible to reproduce the observations with the steep surface density drop-off measured from the simulations. If this transition region has constant width with its inner edge defined by the truncation radius, a moving truncation radius will still naturally give rise to a moving break frequency in the PSD.

However, in order to do this, we need to guide our assumptions with observation.

Currently, there are very few observations in which the disc is confirmed to be significantly variable (due to the high RXTE energy bandpass and comparative sparsity of suitable *XMM Newton* observations) and no one has actually measured the disc PSD or even confirmed if the inner regions of the disc are more variable than the outer regions. I believe it is possible to use Fourier techniques to answer some of these questions. Advances in our theoretical understanding of disc variability are also required. It seems plausible that a transition region between disc and flow will generate a large amount of turbulence, which could be a good candidate for the observed disc variability. However, is has not yet been possible to conduct a simulation of such a two phase flow.

This highlights another challenge. The Fragile et al (2007; 2009) simulations imply that a large scale height accretion flow can precess as a solid body if it is misaligned with the spin axis of the central black hole. In contrast, analytical work suggests the central regions of a thin disc should align with the black hole and the outer regions align with the binary system (the Bardeen-Petterson effect: Bardeen & Petterson 1975; Papaloizou & Pringle 1983; King et al 2005). If the flow is fed by a Bardeen-Petterson disc which aligns with the black hole spin axis from a large radius, it will not be misaligned and thus will not be expected to precess. However, there is uncertainty in the literature as to where this alignment occurs. If this happens at $r < 10$, the flow is intrinsically misaligned and is predicted to precess (although the effect on precession of torque from the disc must also eventually be taken into account). In fact, for relatively low values of α and/or high values of h/r, the disc does not fully align with the black hole spin plane in any region (Zhuravlev & Ivanov 2011). Future simulations considering a large scale height accretion flow with cooling artificially introduced at a few tens of R_g may yield a truncated disc / hot inner flow configuration and go some way to addressing this fundamental uncertainty (P. Chris Fragile; private communication).

Clearly, the model requires further development and refinement but I believe this work should be the first in what will eventually be a widely used technique of power

spectral fitting. Spectral fitting using physical models has been common place for decades and has formed the corner stone of our understanding of XRBs. The next step, as our observational capabilities and theoretical understanding increase, is to complement this with PSD fitting and advancing this even further to incorporate phase information.

Bibliography

[1] Abramowicz M., Jaroszynski M., Sikora M., 1978, A&A, 63, 221

[2] Agol E., Krolik J. H., 2000, ApJ, 528, 161

[3] Altamirano D., 2008, PhDT,

[4] Altamirano D., van der Klis M., Méndez M., Jonker P. G., Klein-Wolt M., Lewin W. H. G., 2008a, ApJ, 685, 436

[5] Altamirano D., van der Klis M., Méndez M., Wijnands R., Markwardt C., Swank J., 2008b, ApJ, 687, 488

[6] Arévalo P., Uttley P., 2006, MNRAS, 367, 801

[7] Arnaud K., Borkowski K. J., Harrington J. P., 1996, ApJ, 462, L75

[8] Axelsson M., Borgonovo L., Larsson S., 2006, A&A, 452, 975

[9] Ballantyne D. R., Ross R. R., Fabian A. C., 2001, MNRAS, 327, 10

[10] Balbus S. A., Hawley J. F., 1998, RvMP, 70, 1

[11] Bardeen J. M., Petterson J. A., 1975, ApJ, 195, L65

[12] Barret D., 2001, AdSpR, 28, 307

[13] Barret D., Olive J. F., Boirin L., Done C., Skinner G. K., Grindlay J. E., 2000, ApJ, 533, 329

[14] Barret D., Olive J.-F., Miller M. C., 2005, AN, 326, 808

[15] Beckwith K., Hawley J. F., Krolik J. H., 2008, MNRAS, 390, 21

[16] Belloni T., van der Klis M., Lewin W. H. G., van Paradijs J., Dotani T., Mitsuda K., Miyamoto S., 1997, A&A, 322, 857

[17] Belloni T., Psaltis D., van der Klis M., 2002, ApJ, 572, 392

[18] Belloni T., Homan J., Casella P., van der Klis M., Nespoli E., Lewin W. H. G., Miller J. M., Méndez M., 2005, A&A, 440, 207

[19] Belloni, T. M. 2010, Lecture Notes in Physics, Berlin Springer Verlag, 794, 53

[20] Belloni T., Homan J., Casella P., van der Klis M., Nespoli E., Lewin W. H. G., Miller J. M., Méndez M., 2005, A&A, 440, 207

[21] Beloborodov A. M., 1999, ApJ, 510, L123

[22] Cabanac, C., Henri, G., Petrucci, P.-O., et al. 2010, MNRAS, 404, 738

[23] Cannizzo J. K., Reiff C. M., 1992, ApJ, 385, 87

[24] Cannizzo J. K., 1993, ApJ, 419, 318

[25] Casella P., Belloni T., Homan J., Stella L., 2004, A&A, 426, 587

[26] Casella P., Belloni T., Stella L., 2005, ApJ, 629, 403

[27] Chaty S., Haswell C. A., Malzac J., Hynes R. I., Shrader C. R., Cui W., 2003, MNRAS, 346, 689

[28] Chakrabarty D., Morgan E. H., 1998, Natur, 394, 346

[29] Chiang C. Y., Done C., Still M., Godet O., 2010, MNRAS, 403, 1102

[30] Churazov E., Gilfanov M., Revnivtsev M., 2001, MNRAS, 321, 759

[31] Cui W., Zhang S. N., Chen W., 1998, ApJ, 492, L53

[32] Cui W., Zhang S. N., Chen W., Morgan E. H., 1999, ApJ, 512, L43

[33] Davis S. W., Done C., Blaes O. M., 2006, ApJ, 647, 525

[34] Deeming T. J., 1975, Ap&SS, 36, 137

[35] Dexter J., Fragile P. C., 2011, ApJ, 730, 36

[36] Di Salvo T., Méndez M., van der Klis M., Ford E., Robba N. R., 2001, ApJ, 546, 1107

[37] Done C., Gierliński M., 2006, MNRAS, 367, 659

[38] Done C., Gierliński M., Kubota A., 2007, A&ARv, 15, 1

[39] Done C., 2010, arXiv, arXiv:1008.2287

[40] Done C., Diaz Trigo M., 2010, MNRAS, 407, 2287

[41] Dove J. B., Wilms J., Maisack M., Begelman M. C., 1997, ApJ, 487, 759

[42] Dubus G., Lasota J.-P., Hameury J.-M., Charles P., 1999, MNRAS, 303, 139

[43] Ergma E., Antipova J., 1999, A&A, 343, L45

[44] Esin A. A., McClintock J. E., Narayan R., 1997, ApJ, 489, 865

[45] Everitt, C. W. F., et al., 2011, PRL, 106, 21101

[46] Fabian A. C., Rees M. J., Stella L., White N. E., 1989, MNRAS, 238, 729

[47] Fabian A. C., Iwasawa K., Reynolds C. S., Young A. J., 2000, PASP, 112, 1145

[48] Fabian A. C., et al., 2012, MNRAS, 3135

[49] Fender R. P., Belloni T. M., Gallo E., 2004, MNRAS, 355, 1105

[50] Fender R. P., Belloni T. M., Gallo E., 2005, Ap&SS, 300, 1

[51] Ferreira B. T., Ogilvie G. I., 2008, arXiv, arXiv:0810.1636

[52] Fragile P. C., Mathews G. J., Wilson J. R., 2001, ApJ, 553, 955

[53] Fragile P. C., Blaes O. M., Anninos P., Salmonson J. D., 2007, ApJ, 668, 417

[54] Fragile P. C., 2009, ApJ, 706, L246

[55] Fragile P. C., Meier D. L., 2009, ApJ, 693, 771

[56] Fragile P. C., Lindner C. C., Anninos P., Salmonson J. D., 2009, ApJ, 691, 482

[57] Fragos T., Tremmel M., Rantsiou E., Belczynski K., 2010, ApJ, 719, L79

[58] Frank J., King A., Raine D., 1992, apa..book,

[59] Galeev A. A., Rosner R., Vaiana G. S., 1979, ApJ, 229, 318

[60] Gammie C. F., Popham R., 1998, ApJ, 498, 313

[61] Gammie C. F., Shapiro S. L., McKinney J. C., 2004, ApJ, 602, 312

[62] Gaskell C. M., 2004, ApJ, 612, L21

[63] George I. M., Fabian A. C., 1991,

[64] Gierlinski M., Zdziarski A. A., Done C., Johnson W. N., Ebisawa K., Ueda Y., Haardt F., Phlips B. F., 1997, MNRAS, 288, 958

[65] Gierliński M., Zdziarski A. A., Poutanen J., Coppi P. S., Ebisawa K., Johnson W. N., 1999, MNRAS, 309, 496

[66] Gierliński M., Done C., Page K., 2008, MNRAS, 388, 753

[67] Gierliński M., Nikołajuk M., Czerny B., 2008, MNRAS, 383, 741

[68] Gilfanov M., Churazov E., Revnivtsev M., 1999, A&A, 352, 182

[69] Gilfanov M., Revnivtsev M., Molkov S., 2003, A&A, 410, 217

[70] Gilfanov, M., & Arefiev, V. 2005, arXiv:astro-ph/0501215

[71] Gilfanov M., 2010, LNP, 794, 17

[72] Gladstone J., Done C., Gierliński M., 2007, MNRAS, 378, 13

[73] Haardt F., Maraschi L., 1991, ApJ, 380, L51

[74] Haardt F., Maraschi L., 1993, ApJ, 413, 507

[75] Haardt F., Maraschi L., Ghisellini G., 1994, ApJ, 432, L95

[76] Haensel, P., Potekhin, A. Y., & Yakovlev, D. G. 2007, Astrophysics and Space Science Library, 326

[77] Hawley J. F., Balbus S. A., 1991, ApJ, 376, 223

[78] Heil L. M., Vaughan S., 2010, MNRAS, 405, L86

[79] Heil L. M., Vaughan S., Uttley P., 2011, MNRAS, 411, L66

[80] Heil L. M., Vaughan S., Uttley P., 2012, MNRAS, 422, 2620

[81] Henisey K. B., Blaes O. M., Fragile P. C., Ferreira B. T., 2009, ApJ, 706, 705

[82] Ibragimov A., Poutanen J., Gilfanov M., Zdziarski A. A., Shrader C. R., 2005, MNRAS, 362, 1435

[83] Ichimaru S., 1977, ApJ, 214, 840

[84] Ingram A., Done C., Fragile P. C., 2009, MNRAS, 397, L101

[85] Ingram A., Done C., 2010, MNRAS, 405, 2447

[86] Ingram A., Done C., 2011, MNRAS, 415, 2323

[87] Ingram A., Done C., 2012a, MNRAS, 419, 2369

[88] Kalemci E., Tomsick J. A., Rothschild R. E., Pottschmidt K., Kaaret P., 2004, ApJ, 603, 231

[89] Kato S., Fukue J., Mineshige S., 1998, bhad.conf,

[90] Kato S., 2008, PASJ, 60, 889

[91] Kawabata R., Mineshige S., 2010, PASJ, 62, 621

[92] King A. R., Kolb U., Burderi L., 1996, ApJ, 464, L127

[93] King A. R., Frank J., Kolb U., Ritter H., 1997, ApJ, 484, 844

[94] King A. R., Ritter H., 1998, MNRAS, 293, L42

[95] King A. R., Pringle J. E., West R. G., Livio M., 2004, MNRAS, 348, 111

[96] King A. R., Lubow S. H., Ogilvie G. I., Pringle J. E., 2005, MNRAS, 363, 49

[97] Klein-Wolt M., van der Klis M., 2008, ApJ, 675, 1407

[98] Kolehmainen M., Done C., 2010, MNRAS, 406, 2206

[99] Kolehmainen M., Done C., Díaz Trigo M., 2011, MNRAS, 416, 311

[100] Kotov O., Churazov E., Gilfanov M., 2001, MNRAS, 327, 799

[101] Krolik J. H., Hawley J. F., 2002, ApJ, 573, 754

[102] Krolik J. H., Hawley J. F., Hirose S., 2005, ApJ, 622, 1008

[103] Kubota A., Makishima K., Ebisawa K., 2001, ApJ, 560, L147

[104] Kumar S., Pringle J. E., 1985, MNRAS, 213, 435

[105] Lachowicz P., Done C., 2010, A&A, 515, A65

[106] Lasota J.-P., 2001, NewAR, 45, 449

[107] Lense J., Thirring H., 1918, Physikalische Zeitschrift, 19, 156

[108] Liu S., Melia F., 2002, ApJ, 573, L23

[109] Liu B. F., Meyer F., Meyer-Hofmeister E., 1997, A&A, 328, 247

[110] Livio M., Pringle J. E., 1992, MNRAS, 259, 23P

[111] Lubow S. H., Ogilvie G. I., Pringle J. E., 2002, MNRAS, 337, 706

[112] Lyubarskii Y. E., 1997, MNRAS, 292, 679

[113] Magdziarz P., Zdziarski A. A., 1995, MNRAS, 273, 837

[114] Makishima K., Maejima Y., Mitsuda K., Bradt H. V., Remillard R. A., Tuohy I. R., Hoshi R., Nakagawa M., 1986, ApJ, 308, 635

[115] Makishima K., et al., 2008, PASJ, 60, 585

[116] Malzac J., Beloborodov A. M., Poutanen J., 2001, MNRAS, 326, 417

[117] Malzac J., Dumont A. M., Mouchet M., 2005, A&A, 430, 761

[118] Malzac J., Belmont R., 2009, MNRAS, 392, 570

[119] Markoff S., Nowak M. A., Wilms J., 2005, ApJ, 635, 1203

[120] Marković D., Lamb F. K., 1998, ApJ, 507, 316

[121] Markowitz A., et al., 2003, ApJ, 593, 96

[122] Matt G., Perola G. C., Piro L., 1991, A&A, 247, 25

[123] Mayer M., Pringle J. E., 2007, MNRAS, 376, 435

[124] McClintock J. E., Shafee R., Narayan R., Remillard R. A., Davis S. W., Li L.-X., 2006, ApJ, 652, 518

[125] Medvedev M. V., 2004, ApJ, 613, 506

[126] Méndez M., 2006, MNRAS, 371, 1925

[127] Menou K., Narayan R., Lasota J.-P., 1999, ApJ, 513, 811

[128] Merloni A., Vietri M., Stella L., Bini D., 1999, MNRAS, 304, 155

[129] Middleton M., Done C., Gierliński M., Davis S. W., 2006, MNRAS, 373, 1004

[130] Middleton M., Done C., Schurch N., 2008, MNRAS, 383, 1501

[131] Miller J. M., Homan J., 2005, ApJ, 618, L107

[132] Miller J. M., Homan J., Miniutti G., 2006, ApJ, 652, L113

[133] Miller J. M., Homan J., Steeghs D., Rupen M., Hunstead R. W., Wijnands R., Charles P. A., Fabian A. C., 2006, ApJ, 653, 525

[134] Miller J. M., Reynolds C. S., Fabian A. C., Miniutti G., Gallo L. C., 2009, ApJ, 697, 900

[135] Miller M. C., Lamb F. K., Cook G. B., 1998, ApJ, 509, 793

[136] Misra R., Zdziarski A. A., 2008, MNRAS, 387, 915

[137] Mitsuda K., et al., 1984, PASJ, 36, 741

[138] Miyamoto S., Kitamoto S., 1989, Natur, 342, 773

[139] Motta S., Muñoz-Darias T., Casella P., Belloni T., Homan J., 2011, MNRAS, 418, 2292

[140] Mueller, M., Madejski, G., Done, C., & Zycki, P. 2004, X-ray Timing 2003: Rossi and Beyond, 714, 190

[141] Mueller M., Madejski G., 2009, ApJ, 700, 243

[142] Narayan R., Yi I., 1995, ApJ, 452, 710

[143] Narayan R., Kato S., Honma F., 1997, ApJ, 476, 49

[144] Negoro H., Matsuoka M., Mihara T., Otani C., Wang T. G., Awaki H., 2000, AdSpR, 25, 481

[145] Nespoli E., Belloni T., Homan J., Miller J. M., Lewin W. H. G., Méndez M., van der Klis M., 2003, A&A, 412, 235

[146] Noble S. C., Krolik J. H., 2009, ApJ, 703, 964

[147] Novikov I. D., Thorne K. S., 1973, blho.conf, 343

[148] Nowak M. A., Vaughan B. A., Wilms J., Dove J. B., Begelman M. C., 1999, ApJ, 510, 874

[149] Nowak M. A., et al., 2011, ApJ, 728, 13

[150] O'Neill S. M., Reynolds C. S., Miller M. C., Sorathia K. A., 2011, ApJ, 736, 107

[151] Oppenheim, A. V., & Schafer, R. W. 1975, Digital Signal Processing,

[152] Papadakis I. E., Lawrence A., 1993, MNRAS, 261, 612

[153] Papaloizou J. C. B., Pringle J. E., 1983, MNRAS, 202, 1181

[154] Pfister H., 2007, GReGr, 39, 1735

[155] Pietrini P., Krolik J. H., 1995, ApJ, 447, 526

[156] Piro A. L., Bildsten L., 2005, ApJ, 629, 438

[157] Pottschmidt K., et al., 2003, A&A, 407, 1039

[158] Poutanen J., Krolik J. H., Ryde F., 1997, MNRAS, 292, L21

[159] Press, W. H., Teukolsky, S. A., Vetterling, W. T., & Flannery, B. P. 1992, Cambridge: University Press, —c1992, 2nd ed.,

[160] Pringle J. E., 1981, ARA&A, 19, 137

[161] Pringle J. E., 1992, MNRAS, 258, 811

[162] Psaltis D., Belloni T., van der Klis M., 1999, ApJ, 520, 262

[163] Psaltis D., Norman C., 2000, astro, arXiv:astro-ph/0001391

[164] Rao F., Belloni T., Stella L., Zhang S. N., Li T., 2010, ApJ, 714, 1065

[165] Rees M. J., Begelman M. C., Blandford R. D., Phinney E. S., 1982, Natur, 295, 17

[166] Reis R. C., Fabian A. C., Ross R. R., Miniutti G., Miller J. M., Reynolds C., 2008, MNRAS, 387, 1489

[167] Reis R. C., Fabian A. C., Ross R. R., Miller J. M., 2009, MNRAS, 395, 1257

[168] Reis R. C., et al., 2011, MNRAS, 410, 2497

[169] Remillard R. A., McClintock J. E., 2006, AAS, 38, 903

[170] Remillard R. A., Sobczak G. J., Muno M. P., McClintock J. E., 2002, ApJ, 564, 962

[171] Revnivtsev M., Gilfanov M., Churazov E., 1999, A&A, 347, L23

[172] Revnivtsev M., Gilfanov M., Churazov E., 2001, A&A, 380, 520

[173] Reynolds C. S., Miller M. C., 2009, ApJ, 692, 869

[174] Rodriguez J., Corbel S., Hannikainen D. C., Belloni T., Paizis A., Vilhu O., 2004, ApJ, 615, 416

[175] Ross R. R., Fabian A. C., 2005, MNRAS, 358, 211

[176] Różańska A., Czerny B., 2000, MNRAS, 316, 473

[177] Rybicki G. B., Lightman A. P., 1979, rpa..book,

[178] Rykoff E. S., Miller J. M., Steeghs D., Torres M. A. P., 2007, ApJ, 666, 1129

[179] Schnittman J. D., 2005, ApJ, 621, 940

[180] Schnittman J. D., Homan J., Miller J. M., 2006, ApJ, 642, 420

[181] Shafee R., Narayan R., McClintock J. E., 2008, ApJ, 676, 549

[182] Shakura N. I., Sunyaev R. A., 1973, A&A, 24, 337

[183] Shapiro S. L., Lightman A. P., Eardley D. M., 1976, ApJ, 204, 187

[184] Sobczak G. J., McClintock J. E., Remillard R. A., Cui W., Levine A. M., Morgan E. H., Orosz J. A., Bailyn C. D., 2000, ApJ, 531, 537

[185] Sobolewska M. A., Życki P. T., 2006, MNRAS, 370, 405

[186] Steiner J. F., et al., 2011, MNRAS, 1036

[187] Stella L., Vietri M., 1998, ApJ, 492, L59

[188] Stella L., Vietri M., Morsink S. M., 1999, ApJ, 524, L63

[189] Stepney S., 1983, MNRAS, 202, 467

[190] Stern B. E., Poutanen J., Svensson R., Sikora M., Begelman M. C., 1995, ApJ, 449, L13

[191] Strohmayer T. E., Markwardt C. B., Kuulkers E., 2008, ApJ, 672, L37

[192] Sunyaev R., Revnivtsev M., 2000, A&A, 358, 617

[193] Tagger M., Pellat R., 1999, A&A, 349, 1003

[194] Tamura M., Kubota A., Yamada S., Done C., Kolehmainen M., Ueda Y., Torii S., 2012, ApJ, 753, 65

[195] Takahashi H., et al., 2008, PASJ, 60, 69

[196] Timmer J., Koenig M., 1995, A&A, 300, 707

[197] Titarchuk L., Osherovich V., 1999, ApJ, 518, L95

[198] Titarchuk L., Osherovich V., 2000, ApJ, 537, L39

[199] Titarchuk L., Shaposhnikov N., Arefiev V., 2007, ApJ, 660, 556

[200] Ueda Y., et al., 2010, ApJ, 713, 257

[201] Uttley P., McHardy I. M., 2001, MNRAS, 323, L26

[202] Uttley P., McHardy I. M., Papadakis I. E., 2002, MNRAS, 332, 231

[203] Uttley P., 2004, MNRAS, 347, L61

[204] Uttley P., McHardy I. M., Vaughan S., 2005, MNRAS, 359, 345

[205] van der Klis M., 1989, tns..conf, 27

[206] van der Klis M., Swank J. H., Zhang W., Jahoda K., Morgan E. H., Lewin W. H. G., Vaughan B., van Paradijs J., 1996, ApJ, 469, L1

[207] van der Klis M., 2004, AdSpR, 34, 2646

[208] van der Klis M., 2005, Compact Stellar X-Ray Sources, eds. W.H.G. Lewin and M. van der Klis, Cambridge University Press:astro-ph/0410551

[209] van der Klis M., 2005, Ap&SS, 300, 149

[210] van der Klis, M. 2006, Compact stellar X-ray sources, 39

[211] van Paradijs J., McClintock J. E., 1994, A&A, 290, 133

[212] van Paradijs J., 1996, ApJ, 464, L139

[213] van Straaten S., van der Klis M., di Salvo T., Belloni T., 2002, ApJ, 568, 912

[214] Vaughan S., Uttley P., 2005, MNRAS, 362, 235

[215] Wagoner R. V., Silbergleit A. S., Ortega-Rodríguez M., 2001, ApJ, 559, L25

[216] Wang Z.-Y., Huang C.-Y., Wang D.-X., Wang J.-Z., 2012, RAA, 12, 661

[217] Wijnands R., van der Klis M., 1999, ApJ, 514, 939

[218] Wilkinson T., Uttley P., 2009, MNRAS, 397, 666

[219] Wilkinson T., 2011, PhD thesis, University of Southampton

[220] Wilson C. D., Done C., 2001, MNRAS, 325, 167

[221] Zdziarski A. A., Johnson W. N., Magdziarz P., 1996, MNRAS, 283, 193

[222] Zdziarski A. A., Lubiński P., Smith D. A., 1999, MNRAS, 303, L11

[223] Zhuravlev V. V., Ivanov P. B., 2011, MNRAS, 415, 2122

[224] Życki P. T., Done C., Smith D. A., 1999, MNRAS, 309, 561